UNIVERSITY OF CAMBRIDGE
INSTITUTE OF ASTRONOMY

EXPLORING THE COSMOS WITH GRAVITATIONAL WAVES

STEPHEN R. TAYLOR

CHRIST'S COLLEGE

THIS DISSERTATION IS SUBMITTED FOR THE DEGREE OF
DOCTOR OF PHILOSOPHY

Supervisor:
DR JONATHAN R. GAIR

March 2014
Cambridge, United Kingdom

Declaration

This dissertation is the result of my own work and includes nothing which is the outcome of work done in collaboration except where specifically indicated in the text. No part of it has been submitted for any other qualification, and it is the result of my work under the guidance of my supervisor Dr Jonathan R. Gair. Use of the pronoun "we" in the main text merely reflects the author's stylistic preference.

The following chapters are based on articles that have been peer-reviewed and published, or are in preparation:

- CHAPTER 2
  Cosmology using advanced gravitational wave detectors alone
  Stephen R. Taylor, Jonathan R. Gair, and Ilya Mandel; Phys. Rev. D **85**, 023535 (2012), arXiv:1108.5161
- CHAPTER 3
  Cosmology with the lights off: Standard sirens in the Einstein Telescope era
  Stephen R. Taylor and Jonathan R. Gair; Phys. Rev. D **86**, 023502 (2012), arXiv:1204.6739
- CHAPTER 4
  Searching for anisotropic gravitational-wave backgrounds using pulsar timing arrays
  Stephen R. Taylor and Jonathan R. Gair; Phys. Rev. D **88**, 084001 (2013), arXiv:1306.5395
- CHAPTER 5
  Accelerated Bayesian model-selection and parameter-estimation in continuous gravitational-wave searches with pulsar-timing arrays
  Stephen R. Taylor, Justin A. Ellis and Jonathan R. Gair; submitted to Phys. Rev. D (2014), arXiv:1406.5224

Specific citation of any of these in the main text reflects work performed in collaboration. In particular, the brief analytic motivation at the beginning of Chapter 2 was developed by Ilya Mandel. In Chapter 4, the datasets analysed in Sec. 4.2 were generated by Alberto Sesana, while the injection software discussed in Sec. 4.5 was written and developed by Jonathan Gair. Also, in Chapter 5, the full-template searches with parallel tempering and thermodynamic integration, which were used for comparisons with my new accelerated search-techniques, were performed by Justin Ellis. The length of this dissertation including footnotes and bibliography is less than 60000 words. In all of the following we take $G = c = 1$.

Stephen R. Taylor
March 2014

Acknowledgements

Writing this dissertation marks the end of a very happy phase of my life in Cambridge. It's been a long road towards the culmination of this PhD, but an incredibly worthwhile one, and in times of frustration I still remind myself of how fortunate I am to make a career out of asking fundamental questions about the cosmos.

First and foremost I would like to thank my supervisor, Jon Gair, whose knowledge and abilities are a continued source of amazement to me. His guidance and advice throughout these past three and a half years have helped to shape whatever raw talent I have in this subject into the workings of a professional scientist. I have learnt much from him, and I feel our mutual collaborations have been very productive. I am indebted to Priscilla Cañizares for great chats, advice on navigating the treacherous early stages of a career in science, and for offering a sympathetic ear when things became stressful. My thanks go to the other members of the IoA Gravity Group, particularly Rob Cole, Chris Moore and former member Christopher Berry, for some great chats on science and life. The wealth of skills, expertise and intelligence found amongst the people I have been fortunate enough to work with during my studies is truly an embarrassment of riches.

It has been my great honour to work within the European and International Pulsar Timing Array organisations in the last stages of my PhD. For many great discussions, exciting collaborations, and for invaluable assistance, I must thank Rutger van Haasteren, Lindley Lentati, Stanislav Babak, Alberto Sesana, Alberto Vecchio, Chiara Mingarelli, Justin Ellis, and too many others to mention here. Our work together has been a fascinating experience, and it has been humbling to find so many great scientists welcome me into their venture to search for gravitational waves.

To my fellow fourth year PhD students: Stephen, Alan, Phil, Alex, Poul, Jonathan, and Adriano, thank you for fun conversations on movies, books, TV, sometimes just incoherent ramblings, and for creating a great working environment. I would also like to thank Siân Owen, Margaret Harding and Paul Hewett for their fantastic advice and willingness to help over the course of my studies. Also, the folks at the IoA's computer helpdesk have been pestered by me more times than they care to remember, but I credit them for putting up with me. Likewise, I would like to acknowledge the tireless efforts of the Cambridge High Performance Computing Service: much of the following work would not have been possible without the Darwin Supercomputer (provided by Dell Inc. using Strategic Research Infrastructure Funding from the Higher Education Funding Council for England).

There are several organisations without which I would not have been able to carry out the research presented here. In particular, I must acknowledge the financial support of the Science

and Technology Facilities Council, in addition to Christ's College, the Royal Astronomical Society, and the gravitational-wave group of Institut de Ciències de l'Espai, for additional travel expenses.

My former house-mates James Snee and Weelee Chan deserve credit for keeping me sane by going on random pub outings, cinema trips, and great banter in between. I also thank my old Oxford pals: Tim, Callum, Aimée, Amy, Joe, MattMatt and Stripes, who I've been fortunate enough to stay in touch with and see regularly during this hectic time in Cambridge. To my friends Chris and Ollie back in Northern Ireland, thank you for your continued friendship and unfathomable depths of Irish insult-based humour.

Finally, the greatest rock of support during all of my education has been my family. My mother, father, brother, and family dog are always there when I need them, welcoming me back home when I can visit, and reminding me of the truly important things in life. My mother is the most loving person I know, my father the hardest working, my brother the funniest, and my dog the most loyal. We've had a tough time recently, with my maternal grandmother unfortunately passing away before she could see me finish this degree, but as always, we will ride the storm together. I hope that I make you proud.

Abstract

Exploring the cosmos with gravitational waves

Stephen R. Taylor

Gravitational-wave (GW) observations of compact-object (CO) binaries will open up a new frontier in astrophysical studies of neutron stars (NSs) and black-holes (BHs). Near-future detections will shine a light on the coalescence rate of CO binaries, present an independent means of constraining cosmological parameters, and offer a host of other exciting opportunities.

In the first part of this thesis, we develop a technique to probe cosmological parameters with GWs in the absence of any electromagnetic counterparts. We exploit the near-future potential of a network of GW interferometers to extract the distance of each system from the measured gravitational waveform. We use the observed intrinsic narrowness of the NS-NS mass-distribution, along with GW-measured redshifted-masses, to deduce candidate redshift distributions for each system, thereby allowing a probe of the distance-redshift relation. We find that an advanced LIGO-Virgo network can place independent, complementary constraints on the Hubble constant, while a third-generation network will be needed to probe the dark-energy equation-of-state, as well as the star-formation rate of the NS-NS progenitor population.

In the second part, we study the potential for high-precision timing of millisecond pulsars to infer the perturbing influence of passing GWs. We develop a robust data-analysis pipeline to constrain the levels of anisotropy in a stochastic GW background using an ensemble of these pulsars. This technique cross-correlates pulse time-of-arrival deviations from many pulsars, leveraging the common influence of a stochastic background against noise sources, and mines the cross-correlation signature for information on the angular-distribution of GW-power. We also develop rapid first-cut techniques to perform parameter-estimation and model-comparison in single-source searches. These sources are most likely supermassive BH binaries, imprinting a signature of their orbital evolution as they roll past each pulsar. We coherently include these signatures within an accelerated pipeline to boost detection prospects.

Contents

Part I

Introduction

We shall not cease from exploration, and the end of all our exploring will be to arrive where we started and know the place for the first time.

T. S. Eliot

Oh! I have slipped the surly bonds of Earth
Put out my hand and touched the Face of God.

John Gillespie Magee, Jr.

1

Listening To The Cosmos

1.1 Gravity - It's All Downhill From Here...

Gravitation is the dominant dynamical influence in the Universe, and yet is the weakest of all forces. The same force that hugs us tightly to terra firma also governs the formation of galaxies and the growth of the Universe.

1.1.1 Standing On The Shoulders Of Giants

In the 16th century, Aristotelian and Ptolemaic astronomy was thrown into serious doubt by the heliocentric model of the Polish astronomer, Nicholaus Copernicus [1, 2], and the precision observations of Danish astronomer, Tycho Brahe. Kepler, who had been assistant to Brahe, made use of the unprecedented quantity and accuracy of the stellar catalogues compiled over more than 20 years of observations at Brahe's observatory, Uraniborg, to derive his three laws of planetary motion. In his 1609 book *Astronomia nova*, Kepler presented the first two of his laws based on precision observations of the orbit of Mars, and in so doing ushered in the revolutionary new heliocentric cosmology with elliptical, rather than circular, orbits[1].

Arguably the greatest scientific breakthrough of this age came in 1687, when Sir Isaac Newton published the *Principia* [3]. Although separately appreciated by contemporaries such

---

[1] Kepler's third law was later published in 1619.

as Hooke, Wren, and Halley, Newton's demonstrations of the universal inverse-square law of gravitation were remarkable for their predictive accuracy and the formulation's ability to derive Kepler's laws of planetary motion. Simply put, this law states that the mutual attraction between two *bodies*, whether they be planets or apples, is proportional to the product of their masses, and the inverse square of their separation. When applied to the motions of celestial bodies it was extraordinarily successful, and remains so today, even having sufficient accuracy to navigate humans to the Moon and back. One of its greatest trials also led to the zenith of its success, when in 1821 Bouvard published predictions of Uranus' position [4] which were subsequently found to deviate from observations. Motivated by this peculiarity, Le Verrier and Adams separately computed the properties of an additional body which might be perturbing Uranus through gravitational interaction. Their calculations were sound, with the new planet Neptune quickly discovered by Galle to be within one degree of Le Verrier's estimate and twelve degrees of Adams'.

Although Newtonian gravity had predicted the existence of a new planet, it still did not propose a mediator to transmit the gravitational influence. Furthermore, the scientist credited with Neptune's discovery, Le Verrier, had by 1859 noticed a peculiar precession of Mercury's orbit [5]. Various mechanisms were proposed, with precedent leading to the new planet *Vulcan* being advanced as a perturbing gravitational influence inside Mercury's orbit. A concerted effort was made to find this new planet, with little success. This problem would require a new way of thinking entirely, and a complete overhaul of the more than 200 years of Newtonian gravity.

1.1.2 The Happiest Thought

Great leaps forward in understanding necessitate a good anecdote, and for the case of General Relativity (GR), Einstein commented that the happiest thought of his life involved a Gedanken-experiment of a man falling from a roof. This led him to realise that the gravitational field is relative: a man in free fall is weightless and feels no pull of gravity. Cast into the Equivalence Principle, this says that an observer (without outside communication) is unable to tell the difference between the force felt in a gravitational field, and the fictitious force felt inside an accelerating reference frame.

In 1907, Minkowski's geometric formulation of special relativity (including time in the geometry) made clear that accelerating particles are represented by curved paths through this new 4-dimensional space-time [6]. Since acceleration is (locally) equivalent to gravitational influence, Einstein began to build connections between the manifestation of gravitation and non-inertial reference frames, eventually leading to the geometric emergence of gravity via curved space-time. Formulated within Riemannian geometry, Einstein's general theory of relativity [7] describes how energy-momentum leads to the deformation and curvature of space-time, causing bodies to follow geodesics of the metric which may themselves appear curved. In searching for a pithy summary, it's difficult to beat Wheeler: "*Space-time tells matter how to move; matter tells space-time how to curve*" [8]. The theory is enshrined within Einstein's field equations,

$$G_{\mu\nu} \equiv R_{\mu\nu} - \frac{1}{2}Rg_{\mu\nu} = 8\pi T_{\mu\nu} \tag{1.1}$$

where $G_{\mu\nu}$ is the Einstein tensor, $R_{\mu\nu}$ and $R = g^{\mu\nu}R_{\mu\nu}$ are the Ricci tensor and scalar, respectively, $g_{\mu\nu}$ is the metric, and $T_{\mu\nu}$ is the stress-energy tensor.

The phenomenal success of this new description of gravity, connecting relativistic electrodynamics with gravity, overturning notions of static space and time, and showing gravity to emerge from the curvature of the fabric of space-time itself, can not be understated. It accounts for the perihelion precession of Mercury as a conservative effect [7], corrects the Newtonian angular-deflection of light by massive bodies [9, 10], and predicts the redshifting of light propagating in a curved space-time [11].

The theory has passed a huge number of precision tests [12]. Doppler tracking of the *Cassini* spacecraft en route to Saturn performed tests of the Shapiro time-delay, showing agreement with GR to the 10^{-3} percent level [13]. The satellite *Gravity Probe B*, launched in 2004, made independent verifications of the general relativistic effects of geodetic and Lense-Thirring precession of a gyroscope's axis of rotation in the presence of the rotating Earth's curved space-time, to an accuracy of 0.28% and 19%, respectively [14]. Furthermore, one of the greatest legacies of the Apollo project is the positioning of retroreflectors on the Moon, permitting lunar laser ranging to test the Nordtvedt effect, geodetic precession, etc. [15].

Despite the manifest power of GR, there remain problems and untested predictions of the theory. Observations of Type Ia supernovae, measurements of temperature fluctuations in the cosmic microwave background (CMB), and data from Baryon Acoustic Oscillations (BAO), have constrained the compositional make-up of the Universe, showing that less than 5% is composed of known substances [16]. To explain the current growth and structure of the Universe, the current concordance cosmology (the ΛCDM model) invokes a form of matter which couples weakly to electromagnetic radiation (the so-called *dark matter*), and a cosmological constant term added to the field equations to produce an accelerated cosmological expansion [17, 18]. The latter effect may be due to the enigmatic *dark energy*, which exerts a negative pressure to induce accelerated growth. Despite ΛCDM being in excellent agreement with observations, the identity of dark energy (Λ) and cold dark matter (CDM) is an open question, even prompting the development of alternative gravitational theories which mimic these effects (see Ref. [19] for a comprehensive review).

Another early prediction of GR, which has yet to be directly tested, is the existence of gravitational radiation [20, 21]. Analogous to the case of electromagnetism, an accelerating body would create ripples of gravitational influence via deformations in the dynamic space-time. Gravitational waves (GWs) have had a colourful history. Their physical existence was the subject of much early doubt (see Ref. [22]). The complexity of the theoretical problems meant it took decades to solve for models of GW signals. Finally, the technological challenges to detect and characterise these signals were such that we are only now in a position to have a chance of directly measuring them. Measurements of the Post-Keplerian orbital parameters of pulsars in binary systems (such as the famous PSR B1913+16 [23, 24], and the double-pulsar J0737-3039 [25]) have provided an extraordinary indirect test of the existence of gravitational radiation, and fascinating astrophysical laboratories with which to probe gravity [26]. Additionally, recent results hint at the detection of a B-mode (or "curl" mode) signal in the CMB polarisation at degree angular scales, which is alleged to have a primordial GW origin [27, 28]. However, the goal now is to directly measure the interaction of GWs with our experiments.

1.2 A Brief Primer On Gravitational Waves

An insight into the nature of gravitational waves (GWs) can be gained by considering Einstein's original linearised treatment [20, 21]. We model the space-time as essentially flat with a small perturbation,

$$g_{\alpha\beta} = \eta_{\alpha\beta} + h_{\alpha\beta}, \tag{1.2}$$

where $\eta_{\alpha\beta}$ is the flat Minkowski metric, and $h_{\alpha\beta}$ is a small perturbation such that we can use the flat metric to raise and lower space-time indices. In this approximation, the linearised Einstein tensor becomes,

$$G_{\alpha\beta} = \frac{1}{2}\left(\partial_\alpha\partial^\mu h_{\mu\beta} + \partial_\beta\partial^\mu h_{\mu\alpha} - \partial_\alpha\partial_\beta h - \Box h_{\alpha\beta} + \eta_{\alpha\beta}\Box h - \eta_{\alpha\beta}\partial^\mu\partial^\nu h_{\mu\nu}\right), \tag{1.3}$$

where $h = \eta^{\alpha\beta}h_{\alpha\beta}$ is the trace of $h_{\alpha\beta}$, and $\Box = \eta^{\alpha\beta}\partial_\alpha\partial_\beta$ is the flat space d'Alembertian operator. This expression can be tidied up by recasting the right-hand side in terms of the trace-reversed perturbation ($\bar{h}_{\alpha\beta} = h_{\alpha\beta} - n_{\alpha\beta}h/2$),

$$G_{\alpha\beta} = \frac{1}{2}\left(\partial_\alpha\partial^\mu \bar{h}_{\mu\beta} + \partial_\beta\partial^\mu \bar{h}_{\mu\alpha} - \Box\bar{h}_{\alpha\beta} - \eta_{\alpha\beta}\partial^\mu\partial^\nu \bar{h}_{\mu\nu}\right). \tag{1.4}$$

We now make use of the fact that slowly varying diffeomorphisms are a symmetry of linearised gravity, allowing us to choose an appropriate gauge. If we consider the coordinate transformation $x^\alpha \mapsto x^\alpha + \xi^\alpha$, the transformation of the metric perturbation to first order is $h_{\mu\nu} \mapsto h_{\mu\nu} - (\partial_\mu\xi_\nu + \partial_\nu\xi_\mu)$. Asserting $\partial_\mu\xi_\nu$ to be of the same order as $|h_{\mu\nu}|$, the transformed metric perturbation retains the condition $|h_{\alpha\beta}| \ll 1$. This symmetry allows us to choose the Lorenz gauge, where $\partial^\mu\bar{h}_{\mu\nu} = 0$, such that the Einstein tensor reduces to the much more compact

$$G_{\alpha\beta} = -\frac{1}{2}\Box\bar{h}_{\alpha\beta}, \tag{1.5}$$

and the field equations reduce to

$$\Box \bar{h}_{\alpha\beta} = -16\pi T_{\alpha\beta}, \tag{1.6}$$

which can be solved using the radiative Green's function to give wave solutions. Expressed in this form, we might be led to think that all components of the metric perturbation are radiative. This is a gauge artefact [29], where, in general, we can split the metric perturbation into (i) gauge degrees of freedom, (ii) physical, radiative degrees of freedom, and (iii) physical, non-radiative degrees of freedom. One can show [30] that the only physical, radiative degrees of freedom in $h_{\mu\nu}$ are the spatial, transverse and traceless components. Hence, $h_{\mu\nu}$ is usually projected into the so-called TT (transverse-traceless) gauge, where the components of the perturbation are orthogonal to the direction of the wave's propagation. Choosing a coordinate system such that we have a plane GW propagating in the z-direction in a vacuum, we can write the metric perturbation as,

$$h_{\mu\nu} = \begin{pmatrix} 0 & 0 & 0 & 0 \\ 0 & h_+ & h_\times & 0 \\ 0 & h_\times & -h_+ & 0 \\ 0 & 0 & 0 & 0 \end{pmatrix}, \tag{1.7}$$

where h_+ and $h_\times$ are the amplitudes of the two distinct polarisations of GWs permitted within general relativity, denoted as "plus" and "cross" modes for how they tidally deform a circular ring of test masses in the plane perpendicular to the direction of propagation. The tidal acceleration caused by a wave as it propagates is at the heart of *all* currently planned ground-based and space-based detection efforts, since what we measure is not an absolute acceleration itself, but rather its difference across an experiment. The fractional change in the *proper* distance between two points separated by $\Delta x = L$ on the x-axis of our coordinate system (or experiment) due to the passage of a GW is given by $\delta L/L \simeq h_+/2$ [30], leading to a definition of the GW amplitude as the *strain*. For a periodic signal such that $h_+(z=0,t) = h_0 e^{2\pi i f t}$, we see that this proper distance separation oscillates according to $\delta\ddot{L} = (2\pi f)^2 L h_0 e^{2\pi i f t}$ [31]. From Eq. (1.7) we see that the "plus"-polarisation will lengthen distances along the x-axis while simultaneously contracting distances along the y-axis. The influence of the $h_\times$ mode is similar, but rotated by $\pi/4$ degrees anti-clockwise in the xy-plane. This tidal deformation in the plane perpendicular to the direction of propagation is illustrated for a full wave-cycle in Fig. 1.1.

If we consider the far-field approximation, then the lowest-order contribution to the solution of Eq. (1.6) is a function of the accelerating quadrupole moment of the source's energy-density distribution. The reason for this is stress-energy conservation: the monopole moment gives the conserved total energy of the system, while the dipole moment gives the conserved momentum of the system's centre-of-mass. Therefore the *quadrupole radiation formula* for the spatial

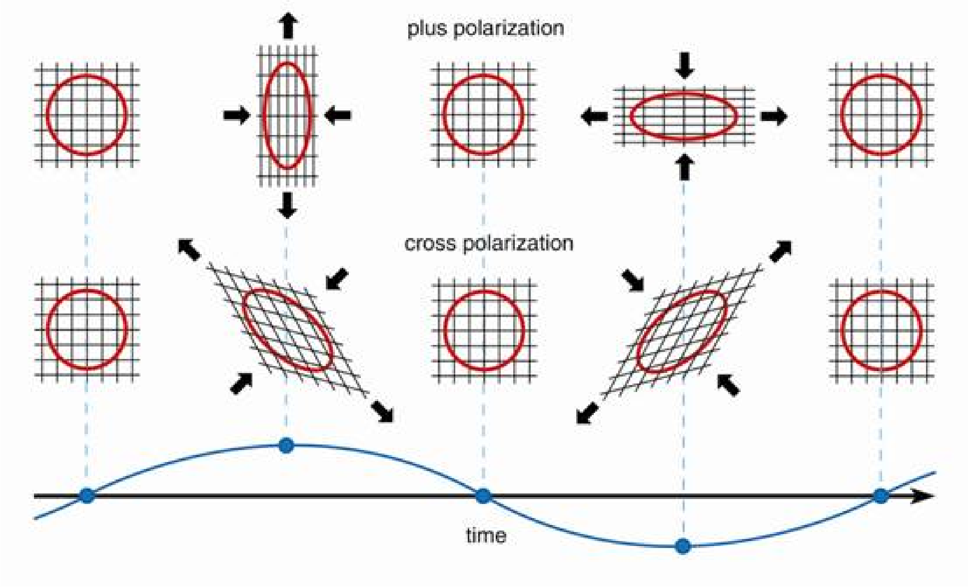

Figure 1.1: The periodic deformation of space-time caused by a GW is shown for the two polarisations permitted within GR. The influence of the GW is entirely in the plane perpendicular to the direction of propagation. Image credit: Tom Dunne, `www.itp.uzh.ch/~chuwyler/index.php?page=gravwaves`.

components of the metric perturbation is [21],

$$h_{ij} = \frac{2}{r}\frac{d^2Q_{kl}}{dt^2}\Lambda_{ik,jl}, \tag{1.8}$$

where r is the distance to the source, and Q_{kl} is the *reduced* quadrupole moment of $\rho(t,\vec{x})$ (the source's energy-density distribution), which is defined as,

$$Q_{ij} = \int d^3x \left(x_i x_j - \frac{1}{3}x^2\delta_{ij}\right)\rho(t,\vec{x}), \tag{1.9}$$

and $\Lambda_{ik,jl}$ is the so-called *Lambda tensor* which projects the metric perturbation in the Lorenz gauge into the TT gauge [32].

We now take a specific example of a source system (see Ref. [33]). Binary systems consisting of compact objects (COs) were very early on recognised as potential sources of gravitational radiation [29, 34, 35]. Let us consider two compact objects, each of mass M, orbiting each other at a distance $R(t)$ from their common centre of mass (assumed to be far enough apart that we can ignore tidal disruption) with slowly varying angular velocity $\omega(t)$. The COs are assumed to be moving at non-relativistic speeds to simplify the calculation of the quadrupole moment tensor. Kepler's third law gives us $\omega^2 = M/4R^3$, such that the total energy of the system is $E = -M^2/4R$.

We define the coordinate origin at the system's centre of mass, with the orbit lying in the

xy-plane. The coordinates of the COs at $t = 0$ are,

$$x_a = -x_b = R\cos\omega t, \quad y_a = -y_b = R\sin\omega t, \quad z_a = z_b = 0. \tag{1.10}$$

We further choose to evaluate the field along the z-axis, such that the direction of wave propagation is along the z-direction. In this case the Lambda tensor serves to remove all z-indexed elements of $h_{\mu\nu}$.

Evaluating the second time-derivative of the reduced quadrupole mass-moment and plugging into Eq. (1.8), one can show that the radiative components of the GWs from this system are,

$$h_{\mu\nu} = -\frac{8MR^2\omega^2}{r}\begin{pmatrix} 0 & 0 & 0 & 0 \\ 0 & \cos 2\omega t & \sin 2\omega t & 0 \\ 0 & \sin 2\omega t & -\cos 2\omega t & 0 \\ 0 & 0 & 0 & 0 \end{pmatrix}. \tag{1.11}$$

Notice that the GW frequency is twice the binary orbital frequency due to the quadrupolar nature of the emission. Also note that the distance to the source system is directly encoded in the amplitude of this leading-order radiative term. By evaluating the energy-flux elements of the *Isaacson expression* [36], and integrating over the sphere, the GW luminosity of the source system is given by [37],

$$L_{\mathrm{GW}} = \frac{1}{5}\left\langle \frac{d^3Q_{ij}}{dt^3}\frac{d^3Q^{ij}}{dt^3} \right\rangle, \tag{1.12}$$

which, for a CO binary, gives,

$$L_{\mathrm{GW}} = \frac{128}{5}M^2R^4\omega^6. \tag{1.13}$$

By equating the change in the binary's orbital energy with the GW luminosity, we can get a qualitative understanding of the frequency and strain-amplitude evolution as the binary inspirals toward an eventual merger. The binary orbital frequency evolves with the time until coalescence, τ, as $\omega \propto \tau^{-3/8}$, while the amplitude of the strain in Eq. (1.11) evolves as $h_0 \propto \tau^{-1/4}$. We see that the orbital evolution, driven by GW emission, causes the frequency and amplitude to characteristically "chirp" as they merge.

This treatment is appropriate when the orbital velocities are small ($v \ll c$), however, when the system evolves closer to the merger phase higher-order corrections to the metric perturbation from the full non-linear structure of the field-equations must be taken into account. In particular, for binaries of comparable mass the *post-Newtonian* (pN) formalism has been studied extensively, where the acceleration of one object due to the gravity of the other includes corrections to higher-order in (v/c) [e.g., 38, 39]. The lowest order correction modifies this such that the acceleration a body feels depends on its *own* mass. This is a manifestation of the space-time curvature caused by the body itself, which influences the orbital dynamics, and is known as the *self-force*. After the pN formalism breaks down, we can model the late-inspiral using the *effective one-body* (EOB) approach [40]. This technique recasts the problem of two merging COs into the equivalent picture of a single body moving in a deformed BH space-time, but is still dependent on numerical relativity (NR; discussed later) solutions to calibrate the computed waveforms.

The self-force is also a crucial feature in the *perturbation theory* treatment of binaries with an extreme mass ratio [e.g., 41]. If we have a small body in orbit around a massive black-hole (BH), then to first approximation we can consider the small body as moving along geodesics of the black-hole metric. However, if we take into account perturbations to the background space-time caused by the small body, then it now follows a *forced* geodesic, where the forcing-term is of the order of the small body's correction to the background space-time, and is composed of conservative and dissipative pieces. Perturbation theory can also successfully model the waveform of the *ringdown phase* of the post-merger remnant, where the frequencies and decay-times of the final BH's quasinormal-modes depend only on its mass and spin.

The difficult phase to model is the merger. As we get closer to the final merger of the objects, no iterative expansion or approximation scheme is helpful. In this scenario, where we have two COs (possibly BHs) in a highly dynamical space-time, we must attempt to solve the full Einstein field-equations numerically. Up until about 10 years ago the field of *numerical relativity* had made little progress, with simulations barely able to model a single binary orbit before the codes crashed. However several breakthroughs since that time have revolutionised the field [42–44], allowing the orbital dynamics and GW emission to be computed right through the merger phase.

We are entering the era of advanced GW detectors equipped with highly successful schemes to compute waveform templates, where combinations of pN, EOB and NR techniques can stitch together a full description of the GWs emitted during a binary's cataclysmic merger [45–48].

1.3 The Gravitational Wave Spectrum

Like electromagnetic radiation, GWs come in a range of frequencies from many different sources, where, roughly speaking, the characteristic frequency scales inversely with the total mass of the system. Most electromagnetic radiation from astronomical sources is an incoherent superposition of radiation from sources much larger than the characteristic observed wavelengths. However, the situation is rather different for GWs since current detection techniques are limited to probing sub-kHz frequencies where the sources are of a comparable size to the emitted wavelengths. As such, near future measurements of GWs will track the coherent motion of extremely massive, compact objects.

The first pioneering efforts to directly detect GWs began when their theoretical study was still in disarray. Joseph Weber developed a strong interest in GWs during the 1950s as a result of collaborative work with Wheeler [49], even going so far as to propose and build his own detection apparatus [50]. Known as a *Weber bar* (or "resonant mass detector"), this instrument made use of the tidal deformation induced by a passing GW to *transfer energy* to and elastically deform an aluminium cylinder, creating longitudinal oscillations which would be measured by piezoelectric transducers. The detector was tuned to operate around 1660 Hz because of experimental feasibility, and because this frequency could be swept through during a supernova core collapse. The community was taken by surprise when Weber reported coincident signals in detectors which were separated by approximately 1000 km [51], giving tentative evidence of the first direct GW detection. Unfortunately, follow-up experiments by independent groups failed to verify his results [52]. Nevertheless Weber deserves credit for kickstarting GW experimental efforts, and reinvigorating theoretical interest.

Although there are several modern resonant mass detectors (such as AURIGA [53], and the spherical MiniGRAIL [54]), contemporary efforts focus on the use of precision timing and interferometry to measure the *strain amplitude* of a passing GW. The foundations of GW interferometry were laid by Forward [55] and Weiss [56]. A full review of ground and space-based interferometry as it pertains to GW detection can be found in Ref. [57].

As a rough guide, the peak sensitivity of our detectors scales inversely with the size of the experiment itself. Figure 1.2 illustrates the GW strain-spectrum, with the sensitivity of current and planned detectors overlaid on the bands of compelling astrophysical targets. At the lowest frequencies we need precisely timed pulsars at kiloparsec distances to probe into the nHz band, where a stochastic background of merging SuperMassive Black-Hole (SMBH) binaries may be found. The 1 Hz to 10^4 Hz band is the terrestrial detector band, where kilometre-scale laser interferometers are targeting core-collapse supernovae, and the chirping signals of inspiraling stellar-mass compact binary systems. The lowest frequency we can probe with terrestrial detectors (~ 1 Hz) is restricted by local gravitational gradients and seismic noise isolation. The only way to overcome this "seismic wall" is by moving our experiment to space. Space-based laser interferometers of $\sim 10^9$ m arm-length are planned which will dig into the 0.1 mHz to 0.1 Hz band, which will allow precision studies of massive BH demographics.

We now discuss these detectors and their targets in more detail, giving particular emphasis to those of greatest relevance to this dissertation.

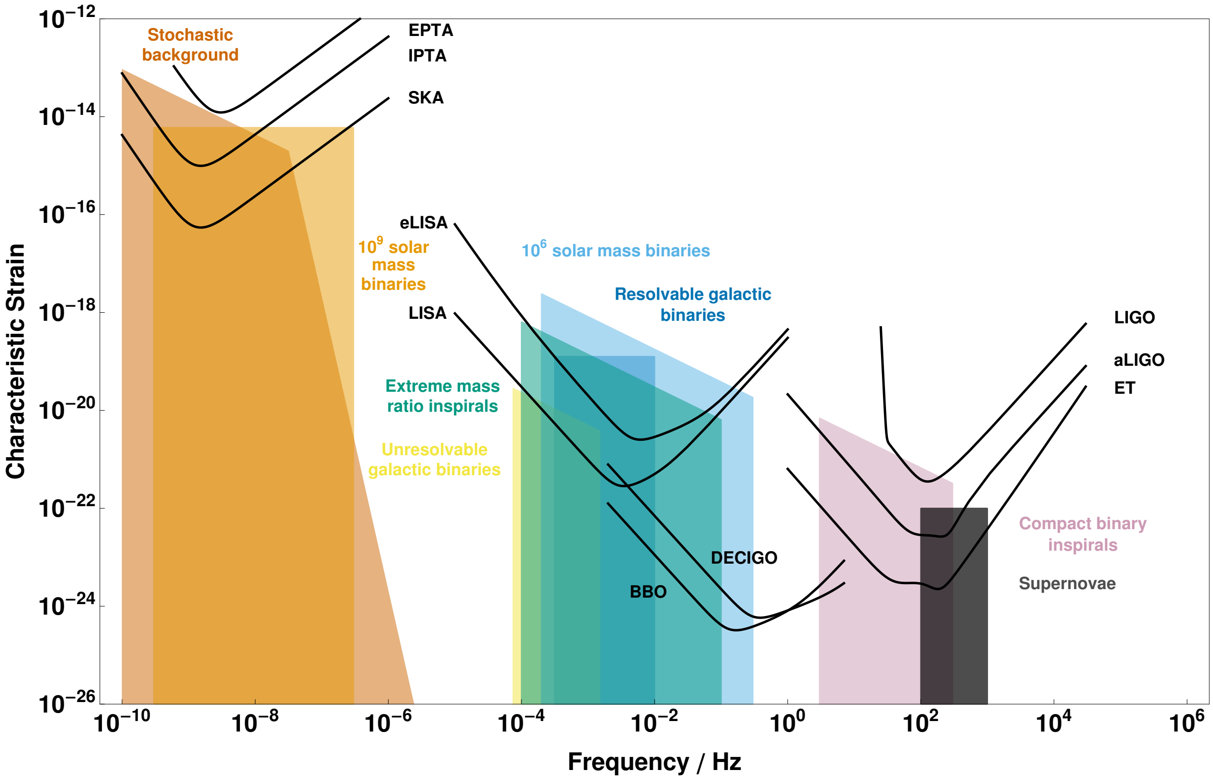

Figure 1.2: A cartoon representation of the GW spectrum, spanning ~ 14 orders of magnitude in frequency. Sources are indicated by their characteristic strain-amplitude, while detectors are indicated by their strain-sensitivity. The question of what the most senstive GW detector is will depend on our figure-of-merit, where the sensitivities of PTAs, LISA, and LIGO are far more comparable when considered in terms of GW energy density. Produced using the web-app at `http://www.ast.cam.ac.uk/~rhc26/sources/`, and modified with the help of Christopher Moore.

1.3.1 High frequency ($1\text{ Hz} \lesssim f \lesssim 10^4\text{ Hz}$)

Detectors

This high-frequency band requires long-baseline terrestrial GW-interferometry, achieving a strain sensitivity of $\sim 10^{-21}$ or lower in order to have a realistic chance of detecting likely astrophysical GW sources. The basic mode of operation is that of a Michelson interferometer, where laser light is injected into the interferometer and subsequently split into two beams to propagate along orthogonal arms. Each laser beam reflects off end test-mass optics, followed by the two beams recombining at the beamsplitter to interfere at a photodiode. The influence of an impinging GW is through the alternate stretching and compression of the proper-length of the arms (see Sec. 1.2), inducing a phase-shift in the recombined laser beams. The detectors are locked on a dark fringe to improve resolution and cancel out laser phase noise [37, 58], however there are many other interfering noise sources.

To achieve the required design sensitivity for science operation, several sophisticated technical advances have been implemented, such as power and signal recycling [59–61], which place additional optics after the laser and before the photodiode, respectively. The aim here is to impede the reflection of light back into the source laser, and to improve signal strength for narrow bandwidth or "chirping" binary searches. Optical cavities (such as a Fabry-Pérot) are also used to increase the effective path-length of laser light within the interferometer, and to minimise photon shot-noise which is the main instrumental noise source at high frequencies [62]. One can overcome shot-noise by simply boosting the laser power, which comes at the price of increasing radiation pressure on the test-mass, but this in turn can be overcome with a heavier mirror. Another important noise consideration is the thermal motion of the test-mass mirrors themselves, which can only be remedied by ensuring the materials used have the lowest feasible mechanical loss factors [63, 64]. The limiting noise sources at the lowest frequencies of the terrestrial detector band are seismic and gravity-gradient noise. The former can be ameliorated by a combination of pendulum isolation, spring suspension, and anti-vibration actuators [65–67], however gravity-gradient noise is a more difficult problem. This is caused by seismic waves on the surface of the Earth creating local mass-density fluctuations whose gravitational influence couples to the test-masses. It can be minimised by monitoring seismic activity to subtract its signal, or moving the detector underground, but below ~ 1 Hz there is no other choice but to completely distance the detector from these surface-wave density fluctuations by moving to space.

The first kilometre-scale detection instrument for GWs was the Laser Interferometer Gravitational wave Observatory (LIGO) [68, 69], operated in partnership between the California Institute of Technology (Caltech) and the Massachusetts Institute of Technology (MIT). There are three instruments in total, all located in the USA, with two sited in Hanford, Washington within a common vacuum envelope (H1, H2 of arm-lengths 4 km and 2 km respectively) and one in Livingston, Louisiana (L1 of arm-length 4 km). By early 2002 all LIGO interferometers had achieved lock on a dark fringe, and have since undergone several upgrades and science runs. By 2005 the detectors had reached their design sensitivities, and it was decided that a final period of data taking would commence before extensive upgrades would take place. This run, S5, was completed in late 2007, where the largest angle-averaged horizon distance to an inspiraling NS-NS system achieved was ~ 15 Mpc in L1/H1 [70].

Following S5, the LIGO instruments underwent enhancements to improve their strain sensitivity in the shot-noise regime by approximately a factor of two. This was achieved by almost tripling the laser power of initial LIGO in H1 and L1, however H2 had to be left in its original configuration as it was still being operated to keep watch while the others were upgraded. This new configuration, known as Enhanced LIGO [71], involved the implementation of prototype technologies and methods which were being road-tested for the upcoming major overhaul of LIGO into Advanced LIGO (aLIGO) [72]. The final science run of Enhanced LIGO was S6 between 2009-2010, where the averaged horizon distance to NS-NS inspirals was $\sim 10-20$ Mpc [73]. After this period of data-taking the LIGO detectors were taken offline to be upgraded to its second-generation configuration.

At the time of writing, LIGO is being upgraded to aLIGO, which is due for completion in ~ 2015, after which the averaged horizon distance for NS-NS inspiral detection will be boosted to ~ 200 Mpc [72], giving an almost thousandfold gain in volume sensitivity of the detectors. The key improvements for aLIGO are much higher laser power (with improved shot-noise behaviour), quadruple-pendulum suspensions which lowers the "seismic wall" to just above 10 Hz, low-mechanical-loss suspension-fibres and mirror materials, and active isolation of the optical benches. Both H1 and L1 are being upgraded, but the fate of H2 is still slightly uncertain. It was suggested that moving H2 to another distantly located site would be a huge advantage, both in terms of common-noise mitigation, and for the increased signal-delays which would improve source triangulation on the sky [74, 75]. The most favourable option would have been to re-locate H2 to Australia where it would have been almost antipodal to H1/L1, however this did not materialise. Fortunately, progress appears to have been made in the prospects for placing the instrument in India, such that LIGO-India, commissioned and operated by the Indian Initiative in Gravitational-wave Observations (IndIGO), would be due to come online by ~ 2020 [76–78].

In addition to the LIGO detectors, there is the French/Italian 3 km Virgo interferometer [79] located at Cascina, near Pisa, in Italy, which began commissioning runs in 2005. Virgo was designed to be of comparable sensitivity to LIGO, and although not quite able to match the peak sensitivity around ~ 150 Hz, the use of a *superattenuator* to give aggressive seismic isolation allowed Virgo to probe GWs down to the $\sim 10-20$ Hz level [80]. Concurrently with the Enhanced LIGO upgrades, Virgo was being upgraded to Virgo+, whereupon it had boosted laser power and increased thermal compensation on the optics [81]. During Virgo Science Run (VSR) 2, Virgo+ achieved close to the design sensitivity of the initial Virgo plans. The final science run of "initial" Virgo was VSR3 in 2010, after which it was taken offline for its upgrades to Advanced Virgo (AdV) [82]. This major upgrade is planned to be on a similar timescale to aLIGO, with the principle modifications being increased laser power and improved mirror coatings.

Additionally, there is a 600 m arm-length interferometer, known as GEO-600 [83], located near Hannover, Germany. With a smaller baseline and lower laser power, GEO-600 cannot match the sensitivity of LIGO/Virgo, but it has been an incredibly useful testbed for advanced technologies and techniques to be implemented in the future second-generation designs. It achieved first lock in 2001, followed by the first implementation of dual (power and signal) recycling in 2003. It has also pioneered the use of multiple pendula suspensions and rod-laser amplification. From 2009, GEO-600 has been upgraded to achieve higher frequency sensitivity by injecting "squeezed" light into the output port. This project, known as GEO-HF, permits the interferometer to operate beyond the standard quantum limit [84]. As of writing, GEO is currently operating in Astrowatch mode, and is the only large-scale terrestrial GW detector taking data while LIGO and Virgo are offline for their upgrades.

The first interferometer to start taking regular data with sufficient stability and sensitivity to have a chance of GW detection was actually the 300 m arm-length TAMA-300 detector [85]. Located at the Mitaka campus of the National Astronomical Observatory of Japan, it had undertaken nine observation runs by 2004, but the short arm-length meant its sensitivity was limited. Attention in Japan has now shifted to the Cryogenic Laser Interferometer Observatory (CLIO) [86] which is a 100 m prototype operating underneath the Kamiokande mountain. The aim of CLIO is to develop technologies for the proposed 3 km arm-length KAmioka GRAvitational wave telescope (KAGRA; formerly LCGT [87]) [88, 89], which will also operate in the Kamioka mine under cryogenic conditions. Placing KAGRA underground dramatically suppresses seismic disturbances and gravity-gradient noise, such that, by the time of full operation in $\sim$ 2018, it should have a similar sensitivity to aLIGO and AdV.

Throughout the last 10 to 15 years, all of the first-generation detectors have operated at some level of coincidence with each other. TAMA-300 operated in coincidence with LIGO and GEO-600 for two data-taking periods [90], while LIGO, Virgo and GEO have been participating in joint searches since 2006 [91]. The first joint search for compact binary coalescence signals during the LIGO S5 science run and the Virgo VSR1 data did not result in direct detections

[70], nor did the "enhanced" detector search during the LIGO S6 science run and the Virgo VSR2+3 data [73]. Furthermore, the upper limits placed on compact-binary coalescence rates from the latter search remain roughly two orders of magnitude above best-guess astrophysical predictions. Nevertheless, in the advanced era we will have a global network of road-tested instruments which have a realistic chance of regular GW detections, helping to turn the field from the search for the first detection, towards precision astrophysics.

Beyond these second-generation detector plans, there are concepts for new third-generation detectors aiming to achieve a broadband order of magnitude improvement in strain-sensitivity and to push operation down into the $\sim 1-10$ Hz range. The most notable of these is the Einstein Telescope (ET) [92], with the European Commission's FP7 framework recently carrying out a design study [93] to evaluate the science case and technological hurdles of such a detector. Some favoured designs emerged, including a triple-interferometer in a 10 km arm-length equilateral triangle configuration [94–96]. A novel "xylophone" design was also proposed, whereby a high-power, high-frequency interferometer (ET-HF) would operate above-ground, while a cryogenic low-power, low-frequency interferometer (ET-LF) would operate underground [97]. There are significant technological challenges to be overcome if these plans are to be realised.

Sources

Binary systems consisting of two compact objects (COs) whose orbital evolution is entirely dictated by GW emission have long been of interest to the GW community, and are the chief target in the high-frequency (terrestrial detector) band. These systems are the final evolutionary state of massive-star binary systems, and the clean GW signal close to merger provides an important testbed of gravitation, stellar evolution, CO formation, and the equation of state (EOS) of nuclear matter. Briefly, the formation of these binaries involves two massive stars evolving quickly through the main sequence, undergoing successive supernovae to form compact objects (which may be NSs or BHs), and inspiraling towards an eventual cataclysmic merger through GW emission. If at least one of the components is a NS, this merger may be associated with an electromagnetic signature which will aid *multi-messenger* astronomy. Here, we briefly review the evolutionary channels for such systems, the stages of the merger process, and the detection prospects within the next several years. For a more comprehensive discussion see Ref. [98–100].

The CO binaries of interest are those which may conceivably merge within a Hubble time. We can estimate the physical parameters of the systems which satisfy this condition using the quadrupole radiation formula, noting that the emission of GWs should act to circularise the binary before it enters the terrestrial band such that we can set the eccentricity to be approximately zero (see Ref. [101, 102] for a more general treatment). The typical GW inspiral timescale is

[99, 102],

$$\tau_{\rm GW} \sim 4.8 \times 10^{10}{\rm yr} \left(\frac{P_b}{\rm d}\right)^{8/3} \left(\frac{\mu}{M_\odot}\right)^{-1} \left(\frac{M_c + M_p}{M_\odot}\right)^{-2/3} (1 - e^2)^{7/2}, \tag{1.14}$$

where M_p, M_c are the masses of the primary and companion remnant COs, respectively; $\mu = M_p M_c/(M_p + M_c)$ is the reduced mass of the system; P_b is the binary orbital period; and e is the binary eccentricity. So, in order for an equal-mass circular binary consisting of two $1.4M_\odot$ NSs to merge within a Hubble time the binary orbital period should be less than a day. Systems with BHs can be more massive and so can have a longer orbital period while still merging within a Hubble time. Hence, we are typically looking for very tight binaries in the very final stages before merger.

In order to form a binary system with two compact remnants it is necessary that we initially have a binary with two massive stars, where typically $M \gtrsim 10 - 12M_\odot$ [100, 103, and references therein][2]. Stars which exceed this initial mass will undergo core thermonuclear evolution until iron-peak elements are synthesised, at which point instabilities will lead to gravitational collapse, resulting in a supernova and the creation of a compact remnant. Above $\sim 30M_\odot$ it is more likely that a BH remnant will form rather than a NS, since the binding-energy of the mantle of a main-sequence star this massive can exceed supernova energies and the ensuing explosion can not expel it [106]. This results in a more massive fallback onto the proto-NS, causing it to exceed the maximum mass permitted by neutron degeneracy pressure within realistic EOSs, and collapse to a BH. Interestingly, stars more massive than $\sim 60M_\odot$ will suffer from significant stellar wind mass-loss (this is a function of the stellar metallicity), such that the fallback onto the proto-NS during the supernova explosion may be insufficient to cause collapse to a BH, and the possibility of forming a NS returns [98, 107].

The standard evolutionary scenario for this massive binary [e.g., 108, 109] is shown as a cartoon in Fig. 1.3. The two high-mass OB main-sequence stars initially lie within their Roche lobes, until after a few million years of core thermonuclear burning the more massive star (the primary) exhausts its central hydrogen supply, leaving a dense helium core, and evolves off the main sequence. The primary begins to expand rapidly, developing a deep convective envelope with a polytropic EOS, such that $R \propto M^{-1/3}$. It will eventually overfill its Roche lobe, triggering mass transfer onto the secondary star, which in turn will cause the primary's Roche lobe to shrink even further. This phase of mass transfer terminates whenever most of the primary's hydrogen envelope has been transferred to the accreting secondary, leaving the primary as a naked helium core. At this stage, the secondary's mass now exceeds that of the primary.

---

[2] While the rate of stellar interactions and dynamical capture of COs in stellar clusters may be high, the formation of double CO binaries from this evolutionary path will not constitute a significant detectable population compared to formation in the stellar field [104, 105].

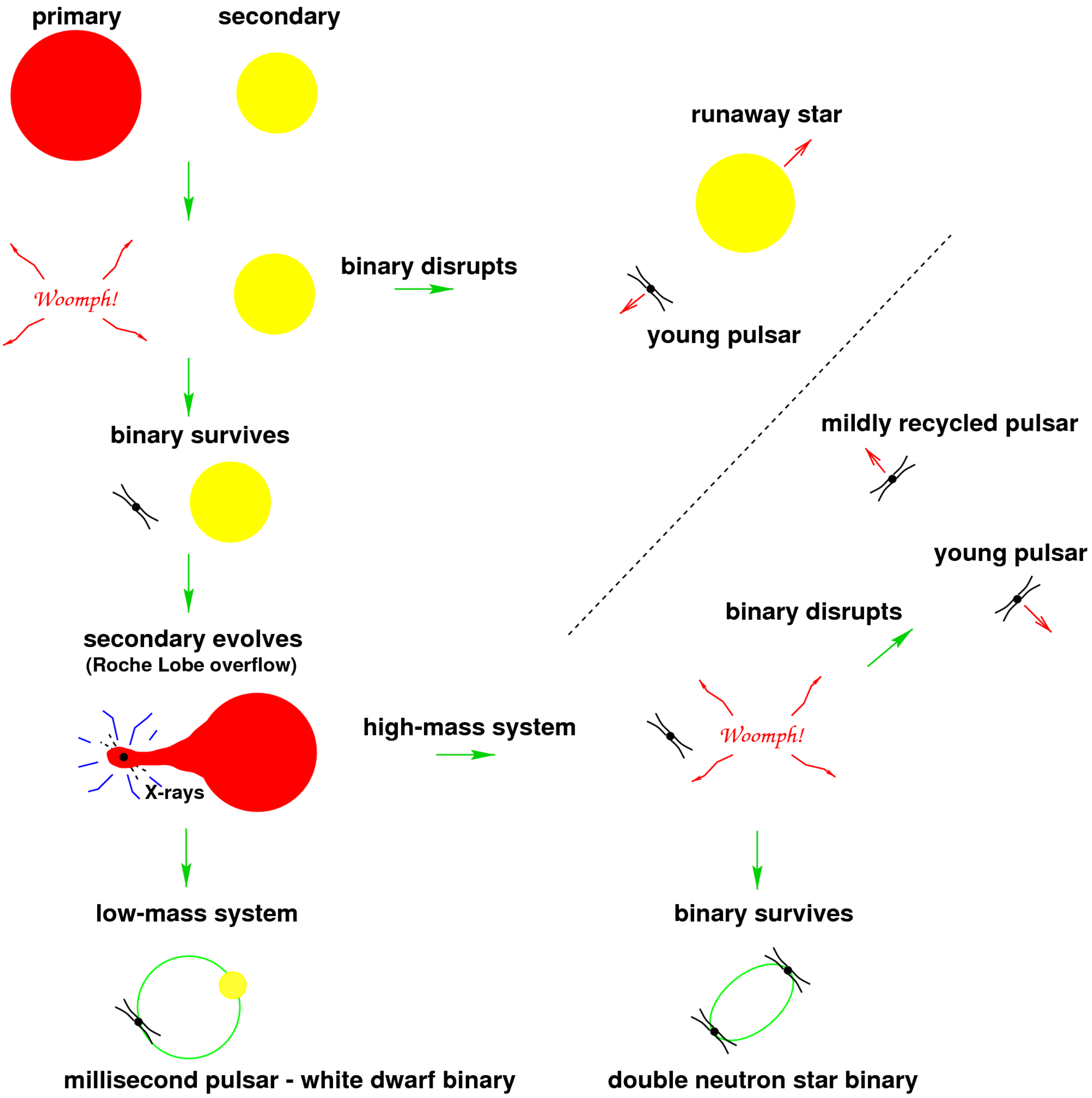

Figure 1.3: Cartoon illustrating the various evolutionary stages of a massive binary system. Reproduced with permission from Ref. [108].

The primary continues to evolve through successive stages of core burning, eventually reaching the iron-peak elements, at which point thermonuclear evolution terminates. Gravitational instabilities develop in the core until it eventually collapses, undergoing a Type Ib, Ic or II supernova, leaving a compact remnant which will be the BH or (the heavier) NS in the eventual double CO binary. Disruption after this first supernova is possible, and the survival probability is heavily dependent on the amount of matter ejected during the explosion and the NS/BH natal-kick distribution. If the first compact remnant formed is a NS then the natal-kick can be significant, as evidenced by the high space-velocities of radio pulsars [e.g., 110]. The physical origin of the natal-kick is still uncertain, but a possibility is an asymmetry in the flux of neutrinos from the newly-formed proto-NS which would cause the final CO to recoil [111, 112, and references therein].

If the system survives the first supernova then the resulting binary consists of a high-mass secondary burning core hydrogen, close to Roche lobe overflow, and expelling material in a stellar wind which is accreted by the CO. In this phase of the evolution the strong X-ray emission produced by the accretion of wind material onto the CO would identify the system as an X-ray binary (for a detailed review, see Ref. [109]). Furthermore, if the first compact object was a rapidly rotating NS with strong radio emission (a pulsar), then the accretion of matter can spin-up the star, recycling it back into a millisecond pulsar [108].

After the X-ray binary phase, the secondary evolves off the main sequence, expanding beyond its Roche lobe to engulf the CO in a common envelope (CE) phase. The CO spirals in towards the core of the secondary via dynamical friction in the envelope, hardening the binary as the envelope extracts energy from the binary's orbit, until eventually the envelope is expelled [100, and references therein][3]. A NS inspiraling within the envelope may actually undergo a hyper-critical accretion phase, releasing the gravitational energy of accreted envelope-material by emitting neutrinos [117–119]. Collapse to a BH may follow, although the survival probability of a NS inside an envelope is still under study [120, 121]. We note that the CE phase, and the associated binary hardening via dynamical friction, is essential to the formation of potentially detectable double CO systems, as without it we would never have binaries which would merge within a Hubble time [99].

What follows is the secondary (stripped of its hydrogen envelope) undergoing a supernova to form a CO. Therefore the binary must survive a second explosion, and avoid the possibility of disruption. If it does so, then we are left with a tight NS-NS, NS-BH, or BH-BH binary, which evolves towards merger purely via GW emission. We note that, although this is the

---

[3] If the CO is a NS and happens to combine with the secondary's core before envelope expulsion (and does not exceed the maximum NS mass) then the final object may be the (still hypothetical) Thorne-Zytkow object [113, 114]. Some candidate systems have recently been identified – see Refs. [115, 116].

standard scenario for double CO binary-formation, there are many variants on the evolutionary path described here [e.g., 122–124].

The waveform behaviour during the inspiral phase of the CO binary evolution has long been well understood, with the pN expansion providing an accurate description up until the last few orbits before merger (for a review, see Ref. [39]). This allows us to construct reliable waveform templates, and to coherently track the GW's phase evolution in our detectors such that optimal "matched filtering" techniques can be applied [125–127]. The frequency and amplitude of the GW "chirps" as the binary evolves towards coalescence. In the last few cycles we must take into account the influence of tidal-deformation of the NS (which depends on the stiffness of the EOS of nuclear matter) [128, 129] on the phase and amplitude of the inspiral signal.

When the binary separation becomes comparable to the stellar radius the system becomes unstable, and the COs plunge together. The GW luminosity during this merger-phase can be $\sim 10^{46}$ W, or equivalent to outshining (in GWs) the entire visible Universe. If the system is a double NS (DNS) binary, full GR magnetohydrodynamical simulations are required to model the merger-phase evolution, where a roughly equal-mass merger resembles a slow collision, and an unequal-mass binary typically involving tidal disruption and accretion of the low-mass component [99]. The GW signal is much simpler than previously thought; as discussed in Sec. 1.2, EOB and NR calculations are making significant headway in modelling this phase. This signal will encode much important information about the structure and EOS of NSs [130, 131]. In fact, two NSs merging together may in fact delay collapse to a BH if the intermediate *hypermassive* NS (HMNS) [132–134] is supported by differential rotation. The HMNS may be deformed by its rotation into a bar-mode structure, emitting GWs which can encode information about the intrinsic mass [135] and size [131] of the system.

The ensuing collapse of the system to a BH may be the engine of the most energetic EM events in the Universe: the short, hard gamma-ray burst (SGRB) [136]. Although the precise mechanism is still under study, it's conceivable that neutrinos and anti-neutrinos produced by shock-heating of collapsing material will annihilate to produce the high-energy gamma-rays characteristic of a SGRB [137]. In this scheme, if a HMNS has delayed the gravitational collapse then there will be a corresponding delay between the GW and EM signals. There may be additional EM signatures, in the form of possible radio-afterglows [138], or even *kilonova* emission, where, in the latter, r-process synthesis of neutron-rich elements is followed by radioactive decay and an isotropic afterglow [139–141]. The kilonova emission may in fact present a better candidate for EM-counterpart identification than SGRBs, since the beamed emission of the latter could inhibit the fraction of systems that we see as both GW and EM events [142]. More speculative EM counterparts are a recently identified population of millisecond radio bursts at cosmological distances [Fast Radio Bursts (FRBs) or "*Lorimer bursts*"] [e.g. 143–145] which may be associated with the sudden collapse of a magnetised HMNS, causing magnetic-field lines in the magnetosphere to snap violently, and producing a bright radio flash ("*blitzar*") [146].

The relative fractions and supernova-survival probabilities of NS-NS, BH-NS, and BH-BH systems depend on a number of factors: (a) the efficiency of binary hardening during the CE phase, and the corresponding accretion rate onto the NS; (b) the maximum allowed NS mass, which is a function of the unknown nuclear matter EOS; (c) the natal-kick distribution of NSs and BHs formed after supernovae. Nevertheless, we can make some estimates of the intrinsic merger-rate of these systems. A comprehensive literature review can be found in Ref. [147], but briefly the estimation techniques can be divided into those that make use of empirical calculations and those that rely on the outcome of population-synthesis studies. The empirical studies either extrapolate the merger-rate based on the observed sample of Galactic DNS systems [148–150] (of which there are currently 9 known systems [151]), or by assuming that SGRBs are the EM signature of a double CO merger and correcting for selection-effects via an appropriate beaming-model, although the latter does not distinguish between NS-NS and NS-BH [152–154]. The population-synthesis studies directly model the stellar evolution of samples of (typically) $\sim 10^6$ stars as a function of many tunable parameters, and can be calibrated to reproduce the Galactic star-formation rate (SFR) or the observed Galactic NS-NS population [e.g., 155–158]. The actual *detection rate* of these systems depends on the relative interplay of the intrinsic merger-rate and the sensitivity of our detectors. However, the number of DNS systems observed per year by an upcoming advanced network of terrestrial interferometric detectors could be $\sim 0.4 - 400$, with a *realistic* rate of $\sim 40\ \mathrm{yr}^{-1}$ [147]. A coincident SGRB will be strong evidence of the merging NS-NS/NS-BH model, and may provide strong prior constraints on the source's sky-location for GW parameter-estimation [159].

Other candidate GW signals such as modelled/unmodelled bursts (from core-collapse supernovae) [91, 160], continuous waves (from pulsar "bumps" which generate a quadrupole mass-moment) [161, 162], and stochastic GW backgrounds (discussed thoroughly in Sec. 1.3.3) [163], are also targeted in the high-frequency band, but will not be discussed further here.

1.3.2 Low frequency ($0.1\ \mathrm{mHz} \lesssim f \lesssim 0.1\ \mathrm{Hz}$)

Detectors

This band requires much longer interferometer arm-lengths, and a complete suppression of the seismic/gravity-gradient noise which plagues the low-frequency operation of terrestrial detectors. To this end, detection at these frequencies necessitates space-based laser interferometers.

The canonical design for a mission in this band is the Laser Interferometer Space Antenna

(LISA) [164], a collaborative project between the National Aeronautics and Space Administration (NASA) and the European Space Agency (ESA). This mission calls for an arrangement of three identical satellites in a 5 Mkm arm-length triangular configuration, trailing the Earth's orbit by $20°$, and forming 2 optical links along each arm. The total of 6 optical links would have enabled the interferometer to operate in *Sagnac*-mode, constructing a data-stream which was completely insensitive to laser, optical-bench, and clock noise [165, 166].

Following the withdrawal of NASA funding, ESA developed an independent de-scoped mission concept in the form of the European New Gravitational wave Observatory (NGO) (informally referred to as evolved LISA (eLISA) [167, 168]), which retains the basic LISA design, but with only 1 Mkm arm-lengths and 4 optical links in a "mother-and-two-daughters" satellite configuration. As of writing, the eLISA science theme has been chosen for the ESA "Cosmic Vision" L3 mission slot, due for launch in 2034 at the earliest. Before then, the LISA Pathfinder satellite will be launched in ~ 2015 to demonstrate the technological feasibility of the full eLISA concept [169].

Possible eLISA follow-up missions [170] to bridge the $0.1 - 10$ Hz gap include the shorter arm-length Advanced Laser Interferometer Antenna (ALIA) [171], which would target the mergers of intermediate MBHs, and the Big Bang Observer (BBO) [172], whose highly ambitious design of multiple LISA-like satellite constellations would target the cosmological GW background. Additionally, the Japanese DECi-hertz Interferometer Gravitational wave Observatory (DECIGO) mission [173, 174], sensitive between $0.1 - 10$ Hz, may be launched as early as 2027 contingent upon successful pathfinder missions [175].

Sources

The low frequency band is rich with astrophysical sources, including the Galactic *verification binaries* (primarily WD binaries) whose properties are well-known electromagnetically, and hence should be detectable within a few weeks or months of instrument operation [176]. Additionally, several thousand unknown ultra-compact binary systems may be individually resolvable [177, 178], while the remaining several million will create a stochastic GW foreground signal [179]. The GW signal of the inspiral, merger and ringdown phases of massive BH (MBH) binary systems in the mass-range $10^4 - 10^7 M_\odot$ also lies in this band. Parameter-estimation of individual systems will be possible, along with detailed studies of the formation and growth of primordial seed BHs into the population we see today [167, and references therein]. Arguably the most exciting sources are the Extreme Mass-Ratio Inspirals (EMRIs), where stellar-mass compact remnants gradually spiral-in towards a much larger BH, and in so doing map out the geometry of the MBH space-time [180–182, and references therein]. Finally, these frequencies may show the signature of a cosmological GW background signal, whose origin may be from turbulence within the primordial plasma, colliding bubbles of "true vacua" after a first-order phase-transition, or the emission from cosmic-string "kinks" [183, and references therein].

1.3.3 Very Low frequency (10^{-9} Hz $\lesssim f \lesssim 10^{-7}$ Hz)

Detectors

This band is unusual in that pulsars, an astrophysical population themselves, are used to detect GWs. Pulsars are extraordinary objects. Not only does the timing stability of their pulsed emission enable them to act as unique laboratories for exploring the interplay of nuclear matter with astrophysical environments, but it also enables them to act as standard clocks in space with which to infer the perturbing influence of passing nanohertz GWs. Since their discovery in 1967 [184], pulsars have helped to shed light on strong-field gravity, the EOS of nuclear matter, evolutionary scenarios for massive binary systems, the interstellar medium, the existence of exoplanets, and much more. It would be difficult to overstate the exquisite astrophysical laboratories presented to us in the form of isolated and relativistic-binary pulsars. For deeper reviews, see Ref. [26, 108].

The basic model of a pulsar (known as the "lighthouse" model) is of a rapidly rotating, highly magnetised NS formed as the result of stellar collapse during a supernova [185, 186]. The magnetic-field (with an axis offset from the rotational-axis) is such that the star acts as a rotating magnetic-dipole, generating a local electric field along which charged particles within the co-rotating magnetospheric plasma are accelerated. It is expected that once these particles exit the velocity-of-light cylinder[4] at the polar caps that they excite beams of radio emission, which we only observe whenever the beam sweeps across our line-of-sight [187, 188]. The pulse period is then a measure of the rotation period of the NS itself.

Early competing theories of oscillating WDs and NSs were able to account for pulsational periods of $\gtrsim 1$ s and $\sim 1 - 10$ ms, respectively [189]. However, the discovery of the Crab pulsar [190, 191] with its 33 ms period, and the observation of a gradual spindown of the pulsar (due to rotational energy being extracted to power the EM outflow), cemented the "lighthouse" model. Additionally, the 1982 discovery of PSR B1937+21, with its 1.5 ms period, was the first of the millisecond pulsars [192]. Pulsar demographics can be broadly split into the "*young*" and the "*millisecond/recycled*" varieties; the young pulsars are ones which have formed relatively recently as a result of a supernova, while the millisecond pulsars are ones which have spun-down and been subsequently recycled back up to millisecond periods via the accretion of material and angular-momentum during mass-transfer from a binary companion (see Sec. 1.3.1 for a discussion of this evolutionary path).

---

[4] This is the boundary at which the co-rotating plasma would be moving at light speed.

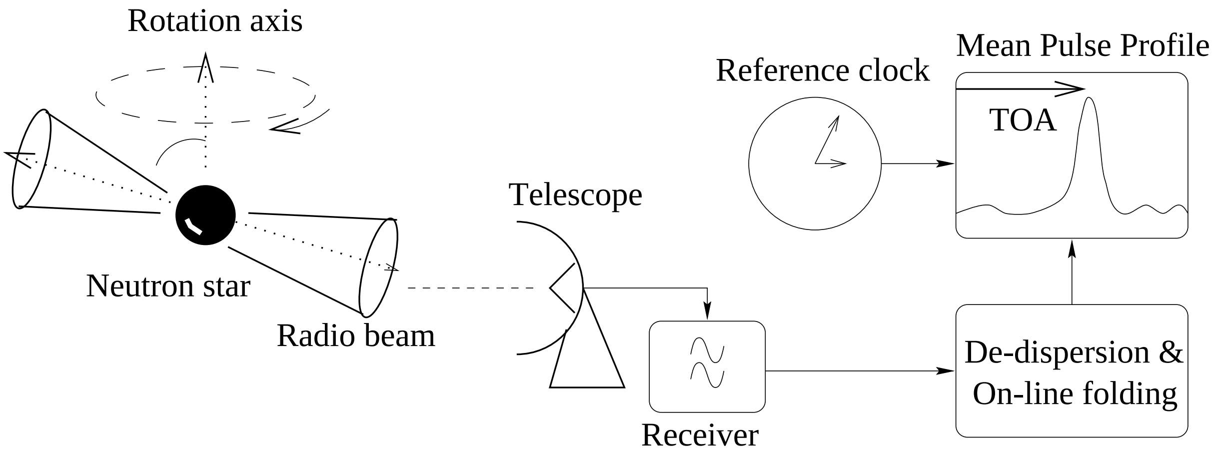

Figure 1.4: A simple representation of the main stages involved in the precision timing of pulsars. Reproduced from [108].

The key to a pulsar's use as an astrophysical probe is that they make excellent standard clocks[5]. Each pulsar has its own signature pulse-shape which can fluctuate dramatically between consecutive rotations, but when we fold (or "integrate") over hundreds (or even thousands) of pulses the result is a pulse-profile which is remarkably stable and reproducible[6]. It is this pulse-profile stability at a given observing frequency that permits precision timing. A simple cartoon of the main stages involved in pulsar-timing is illustrated in Fig. 1.4.

Upon being accelerated to relativistic energies out through the polar caps of the NS's magnetosphere, high-energy charged particles excite beams of radiation with a steep, negative-slope radio spectrum. Individual pulses propagate through the ionised interstellar medium (ISM) where they undergo dispersion (identified in the analysis of the first pulsar [184]) and multipath scattering. Dispersion arises due to the frequency-dependent refractive index of the ISM, such that lower frequencies will have a reduced group-velocity and so will arrive at the telescope later than higher frequency components. The delay is completely determined by the distance travelled through the ISM, such that, with an appropriate model of the electron-density distribution, we can determine the pulsar's distance. Dispersion can be overcome either by splitting the observed band into smaller sub-channels and delaying the higher-frequency components according to the dispersion "$1/f^2$" relationship (incoherent-dedispersion), or by convolving the raw observations with the inverse transfer-function of the ISM (coherent-dedispersion) [194]. Multipath scattering occurs when electron-density irregularities lead to a delay in arrival times, giving the measured pulse a one-sided "scattering-tail". The only way to overcome this is by observing at higher frequencies.

---

[5] Full details of timing procedures can be found in Ref. [193].

[6] Investigations of the evolution of the standard pulse-profile can yield rich information on the details of the emission region, and geodetic precession of the pulsar's spin-axis in a binary system. See Ref. [26].

After the removal of dispersion, hundreds or thousands of pulses are integrated over several minutes of observation to give a boost to the signal-strength and to stabilise the measured profile. This measured profile is then cross-correlated with the *standard pulse-profile* for the specific pulsar at the specific observing frequency. The phase offset between the measured pulse-profile and standard pulse-profile is added to the start (or midway) time of the observation, giving a pulse "Time Of Arrival" (TOA). We must now convert these TOAs to an inertial reference frame, which we usually take to be the Solar System Barycentre (SSB). The times are corrected for (a) Einstein delays due to time-dilation and gravitational redshift in the presence of the Sun and other bodies in the Solar System; (b) Shapiro delays due to light propagating through the gravitational potential-well of the Sun; (c) Roemer delays due to the classic light travel-time across the Solar System from the Earth to the SSB, which (for nearby pulsars) can also factor in delays due to spherical wavefronts. If we are observing a binary pulsar then the times must be additionally corrected for the corresponding delays in the binary system.

After all of these corrections, the final model of the pulsar's phase-evolution is remarkably simple. The "lighthouse"-model has a beam sweeping into our line-of-sight every time the pulsar rotates, where the rotational frequency of the pulsar is decreasing due to "spindown" caused by the EM outflow's tapping of the rotational kinetic energy. Hence, for a pulsar with some rotational frequency ν measured at epoch T_0, the pulse phase is modelled as,

$$\phi(T) = \phi_0 + 2\pi(T - T_0)\nu + \frac{1}{2}2\pi(T - T_0)^2\dot{\nu} + \ldots, \tag{1.15}$$

where T is the SSB time, and ϕ_0 is the pulsar phase at T_0. With initial estimates of the dispersion-measure, rotational frequency, and location of the pulsar, we can perform a least-squares fit of the collection of TOAs to our model TOAs (typically with the software package TEMPO2 [195–197]), forming a series of "timing-residuals". By iterating and refining the "timing-model" to remove systematic trends, we can construct extraordinarily precise predictions of the pulsar's phase. This procedure is discussed in further detail in Part III.

Ideally, the timing-model would incorporate all aspects which could conceivably influence the pulse TOAs. However, despite their incredible pulse-profile stability, some pulsars are known to exhibit small rotational irregularities. In particular, discrete jumps in the rotational frequency of the pulsar ("glitches") are thought to occur as a result of the sudden recoupling and angular momentum transfer between the neutron-superfluid and the crustal lattice, reducing the lag in their rotational frequencies which occurs due to the minimal friction between the two [198]. This glitchy behaviour is suppressed in older and millisecond pulsars [199, 200]. Many pulsars also exhibit "timing-noise" with low-frequency structure (*red timing-noise*). The origin of this may be due to the pulsar's magnetosphere rapidly and sporadically switching between two stable configurations, leading to different pulse-shapes and spindown rates [201]. The variation in spindown rate causes the rotational frequency to wander over a period of

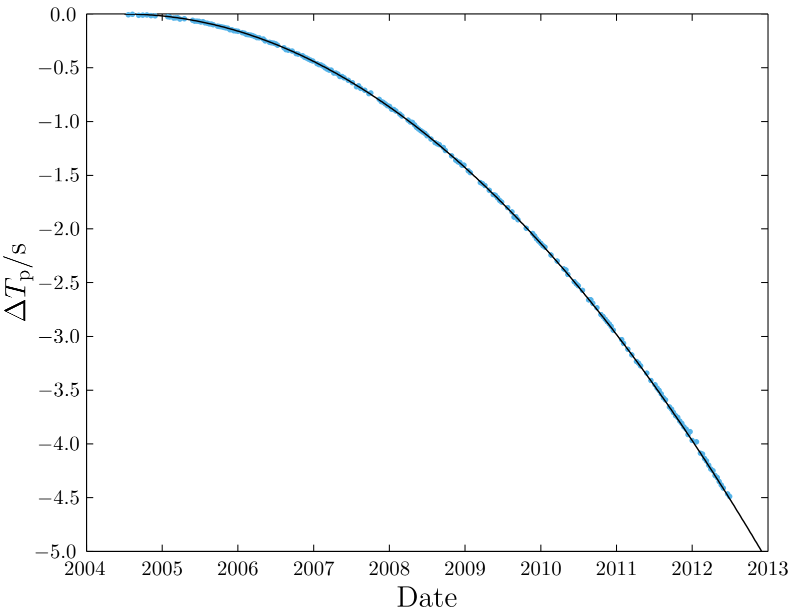

Figure 1.5: The measured cumulative shift in the time of periastron passage is compared to the GR-prediction, where error bars are too small to see. Data and figure courtesy of Michael Kramer and Christopher Berry, respectively.

years, contributing a source of red timing-noise if unmodelled. While magnetospheric mode-switching/nulling is not incorporated into the timing-model, it can be accounted for as an extra stochastic red-noise process [202]. With a model for the deterministic influences on the TOAs, and the various receiver- and intrinsic pulsar-noise processes factored in, we now have a set of remarkably stable clocks in the sky.

The discovery of the binary pulsar PSR B1913+16 [23], and its subsequent high-precision timing, led to an extraordinary indirect verification of the existence of gravitational-radiation [24, 203, 204]. The determination of three Post-Keplerian (PK) parameters [205, 206] (rate of relativistic periastron advance, $\dot{\omega}$; gravitational-redshift and time-dilation, γ; rate of orbital-period decay, $\dot{P}_b$) meant that the system was "overdetermined", such that the binary component masses obtained from two of the PK parameters could be used to predict the GR value of the remaining parameter. The resulting analysis (from over 30 years of observations) yielded a GR-prediction for the rate of orbital-period decay which was within 0.2% of the measured value. Additionally, PSR J0737-3039 is the only known *double pulsar* [207, 208], with its measured five PK parameters allowing for a confluence of GR tests to be passed with flying colours (see Ref. [25]). This is a fascinating system, consisting of young and millisecond pulsars with interacting magnetospheres, binary eclipses, and relativistic precession of the spin-axes. An up-to-date illustration of the agreement between the measured cumulative shift of the time of periastron passage and the GR-prediction is shown in Fig. 1.5, where the error bars are too small to see.

The precision-timing of millisecond pulsars can also be exploited for *direct* GW detection. We essentially treat the pulsar and the SSB as opposite ends of our experimental setup, where the influence of a passing GW is to perturb the space-time metric along the Earth-pulsar line-of-sight [209–212], creating a change in the proper-separation, and thus inducing irregularities in the perceived pulsar rotational frequency. The fractional frequency-shift (or *redshift*) of a signal from a pulsar in the direction of unit vector $\hat{p}$, induced by the passage of a *single* GW propagating in the direction of $\hat{\Omega}$ is [213, 214]

$$z(t,\hat{\Omega}) = \frac{1}{2}\frac{\hat{p}^a\hat{p}^b}{1+\hat{\Omega}\cdot\hat{p}}\Delta h_{ab}(t,\hat{\Omega}), \tag{1.16}$$

where $\Delta h_{ab} \equiv h_{ab}(t_e,\hat{\Omega}) - h_{ab}(t_p,\hat{\Omega})$, is the difference in the metric perturbation at the SSB, $h_{ab}(t_e,\hat{\Omega})$, and at the pulsar, $h_{ab}(t_p,\hat{\Omega})$.

This frequency-shift is integrated over time to give the induced timing-residuals, which describe the perturbation to the TOA of pulses from a given pulsar,

$$r(t) \equiv \int_0^t z(t')dt'. \tag{1.17}$$

The GW-frequencies to which precision pulsar-timing are sensitive lie in the band $1/T \lesssim f \lesssim 1/(2\Delta T)$, where T is the total observation time of the pulsar and ΔT is the observational cadence. For typical observation schedules this is the $\sim 1-100$ nHz band. The frequency resolution is given by $\Delta f \sim 1/T$. As discussed below, the dominant GW signal at these nHz frequencies may not be from single resolvable sources, but rather from a stochastic GW background (GWB) of many overlapping, unresolved sources. Therefore, we can not coherently track the phase evolution of these signals, but rather must measure the statistical properties of the background as a whole.

After fitting for a timing-model, the timing-residuals will have contributions of stochastic signals from timing-noise, receiver-noise (etc.), and the stochastic GWB. By timing an ensemble of Galactic millisecond pulsars [a Pulsar Timing Array (PTA); [215]] to sufficient accuracy, we can cross-correlate the timing-residuals of each pulsar to mitigate nuisance noise processes (such as intrinsic pulsar noise), and strengthen the detection of a common stochastic GW background which is bathing *all* pulsars. Furthermore, for an *isotropic* stochastic GWB in GR, the cross-correlation is a simple function of the angular-separation of the pulsars on the sky. The functional form of this cross-correlation (known as the "*Hellings and Downs curve*" [216], and shown in Fig. 1.6) forms the basis of all current PTA searches, providing leverage of the GWB signal against noise processes.

The tantalising goal of detecting and characterising GWs with millisecond pulsars has led to the establishment of three major PTA consortia. The Parkes Pulsar Timing Array (PPTA) [217, 218] in Australia uses the Parkes radio telescope to observe a large sample of Galactic

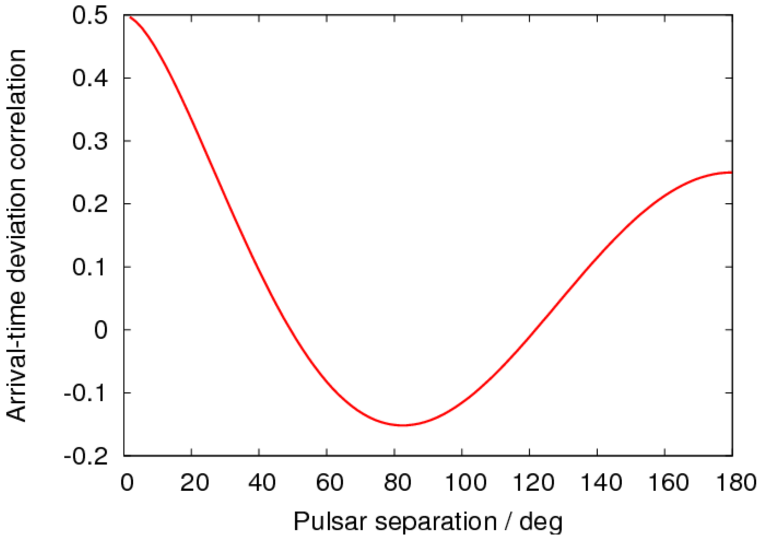

Figure 1.6: The "Hellings and Downs curve" [216], showing the cross-correlation of TOA perturbations induced by an isotropic stochastic GWB in GR.

millisecond pulsars below a declination of $+25^\circ$ and the entire southern Galactic plane. The North American Nanohertz Observatory for Gravitational waves (NANOGrav) [219, 220] is a collaboration between the National Radio Astronomy Observatories (NRAO) and several US universities, using the Arecibo and Green Bank telescopes to perform multi-frequency observations. The European Pulsar Timing Array (EPTA) [221, 222] is a collaboration of European institutions, using the Lovell telescope at Jodrell Bank, the Effelsberg telescope at Bonn, the Westerbork Synthesis Radio Telescope, the Nancy Radio Telescope, and the Sardinia Radio Telescope. These individual PTAs are separate entities with different strategies and techniques, but are ultimately bound together in the International Pulsar Timing Array (IPTA) [223, 224], within which the separate PTAs aim to combine datasets and techniques to enable an enhanced scientific return. The current status of their efforts is given below, after a discussion of their GW targets.

Sources

The dominant GW signal in the PTA band is expected to be from the superposition of many nearby ($z \lesssim 1$), massive ($M \gtrsim 10^8 M_\odot$) BH binaries in the early-inspiral regime, overlapping in frequency to produce an unresolved background at the lowest detectable frequencies [225–227].

It is now well-established that SMBHs are copious in the nuclei of nearby galaxies [e.g., 228], with observational relationships indicating a strong coupling between the evolution of the black-hole and galactic host [e.g., 229–231]. The last decade has seen them identified as keystones in theoretical models of hierarchical galaxy formation [232, 233], where massive galaxies form through continued accretion from cosmic web filaments and through galactic mergers. As such, the massive black-holes we observe in active or nearby galaxies are the natural by-product of initial proto-galaxies (with BH seeds) undergoing hierarchical clustering throughout cosmic time. The formation of massive black-hole binaries naturally follows the ubiquitous galactic mergers in this framework. After a galactic merger, the individual black holes spiral by dynamical friction into the core of the common merger-remnant, eventually residing at the centre of a stellar bulge, and potentially surrounded by massive gas inflows [234]. After the binary becomes hardened via environmental couplings (discussed below) it enters the GW inspiral regime, where orbital evolution is dominated by the emission of GWs.

If we assume that hardened binaries (with sub-pc separations, and emitting GWs in the PTA band) are driven purely by GW emission, then the shape of the resulting GWB strain-spectrum is quite easily determined. For a population of circular inspiraling binaries, the characteristic strain of GW emission is given by [235]

$$h_c^2(f) = \int_0^\infty dz \int_0^\infty dM_1 \int_0^1 dq \frac{d^4N}{dz dM_1 dq dt_r} \frac{dt_r}{d\ln f_r} \delta\left[f - \frac{f_r}{(1+z)}\right] \times h^2(f_r), \qquad (1.18)$$

where $h(f_r) \propto \mathcal{M}^{5/3} f_r^{2/3}$ [236] is the orientation-averaged strain emitted by a binary of chirp-mass $\mathcal{M} = (m_1 m_2)^{3/5}/(m_1+m_2)^{1/5}$ at rest-frame frequency f_r. The factor $d^4N/dz dM_1 dq dt_r$ is the cosmological rest-frame rate of coalescing binaries per redshift (z), largest SMBH mass (M_1), and mass-ratio (q). The factor $dt_r/d\ln f_r$ encodes the time spent by the binary radiating at each frequency, which, for a purely GW-driven binary, is $\propto \mathcal{M}^{-5/3} f_r^{-8/3}$ [102]. The factor $\delta\left[f - \frac{f_r}{(1+z)}\right]$ accounts for the cosmological redshift of each constitutent signal contributing to the background. Collecting the frequency terms together we see that for a GWB composed of purely GW-driven, circular, inspiraling SMBH binaries, the characteristic strain is $h_c(f) \propto f^{-2/3}$ [225–227, 234, 237].

This simple treatment is confirmed by averaging many Monte Carlo realisations of the signal from SMBH binary population models. However, for a *single* realisation, many millions of sources might contribute to the signal, but the GW strain budget is actually dominated by only several hundred [238, 239]. As such the signal can not be described over the entire band as a Gaussian, isotropic background [240]; rather the stochasticity of the signal gradually breaks down at higher frequencies, becoming dominated by only a handful of potentially resolvable binaries [241]. This is not such a terrible issue, since at lower frequencies we still have a steep, negative-slope strain-spectrum which will show up as a correlated stochastic signal in the pulsar timing-residuals, while at higher frequencies we can employ single-source searches.

However, recently the degree to which environmental couplings can affect the frequency evolution of these binaries has been investigated [235, 242], which has significant ramifications for the low-frequency strain-spectrum. To counter potential problems with the GW inspiral timescale of a newly-formed binary being longer than the Hubble time (the "final parsec problem" [243]), various binary-hardening mechanisms have been proposed (see Ref. [244, 245]), such as the scattering of "loss-cone" stars [e.g., 234, 246], and interaction with gaseous circumbinary disks [e.g., 247, 248][7]. These may be sufficient to efficiently drive the binary into the GW-inspiral regime. However, for $10^9 M_\odot$ SMBH binaries decoupling from the environment occurs at $f_{\rm GW} \sim 10^{-9}$ Hz, or right where we expect the signal to be loudest in near-future PTA studies. Continued interaction with the environment can drastically suppress the low-frequency GWB signal, as the binary orbital energy is transferred to stars or gas rather than into GW emission. The binaries evolve faster, with fewer systems emitting at each frequency than in the circular, GW-driven case. Additionally, these environmental couplings can induce significant binary eccentricity [249, 250], distributing radiated GW power into higher harmonics such that the low-frequency signal is again suppressed [251]. These findings could have major implications for the timescale of a GW detection with PTAs [235], and also offer unique opportunities for rich information concerning environmental couplings of the binary population to be mined. However, in the remainder of this dissertation we adopt the standard approach of assuming that a GWB composed of many inspiraling SMBH binaries will have a power-law strain-spectrum.

Indeed, we can also use a power-law to approximate the characteristic strain-spectrum of other potential background sources. Some measurable primordial background contributions may have a power-law index of -1 [252, 253], while the background produced by a network of decaying cosmic strings [254–257] may have an index of $-7/6$ [258]. For most models of interest, we can describe an isotropic, stochastic GWB by $h_c(f) = A\left(f/{\rm yr}^{-1}\right)^\alpha$ [259], where A is the dimensionless strain amplitude at a frequency of $1/{\rm yr}$. This characteristic strain can be related to the one-sided power spectrum of the pulsar timing-residuals induced by the GWB,

$$S(f) \equiv \frac{1}{12\pi^2}\frac{1}{f^3}h_c(f)^2 = \frac{A^2}{12\pi^2}\left(\frac{f}{{\rm yr}^{-1}}\right)^{-\gamma}{\rm yr}^3, \tag{1.19}$$

where $\gamma \equiv 3-2\alpha$. Additionally, the *cross-power* spectrum between pulsars a and b is given by,

$$S_{ab}(f) \equiv \zeta(\theta_{ab})S(f), \tag{1.20}$$

where $\zeta(\theta_{ab})$ is the "Hellings and Downs" function (shown in Fig. 1.6) for an isotropic stochastic GWB, describing the overlap reduction function of the "antenna patterns" of pulsars separated

---

[7] There are potential problems with stellar-scattering, since the SMBH binary quickly depletes its loss-cone, ejecting its supply of stars with which to carry away energy and angular-momentum, and causing the binary-hardening to stall [234]. A possible solution to this, and to ensure continued hardening of the binary down into the GW-inspiral regime, is that real stellar bulges are likely to exhibit non-axisymmetric features which permit a much larger loss-cone [249].

by angle θ_{ab} on the sky, with form [216]

$$\zeta(\theta_{ab}) = \frac{3}{2}f(\theta_{ab})\ln\left[f(\theta_{ab})\right] - \frac{1}{4}f(\theta_{ab}) + \frac{1}{2} + \frac{1}{2}\delta_{ab}, \tag{1.21}$$

and $f(\theta_{ab}) = (1-\cos\theta_{ab})/2$.

Finally, we can express the characteristic strain in terms of the GWB's fractional energy-density contribution to the Universe [237],

$$\Omega_{\rm GW}(f) \equiv \frac{1}{\rho_{\rm c}}\frac{d\rho_{\rm GW}(f)}{d(\ln f)} = \frac{\pi}{4}\frac{f^2 h_c(f)^2}{\rho_c}, \tag{1.22}$$

where $\rho_{\rm c} = 3H^2/8\pi$ is the critical energy-density required for closure.

Over the last several years the three major PTAs have published limits on the GWB amplitude, employing a variety of Bayesian/frequentist methods and time-/frequency-domain techniques. Until recently, the tightest constraint on the amplitude A of the strain spectrum was $A \leq 6\times 10^{-15}$ at the 95% level, which was obtained with the robust, unbiased time-domain Bayesian framework of van Haasteren et al. [260] within the EPTA. This technique will be used exclusively in Part III, where it is discussed in greater detail. Following this, Demorest et al. [261] of NANOGrav obtained a limit of $A \leq 7.2\times 10^{-15}$ at the 95% level. The most recent, and now tightest, constraint is from Shannon et al. [262] of the PPTA, with a limit on the Gaussian (non-Gaussian) amplitude equal to $A \leq 2.4(2.7)\times 10^{-15}$ at the 95% level.

Several recent studies have claimed that PTAs may actually be on the cusp of detecting the nHz GWB [263–265]. Sesana [265] performed a systematic investigation of the expected GW signal from a population of SMBH binaries, factorising the cosmological coalescence rate in Eq. (1.18) in terms of observed galaxy mass-functions and pairing fractions, deriving galactic merger time-scales from numerical simulations, and employing a prescription for populating massive galaxies with SMBHs. The findings indicate that recent upper limits on A obtained by the EPTA and NANOGrav are already in tension with certain SMBH merger scenarios. The new tightest constraint from the PPTA excludes 46% of the set of expected amplitudes from Ref. [265]. Additionally, the PPTA constraint rules out the entirely merger-driven SMBH-growth model of McWilliams et al. [263, 264] at the 91% confidence level. While detection may be possible within the next few years [266], and could even outpace LIGO/Virgo, precision science with PTAs will likely require the exquisite timing of $\sim \mathcal{O}(100)$ pulsars using the Square Kilometre Array (SKA) [267, 268].

There is also an ongoing effort to find and localise single GW sources in the PTA band, where the primary target is the continuous-wave emission from the adiabatic inspiral of SMBH binaries. The algorithms employed variously search for periodic signals in the timing-residuals [269, 270], apply matched-filtering [271], maximise the likelihood over binary parameters [272, 273], or execute a full Bayesian parameter-estimation and evidence search [274]. Notably, pulsar-timing has completely ruled out the possibility of a binary in the system 3C 66B [269]. Single-source detection will be explored in further detail in Chapter 5.

1.4 Bayesian inference

Bayesian statistics provide a robust framework with which to obtain probability distributions of model parameters given a set of observations. To implement this, all we need is a likelihood model describing the probability of observing a dataset given some model parameters, in addition to a prior probability distribution which incorporates constraints from all previous analyses or pre-conceived notions. We use Bayesian statistics in all of the following work.

Bayes' theorem states that the *posterior* probability density function (PDF), $p(\vec{\mu}|D,\mathcal{H})$, of the parameters $\vec{\mu}$ describing a hypothesis model $\mathcal{H}$, and given data D is

$$p(\vec{\mu}|D,\mathcal{H}) = \frac{p(D|\vec{\mu},\mathcal{H})p(\vec{\mu}|\mathcal{H})}{p(D|\mathcal{H})}, \tag{1.23}$$

where,

$$\begin{aligned} p(D|\vec{\mu},\mathcal{H}) &\equiv \mathcal{L}(\vec{\mu}) = \text{likelihood of data given parameters}, \\ p(\vec{\mu}|\mathcal{H}) &\equiv \pi(\vec{\mu}) = \text{prior PDF of parameters}, \\ p(D|\mathcal{H}) &\equiv \mathcal{Z} = \text{Bayesian evidence}. \end{aligned} \tag{1.24}$$

The Bayesian evidence, $\mathcal{Z}$, is the probability of the observed data given the model $\mathcal{H}$

$$\mathcal{Z} = \int \mathcal{L}(\vec{\mu})\pi(\vec{\mu})d^N\mu. \tag{1.25}$$

For posterior inference within a model, $\mathcal{Z}$ plays the role of a normalisation constant and can be ignored. However, if we want to perform model selection then this evidence value becomes key. In Bayesian model comparison we compute the posterior odds ratio

$$\frac{p(\mathcal{H}_2|\vec{D})}{p(\mathcal{H}_1|\vec{D})} = \frac{p(\vec{D}|\mathcal{H}_2)p(\mathcal{H}_2)}{p(\vec{D}|\mathcal{H}_1)p(\mathcal{H}_1)} = \frac{\mathcal{Z}_2 \times p(\mathcal{H}_2)}{\mathcal{Z}_1 \times p(\mathcal{H}_1)}. \tag{1.26}$$

where $\mathcal{Z}_2/\mathcal{Z}_1$ is the Bayes factor, and $p(\mathcal{H}_2)/p(\mathcal{H}_1)$ is the prior probability ratio for the two competing models. This can often be set to one, and we will do so in all of the following. The posterior odds ratio is then just the Bayes factor. Since the evidence is the average of the likelihood over the prior volume, it automatically incorporates Occam's razor: a simpler theory with a compact parameter space will have larger evidence than a more complicated one, unless the latter is significantly better at explaining the data. Hypothesis $\mathcal{H}_1$ is chosen if the Bayes factor is sufficiently large. Jeffreys [275] gave a scale interpretation for the Bayes factor, which is shown in Table 1.1.

Table 1.1: An interpretation of the Bayes factor to discriminate between models, as given by Jeffreys [275].

Bayes factor, $\mathcal{K}$	$\ln(\mathcal{K})$	Strength of evidence
$< 1:1$	< 0	Negative (supports $\mathcal{H}_1$)
$1:1$ to $3:1$	$0 - 1.1$	Barely worth mentioning
$3:1$ to $10:1$	$1.1 - 2.3$	Substantial
$10:1$ to $30:1$	$2.3 - 3.4$	Strong
$30:1$ to $100:1$	$3.4 - 4.6$	Very strong
$> 100:1$	> 4.6	Decisive

We now describe two techniques for sampling from, in general, complicated probability distributions. These techniques are Markov Chain Monte Carlo (MCMC) and Nested Sampling [276] (as implemented in the Bayesian inference package MULTINEST [277–279]).

1.4.1 Markov Chain Monte Carlo sampling techniques

Markov Chain Monte Carlo (MCMC) techniques provide an efficient way to explore a model-parameter space. An initial point, $\vec{x_0}$, is drawn from the *prior* distribution and then at each subsequent iteration, i, a new point, $\vec{y}$, is drawn from a *proposal distribution*, $q(\vec{y}|\vec{x})$ and the Metropolis-Hastings ratio evaluated,

$$R = \frac{\pi(\vec{y})\mathcal{L}(\vec{y})q(\vec{x_i}|\vec{y})}{\pi(\vec{x_i})\mathcal{L}(\vec{x_i})q(\vec{y}|\vec{x_i})}. \tag{1.27}$$

A random sample, u, is drawn from a uniform distribution, $u \in U[0,1]$, and if $u < R$ the move to the new point is accepted and we set $\overrightarrow{x_{i+1}} = \vec{y}$. If $u > R$, the move is rejected and we set $\overrightarrow{x_{i+1}} = \vec{x_i}$.

The MCMC samples can be used to carry out integrals of arbitrary functions, $f(x)$, over the posterior

$$\int f(\vec{x})p(\vec{x}|D,\mathcal{H})d\vec{x} \approx \frac{1}{N}\sum_{i=1}^{N} f(\vec{x_i}). \tag{1.28}$$

The 1D marginalized posterior probability distributions for individual model parameters follows by binning the chain samples in that parameter.

The trick to using this technique efficiently is to choose an appropriate proposal distribution. In Chapter 3 we employ an adaptive MCMC procedure, which utilises an "in-flight" estimation of the sampled chain's covariance matrix to construct an updating proposal distribution. This covariance matrix is updated at each iteration, with a certain chain memory [280–282]. We use several of the procedures outlined in Ref. [282].

For the first n points in the chain (where in the following work $n \sim 100$), simple Gaussian proposal distributions for each individual parameter are used. These points are merely used to provide a starting point for the covariance matrix evaluation and so the exact proposal distribution in this stage is not important. After these first points are sampled, we begin generating points via the adaptive procedure. For a D-dimensional target posterior distribution, we suppose that at the i^{th} iteration we have sampled at least H points, where the fixed integer H is the *memory* parameter. We then generate a D-dimensional vector of trial parameters, $\overrightarrow{y}$, via a linear mapping of an H-dimensional vector of unit-variance Gaussian random scalars, $\overrightarrow{\xi}$,

$$\overrightarrow{y} = \mathbf{C}^{1/2}\overrightarrow{\xi}, \tag{1.29}$$

where $\mathbf{C}^{1/2}$ is the positive-definite square root of the $D \times D$ covariance matrix evaluated using the previous H points. The covariance matrix may be calculated by collecting the previous H points in the chain into an $H \times D$ matrix $\mathbf{K}$, with each row representing one sampled point. Then,

$$\mathbf{C} = \frac{1}{H-1}\tilde{\mathbf{K}}^T\tilde{\mathbf{K}}, \tag{1.30}$$

where the centred matrix, $\tilde{\mathbf{K}}$, is constructed by centring each column of $\mathbf{K}$ around the means of the respective parameters, calculated from the H samples.

We then generate the trial parameter vector $\overrightarrow{y}$ via

$$\overrightarrow{y} \sim \mathcal{N}(\overrightarrow{x}, c_d^2\mathbf{C}) \sim \overrightarrow{x} + \frac{c_d}{\sqrt{H-1}}\tilde{\mathbf{K}}^T\overrightarrow{\xi}, \tag{1.31}$$

where c_d is a variable which depends only on the dimensionality of the target distribution. This variable is used to optimise the efficiency of the sampling process, and we use the value of $\approx 2.4/\sqrt{D}$ [282, 283].

With a memory parameter which is less than the total past history of the chain, this is denoted as the Adaptive Proposal (AP) algorithm [280]. Since the proposal distribution is updated constantly and relies on previous chain information, this procedure is not Markovian, and does not have the correct ergodicity properties for an MCMC algorithm [280]. In principle this can bias the reconstruction of the target posterior; however this bias is ignorable in many practical applications, and for well-behaved target posterior distributions [280, 281]. If the entire previous chain is used to update the covariance matrix, then this algorithm is known as the Adaptive Metropolis (AM) algorithm [281]. The AM algorithm does not suffer from the biases which can occur in the AP algorithm, and ergodicity is retained.[8] We use the AM algorithm in our

---

[8] In the AM algorithm the covariance of the proposal distribution is actually taken to be $\mathbf{C} + \epsilon\mathbf{I}_D$, where $\mathbf{I}_D$ is the D-dimensional identity matrix. Choosing $\epsilon > 0$ allows for the correct ergodicity properties of an MCMC algorithm to be retained, and in practice is useful if the covariance of the chain has a tendency to degenerate. However, this parameter can be set very small with respect to the size of the target space, and in practice can be set to zero.

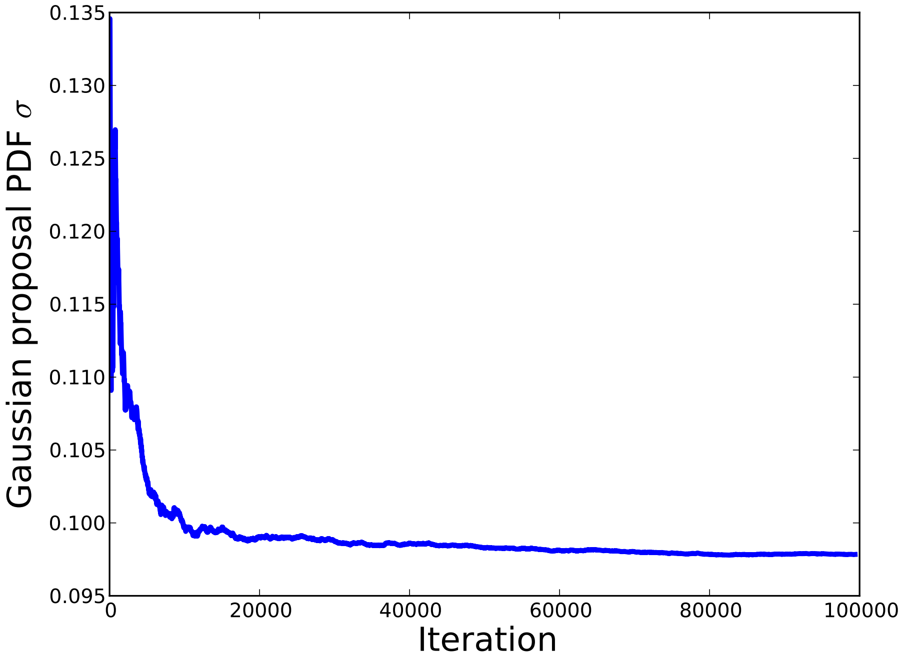

Figure 1.7: The running standard-deviation of a Gaussian proposal distribution in an adaptive-MCMC analysis of noisy data drawn from a Gaussian distribution. The width of the proposal distribution asymptotically approaches a stable value, driving the acceptance rate towards its optimal value.

work. An example of the AM algorithm applied to a simple test case of noisy data drawn from an underlying Gaussian probability distribution is shown in Fig. 1.7, where we see the standard-deviation of the Gaussian proposal PDF asymptotically approaches a stable value as the chain's acceptance rate stabilises at its optimal value.

1.4.2 Nested Sampling & MULTINEST

The nested sampling algorithm is a Monte Carlo method, originally proposed by Skilling [276] for evaluating the Bayesian evidence, $\mathcal{Z}$. For a full description of the MULTINEST algorithm see Ref. [277–279], but we describe the basics in the following section.

The basic idea is to populate parameter space with "live" points drawn from the prior. These points move as the algorithm proceeds, climbing together through nested contours of increasing likelihood. At each iteration, the points are ordered in terms of their likelihood, and the point with lowest likelihood is removed in favour of a higher likelihood replacement.

The biggest difficulty in nested sampling is to efficiently sample points of higher likelihood to allow the live-points to climb. If we were to simply draw points from the prior volume, then the acceptance rate of new points in the live-set would steadily decrease, since at later iterations the live-set occupies a smaller and smaller volume of the prior space as it climbs. MULTINEST overcomes this drawback by using a sophisticated ellipsoidal rejection-sampling technique, whereby the current live-set is enclosed by (possibly overlapping) ellipsoids, and a new point drawn uniformly from the enclosed region. This technique successfully copes with multimodal distributions and parameter spaces with strong, curving degeneracies.

The evidence is calculated by transforming the multi-dimensional integral in Eq. (1.25) into a one-dimensional integral which is easily numerically evaluated. We define the prior volume, X as,

$$dX = \pi(\vec{\mu})d^N\mu, \tag{1.32}$$

such that,

$$X(\lambda) = \int_{\mathcal{L}(\vec{\mu})>\lambda} \pi(\vec{\mu})d^N\mu, \tag{1.33}$$

where the integral extends over the region of the N-dimensional parameter space contained within the iso-likelihood contour $\mathcal{L}(\vec{\mu}) = \lambda$. Hence, Eq. (1.25) can be written as,

$$\mathcal{Z} = \int_0^1 \mathcal{L}\, dX, \tag{1.34}$$

where $\mathcal{L}(X)$ is a monotonically decreasing function of X. If we order the X values $(0 < X_M < \ldots < X_1 < X_0 = 1)$, then the evidence, $\mathcal{Z}$, can be approximated numerically using the simple trapezium rule,

$$\mathcal{Z} = \sum_{i=1}^{M} \mathcal{L}_i w_i, \tag{1.35}$$

where the weights, w_i, are given by $w_i = (X_{i-1} - X_{i+1})/2$.

As a by-product of the exploration of parameter space by the evolving live-set, MULTINEST also permits reconstruction of the parameter posterior PDFs. Once $\mathcal{Z}$ is found, the final live-set, as well as the discarded points, are collected and assigned probability weights to give the posterior probability of each point. These points can be binned to give full and marginalised posterior PDFs.

1.5 Thesis Overview

The first half of this thesis explores the prospects for constraining cosmological parameters using gravitational-wave standard sirens in the absence of EM counterparts. This technique uses the apparent intrinsic narrowness of the NS mass-distribution in NS-NS systems, in addition to measurements of the luminosity distance and *redshifted* chirp-mass of each system, to construct a probe of the distance-redshift relation.

In Chapter 2 we study this for a network of second-generation ground-based interferometers, such as will come online by the end of this decade. We investigate how the measurement error on the Hubble constant varies with the intrinsic narrowness of the NS mass distribution. Some systems may have measurable EM counterparts in the form of SGRBs or kilonovae. We explore how the constraints on the Hubble constant varies by increasing the fraction of the NS-NS catalogue associated with precision EM redshift determinations. This technique is extended in Chapter 3 for a network of third-generation ground-based interferometers, including the Einstein Telescope. The huge distance reach and detection volume of these instruments will allow the dark energy EOS to be explored, while the redshift-evolution of the merger-rate density of NS-NS systems will permit a reconstruction of the background star-formation rate.

The second half of this thesis involves studies of the GW-detection prospects of pulsar-timing. In Chapter 4, we investigate the prospects for constraining levels of anisotropy within the nanohertz stochastic GW background, which may indicate the presence of local GW hotspots on the sky, and help to construct maps of the angular-distribution of the background's energy-density. At the high-frequency end of the pulsar-timing band it's possible that we may be able to resolve individual SMBH binary systems. Their detection and characterisation poses certain practical difficulties, since their influence on the arrival-time of pulsar signals encodes a stamp of the binary's evolution at the time when the emitted GWs pass each pulsar. Without precision constraints on the distance to each pulsar we must include each distance as an extra search-parameter. In Chapter 5 we explore rapid, first-cut techniques for marginalising over these extra parameters, allowing the problem to collapse to lower dimensions, and enabling fast estimates of the posterior odds ratio for detection.

Part II

Cosmography With Gravitational Waves

Nobody ever figures out what life is all about, and it doesn't matter. Explore the world. Nearly everything is really interesting if you go into it deeply enough.

Richard P. Feynman

We know very little, and yet it is astonishing that we know so much, and still more astonishing that so little knowledge can give us so much power.

Bertrand Russell

2

Advanced Era Possibilities

Abstract

We investigate a novel approach for measuring the Hubble constant using *only* near-future GW observations. GW observations of inspiraling NS-NS systems with a network of ground-based interferometers will give a direct, independent measurement of their distance, and if the redshift of the source is known these binary systems can be used as *standard sirens* to extract cosmological information. Unfortunately, the redshift is degenerate with the chirp mass in GW observations. Thus, most previous work has assumed complementary information from an electromagnetic counterpart. Instead, we exploit the intrinsic narrowness of the distribution of masses of the underlying NS population to obtain candidate redshift distributions. We explore what we can learn about the background cosmology and the mass distribution of NSs from the set of mergers detected by such a network. We find that it is possible to constrain the Hubble constant, H_0, and the parameters of the NS mass function using GW data alone, without relying on electromagnetic counterparts. The detection, and cataloguing, of these compact-object mergers will provide a determination of H_0 which is independent of the local distance scale.

This chapter is based on:
Cosmology using advanced gravitational wave detectors alone
Stephen R. Taylor, Jonathan R. Gair, and Ilya Mandel
Phys. Rev. D **85**, 023535 (2012), arXiv:1108.5161

2.1 Gravitational wave standard sirens

GW signals directly encode the properties of the emitting system, which, in the case of an inspiraling compact-binary, include the luminosity distance D_L and the *redshifted* masses of the binary components. Simultaneous measurements of the redshift and the luminosity distance would allow GWs to be used as standard distance-markers, probing the cosmic distance ladder and allowing for measurements of cosmological parameters [284, 285]. However, the redshift and the intrinsic masses for point-mass objects can not be individually determined from GW observations alone. Therefore, previous attempts to use GWs as "*standard sirens*" have generally relied on the existence of electromagnetic counterparts which can be used to unambiguously measure the redshift and break the degeneracy [286–288], or at least do so statistically [289]. In this chapter, we demonstrate that such counterparts are not necessary if the intrinsic mass distribution is sufficiently narrow, as may be the case for double NS (DNS) binaries, although one can do even better by combining the two approaches.

We show that it is possible to use the statistics from a catalogue of GW observations of inspiraling DNS systems to simultaneously determine the underlying cosmological parameters and the NS mass distribution. A given cosmological model determines the redshift as a function of luminosity distance, making it possible to extract the intrinsic mass of a system from a measurement of D_L and the redshifted mass. This permits us to statistically constrain the Hubble constant and the NS mass distribution via a Bayesian formalism, using only GW data. A narrower intrinsic NS mass distribution will more effectively penalise any model parameters which are offset from the true values. We investigate how the precision with which we can recover the underlying parameters scales with the number of detections and the values of the intrinsic parameters themselves.

For the majority of our analysis, we do not consider difficult-to-detect electromagnetic (EM) counterparts to the GW detections, which have been relied on in other analyses, e.g., [287, 288]. Nor do we consider tidal coupling corrections to the late-inspiral phase evolution of DNS inspiral signals, which break the degeneracy between mass parameters and redshift to probe the distance-redshift relation [290, 291], but which only enter at the fifth post-Newtonian order [292] and will likely be very difficult to measure with Advanced LIGO. Furthermore, recent work [135] has explored the possibility of using information from the GW emission of a post-merger hypermassive NS (HMNS) [293], which can survive for several seconds before inevitably collapsing to a black hole [294]. This HMNS develops a bar-mode formation and emits GWs in a narrow frequency range, where the emission spectrum can be used to extract the intrinsic mass of the system. The frequency of this HMNS emission will be out of the sensitivity band of advanced detectors, necessitating third-generation instruments such as the Einstein Telescope.

Rather, we rely on measurements of the redshifted chirp mass, which is expected to be the best-determined parameter, and the luminosity distance. This approach was introduced by Marković [295], where the author extracted candidate source redshifts from the redshifted chirp mass using a constant intrinsic chirp mass (this is later extended to include some spread around the assumed intrinsic value). Chernoff and Finn also explored this technique [296], which was elaborated upon by Finn [297], where the suggestion was made to employ the distribution of signal-to-noise ratios and chirp masses to probe cosmological parameters. We use up-to-date cosmology, mass-distribution models, expectations for detector sensitivity and parameter measurement accuracies to investigate the precision with which the Hubble constant, and NS mass distribution parameters, could be measured by the advanced GW detector network.

This chapter is organised as follows. In Sec. 2.2, we present a simplified analytical calculation and derive scaling laws [298]. Section 2.3 describes the assumptions made in creating a catalogue of sources, including a discussion of the DNS system properties we can deduce from a GW signal, as well as NS mass distributions and merger rates. Section 2.4 details the theoretical machinery for analysing a catalogue of detected DNS systems and the details of our implementation of this analysis. We describe our results in Sec. 2.5, in which we illustrate the possibility of probing the Hubble constant and NS mass distribution via GW data.

N.B. At the time this research was carried out, the placement of an advanced GW interferometer in Australia was being mooted. This is no longer the case and the detector's location is now expected to be India. However, this does not affect the general conclusions we draw about the ability to probe cosmological parameters in the advanced detector era, and indeed we have considered the possibility of a network consisting only of LIGO and Virgo detectors.

2.2 Analytical model

Here, we present a simplified analytical model to show the feasibility of our idea and to derive the main scaling relationships of measurement precisions [298]. We later provide additional justification for the various assumptions made in this model.

The network of advanced detectors will be sensitive to GWs from NS-NS binaries only at relatively low redshifts, $z \lesssim 0.15$ (see Sec. 2.3.1). At such low redshifts, the Hubble law is nearly linear, so that to lowest order, we can write the Hubble constant as (see Section 2.3.1)

$$H_0 \approx \frac{z}{D_L}. \tag{2.1}$$

Therefore, we expect that the uncertainty in the extrapolation of H_0 from redshift and distance measurements will scale as

$$\frac{|\delta H_0|}{H_0} \lesssim \frac{|\delta z|}{z} + \frac{|\delta D_L|}{D_L}. \tag{2.2}$$

The detected NS binaries will yield a catalogue of sources with measured parameters. These parameters will include estimates of the redshifted chirp mass $\mathcal{M}_z = (1+z)\mathcal{M}$ and luminosity distance D_L. The redshifted chirp mass will be measured very accurately, so we can ignore measurement errors for this parameter. However, our ability to extract the redshift of an individual source from the redshifted chirp mass will depend on the narrowness of the intrinsic chirp mass distribution,

$$\frac{|\delta z|}{z} \sim \frac{\sigma_{\mathcal{M}}}{\mathcal{M}}\frac{1+z}{z} \sim \frac{(\sigma_{\mathcal{M}}/\mathcal{M})}{z}, \tag{2.3}$$

where the last approximation follows from the fact that $z \ll 1$. On the other hand, the luminosity distance is estimated directly from the GW signal, but with a significant error that is inversely proportional to the signal-to-noise-ratio (SNR) of the detection.

Existing binary pulsar measurements suggest that the chirp-mass distribution may be fairly narrow, $\sigma_{\mathcal{M}} \approx 0.06M_{\odot}$ (see Sec. 2.3.5). Meanwhile, for the most distant sources at the threshold of detectability, $z \approx 0.15$ and $|\delta D_L|/D_L \approx 0.3$ (see Sec. 2.3.1). Therefore, the first term in Eq. (2.2) is generally larger than the second term (though they become comparable for the most distant sources), and the intrinsic spread in the chirp mass dominates as the source of error.

The errors described above were for a single detection, but, as usual, both sources of uncertainty are reduced with more detections as $1/\sqrt{N}$, where N is the total number of detected binaries. In principle, we could worry whether a few very precise measurements dominate over the remaining $\sim N$, affecting the overall $1/\sqrt{N}$ scaling. The term $(\sigma_{\mathcal{M}}/\mathcal{M})/z$ is larger than $|\delta D_L|/D_L$, so the best measurements will be those where the former term is minimised. The spread in the intrinsic chirp mass $\sigma_{\mathcal{M}}/\mathcal{M}$ is independent of the SNR. Thus, we will learn the most from measurements at high z, even though these will have a worse uncertainty in D_L (the SNR scales inversely with D_L). Therefore, somewhat counter-intuitively, the low SNR observations will be most informative. However, since the detections are roughly distributed uniformly in the volume in which the detector is sensitive, we expect half of all detections to be within $\sim 20\%$ of the most distant detection; therefore, we do expect a $\propto 1/\sqrt{N}$ scaling in $\delta H_0/H_0$.[1]

Using the values quoted above, for $N \sim 100$ detections, we may expect that it will be possible to extract the Hubble constant with an uncertainty of $\sim 5\%$. We carry out a rigorous analysis below, and find that the results of our simplistic model are accurate to within a factor of ~ 2 (see Sec. 2.5).

---

[1] This scaling holds whenever the number of detections is increased, either because the merger rate is higher or because data are taken for longer. On the other hand, if the number of detections increases because the detectors become more sensitive, the distance or redshift to the furthest detection will also increase, scaling with $N^{1/3}$. In that case, as long as the first term in Eq. (2.2) is still dominant, the overall improvement in $\delta H_0/H_0$ scales as $1/N^{5/6}$.

2.3 Source catalogue

2.3.1 System properties from the gravitational waveform

The TT-gauge GW-tensor can be written as,

$$\boldsymbol{h} = h_+ \boldsymbol{e}_+ + h_\times \boldsymbol{e}_\times, \tag{2.4}$$

where $h_{+,\times}$ are the plus/cross polarisation amplitudes, which, for an inspiraling CO binary (and in the far-field approximation), are [32, 236],

$$h_+ = 4\frac{\mathcal{M}_z^{5/3}}{D_L}\left(\pi f\right)^{2/3}\frac{1+\cos^2\iota}{2}\cos\left[\Phi(t)\right], \quad h_\times = 4\frac{\mathcal{M}_z^{5/3}}{D_L}\left(\pi f\right)^{2/3}\cos\iota\sin\left[\Phi(t)\right], \tag{2.5}$$

where f is the GW frequency, D_L is the system's luminosity distance, ι is the binary-orbit inclination angle, and $\Phi(t)$ is the signal's phase. $\mathcal{M}_z = (1+z)\mathcal{M}$ is the redshifted chirp mass, where the chirp mass, $\mathcal{M}$, is a convenient and accurately-measurable parameter which combines the binary component NS masses,

$$\mathcal{M} = \left(\frac{m_1 m_2}{\left(m_1+m_2\right)^2}\right)^{3/5}(m_1+m_2). \tag{2.6}$$

Analysis of the GW phase evolution yields errors on the deduced redshifted chirp mass which vary according to the waveform family being used. Regardless, the precision is expected to be extremely high, even with a single interferometer, where the characteristic error is of the order of $\lesssim$0.1% [299].

The polarisation basis-tensors, $\boldsymbol{e}_{+,\times}$, in the plane perpendicular to the direction of wave propagation are defined as,

$$\boldsymbol{e}_+ \equiv \left(\hat{e}^R_x\otimes\hat{e}^R_x - \hat{e}^R_y\otimes\hat{e}^R_y\right), \quad \boldsymbol{e}_\times \equiv \left(\hat{e}^R_x\otimes\hat{e}^R_y + \hat{e}^R_y\otimes\hat{e}^R_x\right), \tag{2.7}$$

where $\hat{e}^R_{x,y}$ are radiation basis-vectors in the transverse plane.

The GW-induced strain in an interferometer is given by,

$$h(t) = \frac{\delta L(t)}{L} = h_+(t)F_+(\theta,\phi,\psi) + h_\times(t)F_\times(\theta,\phi,\psi), \tag{2.8}$$

where $F_{+,\times}$ are antenna patterns describing the angular response of a detector to the different modes of GW polarisation, and defined as,

$$F_+ \equiv \boldsymbol{d} : \boldsymbol{e}_+, \quad F_\times \equiv \boldsymbol{d} : \boldsymbol{e}_\times. \tag{2.9}$$

The tensor $\boldsymbol{d}$ is known as the detector tensor [300] and defined as $\boldsymbol{d} \equiv (\hat{e}_x\otimes\hat{e}_x - \hat{e}_y\otimes\hat{e}_y)$, where $\hat{e}_{x,y}$ are unit-vectors along the interferometer arms, and the notation $\boldsymbol{d} : \boldsymbol{h}$ corresponds to the Euclidean scalar product $(d_{lm}h^{lm})$ of tensors $\boldsymbol{d}$ and $\boldsymbol{h}$. With these definitions, the antenna patterns can be evaluated explicitly [236, and references therein],

$$\begin{aligned} F_+ &\equiv \frac{1}{2}(1+\cos^2\theta)\cos 2\phi\cos 2\psi - \cos\theta\sin 2\phi\sin 2\psi, \\ F_\times &\equiv \frac{1}{2}(1+\cos^2\theta)\cos 2\phi\sin 2\psi + \cos\theta\sin 2\phi\cos 2\psi, \end{aligned} \tag{2.10}$$

where $(\theta,\ \phi)$ are spherical-polar coordinates describing the angular position of the source relative to the detector. The angle ψ describes a rotation of the radiation basis-vectors in the transverse plane, and together with ι describes the orientation of a binary's orbital plane with respect to the detector.

We now recast Eq. (2.8) into the form given by Ref. [297], such that the dependence of the detector response, $h(t)$, on (θ,ϕ,ι,ψ) is completely encapsulated in one variable, Θ,

$$h(t) = \begin{cases} \frac{\mathcal{M}_z^{5/3}}{D_L}\Theta(\pi f)^{2/3}\cos[\chi+\Phi(t)], & \text{for } t<T, \\ 0, & \text{for } t>T, \end{cases} \tag{2.11}$$

where T is taken as the time of binary coalescence, χ is a constant phase, and Θ is defined as

$$\Theta \equiv 2[F_+^2(1+\cos^2\iota)^2 + 4F_\times^2\cos^2\iota]^{1/2}, \tag{2.12}$$

where $0<\Theta<4$.

Even though the luminosity distance D_L is imprinted in the gravitational waveform, a single interferometer cannot deduce this. The degeneracy in the detector response between Θ and D_L must be broken, necessitating a network of three or more separated interferometers for sky-location triangulation [284]. A network of separated detectors will vary in their sensitivity to the different GW polarisation states through their specific antenna patterns. Since the two polarisation amplitudes have different dependences on the binary inclination angle, the degree of elliptical polarisation measured by a network can constrain ι [68]. The interferometers comprising a network will be misaligned such that their varying responses to an incoming GW can constrain the polarisation angle, ψ.

Once Θ is constrained, D_L can then be deduced from the detector response, giving a typical measurement error of $\sim(300/\rho)\%$, where ρ is the signal-to-noise ratio of the detection (e.g., [299, 301, 302]). The accuracy with which the distance can be measured will depend on the exact network configuration (for example, a detection by a Southern Hemisphere instrument would partially break the inclination–distance degeneracy [75]), but we will use the above as a representative value.

We don't include the impact of detector amplitude calibration errors, which could lead to systematic biases in distance estimates. Unlike statistical measurement errors, these biases would not be ameliorated by increasing the number of detections. For example, calibration errors of order 10%, as estimated for the LIGO S5 search [303], would translate directly into 10% systematic biases in H_0 estimates. Thus, systematic calibration errors could become the limiting factor on the accuracy of measuring H_0 if they exceed the statistical errors estimated in this analysis. However, a recent study in the context of second-generation detectors has found that such systematic shifts are likely to be a small fraction of the statistical measurement errors [304].

2.3.2 Network characteristics

For the purposes of creating a catalogue of sources for our study, we are only interested in determining which binaries are detectable, and how accurately the parameters of these binaries can be estimated. We use the criterion that the network signal-to-noise ratio, $\rho_{\rm net}$, must be greater than 8 for detection. Actual searches use significantly more complicated detection statistics that depend on the network configuration, data quality, and search techniques, which might make our assumed detectability threshold optimistic. Here, we are interested only in a sensible approximation of the detectability criterion.

The network configuration for the advanced detector era is uncertain at present. Possibilities include the two LIGO 4 km detectors at Hanford and Livingston (HHL), probably sharing data with Virgo (HHLV). Alternatively, moving one of the Hanford detectors to Australia (AHL or AHLV) would improve the network's parameter-estimation accuracy[2] [75, 305], while the Japanese detector KAGRA and/or Indian detector LIGO-India may join the network at a later date.

In the HHL configuration all of the sites are located in the United States, such that we may use the approximation of assuming the aLIGO interferometers can be used in *triple coincidence* to constitute a *super-interferometer*. This assumption is motivated by the orientation of the interferometer arms being approximately parallel [306], and also has precedents in the literature [e.g., 157, 297]. However, source localisation and D_L determination is very poor in HHL, and would be greatly improved by the inclusion of data from Virgo or an Australian/Indian detector.

The single-interferometer approximation is less obviously valid for networks with distant, non-aligned detectors, such as AHL(V) or HHLV. In Ref. [307], the authors comment that the proposed LIGO-Australia site was considered so as to be nearly antipodal to the LIGO sites, such that all three interferometers in the AHL configuration would have similar antenna patterns. Furthermore, since the same hardware configuration would be used for LIGO-Australia and aLIGO, the noise spectra would have been expected to be similar [308]. Meanwhile, Virgo

---

[2] While this research was being carried out LIGO-Australia was a distinct possibility, and so is considered in the following. We now expect the H2 instrument to be relocated to India. However, our consideration of a network including an Australian detector does not affect our general conclusions.

does not have the same antenna pattern as the LIGO detectors, and the AdV noise spectrum [82] will be somewhat different from the aLIGO spectrum.

In any case, precise comparisons of the sensitivity of different networks depend on assumptions about search strategies (e.g., coincident vs fully coherent searches[3]) and source distributions (see, e.g., Ref. [75, 307, 309]). We therefore penalise our super-interferometer assumption in two different ways. Firstly, we set the network SNR threshold to correspond to the expected SNR from three identical interferometers, as described below, rather than the four interferometers comprising the AHLV or HHLV networks. We further penalise the HHLV network relative to the network including the more optimally located LIGO-Australia by raising the SNR threshold from 8 to ~ 10. These increases in SNR thresholds have the effect of restricting the network's reach in luminosity distance or redshift; however, similar numbers of detections can be achieved by longer observation times.

With the aforementioned caveats, we proceed with our assumption that a global network can be approximated as a single super-interferometer. This is to provide a proof of principle for the ability of such a network to probe the background cosmology and aspects of the source distribution. We do not anchor our analysis to precise knowledge of the individual interferometer site locations and orientations, but will attempt to correct for any possible bias.

2.3.3 Signal detection

With prescriptions to model gravitational waveforms from every stage of the binary coalescence, we are able to coherently track the phase-evolution of the GW, and employ our waveform templates to optimise the SNR of a detection. Matched filtering is a standard technique in data-analysis to efficiently search for, and extract the properties of, signals with known characteristics (e.g., phase-evolution) in noisy data [125]. Further details on GW data-analysis can be found in Ref. [310, 311].

We consider noise in our detector to be a continuous zero-mean Gaussian random process, $n(t)$. The data stream will be

$$x(t) = h(t) + n(t), \tag{2.13}$$

where $h(t)$ is the signal of interest. The spectral properties of the noise are described by its one-sided power spectral density (PSD), $S_n(f)$,

$$\langle \tilde{n}(f)\tilde{n}^*(f') \rangle = \frac{1}{2} S_n(f)\delta(f - f'), \tag{2.14}$$

---

[3] In a coherent network search the datasets from all interferometers are brought together, an appropriate filter applied, and the detection statistic integrated coherently across all data. In a coincident network search the data from each detector is analysed separately, after which coincidences are searched for in the multi-dimensional source parameter space.

where $\langle\cdot\rangle$ denotes an expectation value, and $\tilde{n}(f) = \int_{-\infty}^{\infty} n(t) \exp(2\pi i f t)\, df$ is the Fourier transform of the noise.

The *correlation* of the data stream with a waveform template (or "filter") $q(t)$ is given by,

$$c(\tau) \equiv \int_{-\infty}^{\infty} x(t) q(t+\tau) dt, \tag{2.15}$$

where τ denotes the lag of the template behind the data stream. Our goal is to maximise this correlation by finding an *optimal* template. The SNR is defined in terms of $c(\tau)$ by,

$$\rho^2 \equiv \frac{S^2}{N^2} \equiv \frac{\langle c(\tau)\rangle^2}{\langle c(\tau)^2\rangle - \langle c(\tau)\rangle^2}. \tag{2.16}$$

We now define a scalar product between waveforms [312],

$$(a|b) \equiv 2\int_0^{\infty} \frac{df}{S_n(f)} \left[\tilde{a}(f)\tilde{b}^*(f) + \tilde{a}^*(f)\tilde{b}(f)\right], \tag{2.17}$$

which allows us to write the SNR in a more compact form,

$$\rho = \frac{(h \exp[2\pi i f \Delta t]\, |S_n q)}{\sqrt{(S_n q | S_n q)}}, \tag{2.18}$$

where Δt is the difference in the template lag-time and the signal arrival-time. Maximising this with respect to template-choice gives the optimal template, and the *optimal SNR*,

$$\rho_{\rm opt} = (h|h)^{1/2} = 2\left[\int_0^{\infty} df \frac{\left|\tilde{h}(f)\right|^2}{S_n(f)}\right]^{1/2}. \tag{2.19}$$

Now, following Ref. [297] (and correcting for a missing square root), we write the optimal matched-filtering SNR of an inspiraling DNS binary in a single detector as

$$\rho = 8\Theta \frac{r_0}{D_L}\left(\frac{\mathcal{M}_z}{1.2M_\odot}\right)^{5/6} \sqrt{\zeta(f_{\rm max})}, \tag{2.20}$$

where

$$\begin{aligned} r_0^2 &\equiv \frac{5}{192\pi}\left(\frac{3}{20}\right)^{5/3} x_{7/3} M_\odot^2, \\ x_{7/3} &\equiv \int_0^{\infty} \frac{df (\pi M_\odot)^2}{(\pi f M_\odot)^{7/3} S_n(f)}, \\ \zeta(f_{\rm max}) &\equiv \frac{1}{x_{7/3}} \int_0^{2f_{\rm max}} \frac{df(\pi M_\odot)^2}{(\pi f M_\odot)^{7/3} S_n(f)}, \end{aligned} \tag{2.21}$$

and $2f_{\rm max}$ is the GW frequency at which the inspiral detection template ends [313]. The SNR of a detected system will vary between the individual network sites, as a result of the different

$S_n(f)$'s and angular dependencies. In a coincident search, the network SNR of a detected system is given by the quadrature summation of the individual interferometer SNRs,

$$\rho^2_{\rm net} = \sum_k \rho^2_k. \tag{2.22}$$

We approximate the sensitivity of the super-interferometer by assuming 3 identical interferometers in the network with the sensitivity of aLIGO, such that $r_{0,\rm net} \approx \sqrt{3}r_0$. Different target noise curves for aLIGO produce different values for the characteristic distance-reach, r_0, which vary between $\sim 80 - 120$ Mpc [308]. We adopt the median value of 100 Mpc for a single interferometer, yielding $r_{0,\rm net} \sim 176$ Mpc for the network.

The SNR also depends on $\zeta(f_{\rm max})$, which increases monotonically as a function of $f_{\rm max}$. This factor describes the overlap of the signal power with the detector bandwidth [297], which will depend on the wave frequency at which the post-Newtonian approximation breaks down, and the inspiral ends. It is usual to assume that the inspiral phase terminates when the evolution reaches the innermost stable circular orbit (ISCO), whereupon the NSs merge in less than an orbital period. This gives

$$f^{\rm GW}_{\rm max} = 2f_{\rm max} = 2\left(\frac{f_{\rm ISCO}}{1+z}\right) = \frac{1570\ \text{Hz}}{1+z}\left(\frac{2.8M_\odot}{M}\right), \tag{2.23}$$

where M is the total mass of the binary system [147]. $f_{\rm ISCO}$ also depends directly on the mass ratio μ/M (μ is the system's reduced mass); however this mass asymmetry term has a negligible effect on $f_{\rm max}$ for the mass range of NSs considered here [313, 314].

The maximum binary system mass could conceivably be $\sim 4.2M_\odot$.[4] The aLIGO horizon distance for $1.4M_\odot$–$1.4M_\odot$ inspirals is ∼445 Mpc, which corresponds to $z \sim 0.1$ in the ΛCDM cosmology. Given that we are evaluating different cosmological parameters, we adopt $z \sim 1$ as a generous upper redshift limit to a second-generation network's reach. This redshift exceeds the reach of aLIGO in all considered cosmologies[5] and chirp masses. With these extreme choices for the variables, the orbital frequency at the ISCO, $f_{\rm max}$, could be as low as ∼262 Hz. For the *zero-detuning-high-power* aLIGO noise curve [308], $\zeta(f_{\rm max} = 262\text{Hz}) \gtrsim 0.98$. Thus, we feel justified in adopting $\zeta(f_{\rm max}) \simeq 1$ for the ensuing analysis.

Thus matched filtering, with an SNR threshold of 8, a characteristic distance reach of ∼176 Mpc and $\zeta(f_{\rm max}) \simeq 1$, provides a criterion to determine the detectability of a source by our network.[6]

---

[4] Both NSs in the binary system would need to have masses 2σ above the distribution mean at the maximum μ and σ considered in this analysis, where $\mu_{\rm NS} \in [1.0, 1.5]M_\odot$, $\sigma_{\rm NS} \in [0, 0.3]M_\odot$.

[5] $H_0 \in [0.0, 200.0]$ km s^{-1}Mpc^{-1}; $\Omega_{k,0} = 0$; $\Omega_{m,0} \in [0.0, 0.5]$

[6] There will be some bias in this approximation, since we are assuming each interferometer records the same SNR for each event. The fact that the different interferometers are not co-located means that this may overestimate

2.3.4 Orientation function, Θ

The angular dependence of the SNR is encapsulated within the variable Θ, which varies between 0 and 4, and has a functional form given by Eq. (2.12). From our catalogue of coincident DNS inspiral detections we will use only $\mathcal{M}_z$ and D_L for each system. The sky location and binary orientation can be deduced from the network analysis, however we will not explicitly consider them here. Without specific vales for the angles (θ, ϕ, ι, ψ) we can still write down the probability density function for Θ [297]. Taking $\cos\theta$, ϕ/π, $\cos\iota$ and ψ/π to be uncorrelated and distributed uniformly over the range $[-1,1]$, the cumulative probability distribution for Θ was calculated numerically in Ref. [315]. The probability distribution can be accurately approximated [297] by,

$$\mathcal{P}_\Theta(\Theta) = \begin{cases} \frac{5}{256}\Theta(4-\Theta)^3, & \text{if } 0 < \Theta < 4, \\ 0, & \text{otherwise.} \end{cases} \tag{2.24}$$

We can use Eq. (2.24) to evaluate the cumulative distribution of Θ,

$$C_\Theta(x) \equiv \int_x^\infty \mathcal{P}_\Theta(\Theta) d\Theta \simeq \begin{cases} 1, & \text{if } x \leq 0 \\ \frac{(1+x)(4-x)^4}{256}, & \text{if } 0 \leq x \leq 4 \\ 0, & \text{if } x > 4. \end{cases} \tag{2.25}$$

2.3.5 NS mass distribution

In recent years, the number of catalogued pulsar binary systems has increased to the level that the underlying NS mass distribution can be probed. There is now a concordance across the literature that the NS mass distribution is multimodal, which reflects the different evolutionary paths of pulsar binary systems [316, 317]. However, we are only concerned with NSs in NS-NS systems for this analysis, and their distribution appears to be quite narrow.

In particular, Valentim et al. [317] found that the NSs in DNS systems populate a lower mass peak at $m \sim 1.37M_\odot \pm 0.042M_\odot$, which agrees well with the earlier work of Thorsett and Chakrabarty [318], who found that an analysis of 26 radio pulsars favoured a very tight Gaussian distribution of NS masses ($1.35\pm0.04M_\odot$). Meanwhile, Kiziltan et al. [316] restricted their sample of NSs to those with secure mass measurements and found that the *maximum-a-posteriori* Gaussian mass distribution for DNS systems had parameters $\mu_{\rm NS} \sim 1.34M_\odot$, $\sigma_{\rm NS} \sim 0.06M_\odot$. Their posterior predictive density estimate gave a NS mass distribution with $\mu_{\rm NS} = 1.35M_\odot$, $\sigma_{\rm NS} = 0.13M_\odot$, while a recent update to their manuscript has modified this very

---

the number of coincident detections. We carry out the analysis here aware of, but choosing to ignore, this bias, and in Sec. 2.5.3 consider raising the network SNR threshold, which has the same effect as reducing the *characteristic distance* reach of the network.

slightly to $M_{\rm NS} = 1.33^{+0.10}_{-0.12} M_\odot$ [319], where errors denote the 68% posterior predictive interval. Finally, a recent study by Özel et al. [320] has found that DNS data are consistent with both pulsar and companion having been drawn from the same underlying distribution of masses.

Population synthesis studies of binary evolution predict similarly narrow mass distributions for NSs in NS-NS binaries (see, e.g., Ref. [124, 157, 321, 322, and references therein]). Some models predict that the mass of NSs at formation is bimodal, with peaks around 1.3 and 1.8 solar masses, and any post-formation mass transfer in DNS systems is not expected to change that distribution significantly. However the $1.8M_\odot$ mode is anticipated to be very rare for DNS systems, with the vast majority of merging NSs belonging to the $1.3M_\odot$ peak. Thus, population synthesis results support the anticipation that NS binaries may have a narrow range of masses that could be modelled by a Gaussian distribution.

Further population synthesis and observational studies in the following decade will help to shed further light on the nature of the NS mass distribution. The assumption of a unimodal (for DNS systems) Gaussian distribution is an approximation, and if future studies show this to be inappropriate, then a more suitable ansatz could be readily incorporated within the framework described here.

To lowest order, the GW signal depends on the two NS masses through the chirp mass, $\mathcal{M}$. We assume that the distribution of individual NS masses is normal, as suggested above. For $\sigma_{\rm NS} \ll \mu_{\rm NS}$, this should yield an approximately normal distribution for the chirp mass as well. We carried out $\sim O(10^5)$ iterations, drawing two random variates from a normal distribution (representing the individual NS masses), and then computing $\mathcal{M}$. We varied the mean and width of the underlying distribution within the allowed ranges (Sec. 2.3.3). Binning the $\mathcal{M}$ values, the resulting $\mathcal{M}$ distribution was found to be normal, as expected.

We now postulate a simple ansatz for the relationship between the chirp mass distribution parameters and the underlying NS mass distribution. If X_1 and X_2 are two independent random variates drawn from normal distributions,

$$\begin{aligned} X_1 \sim N(\mu_1, \sigma_1^2) \quad &; \quad X_2 \sim N(\mu_2, \sigma_2^2) \\ aX_1 + bX_2 \sim N(a\mu_1 &+ b\mu_2, a^2\sigma_1^2 + b^2\sigma_2^2). \end{aligned} \tag{2.26}$$

Since the NS mass distribution is symmetric around the mean (and all NS masses are $\sim O(1M_\odot)$ with the values spread over a relatively narrow range), then we can assume a characteristic value for the pre-factor in Eq. (2.6) is the value taken when both masses are equal i.e. $\sim (0.25)^{3/5}$. The chirp mass distribution should then be approximately normal

$$\mathcal{M} \sim N(\mu_c, \sigma_c^2),$$

with mean and standard deviation

$$\mu_c \approx 2(0.25)^{3/5}\mu_{\rm NS}, \quad \sigma_c \approx \sqrt{2}(0.25)^{3/5}\sigma_{\rm NS}. \tag{2.27}$$

where $\mu_{\rm NS}$ and $\sigma_{\rm NS}$ are the mean and standard deviation of the underlying NS mass distribution, respectively.

The accuracy of such an ansatz depends upon the size of mass asymmetries which could arise in a DNS binary system. We investigated the percentage offset between the *actual* distribution parameters (deduced from least-squares fitting to the sample number-density distribution) and the ansatz parameters, for a few values of $\mu_{\rm NS}$ and $\sigma_{\rm NS}$. The largest offset of the ansatz parameters from the true chirp mass distribution was on the order of a few percent ($\sim$$2.5\%$ for μ_c, and $\sim$$3.5\%$ for σ_c when $\mu_{\rm NS} = 1.0M_\odot$, $\sigma_{\rm NS} = 0.3M_\odot$), and the agreement improved with a narrower underlying NS mass distribution. For the case of $\sigma_{\rm NS} \sim 0.05M_\odot$, the agreement was $\sim$$0.1\%$ for μ_c and $< 0.1\%$ for σ_c. In the case of $\sigma_{\rm NS} \sim 0.15M_\odot$, the agreement was within a percent for both parameters. The sign of these offsets indicates that $\mu_c^{\rm true} < \mu_c^{\rm model}$ and $\sigma_c^{\rm true} > \sigma_c^{\rm model}$.

Given that the literature indicates an underlying NS mass distribution in DNS systems with $\sigma_{\rm NS} \lesssim 0.15M_\odot$, we anticipate that Eq. (2.27) will be appropriate for generating data sets and we use this in the ensuing analysis. The assumption throughout is that for the volume of the Universe probed by our global network, the NS mass distribution does not change.

The observed data will tell us how wide the intrinsic chirp mass distribution is in reality. If it is wider than anticipated, we may not be able to measure H_0 as precisely as we find here, but we will know this from the observations. In principle, we could still be systematically biased if the mass distribution turned out to be significantly non-Gaussian, since we are assuming a Gaussian model. However, it will be fairly obvious if the mass distribution is significantly non-Gaussian (e.g., has a non-negligible secondary peak around $1.8\ M_\odot$), since redshift could only introduce a $\sim$$10\%$ spread in the very precise redshifted chirp mass measurements for detectors that are sensitive to $z \sim 0.1$. In such a case, we would not attempt to fit the data to a Gaussian model for the intrinsic chirp mass distribution.

2.3.6 DNS binary merger rate density, $\dot{n}(z)$

We assume that merging DNS systems are distributed homogeneously and isotropically. The total number of these systems that will be detected by the global network depends on the intrinsic rate of coalescing binary systems *per comoving volume*. We require some knowledge of this in order to generate our mock data sets. Any sort of redshift evolution of this quantity (as a result of star-formation rate evolution etc.) can be factorised out [297], such that

$$\dot{n}(t) \equiv \frac{d^2N}{dt_{\rm e}dV_c} \equiv \dot{n}(z) = \dot{n}_0\xi(z), \tag{2.28}$$

where N is the number of coalescing systems, $t_{\rm e}$ is proper time, V_c is comoving volume, and $\dot{n}_0$ represents the local merger-rate density.

Table 2.1: A compilation of NS-NS merger rate densities in various forms from Tables II, III and IV in Ref. [147]. The first column gives the units. The second, third and fourth columns denote the plausible pessimistic, likely, and plausible optimistic merger rates extrapolated from the observed sample of Galactic binary NSs [149]. The fifth column denotes the upper rate limit deduced from the rate of Type Ib/Ic supernovae [150].

Source	R_{low}	R_{re}	R_{high}	R_{max}
NS-NS (MWEG^{-1}Myr^{-1})	1	100	1000	4000
NS-NS (L$_{10}^{-1}$Myr^{-1})	0.6	60	600	2000
NS-NS (Mpc^{-3}Myr^{-1})	0.01	1	10	50

We will consider an evolving merger-rate density, such that,

$$\xi(z) = 1 + \alpha z = 1 + 2z, \qquad \text{for } z \leq 1, \tag{2.29}$$

which is motivated by a piecewise linear fit [323] to the merger-rate evolution deduced from the UV-luminosity-inferred star-formation-rate history [324].

The appropriate value for $\dot{n}_0$ is discussed in detail in Ref. [147]. In that analysis, the authors review the range of values quoted in the literature for compact binary coalescence rates, i.e. not only NS-NS mergers but also NS-BH and BH-BH. The binary coalescence rates are quoted per Milky Way Equivalent Galaxy (MWEG) and per L_{10} (10^{10} times the Solar blue-light luminosity, $L_{B,\odot}$), as well as per unit comoving volume. In each case, the rates are characterised by four values, a "low," "realistic," "high" and "maximum" rate, which cover the full range of published estimates.

The values for the NS-NS merger rate given by Ref. [147] are listed in Table 2.1. The second row of Table 2.1 is derived assuming that coalescence rates are proportional to the star-formation rate in nearby spiral galaxies. This star-formation rate is crudely estimated from their blue-luminosity, and the merger-rate density is deduced via the conversion factor of 1.7 L_{10}/MWEG [325]. The data in the third row is obtained using the conversion factor of 0.0198 L_{10}/Mpc^3 [326].

To convert from merger-rate densities to *detection rates*, Ref. [147] take the product of the merger-rate density with the volume of a sphere with radius equal to the *volume averaged horizon distance*. The horizon distance is the distance at which an optimally oriented, optimally located binary system of inspiraling $1.4M_{\odot}$ NSs is detected with the threshold SNR. This is then averaged over all sky locations and binary orientations.

$$N_D = \dot{n}_0 \times \frac{4\pi}{3}\left(\frac{D_{\mathrm{horizon}}}{2.26}\right)^3, \tag{2.30}$$

where the $(1/2.26)$ factor represents the average over all sky locations and binary orientations.

This gives ~ 40 detection events per year in aLIGO (using $R_{\rm re}$), assuming that $D_{\rm horizon} = 445$ Mpc and all NSs have a mass of $1.4 M_{\odot}$.

2.3.7 Cosmological model assumptions

We assume a flat cosmology, $\Omega_{k,0} = 0$, throughout, for which the luminosity distance as a function of the radial comoving distance is given by

$$D_L(z) = (1+z)D_c(z) = (1+z)D_H \int_0^z \frac{dz'}{E(z')}, \tag{2.31}$$

where $D_H = 1/H_0$ (the "*Hubble length scale*") and

$$E(z) = \sqrt{\Omega_{m,0}(1+z)^3 + \Omega_{\Lambda,0}}. \tag{2.32}$$

In such a cosmology, the redshift derivative of the comoving volume is given by

$$\frac{dV_c}{dz} = \frac{4\pi D_c(z)^2 D_H}{E(z)}. \tag{2.33}$$

At low redshifts, we can use an approximate simplified form for the relationship between redshift and luminosity distance. Using a Taylor expansion of the comoving distance around $z = 0$ up to $O(z^2)$, and taking the appropriate positive root, we find $D_c(z) = D_L(z)/(1+z)$ is given by

$$\begin{aligned} D_c(z) &\approx D_c(z=0) + z\,\frac{\partial D_c}{\partial z}\bigg|_{z=0} + \frac{z^2}{2!}\,\frac{\partial^2 D_c}{\partial z^2}\bigg|_{z=0} + \ldots \\ &\approx D_H\left[z - \frac{3}{4}\Omega_{m,0}z^2\right]. \end{aligned} \tag{2.34}$$

Hence,

$$D_L \approx D_H\left[z + \left(1 - \frac{3}{4}\Omega_{m,0}\right)z^2\right].$$

Therefore,

$$z \approx \frac{1}{2\left(1 - \frac{3}{4}\Omega_{m,0}\right)}\left[\sqrt{1 + \frac{4\left(1 - \frac{3}{4}\Omega_{m,0}\right)D_L}{D_H}} - 1\right]. \tag{2.35}$$

This approximation is very accurate for the range of parameters investigated ($H_0 \in [0, 200]$ km s^{-1}Mpc^{-1}, $\Omega_{m,0} \in [0, 0.5]$), and for $D_L \lesssim 1$ Gpc (which is comfortably beyond the reach of aLIGO for NS-NS binaries). In this parameter range, the largest offset of this approximation from a full redshift root-finding algorithm is $\sim 4.6\%$, at a luminosity distance of 1 Gpc.

2.3.8 Distribution of detectable DNS systems

The two system properties we will use in our analysis are the redshifted chirp mass, $\mathcal{M}_z$, and the luminosity distance, D_L. Only systems with an SNR greater than threshold will be detected. Thus, we must include SNR selection effects in the calculation for the number of detections. We can write down the distribution of the number of events per year with $\mathcal{M}$, z and Θ [157, 297],

$$\frac{d^4N}{dtd\Theta dzd\mathcal{M}} = \frac{dV_c}{dz}\frac{\dot{n}(z)}{(1+z)}\mathcal{P}(\mathcal{M})\mathcal{P}_\Theta(\Theta), \tag{2.36}$$

where t is the time measured in the observer's frame, such that the $1/(1+z)$ factor accounts for the redshifting of the merger rate [157].

We convert this to a distribution in $\mathcal{M}_z$, D_L and ρ using,

$$\frac{d^4N}{dtd\rho dD_L d\mathcal{M}_z} = \begin{vmatrix} \frac{\partial\mathcal{M}}{\partial\mathcal{M}_z} & \frac{\partial\mathcal{M}}{\partial D_L} & \frac{\partial\mathcal{M}}{\partial\rho} \\ \frac{\partial z}{\partial\mathcal{M}_z} & \frac{\partial z}{\partial D_L} & \frac{\partial z}{\partial\rho} \\ \frac{\partial\Theta}{\partial\mathcal{M}_z} & \frac{\partial\Theta}{\partial D_L} & \frac{\partial\Theta}{\partial\rho} \end{vmatrix} \times \frac{d^4N}{dtd\Theta dzd\mathcal{M}}. \tag{2.37}$$

We use the definitions of the variables in Sec. 2.3.1 and 2.3.2 to evaluate the Jacobian matrix determinant. The redshift is only a function of D_L (in a given cosmology); the intrinsic chirp mass, $\mathcal{M}$, is the redshifted chirp mass divided by $(1+z)$ (again the redshift is a function of D_L); Θ is a function of $\mathcal{M}_z$, D_L and ρ according to Eq. (2.20). The (1,3) component $\left(\partial\mathcal{M}/\partial\rho \equiv (\partial\mathcal{M}/\partial\rho)|_{\mathcal{M}_z,D_L}\right)$ is zero because we are differentiating intrinsic chirp mass (a function of redshifted chirp mass and distance) with respect to SNR, but keeping distance and redshifted chirp mass constant. If these variables are held constant then the derivative must be zero. Similar considerations of which variables are held constant in the partial derivatives are used to evaluate the remaining elements of the matrix. Hence,

$$\begin{vmatrix} \frac{1}{(1+z)} & -\frac{\mathcal{M}}{(1+z)}\frac{\partial z}{\partial D_L} & 0 \\ 0 & \frac{\partial z}{\partial D_L} & 0 \\ -\frac{5}{6}\frac{\Theta}{\mathcal{M}_z} & \frac{\Theta}{D_L} & \frac{\Theta}{\rho} \end{vmatrix} = \frac{1}{(1+z)}\frac{\partial z}{\partial D_L}\frac{\Theta}{\rho}. \tag{2.38}$$

We note that,

$$\mathcal{P}_\rho(\rho)\delta\rho = \mathcal{P}_\Theta(\Theta)\delta\Theta,$$

which gives,

$$\begin{aligned} \mathcal{P}_\rho(\rho|\mathcal{M}_z, D_L) =& \mathcal{P}_\Theta(\Theta)\frac{\partial\Theta}{\partial\rho}\bigg|_{\mathcal{M}_z,D_L} \\ =& \mathcal{P}_\Theta(\Theta)\frac{\Theta}{\rho} \\ =& \mathcal{P}_\Theta\left[\frac{\rho}{8}\frac{D_L}{r_0}\left(\frac{1.2M_\odot}{\mathcal{M}_z}\right)^{5/6}\right] \times \frac{D_L}{8r_0}\left(\frac{1.2M_\odot}{\mathcal{M}_z}\right)^{5/6}, \end{aligned} \tag{2.39}$$

such that we finally obtain,

$$\begin{aligned}\frac{d^4N}{dtd\rho dD_L d\mathcal{M}_z} =& \frac{1}{(1+z)}\frac{\partial z}{\partial D_L}\frac{dV_c}{dz}\frac{\dot{n}(z)}{(1+z)} \times \mathcal{P}(\mathcal{M}|z) \times \underbrace{\mathcal{P}_\Theta(\Theta)\frac{\Theta}{\rho}}_{\mathcal{P}_\rho(\rho|\mathcal{M}_z,D_L)} \\ =& \frac{4\pi D_c(z)^2 D_H}{D_c(z)E(z)+D_H(1+z)}\frac{\dot{n}(z)}{(1+z)^2} \times \mathcal{P}\left(\frac{\mathcal{M}_z}{1+z}\middle| D_L\right)\mathcal{P}_\rho(\rho|\mathcal{M}_z,D_L).\end{aligned} \tag{2.40}$$

We may not necessarily care about the specific SNR of a detection; rather only that a system with $\mathcal{M}_z$ and D_L has SNR above threshold (and is thus detectable). Fortunately the SNR only enters Eq. (2.40) through $\mathcal{P}_\rho(\rho|\mathcal{M}_z,D_L)$, such that we can simply integrate over this term and apply Eq. (2.25),

$$\int_{\rho_0}^{\infty}\mathcal{P}_\rho(\rho|\mathcal{M}_z,D_L)d\rho = \int_x^\infty \mathcal{P}_\Theta(\Theta)d\Theta \equiv C_\Theta(x),$$

$$\text{where,} \quad x = \frac{\rho_0}{8}\frac{D_L}{r_0}\left(\frac{1.2M_\odot}{\mathcal{M}_z}\right)^{5/6}. \tag{2.41}$$

In this case, Eq. (2.40) is modified to give,

$$\begin{aligned}&\left.\frac{d^3N}{dtdD_L d\mathcal{M}_z}\right|_{\rho>\rho_0} \\ =& \frac{4\pi D_c(z)^2 D_H}{D_c(z)E(z)+D_H(1+z)}\frac{\dot{n}(z)}{(1+z)^2} \times \mathcal{P}\left(\frac{\mathcal{M}_z}{1+z}\middle| D_L\right) C_\Theta\left[\frac{\rho_0}{8}\frac{D_L}{r_0}\left(\frac{1.2M_\odot}{\mathcal{M}_z}\right)^{5/6}\right].\end{aligned} \tag{2.42}$$

To calculate the number of detected systems (given a set of cosmological and NS mass distribution parameters, $\vec{\mu}$) we integrate over this distribution, which is equivalent to integrating over the distribution of events with redshift and chirp mass, i.e., $N_\mu = T \times \int_0^\infty \int_0^\infty \left(\frac{d^3N}{dtdzd\mathcal{M}}\right) dzd\mathcal{M}$, where T is the duration of the observation run.

2.3.9 Creating mock catalogues of DNS binary inspiraling systems

The model parameter space we investigate is the 5D space of $[H_0, \mu_{\rm NS}, \sigma_{\rm NS}, \Omega_{m,0}, \alpha]$ with a flat cosmology assumed. To generate a catalogue of events, we choose a set of reference parameters, motivated by previous analysis in the literature. For our reference cosmology, we adopt values consistent with the seven-year WMAP observations [327, 328]: $H_0 = 70.4$ km s^{-1}Mpc^{-1}, $\Omega_{m,0} = 0.27$ and $\Omega_{\Lambda,0} = 0.73$.[7] The parameters of the NS mass distribution were discussed earlier, but as reference we use $\mu_{\rm NS} = 1.35M_\odot$ and $\sigma_{\rm NS} = 0.06M_\odot$. The merger-rate density

---

[7] After this research was performed, a final revision of the WMAP results was published [329], in addition to the first Planck results [16]. As seen later, given the typical measurement accuracies achieved in our analysis, our reference cosmology remains very comfortably consistent with these revised results.

was also discussed earlier, and we take $\alpha = 2.0$ and $\dot{n}_0 = 10^{-6}$ Mpc^{-3}yr^{-1} as the reference. Later, we will investigate how the results change if the width of the NS mass distribution is as large as $0.13M_\odot$, as indicated by the predictive density estimate of Ref. [316].

These reference parameters are used to calculate an expected number of events,[8] and the number of observed events is drawn from a Poisson distribution (assuming each binary system is independent of all others) with that mean. Monte-Carlo acceptance/rejection sampling is used to draw random redshifts and chirp masses from the distribution in Eq. (2.36) for each of the N_o events. The D_L and $\mathcal{M}_z$ are then computed from the sampled $\mathcal{M}$ and z.

With a reference rate of $\dot{n}_0 = 10^{-6}$ Mpc^{-3}yr^{-1} and a constant merger-rate density, we estimate that there should be $\sim$90 yr^{-1} detections, whilst taking into account merger-rate evolution using Eq. (2.29) boosts this to $\sim$100 yr^{-1}. These numbers are for a network SNR threshold of 8. If we ignore merger-rate evolution and raise the SNR threshold to 10 (to represent an AdV-HHL network for which the coincident detection rate is roughly halved relative to the HHL-only network) we get $\sim$45 events in 1 year, which compares well to the 40 events found in Ref. [147].

2.4 Analysis methodology

Given a catalogue of simulated sources with measured redshifted chirp masses and luminosity distances, we use Bayesian statistics to compute posterior distribution functions of cosmological parameters, as well as the mean and standard deviation of the intrinsic NS mass distribution (in DNS systems).

2.4.1 Modelling the likelihood

Expressing the likelihood

We use a theoretical framework similar to that of Ref. [330]. The data are assumed to be a catalogue of events for which redshifted chirp mass, $\mathcal{M}_z$, and luminosity distance, D_L have been estimated. These two parameters for the events can be used to probe the underlying cosmology and NS mass distribution. In this analysis, we focus on what we can learn about the Hubble constant, H_0, the Gaussian mean of the (DNS system) NS mass distribution, $\mu_{\rm NS}$, and the Gaussian half-width, $\sigma_{\rm NS}$. We could also include the present-day matter density, $\Omega_{m,0}$, however we expect that this will not be well constrained due to the low luminosity distances of the sources. We could also include the gradient parameter, α, describing the redshift evolution of the merger-rate density.

---

[8] The observation time, T, is assumed to be 1 year (but the expected number of detections simply scales linearly with time) and a network acting as a super-interferometer with $r_{0,\rm net} \simeq 176$ Mpc is also assumed.

The measurement errors were discussed earlier (Sec. 2.3.1) and we will account for these later. For the first analysis we assume that the observable properties of individual binaries are measured exactly.

We consider first a binned analysis. We divide the parameter space of $\mathcal{M}_z$ and D_L into bins, such that the data is the number of events measured in a particular range of redshifted chirp mass *and* luminosity distance. Each binary system can be modelled as independent of all other systems, so that within a given galaxy we can model the number of inspirals that occur within a certain time as a Poisson process, with DNS binaries merging at a particular rate (e.g., [148, 331]). The mean of the Poisson process will be equal to the model-dependent rate times the observation time, and the actual number of inspirals occurring in the galaxy is a random-variate drawn from the Poisson distribution.

A bin in the space of system properties may contain events from several galaxies, but these galaxies will behave independently and the number of recorded detections in a given bin will then be a Poisson process, with a mean equal to the model-dependent *expected* number of detections in that bin [330]. The data can be written as a vector of numbers in labelled bins in the 2D space of system properties, i.e. $\overrightarrow{n} = (n_1, n_2, \ldots, n_X)$, where X is the number of bins. Therefore, the likelihood of recording data D under model $\mathcal{H}$ (with model parameters $\overrightarrow{\mu}$) is the product of the individual Poisson probabilities for detecting n_i events in a bin, i, where the expected (model-dependent) number of detections is $r_i(\overrightarrow{\mu})$. For the i^{th} bin,

$$p(n_i|\overrightarrow{\mu}, \mathcal{H}) = \frac{(r_i(\overrightarrow{\mu}))^{n_i} e^{-r_i(\overrightarrow{\mu})}}{n_i!}, \tag{2.43}$$

and so the likelihood of the catalogued detections is,

$$\mathcal{L}(\overrightarrow{n}|\overrightarrow{\mu}, \mathcal{H}) = \prod_{i=1}^{X} \frac{(r_i(\overrightarrow{\mu}))^{n_i} e^{-r_i(\overrightarrow{\mu})}}{n_i!}. \tag{2.44}$$

In this work, we take the continuum limit of Eq. (2.44). In this case, the number of events in each infinitesimal bin is either 0 or 1. Every infinitesimal bin contributes a factor of $e^{-r_i(\overrightarrow{\mu})}$, whilst the remaining terms in Eq. (2.44) evaluate to 1 for empty bins, and $r_i(\overrightarrow{\mu})$ for full bins. The product of the exponential factors gives e^{-N_μ}, where N_μ is the number of DNS inspiral detections predicted by the model, with parameters $\overrightarrow{\mu}$. The continuum likelihood of a catalogue of discrete events is therefore

$$\mathcal{L}(\overrightarrow{\overrightarrow{\Lambda}}|\overrightarrow{\mu}, \mathcal{H}) = e^{-N_\mu} \prod_{i=1}^{N_o} r(\overrightarrow{\lambda_i}|\overrightarrow{\mu}), \tag{2.45}$$

where $\overrightarrow{\overrightarrow{\Lambda}} = \{\overrightarrow{\lambda_1}, \overrightarrow{\lambda_2}, \ldots, \overrightarrow{\lambda_{N_o}}\}$ is the vector of measured system properties, with $\overrightarrow{\lambda_i} = (\mathcal{M}_z, D_L)_i$ for system i, and N_o is the number of detected systems. Finally, $r(\overrightarrow{\lambda_i}|\overrightarrow{\mu})$ is the rate of events with properties $\mathcal{M}_z$ and D_L, evaluated for the i^{th} detection under model parameters $\overrightarrow{\mu}$, which is given by Eq. (2.42).

Marginalising over $\dot{n}_0$

We may also modify the likelihood calculation to marginalise over the poorly constrained merger-rate density, $\dot{n}_0$.[9] This quantity is so poorly known (see Table 2.1), that it is preferable to use a new statistic that does not rely on the local merger-rate density, by integrating the likelihood given in Eq. (2.45) over this quantity,

$$\tilde{\mathcal{L}}(\overrightarrow{\overrightarrow{\Lambda}}|\overrightarrow{\mu},\mathcal{H}) = \int_0^\infty \mathcal{L}(\overrightarrow{\overrightarrow{\Lambda}}|\overrightarrow{\mu},\mathcal{H}) d\dot{n}_0. \tag{2.46}$$

The expected number of detections described in Sec. 2.3.8 can be expressed as,

$$N_\mu = \dot{n}_0 \times \int\int \mathcal{I}\, d\mathcal{M}_z dD_L,$$

where,

$$\mathcal{I} = \frac{4\pi D_c(z)^2 D_H}{D_c(z)E(z) + D_H(1+z)} \frac{1+\alpha z}{(1+z)^2} \times \mathcal{P}\left(\frac{\mathcal{M}_z}{1+z}\middle| D_L\right) C_\Theta \left[\frac{\rho_0}{8}\frac{D_L}{r_0}\left(\frac{1.2M_\odot}{\mathcal{M}_z}\right)^{5/6}\right], \tag{2.47}$$

and,

$$r(\overrightarrow{\lambda_i}|\overrightarrow{\mu}) = \dot{n}_0 \times \mathcal{I}_i, \tag{2.48}$$

where $\mathcal{I}_i$ is the integrand evaluated for the i^{th} system's properties. Thus,

$$\begin{aligned}\tilde{\mathcal{L}}(\overrightarrow{\overrightarrow{\Lambda}}|\overrightarrow{\mu},\mathcal{H}) &= \int_0^\infty \left[\exp\left(-\dot{n}_0 \times \int\int \mathcal{I}\, d\mathcal{M}_z dD_L\right) \times \left(\prod_{i=1}^{N_o} \dot{n}_0 \times \mathcal{I}_i\right)\right] d\dot{n}_0 \\ &= \left[\int_0^\infty \dot{n}_0^{N_o} \times \exp\left(-\dot{n}_0 \int\int \mathcal{I} d\mathcal{M}_z dD_L\right) d\dot{n}_0\right] \times \prod_{i=1}^{N_o} \mathcal{I}_i. \end{aligned} \tag{2.49}$$

The integral, $\int\int \mathcal{I}\, d\mathcal{M}_z dD_L$, depends on the underlying model parameters, $\overrightarrow{\mu}$, through $\mathcal{I}$, but it does not depend on $\dot{n}_0$. Therefore, defining

$$\gamma = \dot{n}_0 \times \int\int \mathcal{I}\, d\mathcal{M}_z dD_L = \dot{n}_0 \times \delta.$$

We note that $\dot{n}_0 \in [0,\infty]$, hence $\gamma \in [0,\infty]$. Therefore,

$$\begin{aligned}\tilde{\mathcal{L}}(\overrightarrow{\overrightarrow{\Lambda}}|\overrightarrow{\mu},\mathcal{H}) &= \left(\int_0^\infty \left(\frac{\gamma}{\delta}\right)^{N_o} \times e^{-\gamma} \frac{d\gamma}{\delta}\right) \prod_{i=1}^{N_o} \mathcal{I}_i \\ &= \underbrace{\left(\int_0^\infty \gamma^{N_o} e^{-\gamma} d\gamma\right)}_{\textbf{independent of } \overrightarrow{\mu}} \times \delta^{-(N_o+1)} \prod_{i=1}^{N_o} \mathcal{I}_i. \end{aligned} \tag{2.50}$$

---

[9] A similar technique was used in Ref. [332], where the total number of events predicted by the model is marginalised over.

We will verify in the analysis that this new likelihood does not introduce any systematic bias with respect to the case where exact knowledge of the merger-rate density is assumed. We note that we did not include a prior on $\dot{n}_0$ in the above, which is equivalent to using a flat prior for $\dot{n}_0 \in [0, \infty]$. This reflects our current lack of knowledge of the intrinsic merger rate, although such a prior is not normalisable. We could implement a normalisable prior by adding a cut-off, but this cut-off should be set sufficiently high that it will not influence the posterior and therefore the result will be equivalent to the above.

2.4.2 Calculating the posterior probability

The likelihood statistic $\tilde{\mathcal{L}}$ is used to marginalise over the poorly constrained local merger-rate density. We use a weakly informative prior on the model parameters, so that it doesn't prejudice our analysis. We allow $\mu_{\rm NS}$ to range within the posterior predictive density estimate of the NS mass distribution in Ref. [316], such that the prior on $\mu_{\rm NS}$ is a normal distribution with parameters $\mu = 1.35M_\odot$, $\sigma = 0.13M_\odot$. Our prior on α is also a normal distribution, centred at 2.0 with a σ of 0.5. Uniform priors were used for the other parameters.

We made sure that the size of the sampled parameter space was large enough to fully sample the posterior distribution, so that we could investigate how well GW observations alone could constrain the cosmology and NS mass distribution. The parameter ranges were $H_0 \in [0, 200]$ km s^{-1}Mpc^{-1}, $\Omega_{m,0} \in [0, 0.5]$, $\mu_{\rm NS} \in [1.0, 1.5]M_\odot$, $\sigma_{\rm NS} \in [0, 0.3]M_\odot$ and $\alpha \in [0.0, 5.0]$.

To calculate $\tilde{\mathcal{L}}$ for a given point in the model parameter space we must compute the number of detections predicted by those model parameters (N_μ), and we need to calculate $z(D_L)$ for that model so that $\mathcal{M}$ can be evaluated. For the sake of computational efficiency, some approximations are used. We have verified that our results are insensitive to these approximations. Our approximation for $z(D_L)$ was described in Sec. 2.3.7. We also used an analytic ansatz to calculate the model-dependent expected number of detections, based on factorising the contributions from different model parameters. The agreement between this ansatz and the full integrated model number is excellent, with the biggest discrepancy being $\lesssim 3\%$ of the true value. This allows a direct calculation of N_μ without a multi-dimensional integration for each point in parameter space.

2.5 Results & Analysis

For our first analysis, we will assume that $\mathcal{M}_z$ and D_L for each individual merger are measured perfectly by our observations, so that the $\mathcal{M}_z$ and D_L recorded for the events are the true values. This represents the best case of what we could learn from GW observations. Later, we will consider how the accuracy of the reconstructed model parameters is affected by including measurement errors on the recorded event properties.

2.5.1 Posterior recovery

We carried out the analysis discussed in Sec. 2.4 for a data set calculated from the reference model given in Sec. 2.3.9. With a uniform non-adapting proposal distribution, we found that $\sim 10^6 - 10^7$ samples were necessary for burn-in, for the trace-plots of the MCMC chains to stabilise, and thus for the analysis to recover the underlying posterior distributions.

We found that $\Omega_{m,0}$ and α were not constrained by the observations, but their inclusion in the parameter space did not affect our ability to recover the other parameters. For this reason, we kept them in the analysis, but all remaining results will be marginalised over these model parameters. Given the low redshift range that a second-generation network is sensitive to, it is not surprising that the matter-density and merger-rate evolution were not constrained.

The recovered 1D posterior distributions in the other parameters are shown in Fig. 2.1 for a typical realisation of the set of observed events. We have verified that these marginalised distributions are not biased with respect to those obtained when exact knowledge of the intrinsic $\dot{n}_0$ is assumed. We found that the 1D posterior distributions for H_0, $\ln(\sigma_{\rm NS})$ and $\mu_{\rm NS}$ were well fit by Gaussian distributions of the form $A\exp\left(-(x-\mu)^2/2\sigma^2\right)$. These best-fit Gaussians are also shown in the Figure. Although the distributions do not peak at the model parameters used to generate the data, those values are consistent with the mean and width of the recovered distributions.

In Fig. 2.2, we show the corresponding 2D posterior distribution in H_0 and $\mu_{\rm NS}$ parameter space. We see that a correlation exists between these parameters. Given a catalogued D_L value, a low value of H_0 will imply a low model-dependent redshift. When this redshift is used to compute $\mathcal{M}$ from $\mathcal{M}_z$, we calculate a large value of the chirp mass, which implies a chirp mass distribution (and hence a NS mass distribution) centred at larger values. $\sigma_{\rm NS}$ simply encodes the width of the mass distribution around the mean, so on average it should have no effect on H_0 and $\mu_{\rm NS}$ calculations. Indeed we found that $\sigma_{\rm NS}$ showed no correlation with the other model parameters.

It is clear from Fig. 2.1 that the parameters of the Gaussian fits provide a useful way to characterise the recovered distributions. We can then describe the recovered distributions in terms of two best-fit parameters i.e., the Gaussian mean, μ, and Gaussian half-width, σ.

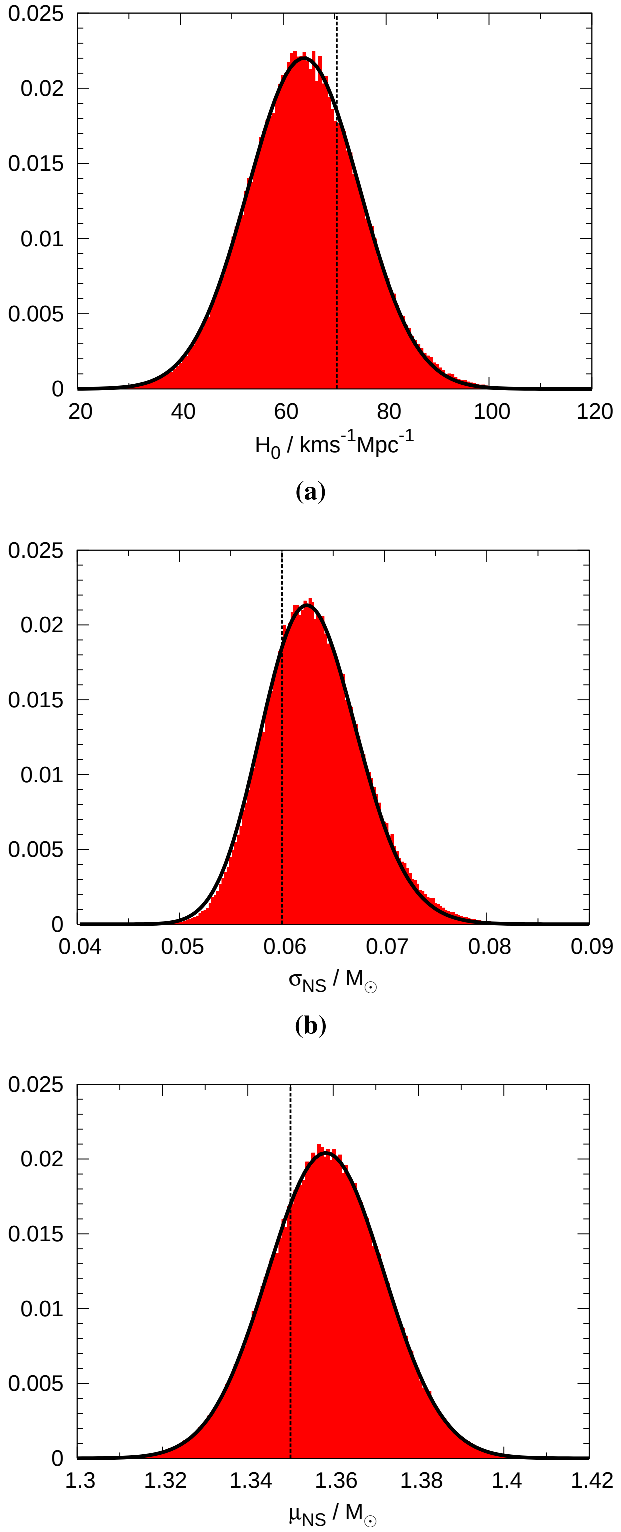

(a)

(b)

(c)

Figure 2.1: Recovered 1D posterior distributions for H_0 (top), $\sigma_{\rm NS}$ (centre) and $\mu_{\rm NS}$ (bottom), computed for one realisation. The black lines represent best-fit Gaussian distributions to H_0, $\ln(\sigma_{\rm NS})$ and $\mu_{\rm NS}$, which were obtained via a least-squares fitting procedure. The vertical lines indicate the values of the injected parameters.

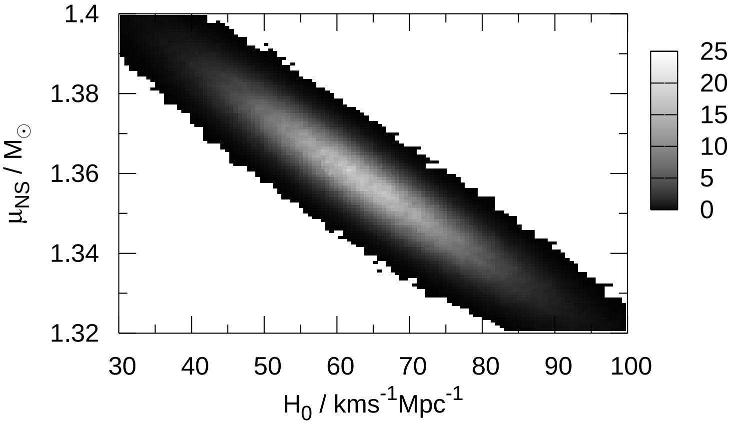

Figure 2.2: Recovered 2D posterior distribution in H_0 and $\mu_{\rm NS}$ space, showing a correlation between these recovered parameters. The model parameter values used to generate the data are the reference values. There appears to be negligible correlation of $\sigma_{\rm NS}$ with H_0 or $\mu_{\rm NS}$.

2.5.2 Random spread of best-fit parameters

No errors in data catalogue

To explore the spread in the best-fit parameters of the recovered posteriors over different realisations of the data catalogue, we generated 100 different realisations, keeping the intrinsic parameter values the same for each.

In each case, we fit a Gaussian to the 1D posteriors and record the mean, μ, standard deviation, σ, and the "error" in the mean. This last quantity is the number of standard deviations that the mean is offset from the intrinsic value, i.e. $\Delta X = (\mu - X)/\sigma$, where X is the value of the parameter used to generate the catalogue [330]. A $\pm 2\sigma$ offset encloses $\sim 95\%$ of the Gaussian probability distribution, so we would reasonably expect most of the realisations to lie within this range.

Figure 2.3 shows the distributions of the Gaussian-fit standard deviations and "errors" for H_0, $\ln(\sigma_{\rm NS})$ and $\mu_{\rm NS}$ over 100 realisations of the aLIGO-network data catalogue. The distribution of the Gaussian-fit means for each parameter roughly resemble their respective posteriors, and the distribution of Gaussian standard deviations also appears approximately Gaussian. As we would have hoped, most of the realisations have a best-fit mean which is offset from the intrinsic value by less than 2σ. As with the Gaussian-fit parameters, the "error" distribution is approximately Gaussian and centred around 0 i.e., centred around the intrinsic value.

The most useful quantity here is the standard deviation of the reconstructed posterior distribution, as it characterises how well we will be able to constrain the model parameters. The distribution over 100 realisations displays the typical range of this "measurement accuracy." Thus, ignoring measurement errors in the data, and with reference parameters used to generate

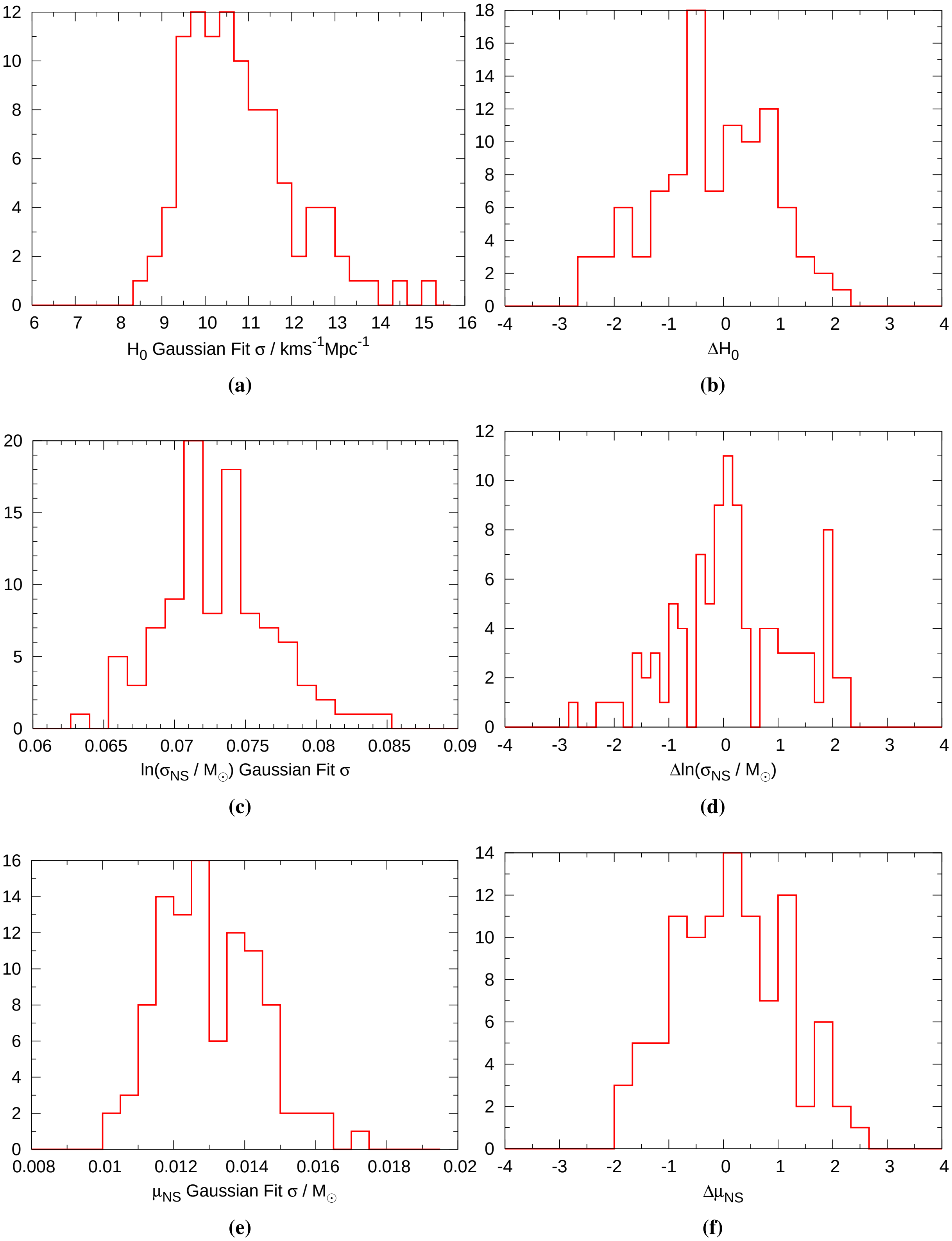

Figure 2.3: Distribution of the Gaussian-fit standard deviations (left) and "errors" (right) of the recovered posteriors over 100 realisations, for H_0 (top), $\ln(\sigma_{\rm NS})$ (centre) and $\mu_{\rm NS}$ (bottom). More details are given in the text.

the catalogue, we could conceivably determine H_0, σ_{NS} and μ_{NS} to an accuracy of $\sim\pm 10$ km $\mathrm{s}^{-1}\mathrm{Mpc}^{-1}$, $\sim\pm 0.004 M_\odot$,[10] and $\sim\pm 0.012 M_\odot$ respectively.

Including & accounting for errors

As discussed in Sec. 2.3.1, the system properties of each event in the catalogue will include some error arising from instrumental noise. The data for each event will actually be in the form of posterior probability density functions (PDFs) for the properties, where previously we have assumed these are δ-functions at the true values. We repeat the analysis assuming uncertainty in the source properties. We can add errors to the system properties during the data generation stage, by choosing the recorded values from a Gaussian distribution centred on the true value, with a standard deviation of 0.04% for $\mathcal{M}_z$ and $(300/\rho)\%$ for D_L, where ρ is the SNR of the detected event.

When we included errors in the data generation, but ignored them during analysis, we found that the model parameter posterior distributions were on average biased toward lower values of H_0, with biases also present in the μ_{NS} and σ_{NS} distributions. When the errors are added, systems will move both to lower and to higher values of the luminosity distance. However, as we discussed in Sec. 2.2, the sources at greatest distance have the most influence on our ability to measure the cosmology. We would therefore expect the sources shifted to greater distances to have most impact on the cosmological parameter estimation, biasing us toward smaller values of H_0, as we found.

However, we can account for these errors in the analysis by modifying the previous likelihood in Eq. (2.45) [330] to

$$\mathcal{L}(\overset{\rightrightarrows}{\Lambda}|\overrightarrow{\mu},\mathcal{H}) = e^{-N_\mu}\int\int\ldots\int\left[p\left(\overrightarrow{n}=\overrightarrow{s}-\sum_i\overrightarrow{h}_i(\overrightarrow{\lambda_i})\right)\times\prod_{i=1}^{N_o}r(\overrightarrow{\lambda_i}|\overrightarrow{\mu})\right]d^k\overrightarrow{\lambda_1}d^k\overrightarrow{\lambda_2}\ldots d^k\overrightarrow{\lambda_{N_o}}, \tag{2.51}$$

where, in our case, each system is associated with two catalogued properties such that $k=2$, and $\overrightarrow{s}$ is the detector output, which is a combination of N_o signals, $\overrightarrow{h_i}$, and noise, $\overrightarrow{n}$. This is as an integral over all possible values of the source parameters that are consistent with the data. The first term inside the square bracket is the computed posterior PDF for the detected population of sources. Typical LIGO/Virgo DNS inspiral detections last only a few seconds, whilst aLIGO/AdV inspiral detections may be in-band for several minutes. Regardless, these detections should be uncorrelated, with independent parameter estimates [333], and so this first term reduces to the product of the posterior PDFs for each detection.

If the posterior PDF for a given source has been obtained via MCMC techniques, then the

---

[10] Evaluated using $\delta(\sigma_{\mathrm{NS}}) = \sigma_{\mathrm{NS}}\times\delta(\ln(\sigma_{\mathrm{NS}}))$, taking σ_{NS} to be the reference value and a typical error in $\ln(\sigma_{\mathrm{NS}})$ of 0.072.

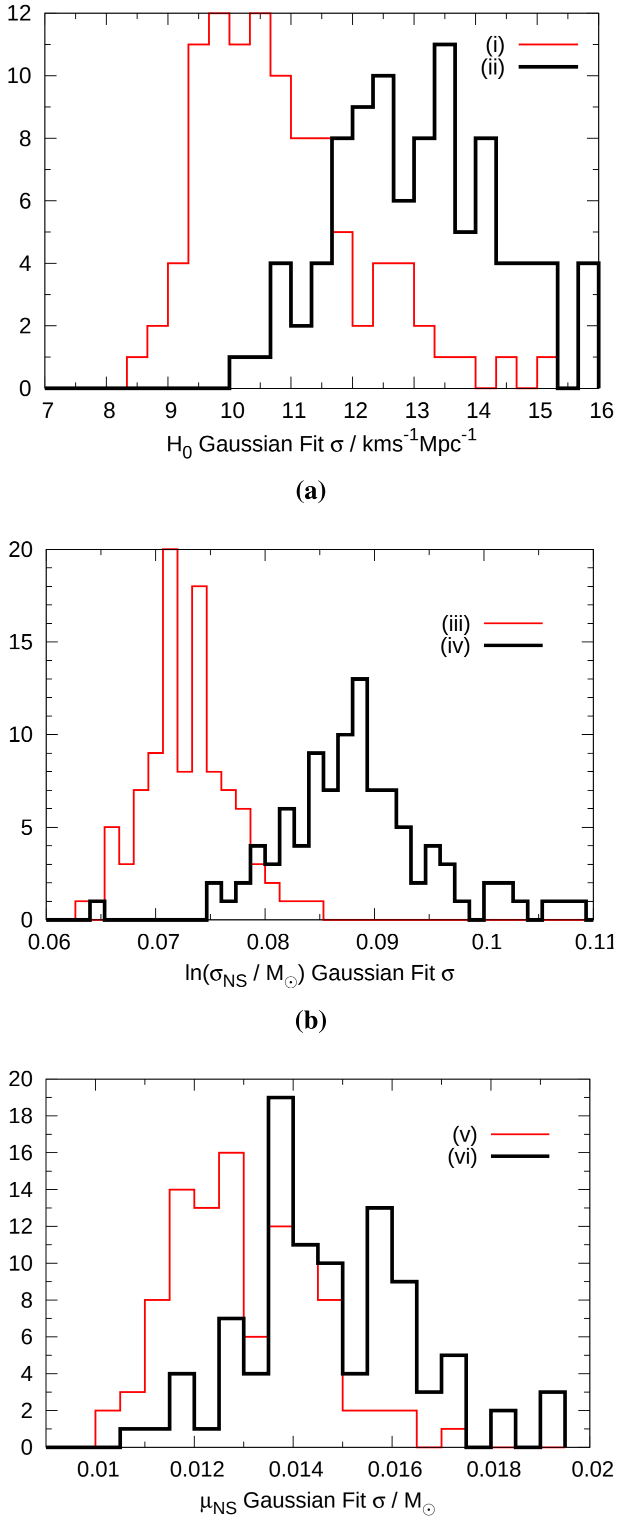

(a)

(b)

(c)

Figure 2.4: A comparison of the best-fit σ distributions over 100 realisations, between the case of no errors present in the data catalogue, and the case of errors applied to system properties in the catalogue. We have attempted to compensate for the errors in the data. (i), (iii) and (v) show the best-fit σ distributions when no errors are applied to the system properties in the data catalogue. (ii), (iv) and (vi) show the best-fit σ distributions when the received data has errors.

integral in Eq. (2.51) may be computed by summing over the chain samples. Thus, errors may be accounted for by making the following replacement in Eq. (2.45),

$$r(\overrightarrow{\lambda_i}|\overrightarrow{\mu}) \longrightarrow \frac{1}{\mathcal{N}_i}\sum_{j=1}^{\mathcal{N}_i} r(\overrightarrow{\lambda_i}^{(j)}|\overrightarrow{\mu}), \tag{2.52}$$

where $\mathcal{N}_i$ is the number of points in the chain for the i^{th} source's PDF, and $\lambda_i^{(j)}$ is the j^{th} element of the discrete chain representing this PDF. This technique does not assume a specific form for the PDF, and can be used in the case of multimodal distributions.[11]

In this analysis, we include errors on D_L only, as those on the *redshifted* chirp mass $\mathcal{M}_z$ are very small and can be ignored. (The uncertainty in the redshift estimate, which dominates the uncertainty in H_0 as discussed in Sec. 2.2, arises from the width of the *intrinsic* chirp-mass distribution.) We represent the D_L posterior PDF for each source by a chain of N points, drawn from a normal distribution with standard deviation $\sigma = (3/\rho)D_L$, and a mean equal to the value in the data catalogue, which in this analysis, as discussed earlier, includes an error to offset it from the true value. Whilst we adopt a simple Gaussian D_L posterior PDF, the methodology we use here to account for errors is not reliant on the specific form of the PDF.

Through experiment, we found that $N = 75$ was sufficient to correct the bias in the posterior means of H_0, σ_{NS} and μ_{NS}. In Fig. 2.4 we show a comparison of the best-fit σ distributions for each of the parameters when measurement errors are included (and accounted for), compared to the case in which they are ignored. It is clear that the presence of measurement errors decreases the measurement precision that we can achieve. However, the distributions overlap in all cases, and the peak of the error distributions is shifted only $\sim$20% higher.

These errors only cause a shift in the measurement precision, so that we can ignore errors in the catalogued properties, with the knowledge that a full analysis would produce broadly the same results, but with $\sim$20% worse precision. The presence of errors (when accounted for) should therefore not affect our general conclusions about what a second-generation global network will be able to tell us about the underlying cosmological and source parameters.

2.5.3 Dependence on number of observed events

The next issue we will explore is how the measurement accuracy of the parameters depends on the number of catalogued events. This can be answered by changing the local merger-rate density, $\dot{n}_0$, or the observation time, T, whilst keeping the other model parameters fixed.

---

[11] Multimodal distributions may result from partial degeneracies with other waveform parameters [333], such as the angular variables encapsulated in Θ. Examples of this are shown in Ref. [287], where the sky position of a detected system is pinned down, and the degeneracy between the inclination angle, ι, and D_L can lead to multimodal posteriors for D_L which skew the peak to higher distances than the intrinsic value.

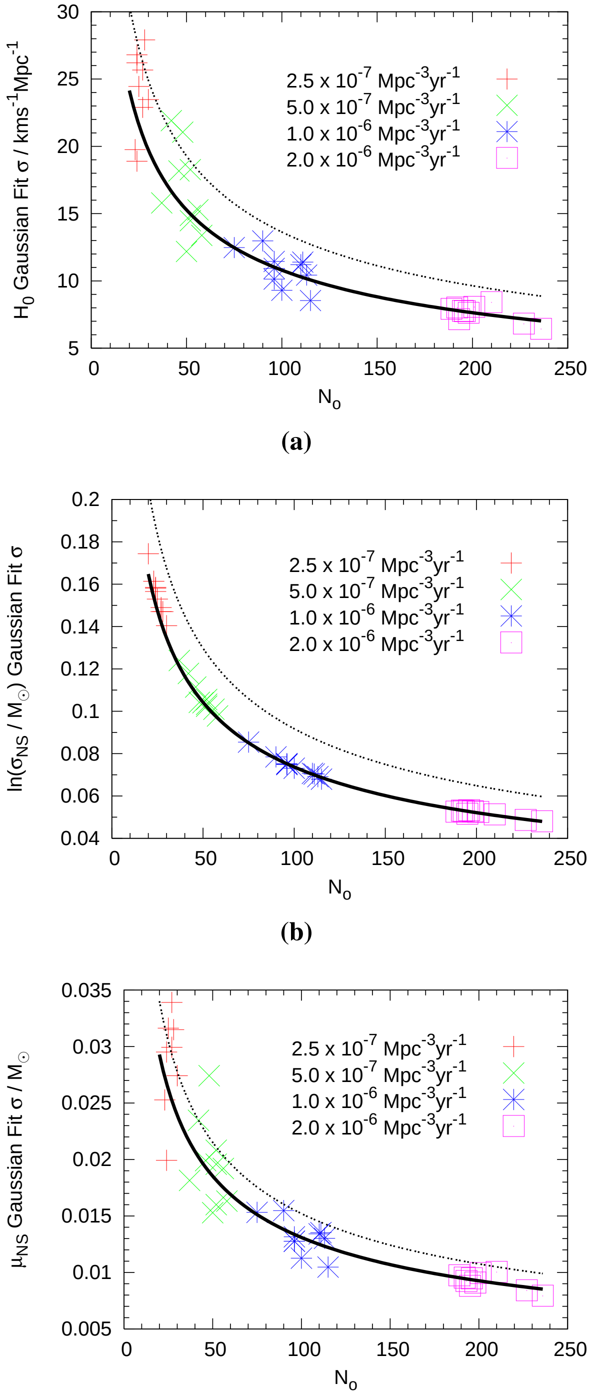

(a)

(b)

(c)

Figure 2.5: Parameter "measurement accuracy" (standard deviation of a Gaussian-fit to the posterior) versus the number of observed events, N_o. Intrinsic parameters are kept fixed whilst the local merger-rate density, $\dot{n}_0$, is scaled up and down. The number of observed events scales linearly with the observation time and the local merger-rate density, such that the same result is achieved for twice the local merger-rate density if the observation time is halved. We see that a $1/\sqrt{N_o}$ relation is favoured. Points and solid lines correspond to the case when we ignore errors, where the curves have gradients 108 km s^{-1}Mpc^{-1}, 0.737, and $0.131 M_{\odot}$ respectively. Dashed lines are best-fit curves for the case where measurement errors are incorporated in the data-analysis, for which the gradients are 136 km s^{-1}Mpc^{-1}, 0.917, and $0.152 M_{\odot}$, respectively.

Table 2.2: The best-fit curves to the plots in Fig. 3.5 are used to compute the percentage measurement precision of the model parameters. The local merger rates match the range quoted in Ref. [147], where in our analysis, $\dot{n}_0 = 1.0$ Mpc^{-3}Myr^{-1} gives $\sim$100 detections in 1 year (at a network SNR threshold of 8). In each case, the mean of the posterior distribution is taken at the reference value.

$\dot{n}_0$ / Mpc^{-3}Myr^{-1}	Accuracy (σ_X/X) / %					
	H_0		$\sigma_{\rm NS}$		$\mu_{\rm NS}$	
	No errors	Errors	No errors	Errors	No errors	Errors
0.01	150	200	80	100	10	11
1.0	15	20	7	9	1.0	1.1
10.0	5	6	2	3	0.3	0.35
50.0	2	3	1.0	1.3	0.14	0.16

We analysed catalogues with different values of $\dot{n}_0$ around the previously used realistic value (2.5×10^{-7}, 5.0×10^{-7}, 1.0×10^{-6} and 2.0×10^{-6} Mpc^{-3}yr^{-1}), injecting 10 realisations in each case.

In Fig. 2.5 we show the standard deviation of the recorded posterior distribution versus the number of catalogued events for each realisation of each $\dot{n}_0$. The distributions are well fit by a function of the form,

$$\sigma_X \propto \frac{1}{\sqrt{N_o}}, \tag{2.53}$$

which one might expect; we have a population of N_o events which we are using to statistically constrain a parameter, so we expect that the rms error on the parameter should scale as $\sim 1/\sqrt{N_o}$. The points and solid lines are the data and best-fit curves when we ignore measurement errors in the data generation, whilst the dashed lines are best-fit curves to data where we account for measurement errors, as in the previous section.

Table 2.2 shows the percentage fractional accuracy to which we could measure each model parameter, in both the case where we ignore errors and when we account for them. The range of local merger-rate densities reflects the quoted values in Ref. [147], and the means of the posterior distributions are taken as the reference values.

The number of detected events will also depend on the SNR threshold, $\rho_{0,\rm net}$ [157]. The result of increasing the threshold SNR to 10 is to approximately halve the detection rate. If the expected detection rate is $\sim$100 yr^{-1} in the $\rho_{0,\rm net} = 8$ case, this becomes $\sim$50 yr^{-1} in the $\rho_{0,\rm net} = 10$ case. This halving of the detection rate is expected since,

$$\frac{V_{c,\rm eff}(\rho_{0,\rm net} = 10)}{V_{c,\rm eff}(\rho_{0,\rm net} = 8)} \simeq \left(\frac{8}{10}\right)^3 = 0.512, \tag{2.54}$$

where $V_{c,\rm eff}$ is the effective comoving volume to which the network is sensitive. We can achieve the same number of detections at higher SNR thresholds by increasing the observation time.

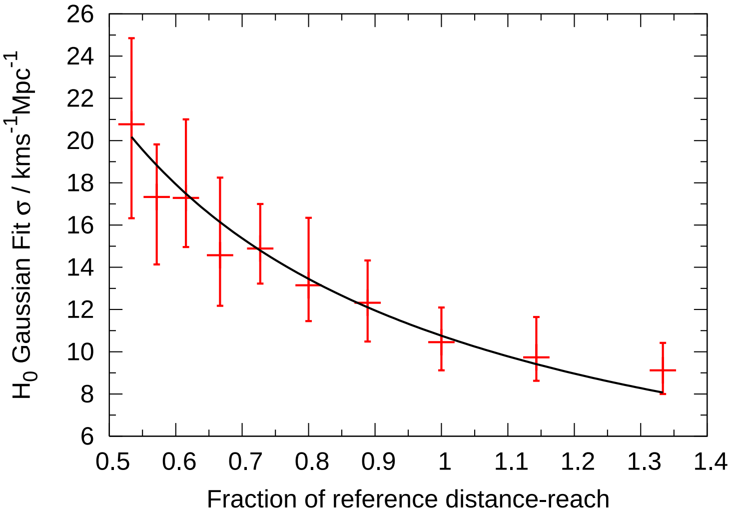

Figure 2.6: The variation of measurement accuracy with instrumental distance reach is shown. Each point represents the weighted mean of the H_0 measurement accuracy from 10 realisations at a particular $r_{0,\mathrm{net}}$, where the error bars show the maximum and minimum values of σ out of the 10 values. All other parameters are at their reference values, and the total number of detections is scaled to 100. The reference distance reach is $r_{0,\mathrm{net}} \sim 176$ Mpc. The curve is a $(1/r_{0,\mathrm{net}})$ fit to the data, with gradient 10.8 ± 0.2 km s^{-1}Mpc^{-1}.

Using a higher network SNR threshold is equivalent to assuming a lower characteristic distance reach for the network. By increasing ρ_0 to 10, we cut the detection rate in half, which is roughly the decrease in the number of coincident detections when we shift from the HHL to HHLV network [309]. A network SNR threshold of 12 reduces the detection rate to ∼30 yr^{-1}.

To investigate the dependence of the H_0 measurement accuracy on the characteristic distance reach of the network (a prediction of our scaling arguments), we computed 10 realisations at each of 10 different network SNR thresholds, ranging from 6 to 15. The detection rates were kept the same at each SNR threshold by rescaling $\dot{n}_0$. The reference values were $\rho_{0,\mathrm{net}} = 8$ and $r_{0,\mathrm{net}} = 176$ Mpc, as used previously. At each $\rho_{0,\mathrm{net}}$ we calculated the mean of the Gaussian-fit half-widths of the parameter posteriors, with error bars determined by the maximum and minimum half-widths out of the 10 realisations. The results for H_0 are shown in Figure 2.6. The fit favours a $(1/r_{0,\mathrm{net}})$ relationship, as expected from scaling arguments. There appears to be no effect on the measurement accuracy of the NS mass distribution parameters. No measurement errors were included on either the recorded D_L or $\mathcal{M}_z$ values, and the detection rate was fixed in this analysis, so it is unsurprising that the measurement precision of the NS mass distribution parameters is unaffected by the reach of the network. In this particular investigation, given that the total number of events is unchanged, and therefore the number of masses to which we fit the NS mass distribution is unchanged, we do not expect the precision of the fit to change either.

This indicates that the measurement accuracies of σ_{NS} and μ_{NS} quoted in this analysis will be achievable at different $\rho_{0,\mathrm{net}}$ and $r_{0,\mathrm{net}}$ by scaling the observation times, or if the Universe has a different $\dot{n}_0$ than expected. However, the measurement accuracy of H_0 is crucially linked to the characteristic distance reach of the network.

2.5.4 Dependence of measurement accuracy on intrinsic parameters

It is also interesting to investigate how the constraints on the parameters of the underlying distributions depend on the values of the injected parameters. This was done by generating 10 data realisations at each of 24 different combinations of the intrinsic μ_{NS} and σ_{NS}. The intrinsic values of H_0, $\Omega_{m,0}$ and α were fixed at their reference values. The recorded measurement precision for a given intrinsic parameter combination was the weighted mean of this value over 10 realisations. Figure 2.7 shows the results of this analysis. One can see that the measurement precision depends on the width of the intrinsic NS mass distribution. An increase in the intrinsic σ_{NS} by a factor of 6 leads to a reduction in the measurement accuracy on H_0 and μ_{NS} by a factor of $\sim$6, but only leads to a modest 10% reduction of the measurement accuracy for $\ln\left(\sigma_{\mathrm{NS}}\right)$.

The improvement of the measurement accuracy with a narrower intrinsic DNS mass distribution is a key result. In order to constrain the Hubble constant to within $\sim\pm10\%$ with $\sim$100 observations, we require the Gaussian half-width of the DNS mass distribution to be smaller than $0.04M_\odot$. The explanation for this is that we estimate the system chirp mass, $\mathcal{M}$, by dividing the redshifted chirp mass, $\mathcal{M}_z$, by $(1+z)$, where the z is model-dependent (having been calculated from D_L with given cosmological parameters). Thus, a narrower NS mass distribution will more effectively penalise model parameters which deviate from the intrinsic values. For $\sigma_{\mathrm{NS}}=0.13M_\odot$ [316], an accuracy of $\sim\pm10\%$ on H_0 would require $\sim O(1000)$ detections.

The dependence of the measurement precision on μ_{NS} is not very clear from the top and bottom panels, but the effect on σ_{NS} is evident in Fig. 2.7(b). Varying the intrinsic μ_{NS} from $1.33M_\odot$ to $1.39M_\odot$ provides a $\sim5-10\%$ gain in $\ln\left(\sigma_{\mathrm{NS}}\right)$ precision. The variation of the expected number of detections with σ_{NS} is less than one event, whilst for μ_{NS} it is more significant. So, all the posterior fit σ values were scaled to the average number of detections for a given μ_{NS}. This varies by $\sim$15 detections over the range of μ_{NS} investigated.

To explain the improvement in measurement precision with larger values of μ_{NS}, we note Eq. (2.20). We see that a larger mass distribution mean will, on average, imply larger individual NS masses. For a fixed SNR threshold, this allows detections to be made from larger D_L values, thereby raising the effective comoving volume to which the network is sensitive. This raises the number of detections, and hence the parameter measurement accuracy. Rescaling all the measurement accuracies to 100 events confirms that this is the dominant effect, as the different μ_{NS} curves in Fig. 2.7 then overlap. Factorising out the dependence on N_o also confirms that the variation of the measurement accuracy with the width of the underlying NS mass distribution is

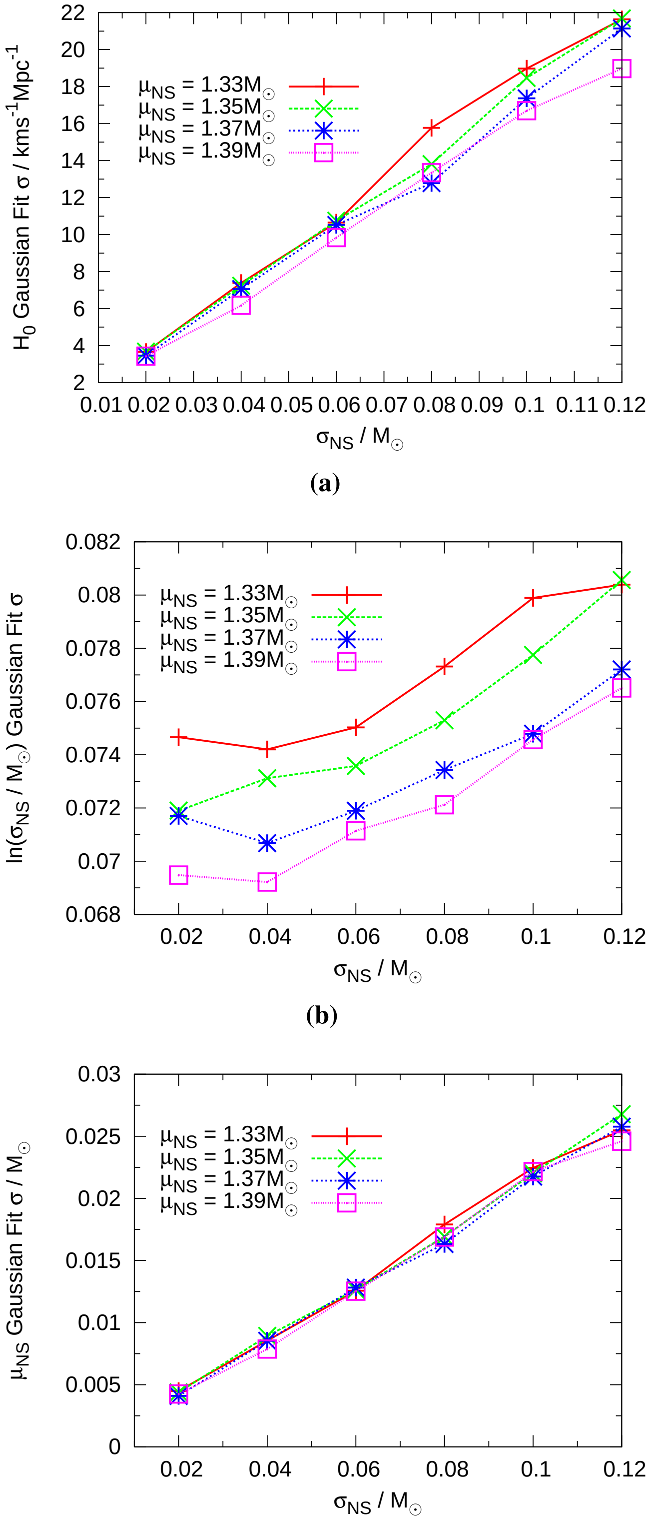

(a)

(b)

(c)

Figure 2.7: The variation of the weighted mean (over 10 realisations) of the Gaussian-fit standard deviations with the parameters of the underlying NS mass distribution. All other parameters are fixed at their reference values. The variation of the expected number of detections with $\sigma_{\rm NS}$ is less than one event, whilst for $\mu_{\rm NS}$ it is more significant. Thus all the posterior fit σ values are scaled to the average number of detections for a given $\mu_{\rm NS}$ e.g. for $\mu_{\rm NS} = 1.33M_{\odot}$ this average event number is $\sim$95, whilst for $1.39M_{\odot}$ it is $\sim$110, in 1 year.

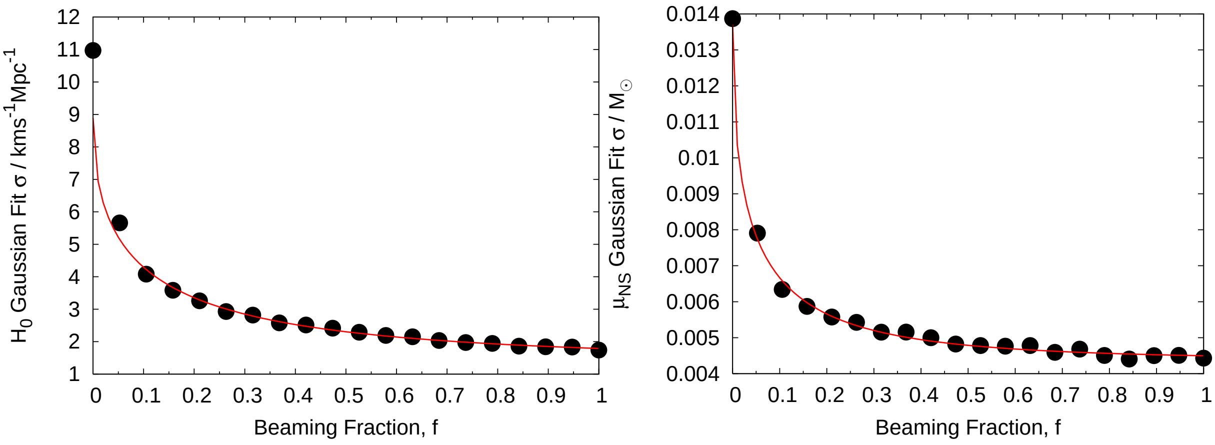

(a) **(b)**

Figure 2.8: Plots of the measurement precision versus the beaming fraction of SGRBs, f. Approximately fN_o events in the catalogue were denoted as SGRBs, while the remaining $\sim(1-f)N_o$ events in the catalogue were assumed to be GW-only events. A single data catalogue was used repeatedly, with larger and larger fractions of it assumed to be observable as SGRBs. The data was generated with the reference parameters. The fitted curves are of the form $a\exp(-b\sqrt{x})+c$, where $(a,b,c) = (9.04, 3.64, 1.59)$ and $(0.00932, 4.46, 0.00439)$ for the H_0 and $\mu_{\rm NS}$ precisions respectively. The corresponding plot for $\sigma_{\rm NS}$ shows no obvious trend.

a real feature.

Repeating the above analysis for fixed $\mu_{\rm NS}$, but with different combinations of H_0 and $\sigma_{\rm NS}$ confirms the variation of precision with $\sigma_{\rm NS}$. However, there appears to be no strong dependence on H_0 as it is varied by ± 10 km s^{-1}Mpc^{-1} around the reference value.

2.5.5 Complementing GW data with GRB redshift data

In the above, we have assumed that only GW observations are available. However, if the redshift of the system is somehow known, then the background cosmological parameters can be directly probed using the luminosity distance, D_L, measured from the GWs [284].

Merging CO binary systems, such as NS-NS or NS-BH, are leading candidates for the engine behind short-duration gamma ray bursts (SGRBs). SGRB events are among the most luminous explosions in the universe, releasing in less than one second the energy emitted by our Galaxy over one year [334], and involving intense outflows of gamma rays. There is therefore a good chance that EM counterparts to GW-detected DNS mergers will be observed. There is strong evidence that the emission from GRBs is not isotropic [335–337], which may be due to the formation of relativistic jets in these systems [334]. The redshift can be determined from the longer-wavelength SGRB afterglow [338].

Therefore, we may only observe the event electromagnetically if we happen to lie within the cone of the radiative outflow, whilst we should be able to detect the GW signal from any DNS merger within the aLIGO-network horizon. We denote the beaming fraction, f, for SGRBs with a double-jet of opening angle θ_j by [337, 339],

$$f = \frac{\Omega_*}{4\pi} = 1 - \cos\left(\frac{\theta_j}{2}\right). \tag{2.55}$$

If we assume the population of SGRBs is randomly oriented on the sky, that their progenitors are all NS-NS mergers, that we will detect all SGRBs that are beamed toward us, and that the required SNR for a GW detection is independent of the existence of a counterpart, then the beaming fraction, f, is also the fraction of DNS inspiraling systems for which we would be able to gather redshift data. In practice, GW searches that are triggered by electromagnetic observations of SGRBs would have a greater distance reach than blind analyses, which would tend to increase the fraction of counterparts. However, gamma-ray telescopes operating in the advanced detector era might not have 100% sky coverage, which would tend to reduce the fraction of counterparts. In addition, even with an SGRB counterpart we might not be able to determine the redshift, as this requires observation of an afterglow. However, all of the GW sources for advanced detectors will be at low redshift, for which the chances of measuring the redshift are significantly higher. In the following, when we refer to the beaming fraction, we will mean the fraction of GW detections with electromagnetically determined redshifts, which will be similar to the intrinsic beaming fraction, but not exactly the same for the reasons just described.

We performed a simple analysis to see how the measurement accuracy would improve if some fraction, f, of redshift data was available. A single data set was generated with the redshift, luminosity distance and redshifted chirp mass of each event recorded (with reference intrinsic parameters). The measured $\mathcal{M}_z$ and D_L were drawn from Gaussian distributions centred at the true value, as described previously. However, as before the small error on $\mathcal{M}_z$ was ignored. When only a GW signal is available the system properties are analysed as previously, with the measured values assumed to be the true values.

If an event is included in the SGRB fraction (with an associated redshift), then the likelihood is the product of the GW likelihood with the redshift posterior PDF, which we take to be a delta function (since spectroscopic redshift determination will be much more precise than GW determinations of D_L). The D_L posterior was taken to be a Gaussian, centred around the measured value, and with a standard deviation of 30% of this distance. This percentage error is a worst case, corresponding to a detection near the threshold SNR, i.e. $(300/\rho)\%$ for $\rho = 10$. Using a constant percentage of the distance as the width of the D_L posterior is pessimistic, since closer events will be measured with greater accuracy. Integrating over redshift in Eq. (2.51) picks out the value of the integrand at the true system redshift, since the redshift posterior is a delta function. Thus, the product in Eq. (2.50) splits into two components,

$$\left[\prod_{i=1}^{N_o}\frac{d^3N}{dtd\mathcal{M}_zdD_L}\bigg|_i\right]\rightarrow\left[\prod_{j=1}^{fN_o}\left(\frac{d^3N}{dtd\mathcal{M}_zdz}\bigg|_j\times\mathcal{N}\left[(D_L^{(j)}-D_L(z_j,\vec{\mu})),0.3D_L^{(j)}\right]\right)\right]$$
$$\times\left[\prod_{k=fN_o}^{N_o}\frac{d^3N}{dtd\mathcal{M}_zdD_L}\bigg|_k\right]. \tag{2.56}$$

The identification of the SGRB as an EM counterpart will vastly improve sky localisation of the source, helping to beat down the degeneracies in the GW observations between D_L and the inclination angle, ι. A fuller investigation could also consider a prior on the inclination angle, given that the source is an SGRB with a collimated outflow [287, 335, 336], and that emission has been observed. This would further help to improve the measurement precision of the luminosity distance.

If $f = 1$, we find the precision for H_0 is $\sim$2.0 km s^{-1}Mpc^{-1}, compared to $\sim$11.0 km s^{-1}Mpc^{-1} when $f = 0$. The results are shown in Fig. 2.8, along with fits to the data of the form $a\exp(-b\sqrt{x})+c$. The important result here is that the accuracy with which we are able to constrain H_0 and $\mu_{\rm NS}$ improves markedly with the beaming fraction. This is to be expected, since by recording z and $\mathcal{M}_z$ we know exactly what the intrinsic chirp mass, $\mathcal{M}$, of the system is. The high accuracy of the redshift measurements restricts the space of model parameters through the Gaussian factor in Eq. (2.56). The same plot for $\sigma_{\rm NS}$ shows no trend at all. This may be because the measurement accuracy of $\sigma_{\rm NS}$ is most strongly linked to the number of catalogued events, rather than whether we include extra system information.

This analysis could be sensitive to the errors we include in the data catalogue, since the normal distribution in the left square-bracket of Eq. (2.56) will favour model parameters, $\vec{\mu}$, such that $D_L^{(j)} = D_L(z_j,\vec{\mu})$. $D_L^{(j)}$ is the mean of the D_L posterior PDF for the $j^{\rm th}$ event, which may be skewed away from the true value. However, the intrinsic values were always consistent with the mean and width of the recovered posteriors, so this does not seem to be a significant problem.

The SGRB jet opening angle is poorly constrained by observations. In Ref. [340], the authors quote the inverse beaming fraction to be in the range, $1 \ll f^{-1} < 100$, giving $f \gtrsim 10^{-2}$ or a jet opening angle $\theta_j \gtrsim 16^\circ$, which is consistent with theoretical constraints on the jet half-opening angle [334]. Such models permit the jet half-opening angle to be as large as 30°, for which the beaming fraction becomes $\sim$0.13 [334]. This would allow H_0 and $\mu_{\rm NS}$ to be measured with a precision more than twice that of their GW-only values (see Figure 2.8).

In Ref. [287], the authors performed an analysis on multiple DNS inspirals detections in the aLIGO-AdV network with associated EM signatures. They assumed the sky location of the sources were known, and that D_L and z were measured, so that they directly probed the distance-redshift relation. With 4 SGRBs they predicted H_0 could be measured with a fractional error of $\sim$13%, improving to $\sim$5% for 15 events. With $f = 1$, and scaling the measurement precision as $1/\sqrt{N_o}$, we find 4 SGRBs gives $\sim$12.5% precision, whilst 15 gives $\sim$6.5% precision. Figure 2.8 indicates an H_0 precision of $\sim$5% when $f = 0.15$; thus the second square bracket on the right of Eq. (2.56) slightly improves the measurement accuracy of H_0 compared to the first square bracket alone. These results are dependent on the modelled D_L errors, but are broadly consistent with Ref. [287]. In contrast, we expect we can constrain H_0 to within $\sim\pm 15\%$ using $\sim$100 GW events, with no EM signatures recorded for any of the GW detections. 15 SGRB events out of the $\sim$100 GW events requires a beaming fraction of $\sim$0.15, which is rather optimistic given the current constraints on the jet opening angle. However this could conceivably be achieved over observation times longer than one year; additionally, the detection of an electromagnetic transient could allow the sensitivity volume to be increased in a triggered search.

In this study we have not considered the possibility of redshift determination of the DNS inspiraling system via its association with a host galaxy. This could prove difficult in practice, since the sky error box is sufficiently large as to contain many candidate galaxies. In Ref. [341] the authors comment that over 100 galaxies can be found in a typical LIGO/Virgo GW signal error box at a distance of 100 Mpc. However, in the same work they introduced a ranking statistic which successfully imaged the true host of a simulated GW signal $\sim$93% of the time, if 5 wide-field images were taken. The caveat here is that this statistic has only been tested out to 100 Mpc, since comprehensive galaxy catalogues are lacking beyond this range. The catalogue completeness is not 100% at 100 Mpc, and even if more distant, complete catalogues were available, the number of potential host galaxies in an aLIGO/AdV sky error box would be much greater. D_L determination via network analysis may help to restrict the redshift range of these searches, but this is an area in need of future attention.

A novel method was proposed in Ref. [289] in the context of LISA EMRI detections. In that case, instead of precisely identifying the host galaxy of a GW detection (and thus the redshift of the source), the value of H_0 was averaged over all galaxies present in LISA's sky error box. Each galaxy in the box was weighted equally, and the chosen host galaxy was not included in the likelihood calculation to take into account the fact that the true host galaxy may not even be visible in available catalogues. They showed that sub-percent accuracies on H_0 would be possible if 20 or more EMRI events are detected to $z \lesssim 0.5$. This method has recently been investigated in the context of DNS inspirals in the advanced detector era, where a precision of a few percent on H_0 was claimed to be possible with 50 detections [342].

2.6 Summary

We have explored the prospects for an advanced global network of GW interferometers to probe aspects of the background cosmology and the nature of the NS mass distribution (for NSs in DNS systems). Current rate estimates suggest these systems could be a strong candidate for the first direct GW detection. With the reach of advanced detectors it may be possible to produce catalogues of tens of these systems along with their associated properties over the first few years of operation.

We simulated catalogues of 100 detected binaries (corresponding to a few years of observation for a local merger-rate density of 10^{-6} Mpc^{-3}yr^{-1} [147]) for reference parameters $H_0 = 70.4$ km s^{-1}Mpc^{-1}, $\Omega_{m,0} = 0.27$, $\mu_{\rm NS} = 1.35M_{\odot}$, $\sigma_{\rm NS} = 0.06M_{\odot}$, $\alpha = 2.0$ (where α is the gradient of the redshift evolution of the NS-NS merger-rate density). From our analysis, we found that it should be possible to measure H_0 to $\sim\pm10$ km s^{-1}Mpc^{-1}, $\ln(\sigma_{\rm NS})$ to $\sim\pm0.07$ and $\mu_{\rm NS}$ to $\sim\pm0.012M_{\odot}$. Taking into account typical luminosity distance measurement errors degraded the parameter measurement accuracies by $\sim 20\%$, but this can be compensated for by longer observation times.

Keeping the intrinsic parameters fixed, and scaling the merger-rate density (or the observation time) allowed us to investigate how this precision varied with the number of catalogued events. We found that precisions varied as $N_o^{-1/2}$ for all three parameters. We also investigated the effect of increasing the network SNR threshold, which has the same effect as reducing the distance reach of the network. Scaling the local merger-rate densities to give equal numbers of detections was enough to achieve the same precision on the NS mass distribution parameters, but the uncertainty in measuring H_0 also scales inversely with the distance reach of the network.

We also checked how the values of the intrinsic parameters themselves affected our ability to constrain them. Varying H_0 over a range of reasonable values had little impact on the measurement precision, but the effect of $\sigma_{\rm NS}$ was considerable. Changing $\sigma_{\rm NS}$ from $0.12M_{\odot}$ to $0.02M_{\odot}$ led to a factor of $\sim$6 increase in the precision on H_0 and $\mu_{\rm NS}$, but a modest $\sim$10% improvement on $\ln(\sigma_{\rm NS})$. Our key result is that for H_0 to be constrained to within $\sim\pm10\%$ using $\sim$100 events (with the intrinsic H_0 and mean of the DNS mass distribution fixed at their reference values), then the half-width of the intrinsic DNS mass distribution would have to be less than $0.04M_{\odot}$.

Finally, considering that NS-NS and NS-BH merger events are leading candidates for the progenitors of short-duration gamma-ray bursts [334, 339], we investigated how the measurement precision would improve if redshift data were available for some fraction of the catalogue. The redshift could be deduced from the afterglow of the SGRB or from the closest projected galaxy. The fraction of GW detections that have observable EM counterparts will depend on the opening angle of the SGRB jets. The most recent GR-MHD simulations permit a half-opening angle of 30°, giving an upper limit of ~ 0.13 on the fraction of DNS inspiraling systems which could have an observable SGRB counterpart [334] (this fraction could be further increased by the greater sensitivity of GW searches triggered on EM transients). This would permit a significant improvement on the measurement precision of H_0 and $\mu_{\rm NS}$ to more than double their GW-only precisions. There appears to be no effect on the measurement precision of $\sigma_{\rm NS}$.

We have shown the significant potential for a network of second-generation detectors to provide an independent measurement of the Hubble constant, and to determine the NS mass distribution for those NSs found in DNS systems. Independent means of inferring the Hubble constant using a technique such as that studied here (which is calibrated entirely by our understanding of gravitation) are crucial given the continued tension between *Planck* CMB measurements and more direct H_0 determinations [343]. However, the restricted cosmological reach of second-generation detectors is such that the evolution of the NS-NS coalescence rate can not be probed, nor can other cosmological parameters. More powerful constraints should be possible with the *Einstein Telescope* (ET), a proposed third generation ground-based interferometer with an arm-length of 10 km [96]. In the next chapter, we study the prospects for a third-generation ground-based network, incorporating ET, to probe the dark energy EOS and the DNS-progenitor star-formation rate.

In this analysis we have considered a global second-generation GW-interferometer network. The improvement offered by a Southern Hemisphere GW detector would be significant for sky localisation (though only moderate for distance estimates), but we now know that this will not be realised in the near-future. However, even with the HHLV network we will still be able to place constraints on the underlying model parameters by overcoming the reduced coincident detection rate with a longer duration network science run.

The most beautiful experience we can have is the mysterious - the fundamental emotion which stands at the cradle of true art and true science.

Albert Einstein

The only way to discover the limits of the possible is to go beyond them into the impossible.

Arthur C. Clarke

3

Astrophysics In The Third-generation

Abstract

Building on our previous work, we explore the prospects for the Einstein Telescope (ET; a proposed third-generation ground-based GW interferometer) to constrain the dark-energy equation of state, and the star-formation rate appropriate to double-NS (DNS) progenitor systems. DNS systems are expected to be detected at a rate of a few tens per year in the advanced era, but the Einstein Telescope could catalogue tens, if not hundreds, of thousands per year. Combining the measured source redshift distributions with GW-network distance determinations will permit not only the precision measurement of background cosmological parameters, but will provide an insight into the astrophysical properties of these DNS systems. Of particular interest will be to probe the distribution of delay-times between DNS-binary creation and subsequent merger, as well as the evolution of the star-formation rate density within ET's detection horizon. Modelling the merger delay-time distribution as a power-law ($\propto t^{\alpha}$) and the star-formation rate (SFR) density as a parametrised version of the Porciani and Madau SF2 model, we find that the associated astrophysical parameters are constrained to within $\sim 10\%$.

This chapter is based on:
Cosmology with the lights off: Standard sirens in the Einstein Telescope era
Stephen R. Taylor and Jonathan R. Gair
Phys. Rev. D **86**, 023502 (2012), arXiv:1204.6739

3.1 Introduction

In our previous analysis, the cosmological parameters that we could constrain were restricted by the sub-Gpc reach of an advanced-era network. We now extend this technique to a third-generation network, which could have a reach out to tens of Gpcs. Proposed third-generation detectors aim for a broadband factor of 10 sensitivity improvement with respect to advanced detectors, and to increase sensitivity in the range $\sim 1-10$ Hz, compared to the $\sim 10-20$ Hz lower frequency cutoff of advanced detectors. As a prototypical third-generation detector we use the Einstein Telescope, consisting of three overlapping 10 km arm-length interferometers in a triangular configuration [94, 95, 344]. Each interferometer may actually be two detectors: a cryogenically cooled, underground detector with good low-frequency sensitivity, and a high laser power detector with good high-frequency sensitivity [345]. Keeping H_0, $\Omega_{m,0}$ and $\Omega_{\Lambda,0}$ fixed, we use the techniques introduced in the previous chapter to probe the dark-energy EOS and NS mass-distribution, as well as the astrophysical distribution of the progenitor systems. The latter will inform us about the average time delay between the formation of these compact-binary systems and their merger, as well as the shape of the underlying star-formation rate density.

Third-generation detectors are unlikely to come online before the late-2020s, but, if realised, the ambitious and novel design for the Einstein Telescope will have far-reaching scientific advantages. Such a detector could detect as many as hundreds of thousands of DNS inspirals per year, which, along with the distance reach of the detectors, will permit precision GW astronomy. In this analysis, we will not consider other methods that have been proposed for using GW observations as cosmological probes. In particular, we do not consider association of GW detections with an electromagnetic (EM) counterpart, which has been studied in Ref. [346, 347], nor do we consider tidal-coupling corrections to the phase evolution of the strain signal [291]. The latter method is also a GW-only technique with significant potential, in that these phase-evolution corrections break the mass-redshift degeneracy at 5PN order and, assuming the NS equation-of-state is well known, will permit the distance-redshift relation to be probed. It may also be possible to apply the method used by Ref. [348], which was investigated in the context of future space-based detectors (e.g., DECIGO/BBO), to third-generation ground-based detectors. Their method relies on the measurement of cosmologically-induced shifts in the GW-phase at 4PN order.

This chapter is laid out as follows. Section 3.2 describes the characteristics of the Einstein Telescope, as well as possible third-generation networks and detection criteria. In Sec. 3.3 we discuss aspects of DNS systems, including the mass distribution of the constituent NSs, and the redshift distribution of DNS mergers. Section 3.4 describes the effect of the dark-energy equation-of-state parameter on catalogued luminosity distances, while Sec. 3.5 describes how

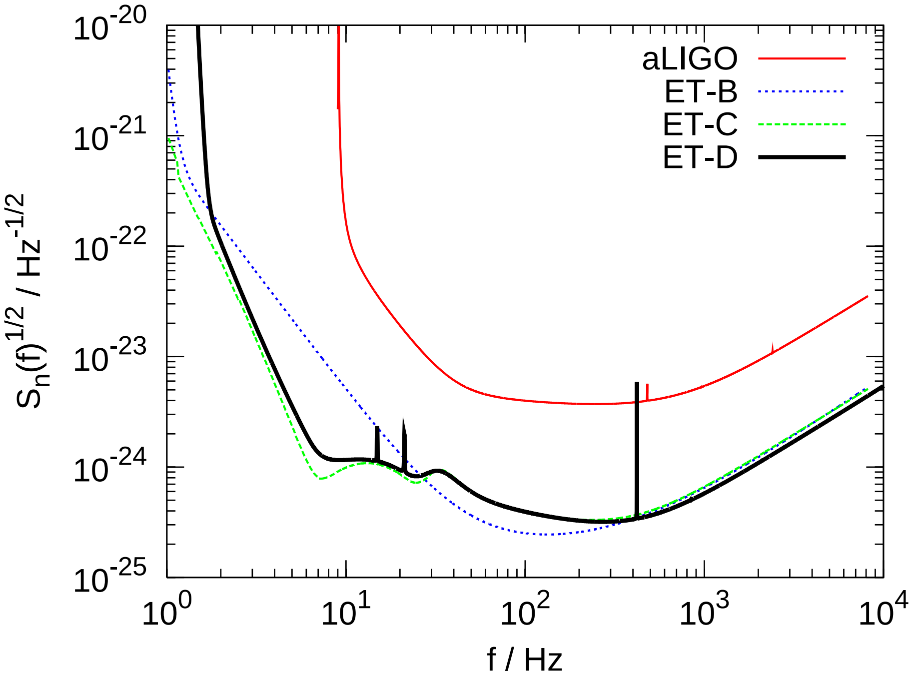

Figure 3.1: Comparison of the different noise curves for aLIGO (high-power-zero-detuning) [308], the initial Einstein Telescope noise curve based on conventional techniques (ET-B [349]), the initial “xylophone” noise curve (ET-C [97]), and the improved, more realistic xylophone noise curve (ET-D [345]). These noise curves are for one 10km right-angled interferometer.

we construct and analyse catalogues of detected DNS-system inspirals. Results are shown in Sec. 3.6, followed by a summary in Section 3.7.

3.2 Detector characteristics and networks

3.2.1 The Einstein Telescope

The Einstein Telescope (ET) is a proposed third-generation ground-based interferometer. A recent design study has been carried out within the European Commission’s FP7 framework [92] to evaluate the science case for such a detector, and to consider the technological advances required for the science goals to be achieved. Through this three-year design study, some favoured designs and configurations have emerged.

The aim for third-generation ground-based detector designs is to achieve a broadband factor of 10 sensitivity improvement with respect to advanced detectors, and to push the sensitivity down into the $\sim 1-10$ Hz range. Early designs examined the prospects for pushing conventional techniques used in advanced detectors to their limits to construct a third-generation interferometer [349]. This gave the ET-B noise curve in Fig. 3.1. Beyond the extension of the arm-length to 10 km, several techniques were proposed to suppress high- and low-frequency noise, including siting the detector underground.

Crucially, the techniques used to suppress high-frequency noise are not necessarily compatible with the suppression of low-frequency noise. Increasing the laser power will reduce the photon shot noise which dominates the high-frequency range, but this worsens the thermal noise which dominates at low frequencies. The "xylophone" design was proposed to address this issue. Instead of having a single broadband instrument, the xylophone design comprises a high-power, high-frequency interferometer (ET-HF) and a cryogenic low-power, low-frequency interferometer (ET-LF) [97]. ET-LF would be an underground instrument, and limited at low frequencies by gravity-gradient noise, while ET-HF would be colocated and co-oriented with ET-LF but surface-sited. ET-HF would employ high-power lasers to suppress high-frequency photon shot noise. The initial xylophone design gave the ET-C curve [97] in Fig. 3.1, which was refined to give the ET-D xylophone design [345]. We will use the ET-D noise curve in the ensuing analysis.

Initial, enhanced, and advanced era ground-based interferometers are right-angled, since an arm opening-angle of 90° maximises their sensitivity. However, if both GW polarisation states are to be measured at a single site, then two or more colocated non-aligned interferometers are required. Furthermore, at least three colocated interferometers are required to construct a null-stream, i.e., a sum of individual interferometer responses that is insensitive to GWs and can be used to identify noise transients in the data stream.

Taking these goals into account, the design requiring the shortest total length of tunnels is a triangular configuration with three identical interferometers positioned at each vertex of the triangle, an arm-opening angle of 60° and rotated relative to each other by 120° [94, 95, 344]. A triangular configuration also provides redundancy, since polarisation constraints are still possible with only two vertices operational.

In the following we consider three ET-D interferometers in the triangular configuration, which we denote as a "single ET". More than one ET would be very optimistic, so we complement our single ET with a network of individual third-generation right-angled interferometers (also with ET-D sensitivity) to permit source distance determination. While different locations are being mooted, we choose the Virgo location as the reference ET site [350].

3.2.2 Signal-to-noise ratio

As before, we employ a coincident search between widely separated detectors, and use optimal matched-filtering techniques to maximise detection prospects. The SNR formalism used here is described in further detail by Eq. (2.13-2.22) in Sec. 2.3.3 of Chapter 2.

The SNR of a detected system will vary between the individual network sites, as a result of the different $S_n(f)$'s and angular dependencies. However, following Ref. [297, 313], we

Table 3.1: The characteristic distance sensitivities [as given by evaluating Eq. (2.21)] of some advanced-detector configurations and various design studies for the third-generation Einstein Telescope.

Second-generation		Third-generation	
Detector	r_0 / Mpc	Detector	r_0 / Mpc
aLIGO[1]	80	ET[2]	1527
aLIGO[3]	110	ET-B[4]	1587
aLIGO[5]	119	ET-C[6]	1918
AdV[7]	85	ET-D[8]	1591

assume the network SNR of a detected system is given by the quadrature summation of the individual interferometer SNRs,

$$\rho_{\rm net} = \sqrt{\sum_k \rho_k^2} = \frac{8}{D_L}\left(\frac{\mathcal{M}_z}{1.2M_\odot}\right)^{5/6} \times \sqrt{\sum_k \left(r_{0,k}\Theta_k\zeta_k(f_{\rm max})\right)^2}, \tag{3.1}$$

where $r_{0,k}$, $\zeta_k(f_{\rm max})$ and Θ_k encode the distance, frequency and angular sensitivities of the $k^{\rm th}$ detector. Definitions for all parameters in this equation were given in the previous chapter. A comparison of the characteristic distance sensitivities of some second- and third-generation detectors is shown in Table 3.1.

3.2.3 Network antenna patterns

The angular dependence of the SNR is encapsulated by the variable Θ. The sky location and binary orientation can be deduced from the network analysis, however in our analysis we will use only D_L and $\mathcal{M}_z$ measurements. We calculate the probability density function for Θ [297] numerically using Eq. (2.12) by choosing $\cos\theta$, ϕ/π, $\cos\iota$ and ψ/π to be uncorrelated and distributed uniformly over the range $[-1, 1]$.

It is unlikely that more than one ET will be constructed. A more likely network configuration will involve a single ET with single third-generation right-angled detectors at other sites. In the interest of verisimilitude we take into account possible detector locations for such a third-generation network. Table 3.2 contains the locations and arm-bisector orientations of various current and planned detectors.

---

[1] Low-power zero detuning [308]

[2] Polynomial noise-curve approximation [127]

[3] High-power zero detuning [308]

[4] Conventional technology [92]

[5] NS-NS optimised [308]

[6] 3rd-generation technology, xylophone configuration [92]

[7] Ref. [82]

[8] 3rd-generation technology, xylophone configuration (updated and more realistic) [92]

Table 3.2: A reproduction of the GW-interferometer geographical locations, and arm-bisector orientations from Ref. [351]. We include updated LIGO-India information [352].

Detector	Label	Longitude	Latitude	Orientation
LIGO Livingston, LA, USA	L	$90^\circ 46' 27.3''$ W	$30^\circ 33' 46.4''$ N	208.0°(WSW)
LIGO Hanford, WA, USA	H	$119^\circ 24' 27.6''$ W	$46^\circ 27' 18.5''$ N	279.0°(NW)
Virgo, Italy	V	$10^\circ 30' 16''$ E	$43^\circ 37' 53''$ N	333.5°(NNW)
KAGRA (formerly LCGT), Japan	J	$137^\circ 10' 48''$ E	$36^\circ 15' 00''$ N	20.0°(NNE)
LIGO-India, India	I	$76^\circ 26'$ E	$14^\circ 14'$ N	45.0°(NE)

To write down the antenna pattern function as a function of the detector position,[9] we use the notation and formalism of Ref. [351]. For a GW source at spherical-polar coordinates (θ, ϕ) on the sky, with polarisation angle ψ, and a detector with opening angle η at latitude β, longitude λ and such that the bisector of its arms points at an angle χ, counter-clockwise from East, the antenna pattern functions are

$$\begin{pmatrix} F_+ \\ F_\times \end{pmatrix} = \sin\eta \begin{pmatrix} \cos(2\psi) & \sin(2\psi) \\ -\sin(2\psi) & \cos(2\psi) \end{pmatrix} \begin{pmatrix} a \\ b \end{pmatrix}, \tag{3.2}$$

where,

$$\begin{aligned} a = \; & \frac{1}{16}\sin(2\chi)[3-\cos(2\beta)][3-\cos(2\theta)]\cos[2(\phi+\lambda)] \\ & + \frac{1}{4}\cos(2\chi)\sin\beta[3-\cos(2\theta)]\sin[2(\phi+\lambda)] + \frac{1}{4}\sin(2\chi)\sin(2\beta)\sin(2\theta)\cos(\phi+\lambda) \\ & + \frac{1}{2}\cos(2\chi)\cos\beta\sin(2\theta)\sin(\phi+\lambda) + \frac{3}{4}\sin(2\chi)\cos^2\beta\sin^2\theta, \\ b = \; & \cos(2\chi)\sin\beta\cos\theta\cos[2(\phi+\lambda)] - \frac{1}{4}\sin(2\chi)[3-\cos(2\beta)]\cos\theta\sin[2(\phi+\lambda)] \\ & + \cos(2\chi)\cos\beta\sin\theta\cos(\phi+\lambda) - \frac{1}{2}\sin(2\chi)\sin(2\beta)\sin\theta\sin(\phi+\lambda). \end{aligned} \tag{3.3}$$

As a reference, we use a network comprising three 60° ET-D sensitivity interferometers at the Virgo location (a single ET), plus right-angled interferometers at the LIGO-Livingston and LIGO-India locations. The characteristic distance reach of all of the interferometers in the network is taken as 1591 Mpc, corresponding to ET-D sensitivity [345]. This is the sensitivity of a 10 km right-angled interferometer. We account for the different detector arm-opening angles in the antenna pattern functions.

The network SNR given by Eq. (3.1) also depends on $\zeta(f_{\rm max})$, which describes the overlap of the signal power with the detector bandwidth [297]. The frequency at the end of the

---

[9] We do not consider modulation of the antenna patterns due to the rotation of the Earth. We justify this in Sec. 3.6.6.

inspiral (taken to correspond to the frequency at ISCO) is given by Eq. (2.23). The maximum binary-system mass could conceivably be $\sim 4.2M_{\odot}$.[10] The ET horizon distance for a system with a total mass of $\sim 4M_{\odot}$ is $\sim$ 25 Gpc [346]. In the ΛCDM cosmology this corresponds to a redshift of ~ 2.9, and from Eq. (2.23) this gives $f_{\rm max} \sim 134$ Hz. Given the ET-D noise curve [345], $\sqrt{\zeta(f_{\rm max} = 134{\rm Hz})} \gtrsim 0.98$. Extending the *redshift* reach out to $z \sim 5$ still gives $\sqrt{\zeta(f_{\rm max} = 87{\rm Hz})} \gtrsim 0.96$. Thus, we feel justified in adopting $\zeta(f_{\rm max}) \simeq 1$ for all interferometers in the ensuing analysis.

Using these expressions we were able to numerically estimate the probability distribution for the *effective* Θ,

$$\Theta_{\rm eff} = \sqrt{\sum_k \Theta_k^2}, \tag{3.4}$$

where the sum is over all detectors in the network. We use this $\Theta_{\rm eff}$ distribution to choose SNRs for each source in the catalogue via Eq. (2.20) and then impose a detection criterion. As a reference, we adopt the detection criterion that the network SNR must be greater than 8.

3.3 NS-NS merger-rate density

In this analysis, we aim to probe not only the background cosmology and NS mass-distribution parameters, but the astrophysical properties of the binary NS population. To this end, we now consider the factors contributing to the coalescence of a binary NS system.

Following several theoretical [353, 354], population synthesis (e.g., Ref. [157, 355]) and observational studies (e.g., Ref. [356]), we define the merger rate per comoving volume as

$$\dot{n}(t) = \int_{t_*}^{t} \lambda \frac{dP_m}{dt}(t - t_b)\frac{d\rho_*}{dt}(t_b)dt_b, \tag{3.5}$$

where λ is a *mass efficiency*, defined as the number of coalescing DNS binaries per unit star-forming mass [157]. dP_m/dt is the probability distribution for a DNS binary to merge at a time $(t - t_b)$ after formation, and $d\rho_*/dt$ is the star-formation rate (SFR) density at cosmological time t_b.

Star formation, and the efficiency of double compact-object formation from the progenitor system, may be sensitive to the host-galaxy morphology and environment (e.g. metallicity). Furthermore, the distribution of delay times between star formation and the corresponding DNS-system coalescence may have contributions from several different evolutionary paths. However, we are interested here only in a third-generation GW-interferometer network's ability to constrain various astrophysical and cosmological parameters. As such we consider a single

---

[10] Both neutron stars in the binary system would need to have masses 2σ above the distribution mean at the maximum μ and σ considered in this analysis, where $\mu_{\rm NS} \in [1.0, 1.5]M_{\odot}$, $\sigma_{\rm NS} \in [0, 0.3]M_{\odot}$.

component star-formation distribution, delay-time distribution and mass efficiency, deferring considerations of the other dependencies to a future study. We now discuss the various terms in Eq. (3.5) in more detail.

3.3.1 Mass efficiency, λ

We use values for λ obtained from the population synthesis calculations of Ref. [355]. Smoothed histograms of the mass efficiency are shown in Fig. 4 of that paper, with modes at $\sim 10^{-5}M_{\odot}^{-1}$ for DNS systems formed in both elliptical and spiral conditions. However the distribution of λ ranges over several orders of magnitude, with $10^{-7}M_{\odot}^{-1} \lesssim \lambda \lesssim 10^{-3}M_{\odot}^{-1}$. We adopt $\lambda = 10^{-5}M_{\odot}^{-1}$ as the reference value for our analysis.

3.3.2 Merger-delay distribution, dP_m/dt

Massive stars in high-mass binary systems evolve into DNS systems on much shorter timescales than typical galaxy evolution or Hubble timescales, such that dP_m/dt is essentially determined by the initial orbital separation, a, of the DNS system [357]. The evolutionary time delay between the formation of the progenitor system (with component masses between $\sim 8-20M_{\odot}$) and the corresponding DNS system is typically $\sim$ 50 Myr [324].[11] This is negligible compared to the GW inspiral timescale, which scales as $\tau_{\rm gr} \propto a^4$, and can be $\mathcal{O}(\rm Gyrs)$. Assuming the number of binaries, N, born with separation a scales as $dN/da \propto a^{\gamma}$ [357], we obtain

$$\frac{dP_m}{dt} \propto \frac{dN}{d\tau_{\rm gr}} = \frac{dN}{da}\frac{da}{d\tau_{\rm gr}} \propto t^{\alpha}, \tag{3.6}$$

where $\alpha = (\gamma-3)/4$. If DNS systems retain the same orbital separation distribution as normal-abundance main-sequence stars [353, 358], then $dN/d\ln(a) \sim \text{const.}$, and therefore $\gamma = \alpha = -1$.[12] This scaling is not well constrained, so we adopt the approach of allowing α to be a free parameter that we attempt to fit from our observations and ask with what precision this can be determined. We use the value $\alpha = -1$ for our reference model, which is justified by current (albeit sparse) analysis of Galactic DNS systems [359–361], and various population synthesis calculations [124, 324, 355, 362–364]. For normalisation purposes, we assume a minimum

---

[11] This evolutionary time scale is an approximate main-sequence lifetime for an $8M_{\odot}$ star, burning $\sim 10\%$ of its core hydrogen, and obtained via the simple scaling relationship, $\tau_{\rm evol} \sim 10^4 (M/M_{\odot})^{-2.5}$ Myr.

[12] This assumes circular orbits, however eccentricity can have a significant effect on inspiral timescales. Also it is not obvious that DNS systems should retain the same orbital separation distribution as main-sequence binaries, since the system must survive two supernovae which are likely to modify this distribution. Furthermore, strictly speaking the joint probability distribution of evolutionary and merger timescales should be considered here [324], since the latter depends on the compact-binary's chirp mass, which depends on the progenitor's component masses, which in turn influences the evolutionary timescale.

delay-time of 50 Myr, and model only DNS systems formed via the classical formation channel [109, 362, 365] for which the $\sim t^{-1}$ delay-time distribution is an appropriate approximation over several orders of magnitude. The power-law index will have a greater impact on merger-rate density calculations than the lower cutoff time. We adopt a maximum delay-time equal to the cosmology-dependent age of the Universe.

3.3.3 Star-formation rate density, $d\rho_*/dt$

The star-formation rate density is also rather uncertain, so we are only looking for a reasonable model which can be easily parametrised. The SF2 model of Ref. [366] attempts to factor in the uncertainties in the incompleteness of data sets and the amount of dust extinction at early epochs. The SF2 model has the form

$$\frac{d\rho_*}{dt}(z) \approx 0.16 \times \left(\frac{\exp(\beta_1 z)}{\exp(\beta_2 z) + 22}\right) \times \frac{E(z)}{(1+z)^{3/2}} \quad M_\odot \mathrm{Mpc}^{-3}\mathrm{yr}^{-1}, \tag{3.7}$$

where

$$E(z) = \sqrt{\Omega_{m,0}(1+z)^3 + \Omega_{k,0}(1+z)^2 + \Omega_\Lambda(z)}, \tag{3.8}$$

and $\beta_1 = \beta_2 = 3.4$. In this model, the SFR density remains roughly constant at $z \gtrsim 2$, which may be incompatible with recent observations [367–369]. This is discussed in more detail in Appendix 3.A. To allow for some uncertainty, we treat β_1 and β_2 as free parameters and explore how precisely we can measure them. While this simple ansatz does not cover all possible forms for the SFR density, using it will provide an indication of what GW observations could tell us. The framework is easily adaptable to more complex SFR models.

We must also specify t_*, the lower integration bound in Eq. (3.5), which represents the time of the earliest period of star formation. Among the highest known redshift objects are GRB 090429B, a long-duration gamma-ray burst (GRB) with a photometric redshift of ~ 9.4 [370], and UDFj-39546284, a candidate $z \sim 10$ galaxy [371][13]. We therefore use $z = 10$ as the earliest time of star formation. Future observations, for instance with the *James Webb Space Telescope*, may be able to probe back to the first phases of galaxy formation at $z \sim 15$ and if objects are found at that epoch, this assumption should be revised. However, our results are fairly insensitive to this choice.

3.3.4 Calculating $\dot{n}(z)$

Evaluating Eq. (3.5) to give the merger-rate density as a function of *redshift* requires a cosmology-dependent calculation of the cosmological time in terms of redshift, followed by an integral over

---

[13] After this research was carried out, the existence of this protogalaxy was confirmed, with an associated photometric redshift of $\sim 11.8 \pm 0.3$ [372].

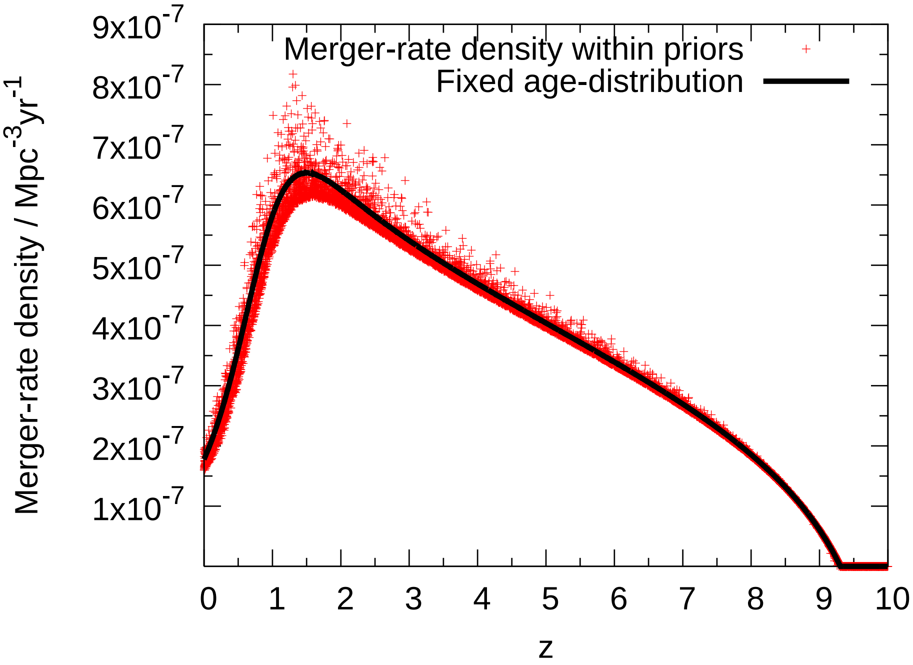

Figure 3.2: Merger-rate densities computed for the reference cosmology (solid line) and for cosmological parameters chosen randomly from within the prior range (red crosses).

the delay-time distribution. This procedure created a bottleneck in our analysis. However, since the priors on the cosmological parameters are narrow (see Sec. 3.5.4), there is little variation in the merger-rate density across this range, as shown in Fig. 3.2. We therefore fixed the cosmological parameters at their reference values for the cosmological time calculation, which made the merger-rate density calculation considerably faster. Although this throws away some of the cosmological information, it did not significantly affect the results and made the analysis more tractable.

3.4 Cosmological models

In the previous chapter, we considered only a flat cosmology with a cosmological constant, but here we allow for curvature and an evolving dark-energy EOS. For a full review of the evidence and models of accelerated expansion of the Universe, see Ref. [373]. From the cosmological field equations we have

$$\dot{\rho} + 3\left(\frac{\dot{a}}{a}\right)\left(\rho + \frac{p}{c^2}\right) = 0, \tag{3.9}$$

where ρ and p are the density and pressure of a cosmological fluid respectively, while a is the scale factor of the universe. Derivatives are with respect to physical time. For a perfect fluid

($p = w\rho c^2$, where w is the EOS parameter), this reduces to

$$\left(\frac{\dot{\rho}}{\rho}\right) = -3(1+w)\left(\frac{\dot{a}}{a}\right). \tag{3.10}$$

Hence,

$$\rho(a) = \rho(a_{\text{today}} = 1) \times e^{-3\int_1^a (1+w)(da'/a')}. \tag{3.11}$$

The last decade has seen many proposals for the origin of accelerated expansion [373], ranging from vacuum energy to modified gravity, or even unmodified gravity within an inhomogeneous Universe. One approach attempts to explain dark-energy as a minimally coupled scalar field ("quintessence") slowly rolling down its potential such that it can exert negative pressure. While it is possible to have a constant EOS in this formalism, this requirement places severe constraints on the potential and so it is natural to expect a time-varying EOS [374].

The simplest approximation is to assume a linear model ($w(z) = w_0 + w_1 z$), but this is only appropriate for local studies due to the divergence at high redshift. The Shafieloo-Sahni-Starobinsky ansatz [375] models the EOS evolution as a "$\tanh$" form that ensures $w = -1$ at early times and $w \rightarrow 0$ at low z. This ansatz prevents the crossing of the "phantom divide" at $w = -1$, desirable since phantom fluids can not be explained by a minimally coupled scalar field [374]. The ansatz we adopt in this work is the Chevallier-Polarski-Linder ansatz [374, 376]

$$w(a) = w_0 + w_a(1-a), \quad w(z) = w_0 + w_a\left(\frac{z}{1+z}\right). \tag{3.12}$$

This ansatz was adopted by the Dark Energy Task Force [377], and has several desirable features: (i) it depends on only two free parameters; (ii) it reduces to the linear model at low z; (iii) it is well-behaved at high redshift, tending to $w_0 + w_a$. Using this EOS,

$$\Omega_\Lambda(z) = \Omega_{\Lambda,0} \times (1+z)^{3(1+w_0+w_a)} \times e^{-3w_a\left(\frac{z}{1+z}\right)}. \tag{3.13}$$

For different global geometries of the Universe the luminosity distance, D_L, is given by

$$D_L(z|\mathcal{C}) = (1+z) \times \mathcal{F}(z|\mathcal{C}),$$

where

$$\mathcal{F}(z|\mathcal{C}) = \begin{cases} \frac{D_H}{\sqrt{\Omega_{k,0}}} \sinh\left(\sqrt{\Omega_{k,0}}\frac{D_c(z|\mathcal{C})}{D_H}\right), & \Omega_{k,0} > 0, \\ D_c(z|\mathcal{C}), & \Omega_{k,0} = 0, \\ \frac{D_H}{\sqrt{|\Omega_{k,0}|}} \sin\left(\sqrt{|\Omega_{k,0}|}\frac{D_c(z|\mathcal{C})}{D_H}\right), & \Omega_{k,0} < 0, \end{cases} \tag{3.14}$$

in which D_H is the Hubble scale ($1/H_0$) and $\mathcal{C}$=$\{H_0, \Omega_{m,0}, \Omega_{\Lambda,0}, \Omega_{k,0}, w_0, w_a\}$ is the set of cosmological parameters describing the large-scale characteristics of the universe.

The comoving radial distance, $D_c(z)$, is given by

$$D_c(z) = D_H \int_0^z \frac{dz'}{E(z')}, \tag{3.15}$$

where $E(z)$ is given by Eq. (3.8). The redshift derivative of the comoving volume is given generally by

$$\frac{dV_c}{dz} = 4\pi D_H \frac{D_L(z)^2}{(1+z)^2 E(z)}. \tag{3.16}$$

3.5 Making & Analysing DNS catalogues

Full details of the techniques we employ to construct and analyse catalogues of merging DNS systems can be found in the previous chapter, but we reiterate the salient details here.

3.5.1 Distribution of detectable DNS systems

The two system properties we will use in our analysis are the redshifted chirp mass, $\mathcal{M}_z$, and the luminosity distance, D_L. We assume that only systems with an SNR greater than a given threshold will be detected. The distribution of the number of events per unit time in the observer's frame with $\mathcal{M}$, z and effective Θ is given by Eq. (2.36). As in Sec. 2.3.8 of the previous chapter, we convert this to a distribution in $\mathcal{M}_z$, D_L and ρ,[14] and integrate over ρ to find the distribution of *detectable* systems (i.e., systems above SNR threshold).

To calculate the number of detected systems (given a set of model parameters, $\overrightarrow{\mu}$) we integrate over this distribution, which is equivalent to integrating the distribution over redshift and chirp mass, i.e. $N_\mu = T \times \int_0^\infty \int_0^\infty \left(\frac{d^3N}{dtdzd\mathcal{M}} \right) \mathrm{d}z\mathrm{d}\mathcal{M}$, where T is the duration of the observation run. We found that assuming the NS mass-distribution was a δ-function centred at the mean given by the trial parameters allowed at least a tenfold speed-up in this calculation by halving the dimensionality of the integral. This gave results consistent with the full 2D integration procedure.

3.5.2 Creating mock catalogues of DNS binary inspiraling systems

The model parameter space we investigate is the 7D space of $[w_0, w_a, \mu_{\rm NS}, \sigma_{\rm NS}, \alpha, \beta_1, \beta_2]$. To generate a catalogue of events we choose a set of reference parameters which are motivated by previous analysis in the literature. For our reference cosmology we adopt $H_0 = 70.4$ kms^{-1}Mpc^{-1}, $\Omega_{m,0} = 0.2726$, $\Omega_{\Lambda,0} = 0.728$, $w_0 = -1.0$ and $w_a = 0.0$ [328]. The reference parameters of the neutron-star mass distribution are $\mu_{\rm NS} = 1.35 M_\odot$ and $\sigma_{\rm NS} = 0.06 M_\odot$

---

[14] The distribution in $\mathcal{M}_z$, D_L and ρ is generalised for an arbitrary curvature Universe through dz/dD_L via Eq. (3.14).

[316]. The delay-time distribution and SFR density were discussed in Sec. 3.3. We adopt a power-law merger-delay distribution with reference power-law index $\alpha = -1.0$, and we take the SFR density to be given by the SF2 ansatz [366], with $\beta_1 = 3.4$ and $\beta_2 = 3.4$.

These reference parameters are used to calculate an expected number of events[15], and the number of observed events, N_o, is drawn from a Poisson distribution (assuming each binary system is independent of all others) with that mean. Monte-Carlo acceptance/rejection sampling is used to draw random redshifts and chirp masses from the distribution in Eq. (2.36) for each event. The D_L and $\mathcal{M}_z$ are then computed from the sampled $\mathcal{M}$ and z.

For these reference parameters, which give a local merger-rate density of $\sim 2 \times 10^{-7}$ Mpc^{-3}yr^{-1}, and assuming detected systems must have a network SNR greater than 8, we find that the expected number of detections in 1 yr is $\sim 10^5$.[16]

3.5.3 Likelihood statistic

In the measurement-parameter space of redshifted chirp mass and luminosity distance, the measured number of detections in a given bin will be a Poisson random variate with a model-dependent mean. If we take the continuum limit of this, such that bin sizes are infinitesimally small and contain either 0 or 1 events, then we can formulate the likelihood of a catalogue of discrete events,

$$\mathcal{L}(\vec{\vec{\Lambda}}|\vec{\mu},\mathcal{H}) = e^{-N_\mu}\prod_{i=1}^{N_o} r(\vec{\lambda_i}|\vec{\mu}), \tag{3.17}$$

where $\vec{\vec{\Lambda}} = \{\vec{\lambda_1}, \vec{\lambda_2}, \ldots, \vec{\lambda_{N_o}}\}$ is the vector of measured system properties, with $\vec{\lambda_i} = (\mathcal{M}_z, D_L)_i$ for system i. N_o is the *actual* number of detected systems, while N_μ is the number of DNS inspiral detections *predicted* by the model with parameters $\vec{\mu}$. Finally, $r(\vec{\lambda_i}|\vec{\mu})$ is the rate of events with properties $\mathcal{M}_z$ and D_L, evaluated for the $i^{\rm th}$ detection under model parameters $\vec{\mu}$, which is given by $(d^3N/dtd\mathcal{M}_z dD_L)\,|_{\rho>\rho_0}$, and discussed in Sec. 3.5.1. The trial cosmological parameters are used to calculate a model-dependent redshift from the catalogued luminosity distance, and, in turn, this redshift is used to infer a model-dependent intrinsic chirp mass from the catalogued value of $\mathcal{M}_z$. These values of $\mathcal{M}_z$, D_L, as well as the model-dependent values of z and $\mathcal{M}$, are used to calculate $r(\vec{\lambda_i}|\vec{\mu})$ for each source, and combined to to compute the

---

[15] The observation time, T, is assumed to be 1 yr, and the mass efficiency is assumed to be $\lambda = 10^{-5}M_\odot^{-1}$ (as mentioned earlier).

[16] This reference local merger-rate density is roughly five times smaller than the realistic value quoted in Ref. [147], but 20 times larger than the pessimistic estimate. Whilst we could scale our merger-rate density calculations to match the realistic value of 10^{-6} Mpc^{-3}yr^{-1}, our modified likelihood statistic makes our analysis insensitive to such scalings. A rescaling to the realistic local merger-rate density of Ref. [147] would lead to an expected detection rate of approximately half a million sources.

likelihood.

In the previous chapter we employed a modified likelihood statistic which marginalised over the local merger-rate density of DNS systems. This approach reflects our current lack of knowledge of this quantity, estimates of which vary over several orders of magnitude. We adopt the same approach in this analysis to eliminate the dependence on poorly known scaling factors. This includes the mass-efficiency parameter, λ, which is a quantity derived from population synthesis studies and can vary over several orders of magnitude.

The modified likelihood statistic is

$$\tilde{\mathcal{L}}(\overrightarrow{\Lambda}|\overrightarrow{\mu},\mathcal{H}) \propto {N_\mu}^{-(N_o+1)} \prod_{i=1}^{N_o} r(\overrightarrow{\lambda_i}|\overrightarrow{\mu}). \tag{3.18}$$

We note that we have not included a prior on the scaling factors in the above, which is equivalent to using an improper flat prior over the range $[0,\infty]$. This reflects our current lack of knowledge of the mass-efficiency. A proper prior could be implemented by setting lower and upper bounds on the mass-efficiency, giving a finite range which is large enough not to affect the likelihood, and leading to results consistent with Eq. (3.18).

3.5.4 Calculating the posterior probability

Given that ET will most likely not be operational until the late-2020s, we must consider what constraints conventional observational cosmology can put on cosmological parameters. In the recent study by Ref. [347], the authors investigated how the dark-energy EOS could be probed by ET observations of DNS systems to provide distance measurements, complemented by electromagnetic measurements of the associated short gamma-ray burst (SGRB) to provide the redshift. They estimated that a combination of the Planck cosmic microwave background (CMB) prior, JDEM BAO results, and future Type Ia supernova observations could provide cosmological constraints by the ET-era of

$$\begin{aligned}
\Delta\Omega_{m,0} = 3.46\times 10^{-3}, &\quad \Delta\Omega_{k,0} = 5.91\times 10^{-4}, \\
\Delta H_0 = 0.336, \quad \Delta w_0 =& 0.048, \quad \Delta w_a = 0.184.
\end{aligned} \tag{3.19}$$

Hence, we assume that H_0, $\Omega_{m,0}$ and $\Omega_{k,0}$ are precisely known quantities, with values of 70.4 kms^{-1}Mpc^{-1}, 0.2726 and -0.0006, respectively. As a prior on w_0 and w_a, we adopt the constraint that $w(z) < -1/3$ at all redshifts. Hence we use uniform priors on the EOS parameters with $w_0 < -1/3$ *and* $w_0 + w_a < -1/3$ and lower bounds set low enough so as not to affect the posterior probability distribution. We also adopt uniform priors for all other parameters under investigation.

3.6 Results

3.6.1 Posterior recovery

An analysis using the full 10^5 observations expected in a year of ET data is computationally prohibitive, so we use a working reference sample of ~ 4500 detections (corresponding to a shorter observation time or a lower merger rate density) and extrapolate to the expected number of detections, as discussed in Sec. 3.6.3. For each analysis, we ran 120 independent adaptive MCMC chains (see Sec. 1.4) of 5000 points on the same data catalogue. We then used the last point from each chain to initialise a follow-up run of another 5000 iterations. The first 2000 points from each chain of the follow-up run were discarded as burn-in. This procedure therefore generated $360,000$ points, with an average acceptance rate of $\sim 30\%$. The analysis of the 4500-event reference catalogue took ~ 3.5 hrs in total. Our sampled points were analysed using the COSMOLOGUI package [378].

3.6.2 Marginalised posterior distributions

In Fig. 3.3 we show the recovered marginalised 2D posterior distributions (with 68% and 95% confidence contours) for the reference catalogue. In Fig. 3.3(c) we observe a correlation between the recovered dark-energy parameters. This is easily explained by the fact that a given catalogued luminosity distance may be consistent[17] with a range of w_0 and w_a values, the combinations of which will depend on the redshift of the source. Since the majority of detected systems will be centred around $z \sim 1$, the $w_0 - w_a$ correlation will be dominated by these sources.[18] In Fig. 3.3(a) a negative correlation is observed between the recovered values for w_0 and $\mu_{\rm NS}$. For a given catalogued luminosity distance and fixed w_a, a low value of w_0 will imply a low redshift in that model. When this redshift is used to compute $\mathcal{M}$ from $\mathcal{M}_z$, we obtain a large value of the chirp mass, which is consistent with a chirp-mass distribution (and hence a NS-mass distribution) centered at larger values. Figure 3.3(b) merely shows the combined information of Figures 3.3(a) and 3.3(c) (where the recovered w_a values are negatively correlated with the w_0 values); therefore the correlation observed in Fig. 3.3(b) is positive.

A strong positive correlation is observed between the SFR-density SF2 ansatz parameters, β_1 and β_2, as seen in Fig. 3.3(d), while Fig. 3.3(e) shows a weak negative correlation between α and β_1. These correlations correspond to keeping the merger-rate density approximately constant. For a variety of redshifts we calculated which combinations of α, β_1 and β_2 were

---

[17] Here, by “consistent” we mean within $\pm 1\%$ of the reference value.

[18] The correlation between the two dark-energy EOS parameters can be reduced by rebinning the MCMC samples using the Wang parametrisation [379]. This simply involves a tranformation from the (w_0, w_a) parametrisation to $(w_0, w_{0.5})$, where $w_{0.5} = w_0 + (w_a/3)$.

consistent with a given merger-rate density. We found that there was a strong positive correlation in these points between β_1 and β_2, but the correlation between α and β_1 changed sign as the redshift increased. The greatest change occurred as the redshift was increased from 0 to 1, where the correlation then flipped sign; however at $z = 4$ the magnitude of the correlation was still not as large as it was at $z = 0.1$. This leads us to believe that although the D_L distribution of detected sources is peaked around ~ 6 Gpc, with a long tail to ~ 45 Gpc, the lower distance sources dominate the $\alpha - \beta_1$ correlation, giving an overall negative correlation.

In Fig. 3.4, we show the marginalised 1D posterior distributions for the model parameters which have been inferred from our reference catalogue. The dotted lines in the plots indicate the 68% and 95% confidence regions of the marginalised distributions.[19]

3.6.3 Precision scaling with number of detections

We performed similar analyses on catalogues containing various numbers of detections, culminating in a run with 10^5 detections. We can characterise the precision with which we can measure the various model parameters by the 95% confidence intervals. Recording these intervals for all parameters for varying catalogue sizes, and dividing by the reference sample intervals gave the results shown in Fig. 3.5. This clearly shows that the precisions scale as $1/\sqrt{N_o}$ as we would expect. Parameter measurement accuracies for the 10^5-event catalogue are shown in Table 3.3. We see that the measurement precisions of the dark-energy EOS parameters are the same order of magnitude as those forecast for CMB+BAO+SNIa [347], as discussed in Sec. 3.5.4.

3.6.4 Including and accounting for errors

Distance measurements from a third-generation GW-interferometer network will not be error-free. Whilst a network consisting of a single ET plus one other right-angled interferometer can place constraints on a source's sky location and luminosity distance, the precisions of these properties are improved to almost the 3-ET network level by the inclusion of a second additional right-angled interferometer [350]. The redshifted chirp mass is expected to be very well constrained ($\lesssim 0.5\%$ error [380]), and so we ignore measurement errors in this parameter. We assume the error in the luminosity distance arising from instrumental noise scales as $\sim 1/\rho$,

---

[19] While these results were computed using the fast merger-rate approximation, we also analysed a catalogue using the full merger-rate density. The 95% confidence intervals of the marginalised posterior distributions were consistent with our approximate analysis, justifying the use of the approximation to compute the rest of our results. No correlations between the merger-rate density parameters and the dark-energy EOS parameters were found, which supports our earlier statement that the dependence of the merger-rate density on the underlying cosmological parameters is weak within the applied priors.

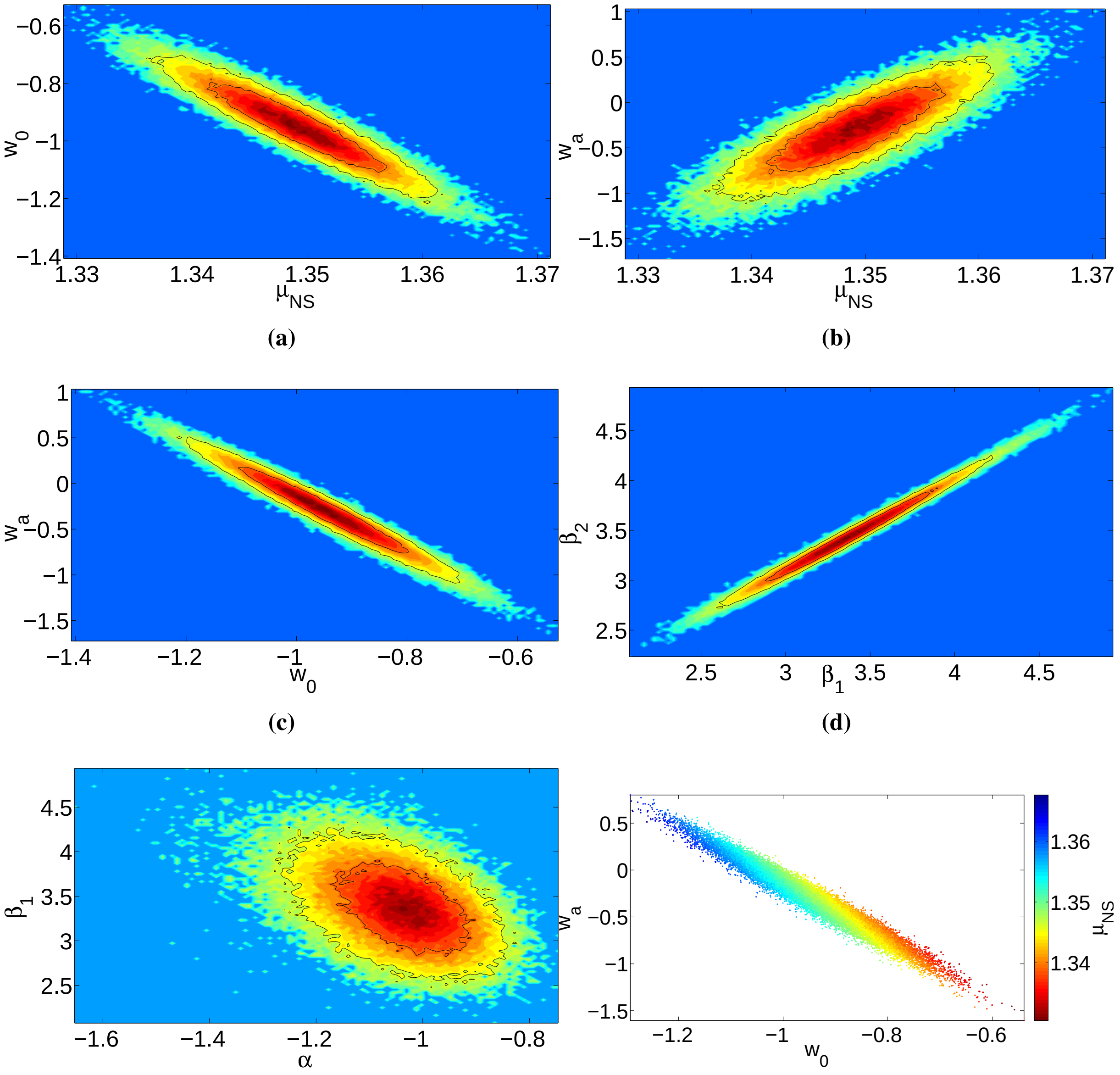

(a) **(b)**

(c) **(d)**

(e) **(f)**

Figure 3.3: Marginalised 2D posterior distributions for the reference catalogue of 4500 detections. Only those 2D distributions showing correlations between parameters are shown. The reference parameters are $\mu_{\rm NS} = 1.35M_{\odot}$, $\sigma_{\rm NS} = 0.06M_{\odot}$, $w_0 = -1$, $w_a = 0$, $\alpha = -1$ and $\beta_1 = \beta_2 = 3.4$.

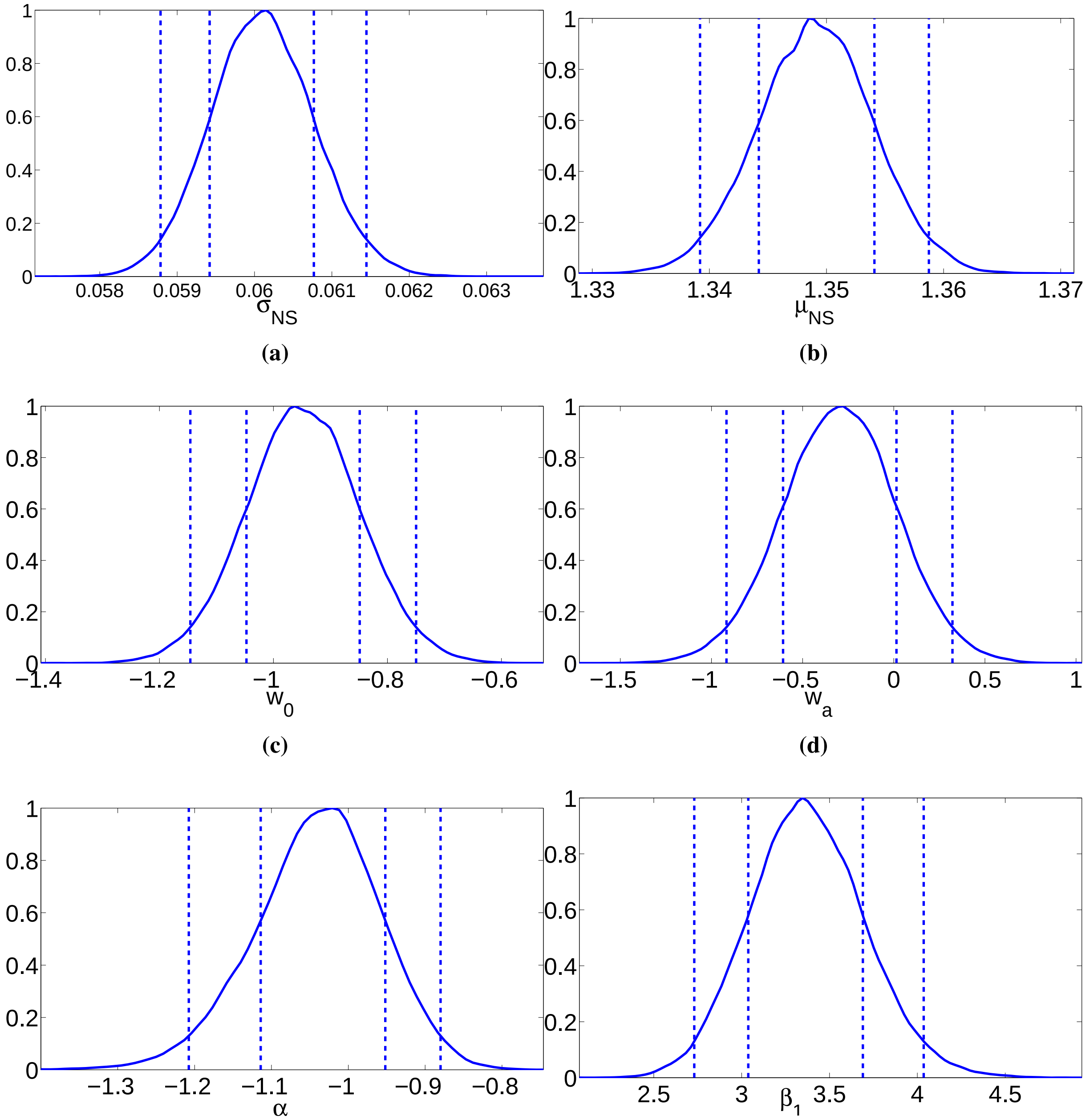

(a) **(b)**

(c) **(d)**

(e) **(f)**

Figure 3.4: Marginalised 1D posterior distributions for the reference catalogue of 4500 detections. Dotted lines indicate the boundaries of the 95% and 68% confidence intervals. The reference parameters are $\mu_{\rm NS} = 1.35M_\odot$, $\sigma_{\rm NS} = 0.06M_\odot$, $w_0 = -1$, $w_a = 0$, $\alpha = -1$ and $\beta_1 = 3.4$.

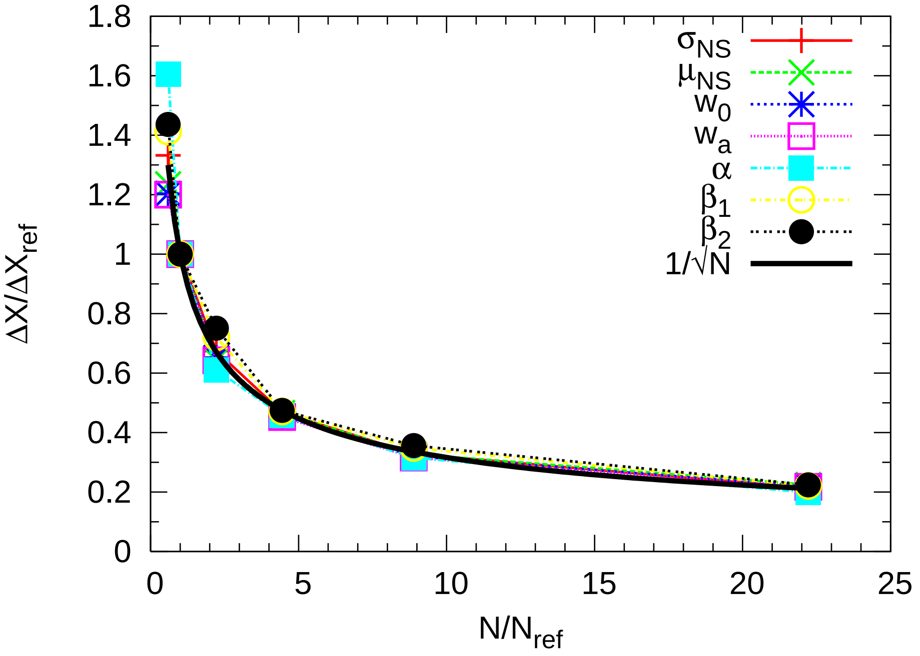

Figure 3.5: 95% confidence intervals of the 1D marginalised distributions relative to those of the 4500-event reference catalogue, shown as a function of the number of catalogued events. The same intrinsic parameters of the underlying distributions are used to create the mock catalogues. The expected $\sim 1/\sqrt{N}$ relationship is overlaid on the plot.

Table 3.3: 95% confidence intervals obtained from a catalogue of 10^5 detections, with reference parameters used to generate the data. ΔX gives the width of the 95% confidence interval.

Parameter	Reference value	95% conf. interval	ΔX
$\sigma_{\rm NS}/M_\odot$	0.06	[0.059688 , 0.060254]	0.000566
$\mu_{\rm NS}/M_\odot$	1.35	[1.347408 , 1.351789]	0.00438
w_0	-1.0	[-1.036403 , -0.949623]	0.0869
w_a	0.0	[-0.195630 , 0.073602]	0.269
α	-1.0	[-1.026691 , -0.961659]	0.0650
β_1	3.4	[3.318136 , 3.605810]	0.288
β_2	3.4	[3.310287 , 3.582895]	0.273

Table 3.4: 95% confidence intervals derived from the reference sample (4500 detections), both in the case where distances are measured precisely, and when distance errors are included and accounted for (using the error averaging technique described in the text, with various numbers of points sampled from the distance posterior PDF). ΔX gives the width of the 95% confidence interval.

Parameter	No errors	Errors (50 points)		Errors (100 points)		Errors (400 points)	
	95% conf. interval	95% conf. interval	$\Delta X/\Delta X_{\mathrm{ref}}$	95% conf. interval	$\Delta X/\Delta X_{\mathrm{ref}}$	95% conf. interval	$\Delta X/\Delta X_{\mathrm{ref}}$
$\sigma_{\mathrm{NS}}/M_{\odot}$	[0.058785 , 0.061447]	[0.066378 , 0.071911]	2.07851	[0.063815 , 0.069409]	2.10143	[0.059309 , 0.064849]	2.08114
$\mu_{\mathrm{NS}}/M_{\odot}$	[1.339198 , 1.358745]	[1.329060 , 1.354066]	1.27928	[1.335499 , 1.361690]	1.3399	[1.335782 , 1.359339]	1.20515
w_0	[-1.145894 , -0.749671]	[-0.880092 , -0.338642]	1.36653	[-1.146052 , -0.537588]	1.53566	[-1.116809 , -0.546566]	1.4392
w_a	[-0.917590 , 0.321901]	[-2.345082 , -0.452114]	1.52722	[-1.651230 , 0.463072]	1.70578	[-1.605299 , 0.377340]	1.59956
α	[-1.207554 , -0.879888]	[-1.215388 , -0.863579]	1.07368	[-1.208005 , -0.874856]	1.01673	[-1.198613 , -0.890136]	0.941437
β_1	[2.730152 , 4.036099]	[2.851895 , 4.260085]	1.07829	[2.729217 , 4.038989]	1.00293	[2.771780 , 4.069150]	0.99343
β_2	[2.842474 , 4.059874]	[2.954584 , 4.274131]	1.08391	[2.863813 , 4.080100]	0.999088	[2.887584 , 4.100009]	0.995918

and include the effects of weak lensing as a further source of error. The weak-lensing error on luminosity distance measurements at $z \sim 1$ is approximately 5%, and we linearly extrapolate this to all other redshifts [346, 347, 381, 382]. While several techniques have been proposed to reduce this weak-lensing error [e.g. Ref. [383, 384] and references therein], we assume no correction has been done, corresponding to a worst-case scenario.

Errors on the distance-redshift relation from binary-system peculiar velocities are much smaller than instrumental and weak-lensing errors at all but the lowest redshifts, becoming comparable with these at $z \sim 0.1$ where the error is $\lesssim 1\%$, and decreasing sharply at higher redshifts [Ref. [348] and references therein]. The lowest redshift in our reference catalogue is ~ 0.05, where the peculiar velocity errors will dominate, but only lead to an error of $\lesssim 2\%$. The sensitivity of the luminosity distance to the dark-energy EOS parameters is very weak in this redshift regime; hence peculiar velocities are unlikely to introduce significant parameter bias/inaccuracy, and we ignore them here.

We also ignore the effect of detector calibration errors, which, unlike statistical measurement uncertainties, would not be mitigated by boosting the detection rate. Such systematic biases have recently been studied in the case of advanced-era detectors [304], and found to induce a systematic shift in the estimated system parameters which is a small fraction of the statistical measurement errors. We ignore waveform-modelling errors in our analysis, since current post-Newtonian models will only break down close to the onset of the merger-phase, and for the neutron-star binaries considered in this analysis this is at frequencies where the instrumental noise is high and which therefore do not contribute much to the overall signal-to-noise of the system. Furthermore, luminosity-distance determination comes primarily from the network triangulation which will not be significantly affected by modelling uncertainties, and so the distance error will be dominated by instrumental-noise and weak-lensing, as discussed earlier. Similarly, the error in the distribution of possible source-redshifts arising from the measured redshifted chirp mass will be dominated by the intrinsic width of the NS mass distribution rather than the small error in the redshifted chirp mass coming from instrumental noise and modelling uncertainties.

We repeat the analysis of the working reference sample, offsetting the catalogued luminosity distance by an amount drawn from a Gaussian distribution, with mean at the true distance, and standard deviation,

$$\sigma = D_L \times \sqrt{(1/\rho)^2 + (0.05z)^2}. \tag{3.20}$$

The data collected for each event will actually be in the form of posterior probability density functions (PDFs) for the parameters, where previously we have assumed these are δ-functions at the true values. We found that if the offset luminosity distances were assumed to be the true values with a δ-function posterior PDF, then the chain does not move away from its starting point. Hence we must take these errors into account in the likelihood calculation stage.

We can account for these errors in the analysis using the techniques of the previous chapter (see Eq. (2.51)), which involves integrating the likelihood over the posterior PDFs of the measured data. Concern has been raised that the high event rate of ET detections may lead to a confusion background, however the *noise-weighted* signals are short enough that there is not expected to be significant overlap [346, 380]. Hence, these detections should be uncorrelated, with independent parameter estimates, and so the posterior PDF for the detected population of sources reduces to the product of the posterior PDFs for each detection.

We represent the D_L posterior PDF for each source by a chain of 50 points, drawn from a normal distribution with standard deviation as in Eq. (3.20), and a mean equal to the value in the data catalogue, which in this analysis, as discussed earlier, includes an error to offset it from the true value. Results are shown in Table 3.4. We see that a significant bias in the reconstructed model parameters still exists. We suspected that this bias arose from using only 50 points to evaluate the distance posterior PDFs. We therefore repeated the analysis with an increasing number of points sampled from the distance posterior PDF.[20] With 100 points, all biases are corrected expect for that in $\sigma_{\rm NS}$, and the ratio of the 95% confidence interval widths to the reference widths is not significantly different from the 50 point case. This suggests that a larger number of points in the error averaging technique will be necessary to correct all biases, but this is not necessary to estimate parameter measurement accuracies in the presence of distance errors. Using 400 points sampled from the distance posterior PDF all biases in the parameter posterior distributions appear to be corrected, in the sense that the reference parameters then lay within the 95% confidence intervals of the 1D marginalised posterior distributions.

Overall, we find that the result of properly accounting for instrumental and weak-lensing errors is that parameter measurement precisions are, at worst, approximately halved. Thus instrumental and weak-lensing induced errors should not affect our general conclusions about the science capabilities of a third-generation GW-interferometer network. We carry out the remainder of this study using catalogues which are generated and analysed without including errors.

3.6.5 Precision scaling with intrinsic parameters

We now investigate how the ability of ET to constrain the parameters of the underlying distributions is affected by the values of the intrinsic parameters themselves. This is similar to the

---

[20] The posterior distributions obtained via this analysis should be considered estimates of the true distributions, since the long likelihood computation time required by this error-analysis means that we did not collect as many samples as when errors are ignored. We performed burn-in runs, and then follow-up runs to estimate the posterior distributions as well as feasible.

Table 3.5: The expected detection rates for different choices of intrinsic parameters of the underlying distribution are compared to the reference expected detection rate. One parameter is varied at a time, with all other parameters kept fixed at their reference values. We found that the variation of the expected detection rate with the intrinsic value of $\sigma_{\rm NS}$ was negligible.

$\mu_{\rm NS}/M_\odot$	$N/N_{\rm ref}$	w_0	$N/N_{\rm ref}$	w_a	$N/N_{\rm ref}$	α	$N/N_{\rm ref}$	β_1	$N/N_{\rm ref}$	β_2	$N/N_{\rm ref}$	$\beta_1 = \beta_2$	$N/N_{\rm ref}$
1.31	0.952	-1.50	1.08	-0.50	1.02	-1.10	1.04	2.90	0.405	3.40	1.00	3.00	0.929
1.33	0.976	-1.25	1.05	-0.25	1.01	-1.00	1.00	3.00	0.475	3.60	0.696	3.20	0.966
1.35	1.00	-1.00	1.00	0.00	1.00	-0.90	0.958	3.10	0.561	3.70	0.595	3.40	1.00
1.37	1.02	-0.75	0.935	0.25	0.986	-0.60	0.810	3.20	0.671	3.80	0.514	3.60	1.03
1.39	1.05	-0.50	0.844	0.50	0.970	-0.50	0.757	3.40	1.00	4.00	0.394	3.80	1.06

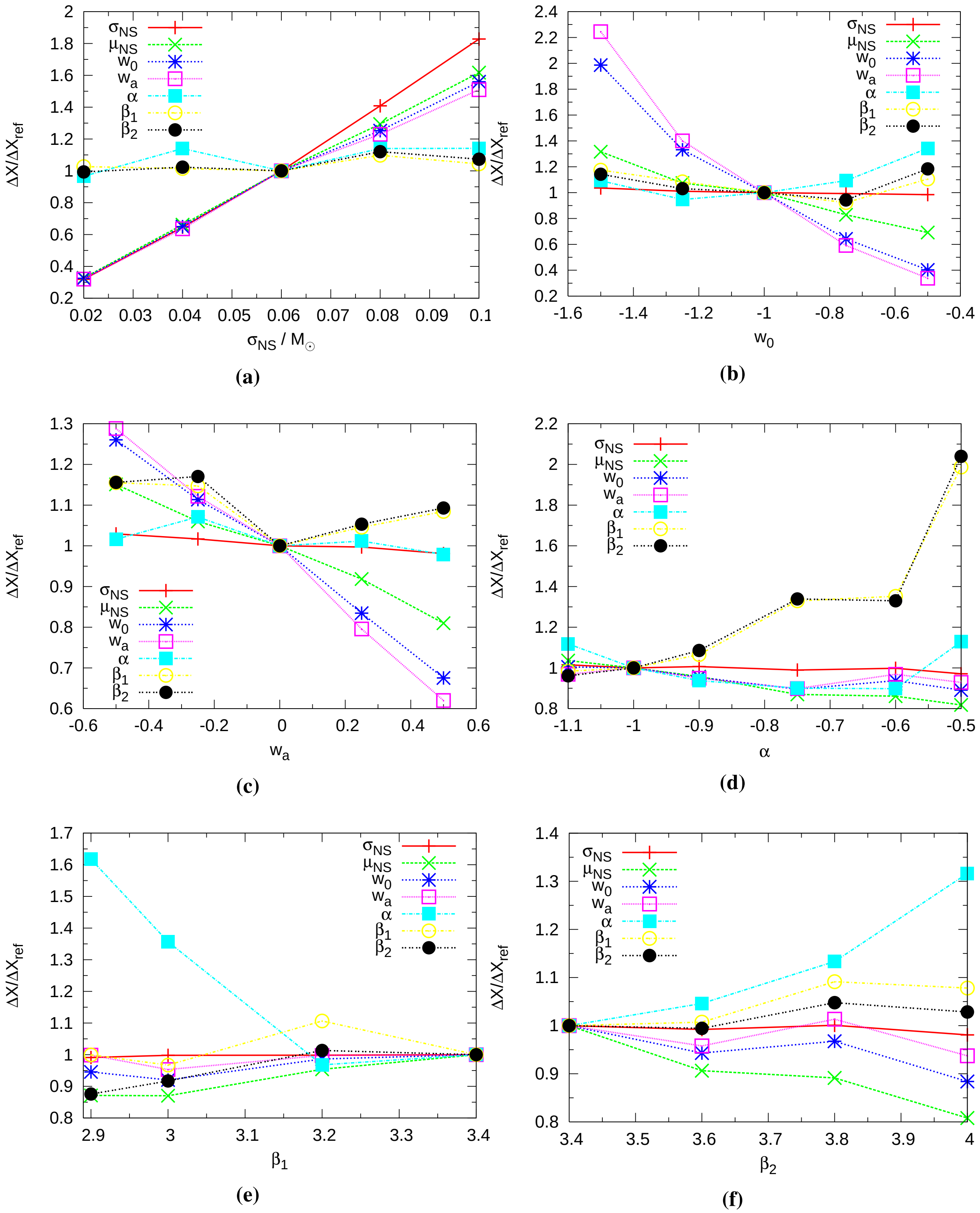

(a) **(b)**

(c) **(d)**

(e) **(f)**

Figure 3.6: The variation of measurement precision with different choices of the intrinsic parameters of the underlying distributions. One parameter is varied at a time, and in the interest of testing how the precision of parameter recovery is affected by the underlying *distribution* of events, all catalogues are generated with the same number of events (4500 to match the reference catalogue). Each point in each panel represents the average 95% confidence interval width of 3 realisations of the catalogue.

kind of analysis performed in the previous chapter for second-generation interferometers. We analyse catalogues generated with different intrinsic parameter combinations; multiple runs are performed on each parameter combination. We vary one parameter at a time, fixing all others to the reference values.

Varying the intrinsic parameters with fixed SNR threshold will alter the expected detection rate. This is illustrated in Table 3.5, where the model with reference parameters has an expected detection rate of $\sim 10^5$ yr^{-1}. The expected $\sim 1/\sqrt{N}$ relationship is well established, as shown in Fig. 3.5. Hence, we remove this number effect by generating catalogues with the same number of events (4500 each in order to compare against the reference catalogue). Therefore we are testing how the cosmological, astrophysical and intrinsic-mass *distributions* of coalescing DNS binaries impact the precision of parameter recovery.

The results of these analyses are shown in Fig. 3.6. We see that as $\sigma_{\rm NS}$ is increased the measurement precision of both the NS mass distribution and dark-energy EOS parameters decreases. We found a similar trend in our second-generation study. This makes sense, since if we have an intrinsically narrow NS mass distribution, then we have a good idea of what the intrinsic masses of the systems are and the range of candidate redshifts produced from a measured redshifted chirp mass will be narrow, improving the precision with which we can recover cosmological parameters.

A variation in the intrinsic $\mu_{\rm NS}$ (not shown) produces accuracies comparable to the reference accuracies. Hence, the impact of the intrinsic value of the NS mass-distribution mean on parameter accuracies is predominantly through the change to the expected detection rates i.e., a larger mean, on average, will lead to larger chirp masses, so that detections can be made from a larger volume (see Eq. (2.20)).

Increasing the value of the EOS parameter w_0 increases the precision with which we can recover w_0, w_a and $\mu_{\rm NS}$. As w_0 is increased, while the intrinsic w_a is fixed at zero, the recovered posteriors for these parameters are squeezed by the prior restrictions, $w_0 < -1/3$ and $(w_0 + w_a) < -1/3$. A larger intrinsic w_0 increases the horizon distance of detections, which permits greater sensitivity to the dark-energy EOS parameters. Furthermore, a narrowed range of cosmological parameters means that the range of candidate redshifts is also narrowed, such that the precision of the recovered NS mass-distribution mean (deduced from the redshifted chirp mass) improves. We also notice these effects when the intrinsic w_a is increased with the intrinsic w_0 fixed at the reference value. However, the effect is less pronounced in this case, since w_a is a first-order correction to w_0.

As the power-law index, α, is increased the average delay between the formation of the massive progenitor system and the merging of the final compact-system increases. This means that more systems formed at higher redshifts survive to merge at lower redshifts, and hence the

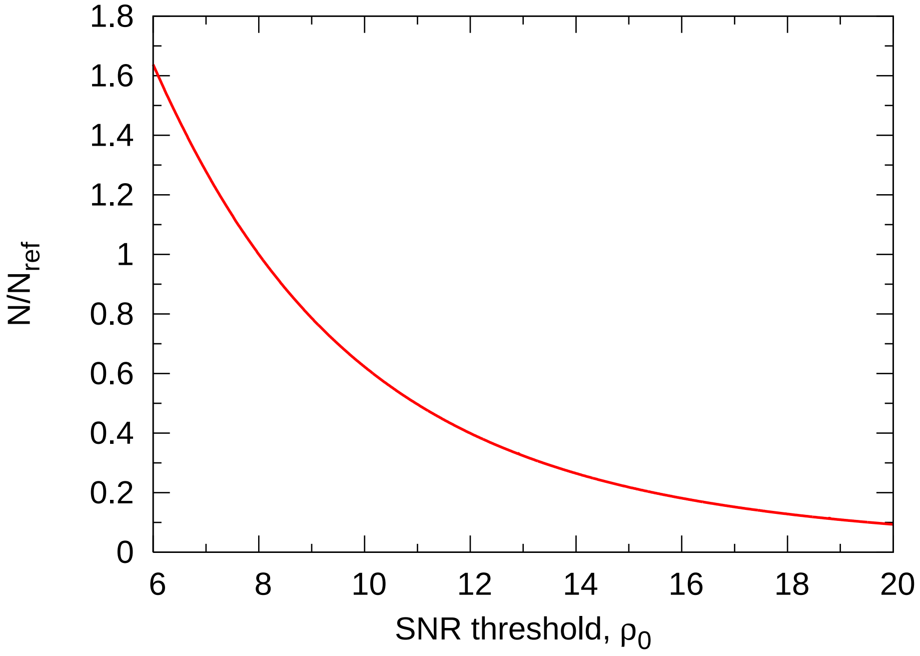

Figure 3.7: We show the variation of the expected detection rate as the SNR threshold, ρ_0, is raised. This can also be interpreted as *lowering* the characteristic distance reach of the network. Since ρ scales as $1/D_L$ (see Eq. (2.20)), and the difference between the luminosity distance and radial comoving distance becomes smaller at lower redshift, one would expect that at high enough values of ρ_0 the comoving detection volume (and hence detection rate) would scale as $1/\rho_0^3$. This is approximately valid for $\rho_0 \gtrsim 15$.

merger-rate density is boosted to higher values at lower redshifts. In addition, as α increases the merger-rate density tracks the underlying SFR-density to a lesser extent, so it becomes more difficult to extract the details of the SFR-density. Hence the $\beta_{1,2}$ distributions widen to reflect this reduced sensitivity to the underlying SFR-density.

When we keep the intrinsic values of β_1 and β_2 equal (not shown), we find that varying these by ± 0.4 around the reference value has a negligible impact on the measurement precision of the parameters. A higher common $\beta_{1,2}$ value leads to a larger expected detection rate, but this is a small effect.

Lowering the intrinsic value of β_1, with β_2 fixed, shifts the distribution of events to lower distances, and changes the shape of the underlying merger-rate density. This distribution is consistent with a wider range of α values than the reference distribution, since the sensitivity of the merger-rate density to α is reduced at lower redshifts. This causes the marginalised α-posterior distribution to widen. The same is true when the intrinsic value of β_2 is increased.

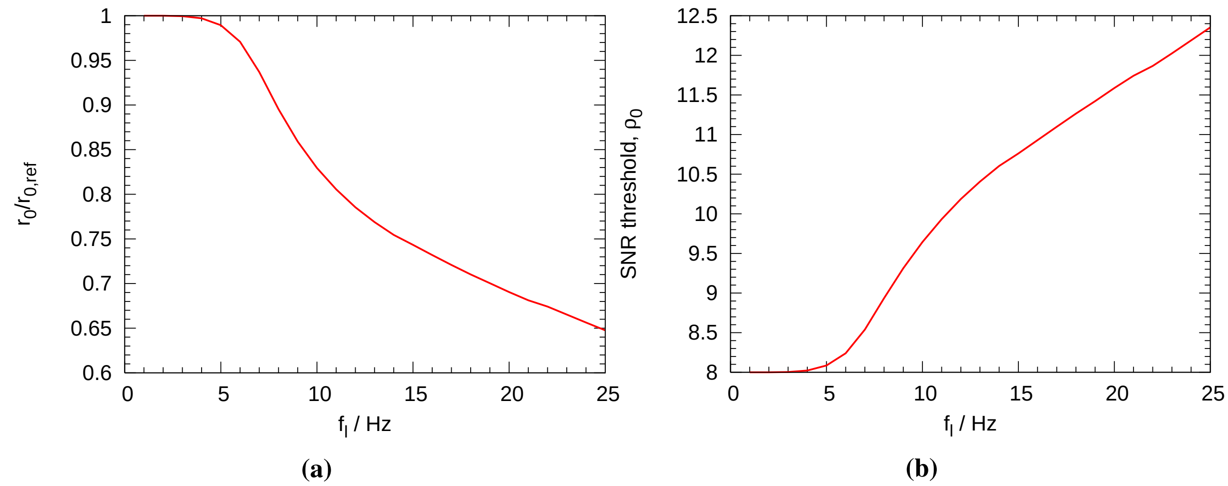

Figure 3.8: The reduction of the characteristic distance reach associated with raising the low-frequency cutoff, f_l, of 3$^{\rm rd}$-generation detectors. This can also be interpreted as raising the network SNR threshold. The figures were produced using the ET-D noise curve [92].

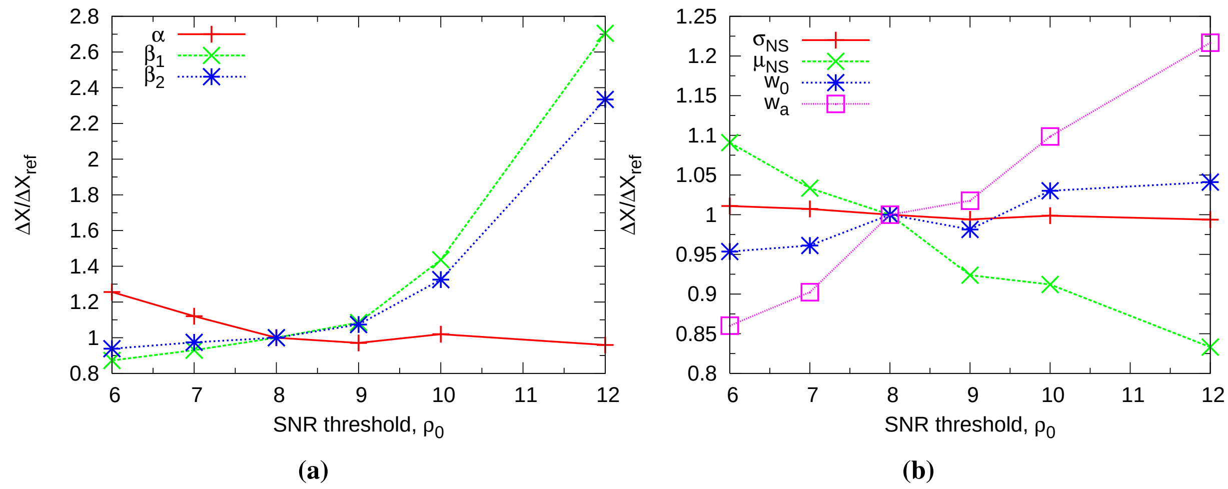

Figure 3.9: The variation of the parameter measurement precisions with the network SNR threshold. The left panel shows precisions, characterised by the width of the 68% confidence intervals, for the merger-rate density parameters, while the right panel shows precisions, characterised by the 95% confidence intervals used elsewhere, for all other parameters. We use the narrower confidence intervals for the merger-rate parameters to mitigate the effect of poor sampling in the low-α region which was observed in some AM-MCMC chains in this particular analysis. All catalogues contain the same numbers of events at each threshold value, which, as in the previous subsection, is 4500 to match the reference catalogue.

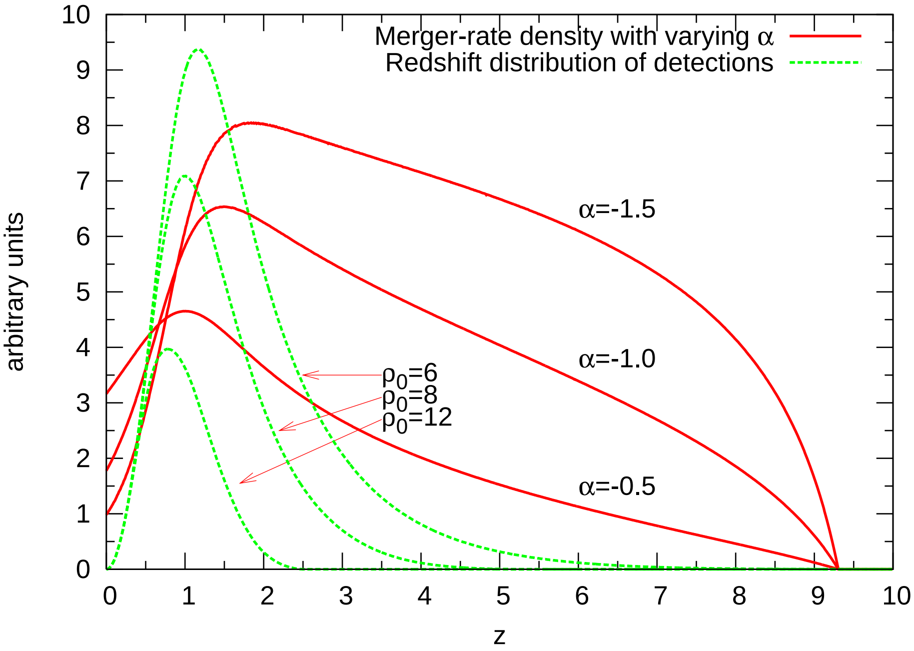

Figure 3.10: We show the redshift distribution of the DNS merger-rate density for various choices of the power-law index of the delay-time distribution, α (all other parameters are fixed at their reference values). The merger-rate density is relatively featureless beyond $z \sim 2.5$, making it difficult for our analysis (which is insensitive to linear scalings of the merger-rate density) to discriminate between values of α in this range. Overlaid on this figure we show the redshift distribution of detections for various SNR thresholds.

3.6.6 Varying the SNR threshold

We also generated catalogues for different values of the SNR threshold. Multiple catalogues were analysed for each SNR threshold, but once again the number of events was fixed at 4500 to match the reference catalogue (see Fig. 3.7). An increase in the SNR threshold is equivalent to the characteristic distance reach of the detectors decreasing. Hence we would expect the sensitivity of the data to varying dark-energy EOS parameters, which have a greater influence at larger redshifts, to be reduced. A reduced characteristic reach would also result from a larger low-frequency cutoff, f_l, in the detector's noise spectrum. In the recent mock ET data challenge, Ref. [380] found that confusion between two or more signals rarely affected the analysis performance when $f_l = 25$ Hz. Standard algorithms currently employed for LIGO-Virgo analyses cannot handle templates longer than a few minutes; however multiband filter methods are being developed which will allow f_l to be pushed below 25 Hz. In Fig. 3.8 one can see that with $f_l = 25$ Hz, the effective SNR threshold is raised from the reference value of 8 (with $f_l = 1$ Hz) to ~ 12.4.

From Fig. 3.9(a), we see that as the SNR threshold is increased, with the number of catalogued events fixed, the accuracies of β_1 and β_2 degrade sharply. At higher SNR thresholds (or, equivalently, at lower distance reaches) the sensitivity of the merger-rate density to varying $\beta_{1,2}$ is reduced; hence the wider posterior distributions. The measurement precision of α increases slightly as the SNR threshold is increased from $6-12$. One might expect α to show the same trend as β_1 and β_2, since an increasing SNR threshold pushes the events to lower redshifts where the sensitivity of the merger-rate density to α is reduced. However, we see in Fig. 3.10 that the merger-rate density, for various choices of α (but all other parameters fixed), is relatively featureless beyond ~ 2.5. The distribution of the merger-rate density in the redshift window of $\sim 2.5-7$ could be approximately linearly scaled to satisfy a large range of α.[21] Therefore, given that our likelihood statistic is insensitive to linear scalings of the merger-rate density [see Eq. (3.18)], the significant number of high-redshift detections in a $\rho_0 = 6$ catalogue will widen the α posterior distribution, while most α-information is found in the redshift window $\sim 1-2$, where the merger-rate density has more features.

In Fig. 3.9(b), we see that the measurement accuracy of w_0 and w_a is slightly reduced for higher SNR thresholds; this is a small effect, and is expected with a catalogue shifted to lower redshifts, where distances are less sensitive to varying dark-energy EOS parameters. The accuracy of w_0 only varies by $\sim \pm 5\%$, since we remain sensitive to detections at tens of Gpcs even with an SNR threshold of 12. However, w_a shows a stronger variation since it is a higher

---

[21] The same argument did not apply when $\beta_{1,2}$ was varied, since this not only shifted the distribution to lower redshifts but altered the *shape* of the merger-rate density in a way that could not be equated with a linear scaling in any redshift window.

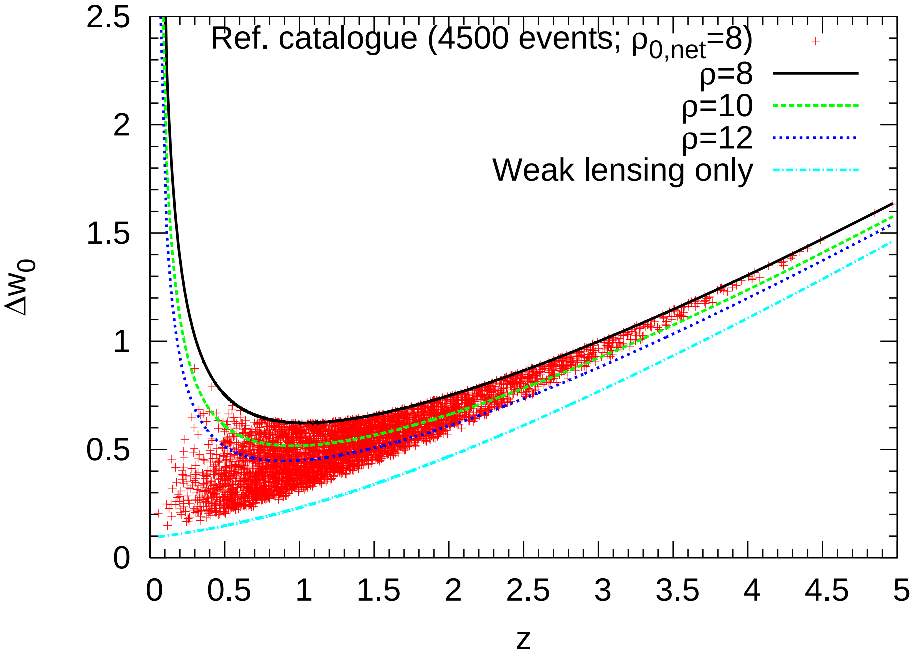

Figure 3.11: The redshift dependence of the sensitivity of the luminosity distance to w_0. This parameter has a very weak intrinsic impact on D_L at low redshifts, whilst distance errors from instrumental noise and weak-lensing dominate at higher redshifts. This results in a redshift "sweet-spot", where these effects are minimised for lines of constant SNR. We also plot the individual Δw_0 values calculated for the reference catalogue events.

order correction to the EOS parameter, and distances become sensitive to this parameter at higher redshifts than they do to w_0. We also see that the measurement precision of $\mu_{\rm NS}$ and $\sigma_{\rm NS}$ is increased slightly as we move to larger SNR thresholds. This small effect is probably due to the fact that a lower redshift range in the data catalogue will mean that the redshifted chirp mass is closer to the intrinsic chirp mass.

Although this suggests that a greater distance reach will improve the precision of cosmological parameter recovery, we have so far ignored distance errors. In fact, instrumental and weak-lensing errors impart an interesting redshift evolution to the w_0-sensitivity, which we approximate as [385]

$$\Delta w(z) \sim \left|\frac{\partial w_0}{\partial D_L}\right| \times D_L \times \sqrt{(1/\rho)^2 + (0.05z)^2}. \tag{3.21}$$

In Fig. 3.11 we see that the sensitivity of the luminosity distance to the cosmological parameter w_0 is greatest at $z \sim 1$, since w_0 has a very weak intrinsic impact on D_L at low redshifts and distance errors dominate at higher redshifts. Increasing a detector's distance reach will raise the fraction of high-redshift catalogued events. We calculate the effective measurement precision of w_0 from our reference catalogue by adding the Δw_0 values from each event in quadrature i.e. $1/\Delta w_{0,\rm eff} = \sqrt{\sum(1/\Delta w_{0,i})^2}$. This is repeated for various lower and higher SNR threshold

Table 3.6: The events from catalogues with different SNR thresholds are used to compute an effective w_0 precision, by adding the Δw_0 values of each event in quadrature. This analysis is performed for catalogues with the same number of events, and for catalogues with the numbers of events scaled to match the expected detection rate for each SNR threshold.

$\rho_{0,\mathrm{net}}$	$f = N/N_{\mathrm{ref}}$	$\Delta w_{0,\mathrm{eff}}/10^{-3}$	
		$(N_o = N_{\mathrm{ref}})$	$(N_o = f \times N_{\mathrm{ref}})$
6	1.64	8.08	6.33
8	1.00	6.82	6.82
12	0.399	5.33	8.35
20	0.0936	4.00	13.1
30	0.0271	3.38	20.6

values. We perform these calculations for catalogues containing the same number of events (4500 to match the reference catalogue), and for catalogues with the number of events scaled by the ratio of the expected detection rate for each SNR threshold to the reference threshold (which in this analysis is 8). The results are shown in Table 3.6, where we see that for catalogues with the same number of events, lowering the SNR threshold actually worsens the precision of w_0 recovery since the distribution of events is weighted to higher redshifts, where distance errors degrade the precision. Increasing the SNR threshold reduces the number of events at high redshift and hence mitigates the degradation of precision due to distance errors (see Fig. 3.11). However, this effect slows down with increasing SNR threshold. For catalogues with numbers of events scaled to match the expected detection rate for each SNR threshold, we see that the increased number of events associated with a lower SNR threshold is enough to compensate for degradation of precision from higher redshift events. However this loss of precision means that lowering the SNR threshold does not lead to the $1/\sqrt{N}$, or $1/\rho_0^{3/2}$ improvement in parameter measurement precision which one would naively expect.

Finally we address the issue of having assumed that Earth motion does not modulate the antenna patterns of the detectors. The time spent "in-band" by an inspiraling-event scales as [380]

$$\tau \sim 5.4 \left(\frac{\mathcal{M}_z}{1.22 M_\odot} \right)^{-5/3} f_l^{-8/3} \quad \text{days}. \tag{3.22}$$

Hence, a detector with a low-frequency cutoff of 1 Hz (as we have assumed) could have events in band for as long as ~ 5 days. In this case, a correct treatment of the antenna pattern modulation would be needed. However, if we increase f_l to ~ 8 Hz, then the maximum time spent in-band is less than 30 minutes, and ignoring the antenna pattern modulation is reasonable. In Fig. 3.8 we see that a low-frequency cutoff of 8 Hz is equivalent to raising the SNR threshold to ~ 9, and from Fig. 3.9 we see that the precision of parameter recovery is within $\sim \pm 10\%$ of the reference precisions for an SNR threshold of 9. Therefore our approximate treatment of the network antenna patterns would seem reasonable.

3.7 Summary

We have built on the previous chapter, which explored the capabilities of an advanced (i.e. second-generation) GW-interferometer network to constrain aspects of the NS mass distribution in DNS systems, as well as the Hubble constant. The technique we employed used only information obtained via analysis of the GWs detected in such a network. In this chapter we extended the analysis to a possible third-generation network, consisting of the proposed Einstein Telescope, and complemented by third-generation right-angled interferometers at LIGO Livingston and LIGO-India. The sources of interest in this study are inspiraling double NS systems, which could be observed at rates of ~ 40 yr^{-1} by advanced detectors [147] and rates of $\mathcal{O}(10^5 - 10^6)$ yr^{-1} by a third-generation network [344, 346, 380].

We used a Bayesian theoretical framework to assess the capability of a third-generation network to measure cosmological and astrophysical parameters. We performed 7-dimensional adaptive MCMC analysis on the catalogues of detections, using reference parameters $H_0 = 70.4$ kms^{-1}Mpc^{-1}, $\Omega_{m,0} = 0.2726$, $\Omega_{k,0} = -0.0006$, $w_0 = -1$, $w_a = 0$, $\mu_{\rm NS} = 1.35 M_\odot$ and $\sigma_{\rm NS} = 0.06 M_\odot$. Keeping H_0, $\Omega_{m,0}$ and $\Omega_{\Lambda,0}$ fixed, we found that the measurement precisions of the dark-energy EOS parameters possible with a 10^5-event catalogue were of the same order of magnitude as forecasted constraints from future CMB+BAO+SNIa measurements [347]. Furthermore the power-law index of the merger delay-time distribution, α, and the parameters of the underlying star-formation-rate (SFR) density were constrained to within $\sim 10\%$. Accounting for measurement errors degraded precisions by a factor of $\lesssim 2$, while increasing the network SNR threshold required for detection from 8 to 9 (which is equivalent to considering only the ~ 30 minute section of inspiral above 8 Hz) changed the precisions by only $\sim 10\%$.

We also investigated how the precision of parameter recovery scaled with the values of the intrinsic parameters themselves, keeping the number of detected events fixed to factor out pure number-of-event effects. Varying the intrinsic $\sigma_{\rm NS}$ showed a linear scaling of parameter precision, with narrower intrinsic NS mass distributions favouring tighter parameter constraints. The precisions of the merger-rate density parameters did not appear to be affected in this case. Increasing the intrinsic w_0 and w_a had the effect of increasing their measurement precision, as well as that of $\mu_{\rm NS}$. This was probably due to the fact that larger w_0 and w_a give detections out to greater distances, where the sensitivity to these parameters is higher. Tighter cosmological constraints implies narrower candidate redshift distributions from the catalogued distances, which improves $\mu_{\rm NS}$ precision. Increasing the intrinsic value of α meant that the merger-rate density tracked the underlying SFR density to a lesser extent and hence worsened the precision of SFR-density parameter recovery. As we changed the shape of the underlying SFR density to favour closer detections, the measurement precision of α worsened, since the sensitivity of the merger-rate density to α is reduced at lower redshifts.

Finally, we varied the criterion for a network detection, which we denoted by a threshold value of the network SNR. This could also be interpreted as varying the characteristic distance reach of the network, which, in turn, could be caused by varying the detector's low-frequency cutoff. Varying the SNR threshold between $6 - 12$ caused a slight decrease in w_0 and w_a precision, as catalogues with lower distance events will be less sensitive to these cosmological parameters. However, catalogues with, on average, closer events will provide better NS mass-distribution parameter precision, since the redshifted chirp mass will be less offset with respect to the intrinsic chirp mass. Increasing the SNR threshold, and hence decreasing the characteristic distance reach of the network, caused a significant decrease in SFR-density parameter precision, since the merger-rate density is less sensitive to the SFR-density parameters at lower redshift.

While the sensitivity of distances to the dark-energy EOS will obviously be intrinsically weak at low redshifts, distance-measurement errors begin to dominate at higher redshifts. We found that for a fixed number of events in a catalogue, lowering the SNR threshold actually worsened the precision of w_0 recovery since events are weighted to higher redshifts, where distance errors degrade the measurement precision. The larger expected detection rate associated with lower SNR thresholds is enough to reverse this effect, but means that lowering the SNR threshold (or increasing the network's distance reach) does not lead to the great improvement in parameter measurement precision which one would naively expect.

We have not considered association of GW detections with an EM counterpart, either through precise SGRB [346, 347] or host-galaxy association. The latter technique may only be possible with $\sim 0.01\%$ of detectable GW events [348]. However, as shown in the previous chapter, our techniques are well complemented by precision redshift information.

This chapter completes our proof-of-principle study of this GW-only cosmographic technique. We have shown the significant potential for a third-generation network including the Einstein Telescope to place interesting constraints on: (i) the NS mass distributions in DNS systems; (ii) the dark-energy EOS; (iii) the average delay between the formation of the DNS-system progenitors and the final merger; (iv) the underlying SFR density in the Universe. Over the following decade tighter constraints will be derived for the NS mass distribution, delay-time distribution of DNS systems, and the SFR density, which can be readily incorporated within this technique. Unshackling GW cosmography from its reliance on EM counterparts will be an important step in establishing DNS systems as physical distance indicators, and contribute to GW-analysis becoming a precision astrophysical tool.

3.A Star-formation rate density, $d\rho_*/dt$

For a comprehensive review of the cosmic star-formation history, see Ref. [386] and references therein. High-redshift star-formation rate estimates are obtained via measurements of UV luminosity functions, which tell us how many galaxies emit light in the UV-band in a given epoch. For all but the oldest galaxies, UV-continuum emission has been shown to be a good tracer of the SFR since it is dominated by short-lived massive stars (Ref. [367, 387] and references therein). Dust-extinction of UV light can be investigated, and hence corrected for, via the measurement of the UV-continuum slope, which has been shown to be well-correlated with dust extinction in the local Universe (Ref. [367] and references therein).

A systematic study of the high-redshift SFR density was undertaken by Ref. [369] using *Hubble Space Telescope* data. Correcting their UV luminosity density calculations for dust extinction, and converting this to an estimate of the SFR density, yielded significant evolution of the SFR density between $0 < z \lesssim 10$. The SFR density is shown to rise out to $z \sim 2 - 4$, followed by a decrease out to $z \sim 8 - 10$ (e.g., Ref. [368, 369]).

Given that only a handful of techniques exist to probe the high-redshift star-formation history, we will have to wait until further studies are carried out, or new techniques are developed, to complement the analyses in Ref. [368, 369]. In our present study, we are only interested in a sensible model of the redshift evolution of the SFR density, which we can parametrise for a Bayesian inference analysis. Several of the studies (e.g., Ref. [360, 361, 388]) mentioned in Sec. 3.3.2, as well as several other studies which attempt to fit GRB densities to delayed SFR-density models (e.g., Ref. [389]), employed the SF2 model of Ref. [366]. Of the three models considered in the aforementioned paper, the SF2 model attempts to factor in the uncertainties in the incompleteness of data sets and the amount of dust extinction at early epochs. As such, the SFR density remains roughly constant at $z \gtrsim 2$.

Obviously, if studies in the following decade confirm the SFR-density trends found in Ref. [368, 369] we would not attempt to fit any ET data with the SF2 model. This model would need to be updated with a more realistic parametrisation. But for now, we adopt the SF2 model as a useful ansatz.

Part III

Gravitational Wave Detection Via Pulsar Timing

To myself I seem to have been only like a boy playing on the sea-shore, [. . .] whilst the great ocean of truth lay all undiscovered before me.

Sir Isaac Newton

Somewhere, something incredible is waiting to be known.

Carl Sagan

4

Anisotropy In The GW Background

Abstract

The dominant signal in the nanohertz GW band will likely be the incoherent superposition of inspiral signals from many SMBH binaries, overlapping in frequency to produce a stochastic GW background (GWB). Deviations of the background energy-density from isotropy may be indicative of local hotspots or continuous anisotropy in the angular distribution of GW power. We present the first Bayesian pulsar-timing pipeline capable of investigating the angular structure of such a background. The overlap of pulsar "*antenna patterns*" leads to a distinctive angular signature in the cross-correlation of TOA deviations induced by a GWB. For an isotropic background this signature is the *Hellings and Downs curve*, and depends only on the angular separation of the pulsars. If the background is anisotropic, the signature is different, but predictable, and also depends on the absolute position of the pulsars. By simulating data sets containing GWBs with various anisotropic configurations, we have explored the prospects for constraining anisotropy using near future data.

This chapter is based on:
Searching for anisotropic gravitational-wave backgrounds using PTAs
Stephen R. Taylor and Jonathan R. Gair
Phys. Rev. D **88**, 084001 (2013), arXiv:1306.5395

4.1 Introduction

If a GWB is produced by processes occurring in the early Universe, or a superposition of high-redshift signals, then one would expect the resulting background to be reasonably isotropic. However, if the background signal is dominated by close, bright sources (such as SMBH binaries) over the entire PTA-sensitivity band [240], or even just at high frequencies [241], the breakdown of stochasticity and resulting deviation from isotropy motivates a more general characterisation of the angular distribution of GW-power on the sky.

As discussed in Sec. 1.3.3, the EPTA, NANOGrav, and PPTA have all performed searches for GW signals in the nanohertz band, targeting either an *isotropic* stochastic GWB, or single resolvable sources. The stochastic GWB searches use techniques which rely on the fact that a GWB is bathing *all* pulsars in our array, and hence induces correlated TOA-deviations between pulsars which are widely separated on the sky. This provides leverage against noise processes which may have similar spectral properties to the GWB, but which are uncorrelated. In fact, for an isotropic GWB (with GR polarisation modes) this cross-correlation has a unique, distinctive angular signature dependant only on the angular-separation of the pulsars: this is the famous Hellings and Downs curve [216].

Recently, Ref. [390] proposed a cross-correlation statistic aimed at targeting the brightest sources in each frequency-bin to account for anisotropy in the signal power. This statistic modifies the existing isotropic correlation techniques to account for finiteness of the source population. Essentially, instead of integrating the directional correlation function over the sky to produce the Hellings and Downs curve, this modified statistic sums the cross-correlation function over the brightest sources to infer their sky-positions.

Alternatively, we can extend the techniques of Ref. [391, 392] (developed in the context of ground-based detectors) to PTAs. By decomposing the angular power distribution in terms of spherical harmonics, Ref. [393, 394] have generalised the existing isotropic cross-correlation technique to account for arbitrary levels of anisotropy in a GWB. Isotropy is represented by the monopole solution. For higher multipoles, the cross-correlation is no longer a simple function of pulsar angular separation, but rather depends on the position of each pulsar relative to the orientation of the background anisotropy. Thus the concept of a one-parameter relationship to describe correlations induced by a GWB is no longer appropriate, and the relationship will instead become PTA- and GWB-specific, depending on the observed pulsars and the angular distribution of background power.

In this chapter we develop and test the first anisotropic Bayesian search-pipeline for the characterisation of a GWB using PTAs, employing the previously mentioned generalised spherical-harmonic decomposition of the cross-correlation. We have developed a suite of new plugins [395] for the popular pulsar-timing analysis package TEMPO2 [195–197], which can be used to inject GWBs with any user-defined anisotropy. For this first investigation we inject backgrounds composed of typically 10^4 sources, with sources placed according to various tested angular distributions. As such, we are investigating continuous anisotropy in the distribution of source-positions, rather than anisotropy through finiteness of the background, which we defer to future work.

This chapter is organised as follows. In Section 4.2 we perform some theoretical estimates of the expected level of anisotropy in a background composed of a superposition of many GW-signals, where the anisotropy either derives from varying source brightness or sparseness of the source-population. In Section 4.3 we review the theory of time- and angular-correlations of GWB-induced timing-residuals in pulsar signals, and outline a generalised formalism for modelling correlations in anisotropic backgrounds. The standard Bayesian time-domain formalism for stochastic GWB searches is reviewed in Sec. 4.4. A pipeline for producing simulated pulsar datasets containing an anisotropic GWB signal is described in Sec. 4.5, followed by the results of Bayesian parameter-estimation and evidence-evaluation on these simulated datasets in Sec. 4.6, with a summary in Sec. 4.7.

4.2 The expected level of anisotropy

We wish to motivate a Bayesian search-pipeline which is generalised to arbitrary levels of anisotropy in the energy-density of the GW background. We take a realistic population of SMBH binaries, generated by grafting baryonic physics onto the dark-matter haloes of a Millennium Simulation realisation, and extract those systems with observed GW frequencies which fall within PTA observation-frequencies [238]. These are typically massive and close systems ($z < 2$). A typical catalogue contains $\sim 2 \times 10^4$ sources, each with associated chirp masses, $\mathcal{M}$, observed GW-frequencies, f, and redshifts, z. Most importantly, the source positions are distributed isotropically on the sky. Hence, with this many sources making up our background we would expect any anisotropy to derive from varying source brightnesses. The radiated GW-power of each binary in the source rest-frame is estimated using the quadrupole formula [102],

$$\frac{dE}{dt} = \frac{32}{5}\left[\pi\mathcal{M}f(1+z)\right]^{10/3}. \tag{4.1}$$

The radiated energy flux in the observer frame is then given by,

$$\mathcal{F} = \frac{dE}{dt} \times \frac{1}{4\pi D_L(z)^2}, \tag{4.2}$$

where D_L is the source luminosity distance. The energy-density in GWs, ρ, received from each source is then simply given by $\mathcal{F}/c$.

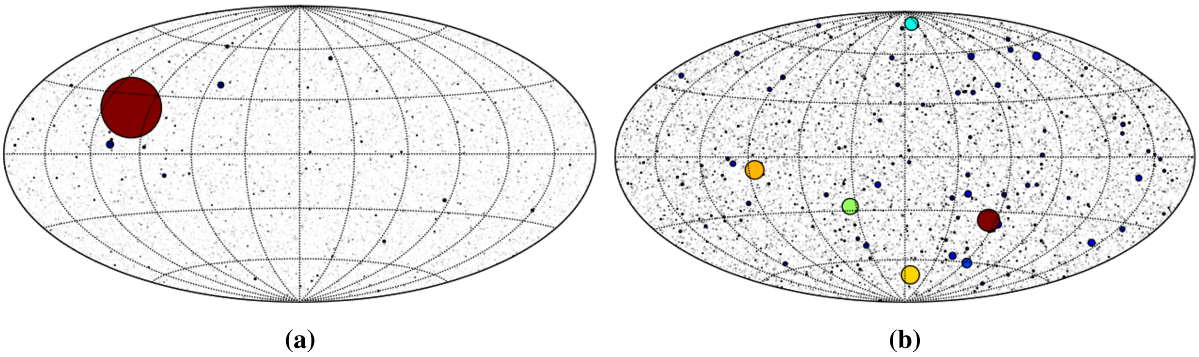
(a) **(b)**

Figure 4.1: Skymaps of GW source-populations generated by evolving a population of SMBH binary systems. There are $\sim 2\times 10^4$ systems in each catalogue, which are typically massive ($10^7 - 10^{10} M_\odot$) and close ($z < 2$). The relative size and colour of points within each skymap is indicative of the GW energy-flux from each system, where larger and redder denotes a bright source. The GW signal from the first dataset in (a) is clearly dominated by one very bright source. In the second dataset (b) we have several bright sources, however no outliers as in the first dataset.

We now perform a spherical-harmonic decomposition of the energy density from a GW-population, for the purposes of evaluating the angular power-spectrum. Thus,

$$\rho(\hat{\Omega}) = \sum_{l=0}^{\infty}\sum_{m=-l}^{l} c_{lm} Y_{lm}(\hat{\Omega}). \tag{4.3}$$

where $Y_{lm}(\hat{\Omega})$ are spherical-harmonic functions evaluated at the source positions, $\hat{\Omega}$. We then extract the anisotropy coefficients,

$$c_{lm} = \int_{S^2} d\hat{\Omega}\ \rho(\hat{\Omega}) Y_{lm}(\hat{\Omega}). \tag{4.4}$$

We define the observed angular power-spectrum as $C_l = \sum_m |c_{lm}|^2/(2l+1)$. Since we are dealing with a population of point sources, the energy-density distribution is just a sequence of delta-functions at the source positions, such that the spherical-harmonic decomposition becomes

$$c_{lm} = \sum_{i=1}^{N} \rho_i Y_{lm}(\hat{\Omega}_i), \tag{4.5}$$

which is just a summation over the spherical-harmonic functions evaluated at the N source-positions, and weighted by the GW energy-density of each source.

We analyse two catalogues, whose skymaps are shown in Fig. 4.1. The first dataset clearly includes a source which swamps the signal, while the second dataset is dominated by several bright sources. Figure 4.2a shows the angular power-spectrum of the first dataset, evaluated up to $l = 50$. We see that the single brightest source swamps the power at all l, such that we are almost trivially satisfying Unsöld's Theorem by having $[C_l/C_0] = 1$ at each l. If we remove

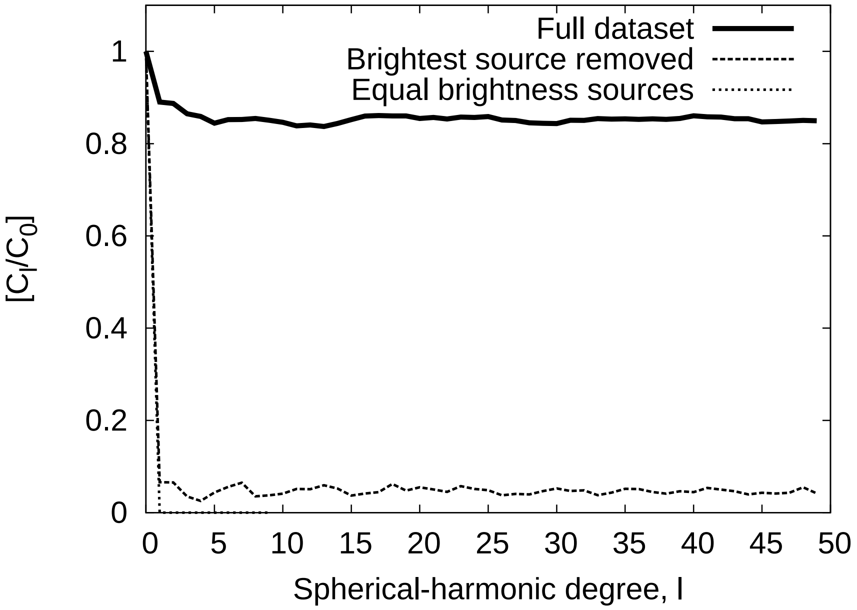

(a)

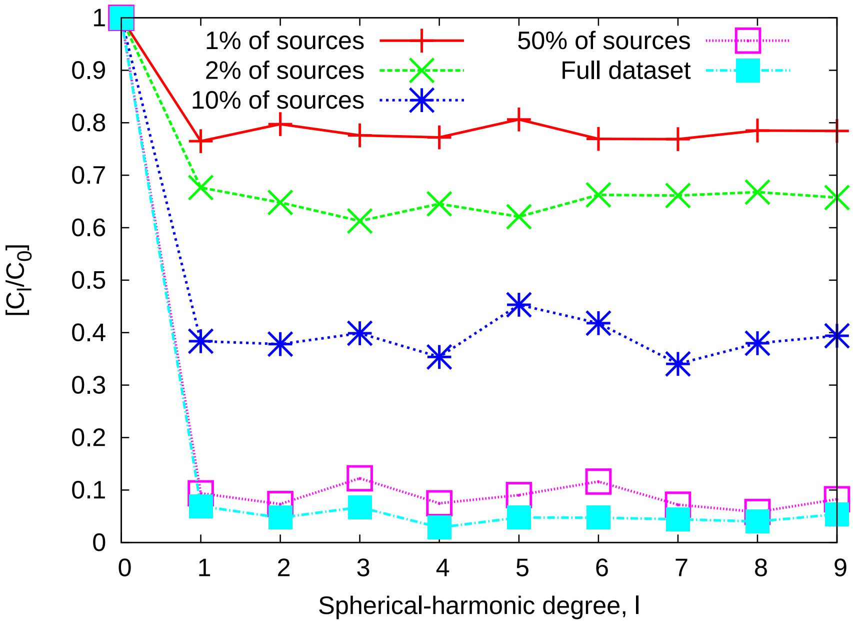

(b)

Figure 4.2: We perform a spherical-harmonic decomposition of the distribution of the GW energy density on the sky resulting from a population of inspiraling SMBH binary systems, and compute the angular power spectrum, C_l. In (a) the influence of one very bright source in Fig. 4.1a clearly swamps all other influences. Removing the brightest source causes the anisotropic power to drop to less than 0.1 relative to the monopole (isotropic). Even this level of anisotropy is most likely due to the second-brightest sources, since if we assume equal brightness sources the $l \neq 0$ power drops to $\sim 10^{-5}$. In (b) we analyse Fig. 4.1b. The full dataset is predominantly isotropic, however if we simulate source sparseness or intrinsic anisotropy by analysing sub-populations, then the level of anisotropy can be quite high.

the brightest source, then we get a power-spectrum in which the power is predominantly in the monopole (isotropic), with typically less than 10% of the isotropic power in the other l values. This small level of power in other l values most likely derives from the few next-brightest sources, since if we fix all source brightness to the same value we obtain a power fraction of $\sim 10^{-5}$ in $l \neq 0$ values, which is what we expect when analysing a large population of equal-brightness sources which have been isotropically distributed on the sky.

The second dataset has several very bright sources, but no outliers like in the first dataset. When analysed, most of the power lies in the monopole, with typically less than 10% of the isotropic power in modes with $l \neq 0$. However, if we simulate source sparseness, or some form of intrinsic anisotropy through source-clustering, then the potential level of anisotropy is much higher. In Figure 4.2b the dataset has been shuffled and split into sub-populations. We compute the angular power-spectrum of each sub-population, and display the 95% upper limit of the power in each l derived from the ensemble of sub-populations. With a very sparse population the power in the modes with $l \neq 0$ could conceivably be $\lesssim 80\%$ of the isotropic power. This anisotropic power fraction tends to the value for the full dataset as we include more sources in the sub-populations.

Thus, if we have several very bright sources dominating our background, or some form of intrinsic anisotropy through source-clustering, then the level of anisotropy in the sky-distribution of GW energy-density could conceivably be high. In the following, we simulate anisotropic backgrounds through a continuous anisotropy in GW source-positions, and test the robustness of a Bayesian anisotropic search-pipeline.

4.3 Correlations induced by a GWB

In this section we provide a brief overview of the correlations found in pulsar timing-residuals which are induced by a stochastic GWB. We reiterate some of the formalism of Ref. [393] for ease of reference.

4.3.1 Cross-correlating the timing-residuals

As discussed in Sec. 1.3.3, the perturbation to the space-time metric along the Earth-pulsar line-of-sight induced by the passage of a GW causes a change in the perceived rotational-frequency of the pulsar [209–212]. The fractional frequency-shift of a signal from a pulsar in the direction of unit vector $\hat{p}$, induced by the passage of a *single* GW propagating in the direction of $\hat{\Omega}$ is [213, 214],

$$z(t,\hat{\Omega}) = \frac{1}{2}\frac{\hat{p}^a\hat{p}^b}{1+\hat{\Omega}\cdot\hat{p}}\Delta h_{ab}(t,\hat{\Omega}), \tag{4.6}$$

where $\Delta h_{ab} \equiv h_{ab}(t_e, \hat{\Omega}) - h_{ab}(t_p, \hat{\Omega})$, is the difference in the metric perturbation at the SSB, $h_{ab}(t_e, \hat{\Omega})$, and at the pulsar, $h_{ab}(t_p, \hat{\Omega})$.

This frequency-shift is integrated over time to give the induced timing residuals, which describe the perturbation to the TOA of pulses from a given pulsar,

$$r(t) \equiv \int_0^t z(t')dt'. \tag{4.7}$$

In the TT-gauge, the GW-tensor can be expressed as in Eq. (2.4), such that a plane-wave expansion of the polarisation amplitudes leads to the metric perturbation at a position $\vec{x}$ having the form,

$$h_{ab}(t, \vec{x}) \equiv \sum_{A=+,\times} \int_{-\infty}^{\infty} df \int_{S^2} d\hat{\Omega}\ h_A(f, \hat{\Omega}) e^{2\pi i f(t - \hat{\Omega}\cdot\vec{x})} e^A_{ab}(\hat{\Omega}), \tag{4.8}$$

where $e^{+,\times}_{ab}(\hat{\Omega})$ are the polarisation basis-tensors, defined in terms of orthonormal basis vectors around $\hat{\Omega}$,

$$e^+_{ab}(\hat{\Omega}) = \hat{m}_a\hat{m}_b - \hat{n}_a\hat{n}_b, \quad e^\times_{ab}(\hat{\Omega}) = \hat{m}_a\hat{n}_b + \hat{n}_a\hat{m}_b, \tag{4.9}$$

where $\hat{m} = (\hat{\Omega} \times \hat{q})/|\hat{\Omega} \times \hat{q}|$, $\hat{n} = (\hat{\Omega} \times \hat{m})$, and q is a polarisation axis, which, because we have a background composed of independent sources, we are free to fix as $[0, 0, 1]$. If the direction of GW-propagation is $\hat{\Omega} = [\sin\theta\cos\phi, \sin\theta\sin\phi, \cos\theta]$, the polarisation basis vectors are,

$$\hat{m} = [\sin\phi, -\cos\phi, 0], \quad \hat{n} = [\cos\theta\cos\phi, \cos\theta\sin\phi, -\sin\theta]. \tag{4.10}$$

We choose a co-ordinate system centred at the SSB, with the pulsar some distance L away (such that $t_p = t_e - L = t - L$, $\hat{x}_e = 0$, and $\hat{x}_p = L\hat{p}$). Integrating the $\Delta h_{ab}(t, \hat{\Omega})$ term in Eq. (4.6) over all positions of sources constituting the stochastic GWB gives,

$$\Delta h_{ab}(t) = \sum_{A=+,\times} \int_{-\infty}^{\infty} df \int_{S^2} d\hat{\Omega}\ e^A_{ab}(\hat{\Omega}) h_A(f, \hat{\Omega}) e^{2\pi i f t} \times \left[1 - e^{-2\pi i f L(1+\hat{\Omega}\cdot\hat{p})}\right]. \tag{4.11}$$

where $h_A(f, \hat{\Omega})$ are complex random fields ($h^*_A(f, \hat{\Omega}) = h_A(-f, \hat{\Omega})$) whose moments define the statistical properties of the background.

The redshift of a signal induced by a stochastic GWB can now be written as,

$$z(t) = \sum_{A=+,\times} \int_{-\infty}^{\infty} df \int_{S^2} d\hat{\Omega}\ F^A(\hat{\Omega}) h_A(f, \hat{\Omega}) e^{2\pi i f t} \times \left[1 - e^{-2\pi i f L(1+\hat{\Omega}\cdot\hat{p})}\right], \tag{4.12}$$

where the "*antenna pattern*" for each polarisation in the PTA formalism is,

$$F^A(\hat{\Omega}) \equiv \frac{1}{2} \frac{\hat{p}^a\hat{p}^b}{1 + \hat{\Omega}\cdot\hat{p}} e^A_{ab}(\hat{\Omega}), \tag{4.13}$$

corresponding to,

$$F^+(\hat{\Omega}) = \frac{1}{2} \frac{(\hat{m}\cdot\hat{p})^2 - (\hat{n}\cdot\hat{p})^2}{1 + \hat{\Omega}\cdot\hat{p}}, \quad F^\times(\hat{\Omega}) = \frac{(\hat{m}\cdot\hat{p})(\hat{n}\cdot\hat{p})}{1 + \hat{\Omega}\cdot\hat{p}}. \tag{4.14}$$

Now, explicitly evaluating Eq. (4.7) we find,

$$r(t) = \frac{i}{2\pi}\sum_{A=+,\times}\int_{-\infty}^{\infty} df \int_{S^2} d\hat{\Omega}\; F^A(\hat{\Omega})\frac{h_A(f,\hat{\Omega})}{f} \times \left[1 - e^{-2\pi i f L(1+\hat{\Omega}\cdot\hat{p})}\right]\left[1 - e^{2\pi i f t}\right]. \quad (4.15)$$

We now compute the correlation between the timing-residual at time t in pulsar a with timing-residual at time $(t+\tau)$ in pulsar b (removing the unobservable constant offset in $r(t)$)[1],

$$\begin{aligned}\langle r_a^*(t) r_b(t+\tau)\rangle = &\\ &\frac{1}{4\pi^2}\left[\sum_A\sum_{A'}\int_{-\infty}^{\infty} df \int_{-\infty}^{\infty} df' \int_{S^2} d\hat{\Omega}\int_{S^2} d\hat{\Omega}'\; F_a^A(\hat{\Omega})F_b^{A'}(\hat{\Omega}')\frac{\langle h_A^*(f,\hat{\Omega})h_{A'}(f',\hat{\Omega}')\rangle}{ff'}\right.\\ &\left.\times\left(1 - e^{2\pi i f L_a(1+\hat{\Omega}\cdot\hat{p}_a)}\right)\left(1 - e^{-2\pi i f' L_b(1+\hat{\Omega}'\cdot\hat{p}_b)}\right)e^{2\pi i(f't+f'\tau-ft)}\right]. \quad (4.16)\end{aligned}$$

For a stationary, unpolarised, Gaussian stochastic background, the expectation value of the Fourier amplitudes, $h_A(f,\hat{\Omega})$, is given by [396, 397],

$$\langle h_A^*(f,\hat{\Omega})h_{A'}(f',\hat{\Omega}')\rangle = \delta_{AA'}\delta(f-f')\delta^2(\hat{\Omega},\hat{\Omega}')\mathcal{P}(f,\hat{\Omega}) \quad (4.17)$$

where $\mathcal{P}(f,\hat{\Omega})$ describes the spectral and angular properties of the GWB. In this analysis we only consider backgrounds whose angular properties are frequency-independent, thus $\mathcal{P}(f,\hat{\Omega}) = H(f)P(\hat{\Omega})$.

So,

$$\begin{aligned}\langle r_a^*(t) r_b(t+\tau)\rangle =& \frac{1}{2\pi^2}\left[\sum_A\int_0^{\infty} df \int_{S^2} d\hat{\Omega}\; P(\hat{\Omega})F_a^A(\hat{\Omega})F_b^A(\hat{\Omega})\frac{H(f)}{f^2}\right.\\ &\left.\times\left(1 - e^{2\pi i f L_a(1+\hat{\Omega}\cdot\hat{p}_a)}\right)\left(1 - e^{-2\pi i f L_b(1+\hat{\Omega}\cdot\hat{p}_b)}\right)e^{2\pi i f\tau}\right]\\ =& \frac{1}{2\mathcal{N}\pi^2}\left[\int_0^{\infty} df\; \Gamma_{ab}(f)\frac{H(f)}{f^2}e^{2\pi i f\tau}\right], \quad (4.18)\end{aligned}$$

where,

$$\begin{aligned}\Gamma_{ab}(f) &\equiv \mathcal{N}\int_{S^2} d\hat{\Omega}\; P(\hat{\Omega})\kappa_{ab}(f,\hat{\Omega})\left[\sum_A F_a^A(\hat{\Omega})F_b^A(\hat{\Omega})\right],\\ \kappa_{ab}(f,\hat{\Omega}) &\equiv \left[1 - e^{2\pi i f L_a(1+\hat{\Omega}\cdot\hat{p}_a)}\right]\left[1 - e^{-2\pi i f L_b(1+\hat{\Omega}\cdot\hat{p}_b)}\right]. \quad (4.19)\end{aligned}$$

In this case $\Gamma_{ab}(f)$ takes on the role of the "*overlap reduction function*" (ORF) due to separated and non-aligned detectors, which is often seen in the LIGO/LISA literature. As discussed in Ref. [393], in the large fL limit applicable to PTAs, the $\kappa_{ab}(f,\hat{\Omega})$ term can be well approximated by $(1+\delta_{ab})$, where δ_{ab} is the Kronecker delta. Therefore $\Gamma_{ab}(f)$ is in fact frequency independent.

---

[1] The pulsar labels a and b should not be confused with the spatial indices of the metric-perturbation in h_{ab}.

The function $H(f)$ can be related to the fractional energy-density in GWs through,

$$\Omega_{\rm GW}(f) \equiv \frac{1}{\rho_c}\frac{d\rho_{\rm GW}}{d\ln f} = \frac{f}{\rho_c}\frac{d}{df}\left[\frac{1}{32\pi}\langle \dot{h}_{ab}\dot{h}^{ab}\rangle\right]. \tag{4.20}$$

Plugging the plane-wave expansion into this definition, and using the expectation value of the Fourier amplitudes, gives,

$$\Omega_{\rm GW}(f) = \frac{32\pi^3}{3H_0^2}f^3 H(f), \tag{4.21}$$

where we see by comparison with Eq. (1.22) that $H(f) = h_c^2(f)/(16\pi f)$.

Finally,

$$C_{ab}(\tau) \equiv {\rm Re}\left\{\langle r_a^*(t) r_b(t+\tau)\rangle\right\} = \Gamma_{ab}\left[\int_0^\infty df\, \frac{h_c(f)^2}{32\mathcal{N}\pi^3 f^3}\cos(2\pi f\tau)\right]. \tag{4.22}$$

4.3.2 Angular-correlations induced by a GWB

We now shift attention to the cross-correlation Γ_{ab} between pulsars a and b. If we have a GWB composed of a superposition of individually unresolvable single-sources, then we can express their angular distribution on the sky as a decomposition in spherical harmonics. For the remainder of this analysis we decompose in terms of the real spherical harmonics, Y_{lm}, which are formed by the following linear combinations of their complex analogues, Y_l^m,

$$Y_{lm} = \begin{cases} \frac{1}{\sqrt{2}}\left[Y_l^m + (-1)^m Y_l^{-m}\right] & m > 0, \\ Y_l^0 & m = 0, \\ \frac{1}{i\sqrt{2}}\left[Y_l^{-m} - (-1)^m Y_l^m\right] & m < 0, \end{cases} \tag{4.23}$$

such that the angular distribution of the GWB radiation is expressed as,

$$P(\hat{\Omega}) \equiv \sum_{l=0}^{\infty}\sum_{m=-l}^{l} c_{lm} Y_{lm}(\hat{\Omega}), \tag{4.24}$$

with normalisation $\int_{S^2} P(\hat{\Omega})d\hat{\Omega} = 4\pi$. Examining the form of Γ_{ab} in Eq. (4.19), we see that the overlap reduction function can also be decomposed into a set of "*correlation basis-functions*",

$$\Gamma_{ab} = \sum_{l=0}^{\infty}\sum_{m=-l}^{l} c_{lm}\Gamma_{lm}^{(ab)}, \tag{4.25}$$

where,

$$\Gamma_{lm}^{(ab)} \equiv \mathcal{N}\int_{S^2} d\hat{\Omega}\; Y_{lm}(\hat{\Omega})\kappa_{ab}(f,\hat{\Omega})\left[\sum_{A=+,\times} F_a^A(\hat{\Omega})F_b^A(\hat{\Omega})\right], \tag{4.26}$$

are the generalised ORFs, or "*correlation basis-functions*".

Using the formalism of Ref. [391], we define a "*cosmic-frame*" and a "*computational-frame*". In the former, pulsars have their usual RA and DEC positions on the sky. The latter frame places one pulsar along the z-axis of the coordinate system, and the other pulsar in the $(x - z)$ plane. This choice permits simple analytic expressions for the $\Gamma_{lm}^{(ab)}$ to be determined, but we must remember that each distinct pair of pulsars defines a unique computational-frame, so we must rotate the computed values of $\Gamma_{lm}^{(ab)}$ back into the common cosmic-frame.

We now quote the computational-frame correlation basis-functions from Ref. [393], which have been converted to their real-form. Let the angular-separation between pulsars a and b be ζ, with $\alpha = (1 + \cos\zeta)$ and $\beta = (1 - \cos\zeta)$. The monopole ($l = m = 0$) correlation function is then

$$\Gamma_{00} = \mathcal{N}\frac{\sqrt{\pi}}{2}\left[1 + \frac{\cos\zeta}{3} + 4(1-\cos\zeta)\ln\left(\sin\frac{\zeta}{2}\right)\right]\kappa_{ab}. \tag{4.27}$$

which is the Hellings and Downs solution, as expected. We choose the normalisation to be $\mathcal{N} = 3/8\pi$ such that an isotropic background with $c_{00} = 2\sqrt{\pi}$ will have $\Gamma_{aa}(f) = c_{00}\Gamma_{00}^{(aa)}(f) = 1$.

In the following we refer to Γ_{lm} as $\Gamma_{l,m}$ to easily distinguish negative m values. The dipole correlation basis-functions have the following form,

$$\begin{aligned}
\Gamma_{1,-1} &= 0,\\
\Gamma_{1,0} &= -\mathcal{N}\frac{1}{2}\sqrt{\frac{\pi}{3}}\left[\alpha + 3\beta\left(\alpha + 4\ln\left(\sin\frac{\zeta}{2}\right)\right)\right]\kappa_{ab},\\
\Gamma_{1,1} &= \mathcal{N}\frac{1}{2}\sqrt{\frac{\pi}{3}}\sin\zeta\ln\left[1 + 3\beta\left(1 + \frac{4}{\alpha}\ln\left(\sin\frac{\zeta}{2}\right)\right)\right]\kappa_{ab}.
\end{aligned} \tag{4.28}$$

An alternative phrasing of the correlation induced by a dipole anisotropy in the GWB was derived in Ref. [213], but as shown in Ref. [393] it is completely consistent with the formalism above:

$$\Gamma_{ab,\text{dip}} = \mathcal{N}\pi(\cos\gamma_a + \cos\gamma_b)\left(\cos\zeta - \frac{4}{3} - 4\tan^2\left(\frac{\zeta}{2}\right)\ln\left(\sin\frac{\zeta}{2}\right)\right)\kappa_{ab}, \tag{4.29}$$

where γ_a and γ_b are the angular separations between pulsars a, b and the direction of the dipole moment of the GWB.

The quadrupole correlation basis-functions have the following form in the computational frame,

$$\begin{aligned}
\Gamma_{2,-2} &= 0 = \Gamma_{2,-1},\\
\Gamma_{2,0} &= \mathcal{N}\frac{1}{3}\sqrt{\frac{\pi}{5}}\left[\cos\zeta + \frac{15\beta}{4}\left(\alpha(3+\cos\zeta) + 8\ln\left(\sin\frac{\zeta}{2}\right)\right)\right]\kappa_{ab},\\
\Gamma_{2,1} &= \mathcal{N}\frac{1}{2}\sqrt{\frac{\pi}{15}}\sin\zeta\left[5\cos^2\zeta + 15\cos\zeta - 21 - 60\frac{\beta}{\alpha}\ln\left(\sin\frac{\zeta}{2}\right)\right]\kappa_{ab},\\
\Gamma_{2,2} &= -\mathcal{N}\frac{1}{4}\sqrt{\frac{5\pi}{3}}\frac{\beta}{\alpha}\left[\alpha(\cos^2\zeta + 4\cos\zeta - 9) - 24\beta\ln\left(\sin\frac{\zeta}{2}\right)\right]\kappa_{ab}.
\end{aligned} \tag{4.30}$$

The reason why the negative-m Γ_{lm} values are zero can be easily understood from the form of the negative-m real spherical-harmonic functions. These are proportional to $\sin(|m|\phi)$, which is an odd function. Since the evaluation of Γ_{lm} involves integrating over ϕ between 0 and 2π, then this will trivially yield zero.

We rotate these computational-frame functions back into the cosmic-frame by using the rotational transformations of the real-form spherical harmonics. Finally, for a prescribed array of pulsars with known positions, we can completely pre-compute the cosmic-frame correlation basis-functions. These can be read-in to a search pipeline to be multiplied with model-dependent anisotropy coefficients, c_{lm}. The c_{lm} values will be the search parameters in such a pipeline.

4.4 Pulsar-timing Analysis

Repeated observation and study of a pulsar leads to a catalogue of the arrival-times of its pulses. After the actual radio-telescope observations are performed, the data is processed into the form of pulsar parameter files (".par") and timing files (".tim"). The parameter file contains first estimates of the pulsar timing-model parameters; these parameters describe deterministic contributions to the arrival times. The vector of measured arrival times will be composed of a deterministic and a stochastic contribution (from time-correlated stochastic signals which are modelled by a random Gaussian process),

$$\vec{t}^{\mathrm{arr}} = \vec{t}^{\mathrm{det}} + \delta\vec{t}^{\mathrm{rgp}}. \tag{4.31}$$

The stochastic process is characterised by its auto-correlation,

$$C_{ab}(\tau_{ij}) = \langle \delta t^{\mathrm{rgp}}_{(a,i)} \delta t^{\mathrm{rgp}}_{(b,j)} \rangle. \tag{4.32}$$

where $\tau_{ij} = 2\pi|t_i - t_j|$. Using Eq. (4.22) we can write down the cross-correlation induced by a GWB,

$$C_{ab}(\tau_{ij}) = \Gamma_{ab}\left[\int_0^\infty df\,\frac{h_c(f)^2}{12\pi^2 f^3}\cos(2\pi f\tau_{ij})\right]. \tag{4.33}$$

An analytic expression for the auto-correlation of a time-series influenced by an underlying power-law PSD was first derived in Ref. [398], and has the form,

$$C_{ab}(\tau_{ij}) = \frac{A^2}{12\pi^2}\Gamma_{ab}\left(\frac{1\mathrm{yr}^{-1}}{f_l}\right)^{\gamma-1}\left[\Gamma(1-\gamma)\sin\left(\frac{\pi\gamma}{2}\right)(f_l\tau_{ij})^{\gamma-1} - \sum_{n=0}^{\infty}(-1)^n\frac{(f_l\tau_{ij})^{2n}}{(2n)!(2n+1-\gamma)}\right], \tag{4.34}$$

where A and γ are defined in Sec. 1.3.3, and f_l is a low-frequency cut-off, chosen such that $f_l\tau \ll 1$. A discussion of f_l and a complete derivation of this expression is given for completeness in Appendix 4.A.

We now describe the stages of pulsar-timing analysis in terms of *offline* and *online* procedures, depending on whether they are performed before or during the sampling of parameter-space via likelihood evaluations.

4.4.1 Processing raw arrival-times *(offline)*

The ".par" and ".tim" files are fed to the TEMPO2 software package [195–197] which processes the raw arrival-times. A vector of "pre-fit" timing-residuals are computed using the first guesses, $\beta_{0,i}$, of the "m" timing-model parameters from the ".par" files. This first guess is usually precise enough to allow a linear approximation to be used in the TOA fitting procedure. The post-fit timing residual are then given by

$$\delta\vec{t} = \delta\vec{t}^{\rm prf} + M\vec{\xi}, \tag{4.35}$$

where $\delta\vec{t}^{\rm prf}$ are the pre-fit timing-residuals (length n), $\vec{\xi}$ is the vector of deviations from the pre-fit parameters (length m) defined as $\xi_a = \beta_a - \beta_{0,a}$, and M is the $(n \times m)$ "design-matrix", describing how the residuals depend on the timing-model parameters. TEMPO2 does not take into account the possible time-correlated stochastic signal in the TOAs, but performs a weighted least-squares fit for the timing-model parameter values. Hence it is possible that some of the time-correlated stochastic signal is removed by this fitting procedure, which is undesirable.

The TEMPO2 analysis provides output-residuals and the design matrix, M. The output-residuals form the input data vector for further study.

4.4.2 The time-domain likelihood *(online)*

We now use the TEMPO2 output-residuals to search for the presence of any correlated stochastic signal affecting the pulse arrival times. We assume that the part of the stochastic signal removed by the fitting procedure is small, so that the TEMPO2 output-residuals are related linearly to the stochastic contribution to the residuals [399]

$$\delta\vec{t} = \delta\vec{t}^{\rm tgp} + M\vec{\xi}, \tag{4.36}$$

where, in this case, $\delta\vec{t}$ refers to the output-residuals from TEMPO2. We note that the $\vec{\xi}$ appearing in this equation is different from that appearing in Eq. (4.35).

The stochastic timing residuals, $\delta\vec{t}^{\rm tgp}$, arise from a time-correlated stochastic process with covariance matrix C (see Eq. (4.32)). This covariance matrix may contain contributions from the GWB, white-noise from TOA-errors, and possibly red-timing noise which is uncorrelated between different pulsars. The likelihood of measuring post-fit residuals $\delta\vec{t}$, given stochastic parameters $\vec{\phi}$, and marginalising with flat-priors over all timing-model parameters is [399],

$$\mathcal{L}(\delta\vec{t}|\vec{\phi}) = \frac{1}{\sqrt{(2\pi)^{n-m}\det(G^T C(\vec{\phi})G)}} \times \exp\left(-\frac{1}{2}\delta\vec{t}^T G\left(G^T C(\vec{\phi})G\right)^{-1} G^T\delta\vec{t}\right), \tag{4.37}$$

where G is the matrix constructed from the final $(n-m)$ columns of the matrix U in the SVD of the design matrix, $M = U\Sigma V^\dagger$. The matrix G can be pre-computed and stored in memory for use in each likelihood calculation (hence the computation of G is *offline*). Equation (4.37), with appropriate priors on the stochastic parameters, not only provides a robust, unbiased Bayesian framework for the search for correlated signals in PTAs, but also incorporates a lossless data compression through the G-matrix projection [400]. For completeness, a full derivation of the origin of this G-matrix expression is given in Appendix 4.B.

In the case of multiple pulsars processed independently with TEMPO2, the total covariance matrix, total G matrix and total residual vector are given by,

$$C = \begin{pmatrix} C_{11} & C_{12} & \dots \\ C_{21} & C_{22} & \dots \\ \vdots & \vdots & \ddots \end{pmatrix}, G = \begin{pmatrix} G_1 & & \\ & G_2 & \\ & & \ddots \end{pmatrix}, \delta\vec{t} = \begin{pmatrix} \delta\vec{t}_1 \\ \delta\vec{t}_2 \\ \vdots \end{pmatrix},$$

where C_{ab} is the covariance matrix between pulsars a and b, G_a are the individual pulsar timing-model marginalisation-matrices, and $\delta\vec{t}_a$ are the individual pulsar residual vectors. We can split C_{ab} into contributions from various stochastic sources. In this analysis we consider only the stochastic influence due to a GWB (which has correlation Γ_{ab} between pulsar a and b), TOA error-bars (white and uncorrelated between different pulsars), and intrinsic pulsar red-noise (uncorrelated between different pulsars). So, the covariance between the ith residual of pulsar a and the jth residual of pulsar b is,

$$C_{(ai)(bj)} = C^{\rm GW}_{(ai)(bj)} + C^{\rm TOA}_{(ai)(bj)} + C^{\rm RN}_{(ai)(bj)}, \tag{4.38}$$

where $C^{\rm GW}_{(ai)(bj)}$ is given by Eq. (4.34); $C^{\rm TOA}_{(ai)(bj)} = \Delta t^2_{(ai)}\delta_{ab}\delta_{ij}$, where $\Delta t_{(ai)}$ is the error-bar of the ith TOA in pulsar a; and $C^{\rm RN}_{(ai)(bj)}$ has the same form as $C^{\rm GW}_{(ai)(bj)}$, but with Γ_{ab} replaced by δ_{ab}. These matrices are block-symmetric, diagonal, and block-diagonal, respectively.

4.5 Simulating an anisotropic background

To simulate anisotropy in a GWB we have developed a suite of new TEMPO2 plugins [395]. These permit a user to define not only the amplitude and spectral-index of the underlying characteristic strain spectrum of the background, as in the **GWbkgrd** plugin, but also the angular distribution of the sources comprising the background. We can also define the polarisation of the

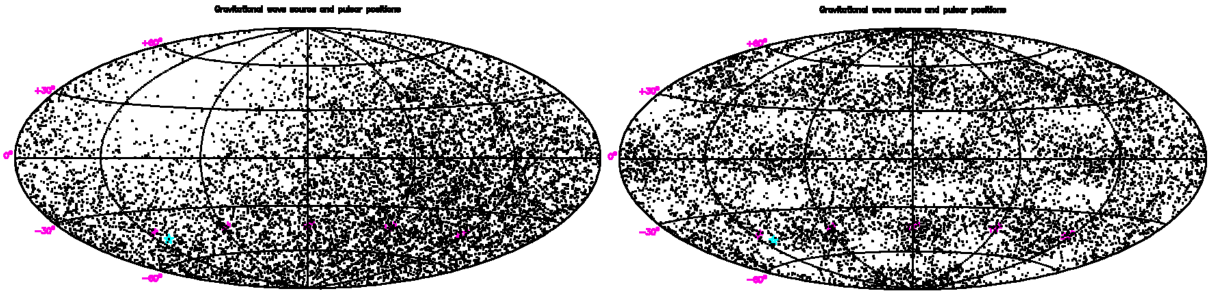

(a) **(b)**

Figure 4.3: Screenshots from the TEMPO2 plugins. The title of each plot is "Gravitational wave sources and pulsar positions", with a test-pulsar shown as a light-blue star and GW sources shown as black points. Lines of declination and right-ascension are $[0°, \pm 30°, \pm 60°]$ and $[4h, 8h, 12h, 16h, 20h]$, respectively. In (a) the over- and under-density of sources in the different regions of the sky indicate the user-specified dipole direction using the **GWdipolebkgrd** plugin. Likewise, the density of sources in (b) follows the user-specified multipolar structure of GW-power using the **GWanisobkgrd** plugin.

sources comprising the background, which we have not limited to the Einsteinian polarisation states.

To generate an anisotropic background we define a probability density function for the placement of sources on the sky,

$$\mathcal{P}(\theta \in [\Theta, \Theta + d\theta], \phi \in [\Phi, \Phi + d\phi]) = P(\Theta, \Phi) d\theta d\phi, \tag{4.39}$$

where we enforce $P(\Theta, \Phi) \geq 0$.

The background structure is user-defined, and is set by entering a multipolar decomposition of the sky-location PDF, as well as the usual dimensionless background-amplitude, A, and strain-spectrum slope, α. We now give a brief description of the individual plugins.

GWdipolebkgrd - Generates a background with a dipolar angular distribution of the GW-power. The user specifies the multipole coefficients, $\{c_{00}, c_{1-1}, c_{10}, c_{11}\}$, or the direction of the dipole moment.

GWanisobkgrd - Generates a background with arbitrary angular distribution of the GW-power. The user specifies the multipole coefficients, $\{c_{lm}\}$.

GWgeneralbkgrd - Generates an isotropic background composed of source-populations with different GW-polarisations, i.e. TT (GR modes), ST (scalar transverse, or *breathing*, mode), SL (scalar longitudinal) or VL (vector longitudinal) [401]. User specifies A and α for each polarisation.

GWgeneralanisobkgrd - Same as **GWgeneralbkgrd**, but with an arbitrary angular distribution of sources for each polarisation, specified by a set of multipole coefficients, $\{c^A_{lm}\}$, for each polarisation state A.

Figure 4.3 shows screen-shots displaying the distribution of sources comprising several examples of user-specified backgrounds. These plugins were written by Jonathan Gair, and can be downloaded from `https://github.com/jonathangair/tempo2-anisotropy-plugins`.

4.6 Results

We generated datasets similar to those used for Open Dataset 1 of the first IPTA Mock Data Challenge [223], which contained 36 pulsars distributed across the sky and timed fortnightly for 5 years. The injected signal was consistent with a GW background of inspiraling SMBH binaries (i.e., $\gamma = 13/3$), and the pulsars were timed to 100 ns accuracy.

For a full dataset this amounts to 4680 timing-residuals. Even with highly-tuned libraries and multi-threading, the required matrix operations are very costly. We employ a high-fidelity data-compression technique developed by Ref. [400] for the purposes of throwing away unwanted high-frequency information and retaining as much information about the GWB as possible, which has a steep, red spectrum.

The data-compression is based on diagonalising the expected signal covariance-matrix, and determining which basis vectors have the greatest contribution to the Fisher information. A set of reduced basis vectors are then found which capture as much information about the signal-of-interest as possible. In the lexicon of Ref. [400], we demand a minimum fidelity of 0.99. With $A = 5 \times 10^{-14}$, $\sigma_{\rm WN} = 100$ ns and 0.99 fidelity we can compress the number of residuals by approximately a factor of 5. Matrix multiplications and inversions are $\mathcal{O}(n^3)$ operations, such that we achieve significant acceleration.

All evidence evaluation and parameter estimation was performed using nested sampling with the MULTINEST package.

4.6.1 Dipole injections

A dipole anisotropy in a GW-source distribution is shown in Fig. 4.3a, where we see an overdensity of sources in a particular sky-location, as well as a paucity of sources in the opposite sky-direction. Figure 4.4 shows the angular-correlations of pulsar-pairings with non-zero angular-separation, Γ_{ab}, for all pulsars in our array. We also show the isotropic angular-correlation, which is the familiar Hellings and Downs curve [216] and only depends on the angular-separation of the pulsars. However if we have a dipole anisotropy in the angular distribution of GW-sources on the sky, then the resultant pulsar angular-correlations depend not only on the angular-separation between the pulsars, but also on the absolute positions of the

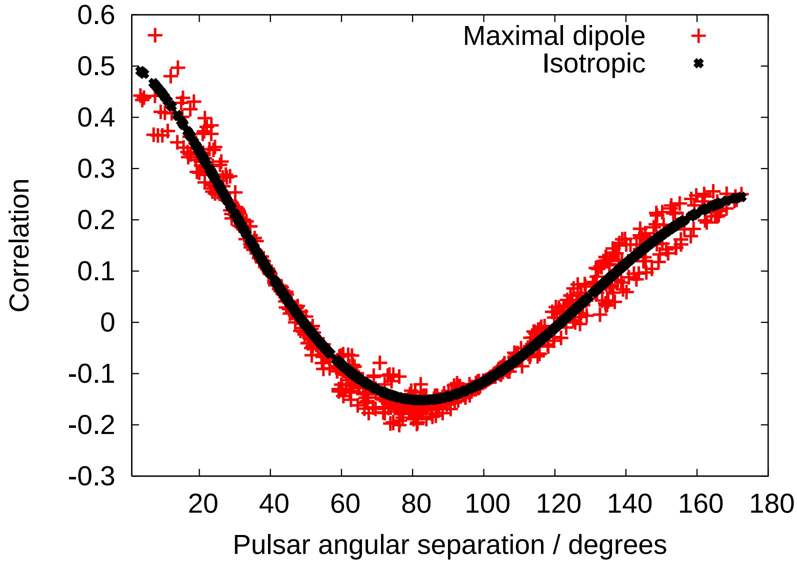

Figure 4.4: Angular-correlations for all pulsar-pairings with non-zero angular-separation in the IPTA Mock Data Challenge array of 36 pulsars. Black points indicate the angular-correlation induced by an isotropic distribution of GW-sources, which follows the expected Hellings and Downs curve. Red points show the angular-correlations when the angular-distribution of sources is proportional to $(1 + \cos\theta)$, which corresponds to a dipole in the $+z$-direction.

pulsars relative to the GW-source anisotropy. Hence pulsar-pairs which may have equal angular separations will not necessarily have equal angular-correlations if there is anisotropy in the GW-source population. Fig. 4.4 shows the angular-correlation when the angular distribution of sources has the maximum dipole amplitude that satisfies Eq. (4.39) and the dipole-direction is along the $+z$-axis. Such a maximal dipole distribution is proportional to $(1 + \cos\theta)$. We see that a dipole anisotropy induces a small deviation away from the isotropic Hellings and Downs curve, which encodes information about the angular structure of the GWB.

We generated datasets with dipole anisotropies in various different directions on the sky, and used the formalism of Sec. 4.3.2 to constrain the properties of the underlying GWB spectrum, as well as the direction of the dipole. For the latter, the alternative phrasing of dipole anisotropy of Ref. [213] is useful, since the dipole-correlation is simply expressed as a function of the pulsar-pulsar separations and the pulsar-dipole separations.

The results of these injections are shown in Fig. 4.5, where we show the recovered posterior probability distributions for the search-parameters. These posterior probability distributions show the ability of a Bayesian analysis to constrain the direction of a dipole in the GW-source population. As we can see there is negligible correlation between γ and the dipole-direction, which indicates that we can fix γ to its injected value without biasing the anisotropy constraints. Fixing γ accelerates the analysis since we can pre-compute various matrices and avoid some expensive matrix multiplications. We repeated the analysis of Fig. 4.5 with γ fixed to its reference

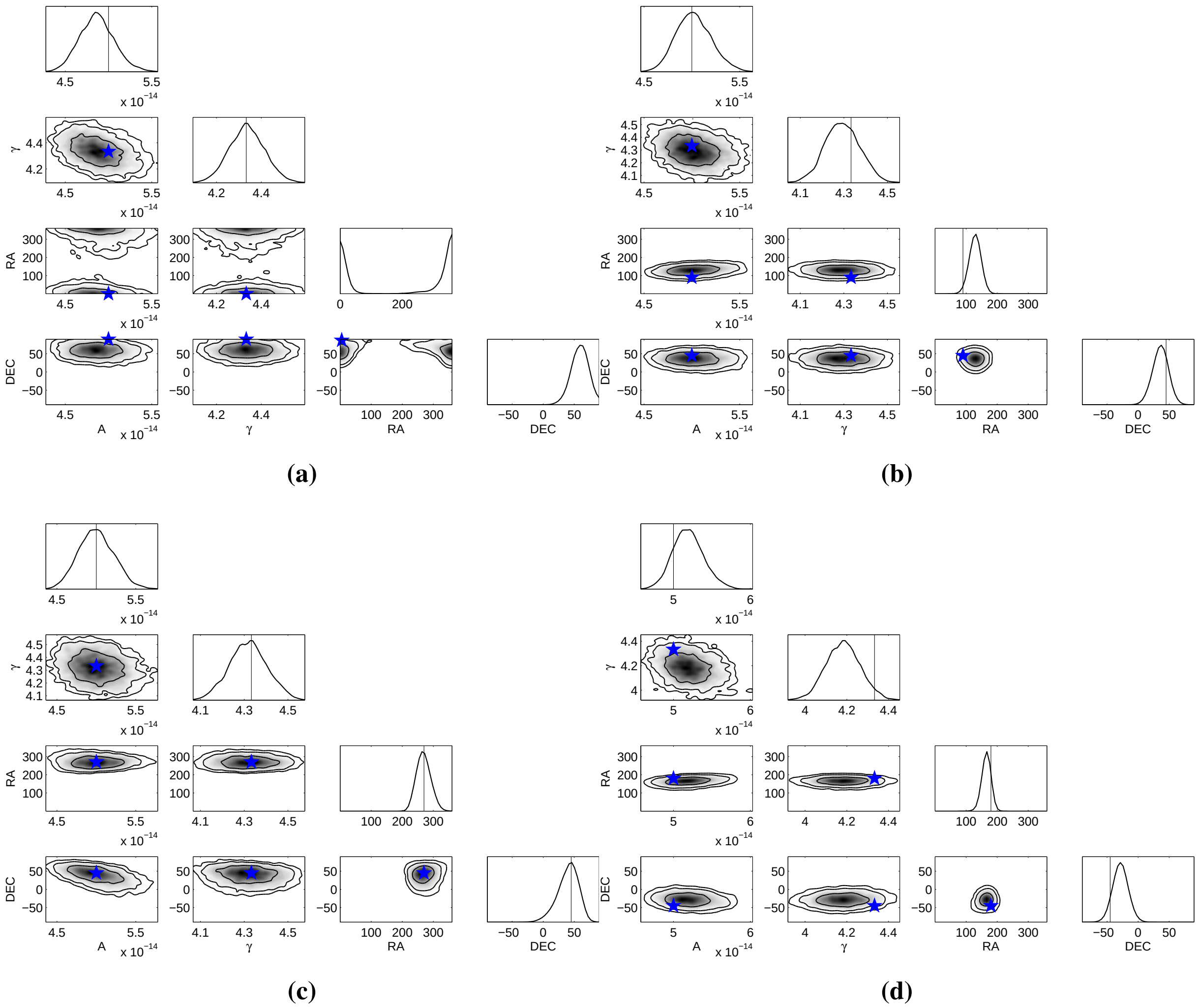

(a) (b) (c) (d)

Figure 4.5: Recovered posterior probability distributions for a Bayesian parameter-estimation of four different dipolar GWBs in simulated PTA data. The strain-spectrum is a power-law in all cases, with $(A = 5 \times 10^{-14}, \gamma = 13/3)$, and the injected dipole-direction is (a) (RA$= 0°$,DEC$= 90°$), (b) (RA$= 90°$,DEC$= 45°$), (c) (RA$= 270°$,DEC$= 45°$), (d) (RA$= 180°$,DEC$= -45°$).

value, and saw that the strain-amplitude and dipole-direction were recovered without bias.[2]

There is also the question of the significance of accounting for the anisotropy. In other words, does the anisotropic model provide a significantly better fit to the data than standard isotropic search would? We answer this question by inspecting the difference in $\ln(\mathcal{Z})$ between models which account for anisotropy, and for models which assume isotropy. The results are shown in Table 4.1, where we see that in all cases the true model is favoured, despite it having two extra dimensions compared to the isotropic model. However, we emphasise that the large Bayes factors are partially the result of our injections being in the very strong-signal regime.

To test the robustness of the *generalised* anisotropy formalism, we repeated the analysis of a maximal-dipole dataset in the direction (RA$=0^\circ$, DEC$=90^\circ$), but attempt a reconstruction of all the $c_{1,m}$ coefficients. We sample the anisotropy coefficients uniformly over the range $\in[-5,5]$. Since this is a strong anisotropic signal, and we expect to be likelihood-dominated, we adopt this uniform sampling range as a prior over the anisotropy coefficients and defer discussion of a physically-motivated prior (required for the analysis of real data) until Sec. 4.6.3.

We fix $c_{0,0}$ to $2\sqrt{\pi}$, and absorb the variation of the isotropic-power into the overall amplitude A. So, in this sense, we are searching for deviations from isotropy, rather than highly anisotropic backgrounds. Furthermore, by freely searching over $c_{1,m}$ we are removing our assumption of the anisotropy being maximal dipole. The results are shown in Fig. 4.6, where we see that the recovered dipole-coefficients are completely consistent with the injected values of $\{c_{1,-1}=0, c_{1,0}=2\sqrt{\pi/3}, c_{1,1}=0\}$, which correspond to a maximal-dipole in the $+z$-direction. The results of an analysis where we relax the assumption of *dipole* anisotropy, and perform a search over all anisotropy coefficients up to and including quadrupole, are shown in Fig. 4.7. The posterior is consistent with the injected anisotropy, however the increased dimensionality degrades the precision of parameter recovery such that we could conceivably be consistent with a large range of anisotropic distributions.

We now investigate the degree to which an isotropic search is sub-optimal, and deleterious to detection prospects, by generating many dipole-anisotropy datasets with different GWB amplitudes. The white-noise level is fixed at 100 ns, such that we are effectively varying the signal-to-noise ratio (SNR) in the datasets. We form a simple proxy for the SNR in the form of the *single-pulsar* ratio of the post-fit timing-residual rms induced by the GWB to the rms of the noise,

$$\mathrm{SNR}\sim\frac{\sigma_{\mathrm{GW}}}{\sigma_{\mathrm{WN}}}, \tag{4.40}$$

---

[2] The only inconsistency in the reconstructed direction was found when the dipole-direction was (RA=0.0, DEC=90.0). This arose because we sample uniformly in $\cos\theta$ so there is little prior-weight at high declinations.

Table 4.1: Bayes factors for a comparison between an anisotropic and isotropic model when analysing datasets which have dipole-anisotropies injected in various different directions. In each case we favour the model which accounts for this anisotropy rather than the isotropic model. This is true even when the direction of the dipole is searched over, which adds an extra two dimensions to the parameter space. The Bayes factor varies little when the spectral-index $\gamma \equiv 3 - 2\alpha$ is fixed to $13/3$, which is the expected value for a background composed of inspiraling SMBH binaries.

Dipole direction / degrees	$\ln(\mathcal{B}) = \ln(\mathcal{Z}_{\rm true}) - \ln(\mathcal{Z}_{\rm iso})$	
	$\gamma = 13/3$	γ varied
RA=0.0 DEC=90.0	7.0	7.2
RA=90.0 DEC=45.0	10.5	10.3
RA=270.0 DEC=45.0	4.4	4.4
RA=180.0 DEC=-45.0	7.3	7.5

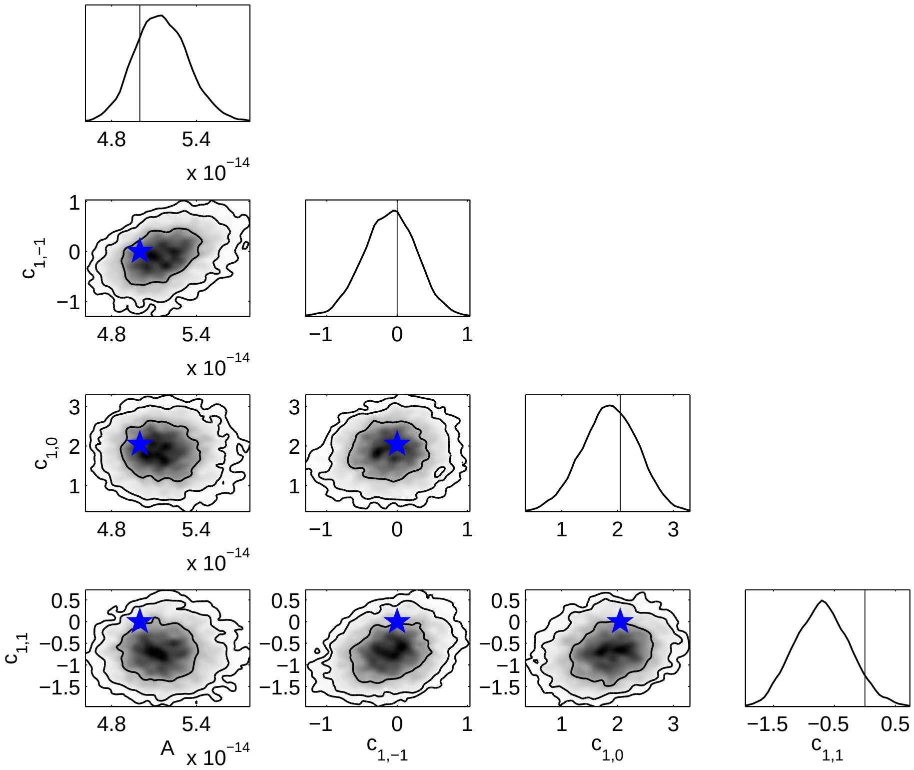

Figure 4.6: A search over strain-amplitude and dipole anisotropy coefficients. The injected anisotropy was maximal-dipole with $c_{0,0} = 2\sqrt{\pi}$ and $c_{1,0} = 2\sqrt{\pi/3}$, corresponding to a dipole-direction of RA$= 0.0^\circ$, DEC$= 90^\circ$.

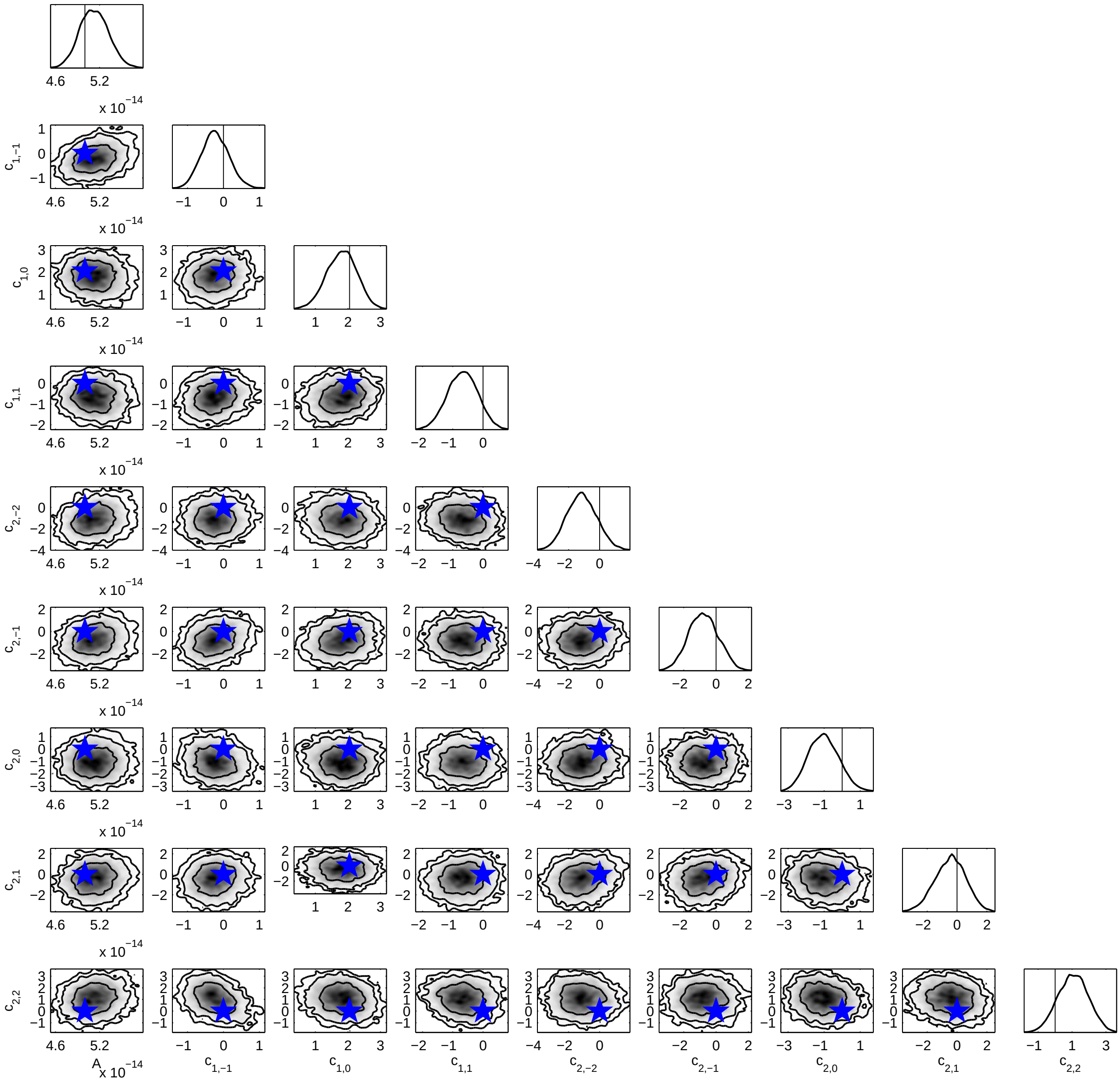

Figure 4.7: A search over all anisotropy coefficients, c_{lm}, up to, and including, quadrupole order. The injected anisotropy was maximal-dipole with $c_{0,0} = 2\sqrt{\pi}$ and $c_{1,0} = 2\sqrt{\pi/3}$, corresponding to a dipole-direction of RA= $0.0°$, DEC= $90°$.

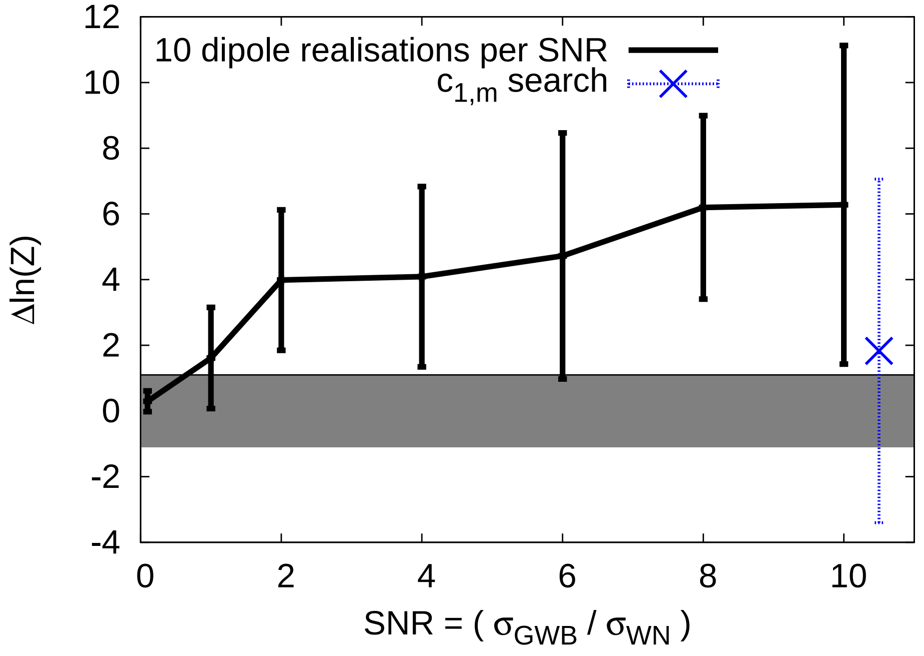

Figure 4.8: Evidence for anisotropy versus isotropy as a function of GWB strain-amplitude in the range $5 \times 10^{-16} - 5 \times 10^{-14}$, and with γ fixed to $13/3$. We generate 10 datasets at each SNR with dipole-anisotropy such that the angular-distribution of GW-sources is $\propto (1 + \cos\theta)$. We compute the "injected-anisotropy vs. isotropy" Bayes factor $[\ln(\mathcal{B}) = \Delta\ln(\mathcal{Z})]$. The shaded area is the region of model ambiguity, however even at SNR $= 0.1$ the GWB is loud enough to be detected with substantial evidence (see text for details). The blue, dotted point is a calibration-point for more general searches over $\{A, c_{1,m}\}$ at SNR $= 10$, but offset on the x-axis for ease of viewing (see text for details).

where,

$$\sigma_{\rm GW} \sim 1.37 \times \left(\frac{A}{10^{-15}}\right)\left(\frac{T}{\rm yr}\right)^{5/3} \;\text{ns}, \quad \text{if } \gamma = 13/3,$$

$$\sigma_{\rm WN} = 100 \;\text{ns}, \tag{4.41}$$

and $\sigma_{\rm GW}$ is determined from an evaluation of the post-fit covariance function for power-law spectral densities. An estimate of this is obtained analytically by projecting the pre-fit covariance function into a new basis, which replicates the effect of fitting for quadratics. Given that fitting for the pulsar's quadratic-spindown is the dominant influence on the covariance matrix, Eq. (4.41) provides a good estimate of $\sigma_{\rm GW}$ for given A (and vice versa) [399, 400, 402].

Varying the amplitude of the GWB between $5 \times 10^{-16} - 5 \times 10^{-14}$ gives a proxy SNR span of $0.1 - 10$. At each SNR in this range we generated 10 dataset realisations and evaluated the difference in $\ln(\mathcal{Z})$ values for an anisotropic and an isotropic model. This was performed with an optimal correlation filter, with the GWB correlations fixed to those corresponding to the injected level of anisotropy, which in this case was the maximal-dipole in the $+z$-direction described earlier. These results are shown in Fig. 4.8. We note that this figure does not show the true odds ratio for the anisotropic versus isotropic model, since the degrees of freedom corresponding to the dipole direction have not been included in the parameter space for the anisotropic model. Instead, this figure indicates a best case scenario for when the evidence would start to favour the anisotropic model. Also, one should note that because the injected noise is white-uncorrelated, and we have compressed to preserve information about a steep red-noise process, even with a proxy SNR of 0.1 the GWB is loud enough to be detected with substantial evidence. At this SNR the largest noise-versus-(isotropic-)GWB log-Bayes factor is 0.03, with a mean and median of -6.30 and -2.62, respectively. So, we can detect a GWB with angular-correlation of *approximate* Hellings and Downs form, but the background is not yet loud enough for anisotropy-induced deviations to be visible.

In these idealised circumstances the anisotropic model is marginally favoured for SNRs above ~ 1 and decisively favoured for SNRs above ~ 5. Including the dipole direction parameters (or searching over $c_{1,m}$) in the parameter space reduces the anisotropic evidence by several and so in practice SNRs of ~ 5–10 would be required before the presence of anisotropy would become clearly visible to an analysis of this type (see also Fig. 4.10 below). We provide a calibration point at SNR $= 10$, where we search over $\{A, c_{1,m}\}$ for the 10 dataset realisations at this SNR. We see that the increased dimensionality of the search penalises the recovered Bayes factors, however the average log-Bayes factor implies that the presence of anisotropy may become clearly visible at proxy SNRs greater than 10.

The datasets described so far have contained only white-noise. Now we generate datasets with an additional red-noise component uncorrelated between different pulsars. The red-noise shares a common spectrum, but with a different realisation for each pulsar. The spectral-index was taken to match that of the IPTA Open3 dataset ($\gamma_{\rm red} = 1.7$) which is similar to the expected red-noise spectrum arising from pulse phase-noise [202]. As before, we include an uncorrelated white-noise component of 100 ns in each pulsar. Following Eq. (4.41), we parametrise the SNR as,

$$\text{SNR} \sim \frac{\sigma_{\rm GW}}{\sigma_{\rm RED}} \sim 0.4 \times \left(\frac{A}{A_{\rm red}}\right) \times \left(\frac{T}{\rm yr}\right)^{79/60}, \tag{4.42}$$

where $\sigma_{\rm RED}$ follows from the more general form of the post-fit rms-residual induced by a stochastic process with power-law spectrum of arbitrary slope [399].

The analysis is more expensive than a GWB-only analysis, since we must also characterise and constrain the red-noise properties. Furthermore, the red-noise has a shallower spectrum, such that our residuals contain more high-frequency noise, and we can not compress to the same degree as in the case of a GWB-only dataset. Figure 4.9 shows the results of a proxy SNR ~ 4 analysis. We see that at this SNR we can characterise the GWB, red-noise and anisotropy properties. In fact, for this dataset realisation, the value of $\ln(\mathcal{B})$ for anisotropy versus isotropy was ~ 4.4, which is borderline decisive evidence for anisotropy. Since the

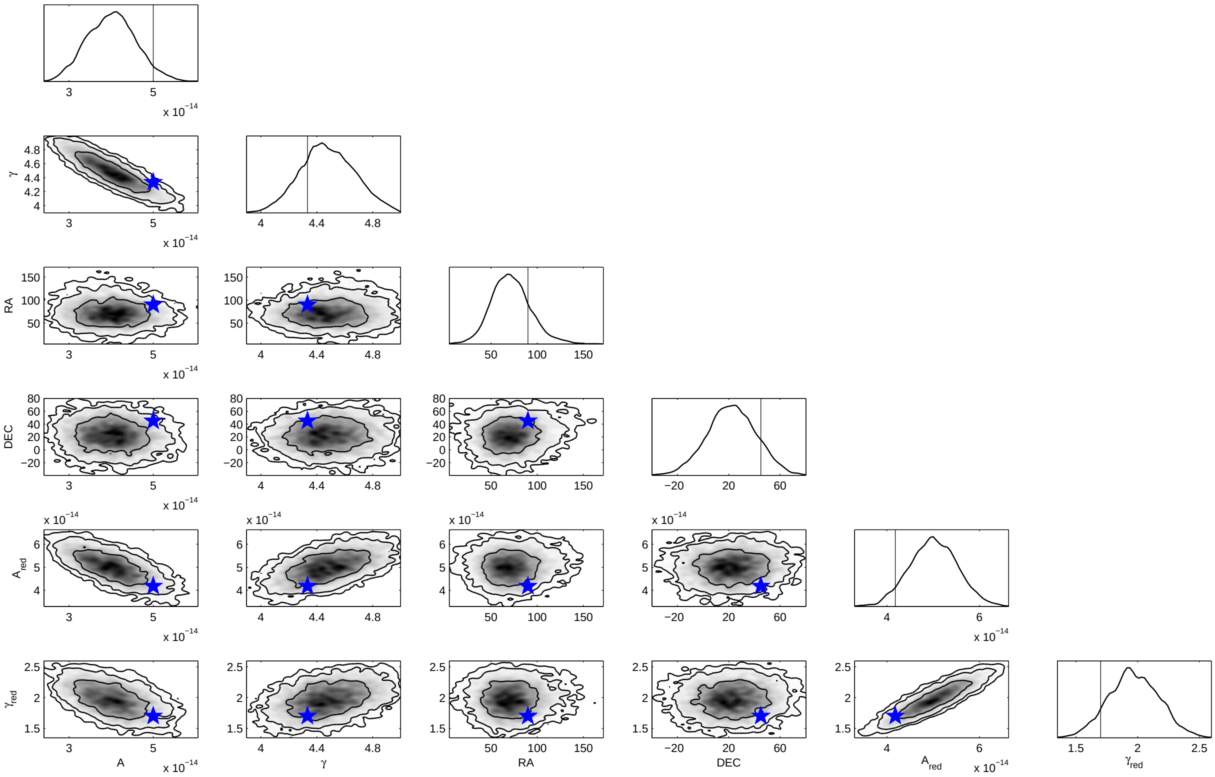

Figure 4.9: An example of anisotropy reconstruction when uncorrelated red-noise is present in the dataset. The anisotropy is maximal-dipole, with direction (RA= $90°$, DEC= $45°$). The injected GWB parameters are ($A = 5 \times 10^{-14}$,$\gamma = 13/3$). The red-noise is uncorrelated between different pulsars, but shares a common spectrum, with ($A_{\rm red} = 4.2 \times 10^{-14}$,$\gamma_{\rm red} = 1.7$), such that we have an effective SNR of ~ 4.2. In this dataset, the $\ln(\mathcal{B})$ for anisotropic versus isotropic was ~ 4.4, which is borderline decisive evidence for anisotropy.

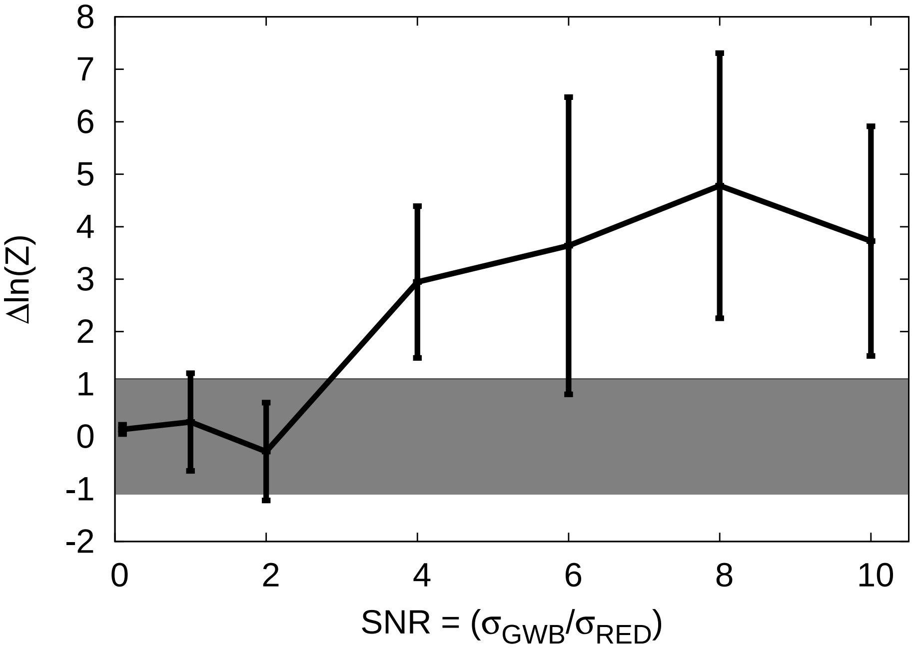

Figure 4.10: As Fig. 4.8, but now for datasets containing red-noise. We generate 5 datasets per SNR with dipole-anisotropy, varying the SNR by fixing the GW amplitude, A, at 5×10^{-14} and varying $A_{\rm red}$ between $\sim 1.8 \times 10^{-12} - 1.8 \times 10^{-14}$ to give a proxy SNR span of $0.1 - 10$. In the analysis the spectral slopes γ and $\gamma_{\rm red}$ are fixed to $13/3$ and 1.7, respectively. We evaluate the evidence for models which assume a maximal-dipole anisotropy (direction searched over) and isotropy.

analysis is quite computationally expensive, and we wish to perform a more systematic study over many background realisations, we repeat this analysis but fix γ and $\gamma_{\rm red}$ to the injected values of $13/3$ and 1.7, respectively. Fixing these spectral indices accelerates the analysis, does not bias the parameter reconstruction, and only raises the value of $\ln(\mathcal{B}) = \Delta\ln(\mathcal{Z})$ by ~ 0.8.

We perform a similar study to Fig. 4.8, generating 5 datasets per SNR, each with common GWB properties ($A = 5 \times 10^{-14}$,$\gamma = 13/3$), $\gamma_{\rm red} = 1.7$, but varying the red-noise amplitude, $A_{\rm red}$ to simulate the different SNRs. The injected anisotropy is maximal-dipole in the (RA$=$ 90°, DEC$=$ 45°) direction in all cases. We search over the parameters $\{A, A_{\rm red}$,RA,DEC$\}$. The results are shown in Fig. 4.10, where we see that the presence of uncorrelated red-noise in the datasets can be accounted for, but its presence means that the SNR required to identify the presence of anisotropy in the data appears somewhat higher. However, in this case we include a search over the dipole direction in the evaluation of the evidence, so these results are much closer to what might be achievable in practice (although fixing the slope of the red-noise spectrum in particular might not be a valid assumption). Fig. 4.10 suggests that even in the presence of pulsar red-noise the evidence for anisotropy will become apparent for proxy SNRs around 3 and will become decisive for proxy SNRs of ~ 6.

For the remainder of this analysis we ignore red-noise and inject only uncorrelated white-

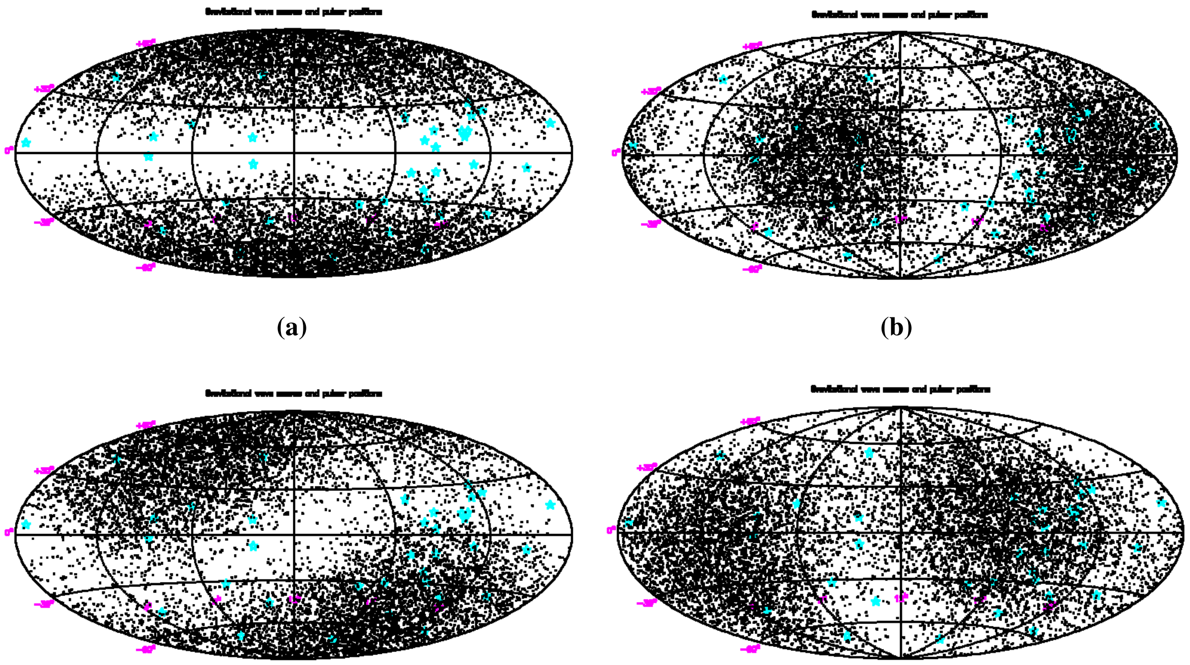

(a) (b) (c) (d)

Figure 4.11: Skymap screenshots from the **GWanisobkgrd** TEMPO2-plugin showing the quadrupolar angular-distribution of GW sources constituting various GWB realisations. The title of each plot is “Gravitational wave sources and pulsar positions”, with pulsars shown as light-blue stars and GW sources shown as black points. Lines of declination and right-ascension are $[0^\circ, \pm 30^\circ, \pm 60^\circ]$ and $[4h, 8h, 12h, 16h, 20h]$, respectively. The anisotropy-coefficients for each dataset are (a) $\{c_{0,0} = 2\sqrt{\pi};\ c_{2,0} = 4\sqrt{\pi/5}\}$ (b) $\{c_{0,0} = 2\sqrt{\pi};\ c_{2,-2} = -0.9c_{0,0};\ c_{2,0} = -0.3c_{0,0}\}$ (c) $\{c_{0,0} = 2\sqrt{\pi};\ c_{2,-1} = -0.8c_{0,0};\ c_{2,0} = 0.5c_{0,0};\ c_{2,2} = -0.3c_{0,0}\}$ (d) $\{c_{0,0} = 2\sqrt{\pi};\ c_{2,-2} = 0.56c_{0,0};\ c_{2,-1} = 0.20c_{0,0};\ c_{2,0} = -0.32c_{0,0};\ c_{2,1} = 0.27c_{0,0};\ c_{2,2} = -0.40c_{0,0}\}$.

noise in the form of TOA error-bars, but expect that the effect of red-noise will be to slightly increase the SNR (by a few) required for a confident detection of anisotropy.

4.6.2 Quadrupole injections

A GWB with a maximal quadrupole-anisotropy (corresponding to an angular distribution $\propto 3\cos^2\theta$) is shown in Fig. 4.11a. Figure 4.12 shows the distinct angular-correlations for all pulsars in the array when there is a quadrupole anisotropy in the GW-source population.

We perform a similar analysis to Fig. 4.8, varying the GWB amplitude between $5 \times 10^{-16} - 5 \times 10^{-14}$, thus giving an effective SNR span of $0.1 - 10$. At each SNR we generate 10 dataset realisations of a quadrupole GWB-anisotropy in white uncorrelated noise. The only parameter we search for in the analysis of each dataset is the amplitude, A, of the background. Hence, as before, this study represents a best case assessment of when we will be able to identify the

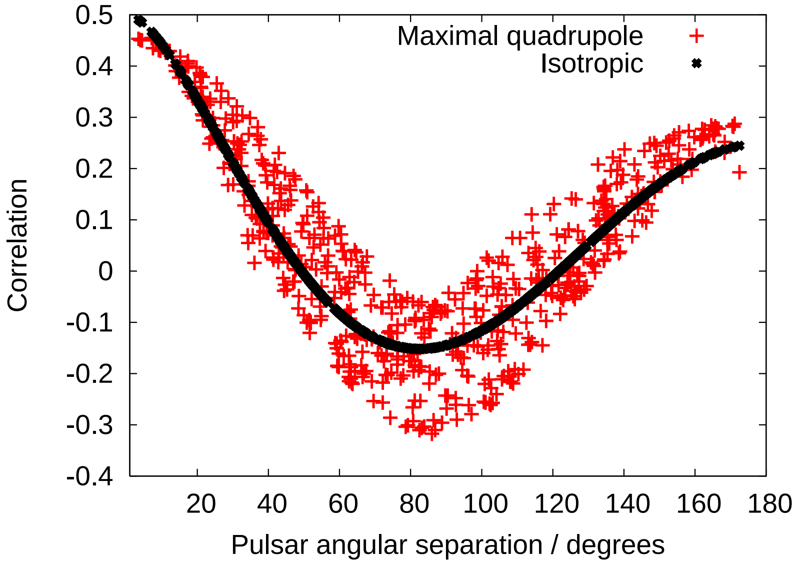

Figure 4.12: Angular-correlations for all pulsar-pairings with non-zero angular-separation in the IPTA Mock Data Challenge array of 36 pulsars. Black points indicate the angular-correlation for an isotropic GW background, which follows the expected Hellings and Downs curve. Red points show the correlations when the angular-distribution of sources follows $\propto 1 + (3\cos^2\theta - 1)$, which corresponds to a maximal quadrupole anisotropy.

presence of a quadrupole anisotropy (of the form $P(\theta, \phi) = 3\cos^2\theta$) in the data. In reality, we will not know the direction of the quadrupole anisotropy in advance, which introduces extra dimensionality into the parameter space that must be searched over. This will tend to reduce the log-evidence value and so larger SNRs will be required to identify quadrupole anisotropies in practice. As in the dipole case, one should note that because the injected noise is white-uncorrelated, and we have compressed to preserve information about a steep red-noise process, even at SNR$= 0.1$ the GWB is loud enough to be detected with substantial evidence. At this SNR the largest noise-versus-(isotropic-)GWB log-Bayes factor is 0.3, with a mean and median of -9.3 and -5.8, respectively. As discussed previously, at SNR = 0.1 the GWB is loud enough such that we can detect a background which has *approximate* Hellings and Downs form, but not yet loud enough to allow inference of anisotropy-induced deviations.

The results of this study can be seen in Fig. 4.13, and are quite similar to the dipole case – the presence of anisotropy becomes identifiable at a proxy SNR of about 1, while the evidence is decisive for a proxy SNR of ~ 5. We provide a calibration point at SNR $= 10$, where we search over $\{A, c_{2,m}\}$ for the 10 dataset realisations at this SNR. As expected, we see that the increased dimensionality of the search penalises the recovered Bayes factors, however the average log-Bayes factor implies that the presence of anisotropy may become visible with substantial evidence at proxy SNR $= 10$, but we will require SNR > 10 for it to be clearly visible.

As in the dipole case, we test the robustness of the generalised anisotropic formalism by

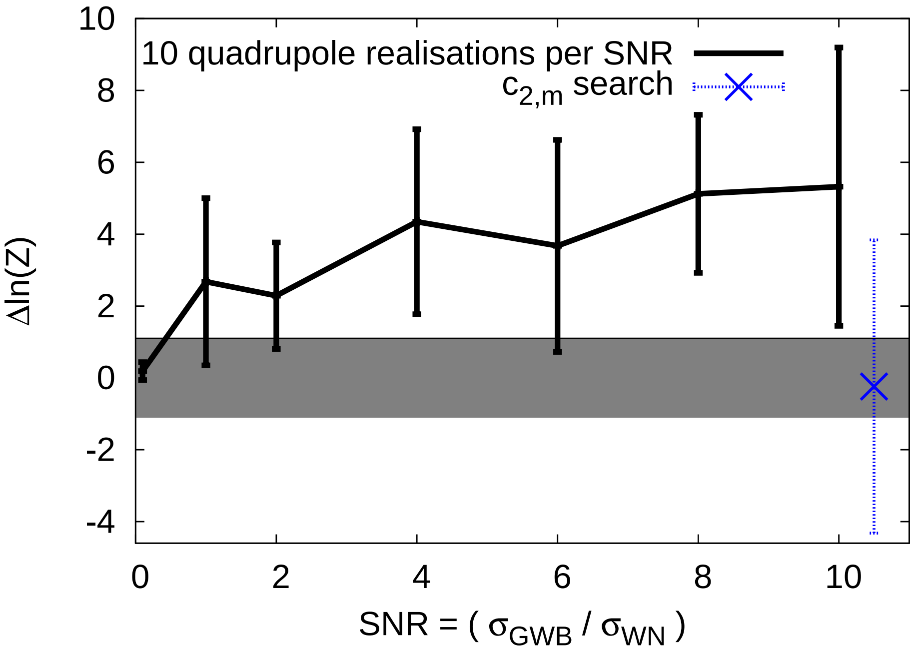

Figure 4.13: As Fig. 4.8, but now for datasets containing a maximal quadrupole-anisotropy such that the angular-distribution of GW-sources is $\propto 1 + (3\cos^2\theta - 1)$. We compute the "injected-anisotropy vs. isotropy" Bayes factor $[\ln(\mathcal{B}) = \Delta\ln(\mathcal{Z})]$. The shaded area is the region of model ambiguity. The blue, dotted point is a calibration for more general searches over $\{A, c_{2,m}\}$ at SNR $= 10$, but offset on the x-axis for ease of viewing (see text for details).

generating datasets with quadrupole anisotropies in a variety of configurations. The GW-source distribution for each of the tested configurations is shown in Figure 4.11. As can be seen in Fig. 4.14, the generalised anisotropic-search pipeline recovers anisotropy coefficients which are consistent with the injected values. However the dimensionality is significantly larger than an isotropic search, and even in these high SNR datasets the posterior probability distributions are consistent with a wide range of possible anisotropies. Finally, we repeat the analysis of the maximal-quadrupole dataset (with $P(\theta, \phi) = 3\cos^2\theta$), but relax the assumption of quadrupole-anisotropy in the analysis. The results of this analysis are shown in Figure 4.15, where we have accurately recovered the nature of the injected anisotropy. However, as observed in the case where we performed an arbitrary-anisotropy search on a pure-dipole dataset, the increased dimensionality of the arbitrary-anisotropy search widens the recovered posterior distributions to be consistent with a wide range of anisotropies.

4.6.3 Arbitrary anisotropy

Arbitrary anisotropy search, and a physical prior

We now test our search-pipeline on a dataset with power spread between monopole, dipole and quadrupole components. The coefficients characterising the anisotropy are $\{c_{0,0} = 2\sqrt{\pi};\ c_{1,-1} = -0.4c_{0,0};\ c_{1,0} = 0.4c_{0,0};\ c_{2,0} = 0.20c_{0,0};\ c_{2,2} = -0.45c_{0,0}\}$, with all other anisotropy coefficients set to zero. The sky-map for the distribution of GW-sources on the sky corresponding to these anisotropy coefficients is shown in Fig. 4.16a.

Taking a wide flat prior on the anisotropy coefficients as before, the results of a search are shown in Fig. 4.17. The injected anisotropy coefficients all lie within the 2σ contours of the posterior distributions for the recovered coefficients. However the high search-dimensionality degrades the precision with the coefficients can be recovered so that the posterior is consistent with a wide range of anisotropic distributions.

We now address this with a more physically-motivated prior choice. Until now we have assumed that all combinations of anisotropy-coefficients are *a priori* equally likely. However, when generating these anisotropic-datasets we have had to take into account that some combinations do not represent physical anisotropies, since they fail the condition in Eq. (4.39) that the PDF for the distribution of GW-sources on the sky is positive at all sky-locations,

$$P(\hat{\Omega}) \propto \frac{dN}{d\hat{\Omega}} \propto \sum_{l,m} c_{lm} Y_{lm}(\hat{\Omega}) \geq 0, \quad \forall\, \hat{\Omega}. \tag{4.43}$$

Therefore, if we are to correctly perform parameter estimation on anisotropic datasets, this condition is the only physically meaningful prior on the anisotropy-coefficients. We impose it by setting the likelihood of any combination of $c_{l,m}$ which fails this condition to be very low, so

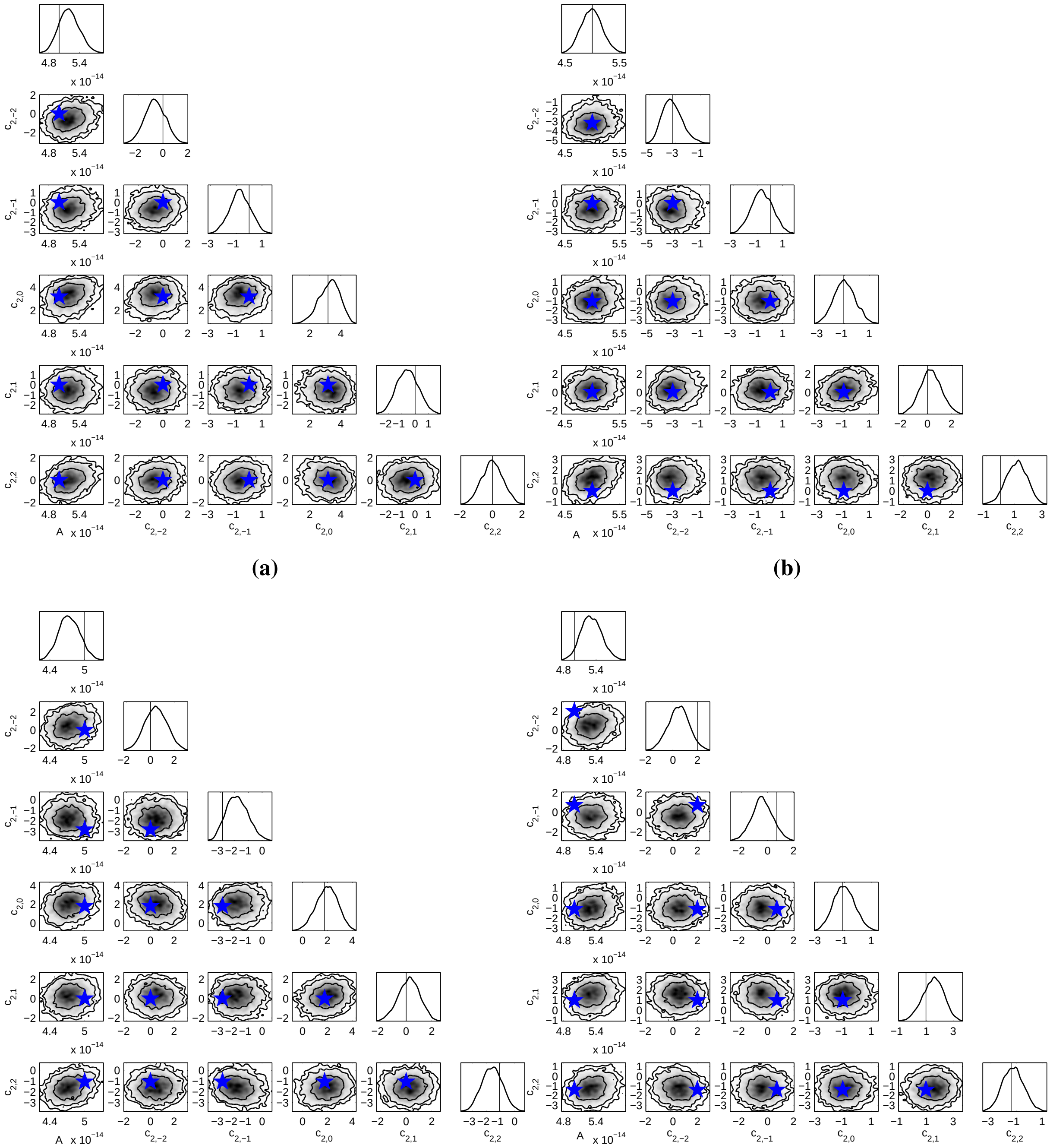

(a) (b)

(c) (d)

Figure 4.14: The results of constraining the quadrupole-anisotropy coefficients, $c_{2,m}$ in datasets containing quadrupole anisotropies with a variety of configurations. The GW-source distributions corresponding to the injected anisotropies in each of these datasets are visualised in Figure 4.11. The parameters of the injected anisotropies are (a) $\{c_{0,0} = 2\sqrt{\pi};\ c_{2,0} = 4\sqrt{\pi/5}\}$ (b) $\{c_{0,0} = 2\sqrt{\pi};\ c_{2,-2} = -0.9c_{0,0};\ c_{2,0} = -0.3c_{0,0}\}$ (c) $\{c_{0,0} = 2\sqrt{\pi};\ c_{2,-1} = -0.8c_{0,0};\ c_{2,0} = 0.5c_{0,0};\ c_{2,2} = -0.3c_{0,0}\}$ (d) $\{c_{0,0} = 2\sqrt{\pi};\ c_{2,-2} = 0.56c_{0,0};\ c_{2,-1} = 0.20c_{0,0};\ c_{2,0} = -0.32c_{0,0};\ c_{2,1} = 0.27c_{0,0};\ c_{2,2} = -0.40c_{0,0}\}$.

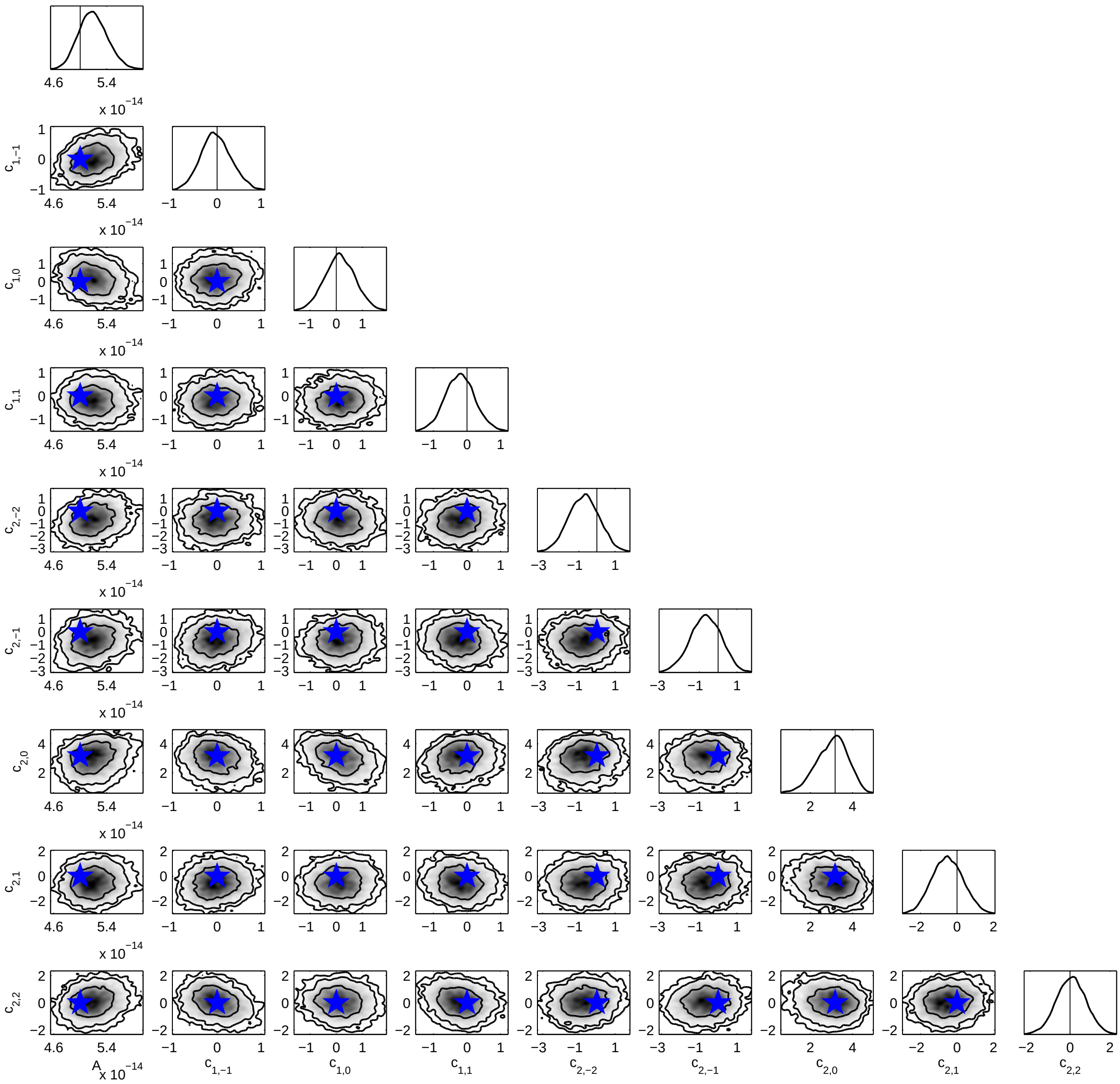

Figure 4.15: A search over all anisotropy coefficients, c_{lm}, up to, and including, quadrupole order. The injected anisotropy was maximal-quadrupole with $c_{0,0} = 2\sqrt{\pi}$ and $c_{2,0} = 4\sqrt{\pi/5}$, and all other dipole/quadrupole coefficients set to zero.

as to prevent sampling in these regions. In practice this is achieved by pixelating the sky with a 20×20 grid in $[\cos\theta, \phi]$, and testing the condition in each pixel.[3] If the condition is not met in *every* pixel, then the sample is rejected. The result of such an application of this prior on the previously analysed arbitrary-anisotropy dataset is shown in Fig. 4.18. For the most part, the recovered posterior distributions are consistent with the injected anisotropy. The exception is for the $c_{2,2}$ coefficient, where the injected amplitude lies in the tails of the recovered posterior distribution. The reason for this apparent inconsistency is actually quite straightforward. If we attempt to generate a dataset with all anisotropy coefficients as before, except for $c_{2,2}$, which we lower from $-0.45c_{0,0}$ to $-0.47c_{0,0}$, then the **GWanisobkgrd** plugin fails, since this PDF for the placement of GW-sources on the sky is negative in some sky-locations. Thus the reason that the injected $c_{2,2}$ amplitude is in the tails of the recovered posterior distribution is because this value is *a priori* disfavoured, and very close to the boundary of non-physicality.

Despite the apparent inconsistency of the $c_{2,2}$ coefficient, we are still able to accurately recover the distribution of GW-sources on the sky. In Figure 4.16 we compare the sky-maps of GW-background realisations for: (a) the injected anisotropy; (b) *maximum a posteriori* anisotropy of an analysis with the physical-prior imposed on the $c_{l,m}$ coefficients; (c) the maximum-likelihood anisotropy where the relative power in $l = 0$ has been boosted to ensure physicality over the entire sky. As can be seen, the anisotropic-search pipeline has correctly recovered the features of this background. Even the maximum-likelihood anisotropic configuration, despite being unphysical, can have the relative power of its isotropic component boosted to ensure physicality over the entire sky, producing a GW source-distribution which is adequately close to the injected distribution.

Anisotropy misfits

We now test the ability of the anisotropic-search pipeline to recover the *nature* of the GW-background anisotropy. Taking isolated realisations of isotropic, dipole, quadrupole and arbitrary anisotropy datasets with a proxy SNR $= 10$, we computed the evidence for isotropic, dipole, quadrupole and arbitrary models. We also computed the evidence for the true injected anisotropy, searching only over the amplitude of the background. The results are shown in Table 4.2, where all numbers indicate log-Bayes factors relative to an isotropic model.

For these evidence calculations we adopt flat priors on the anisotropy coefficients. Although in practice we should be imposing the physicality conditions, we have found that the physical-prior studied in the previous sub-section is actually highly informative, and can truncate regions of high-likelihood. The anisotropic configurations we have studied are close to maximal, which

---

[3] Each pixel corresponds to ~ 41 deg^2, which, upon using the relationship $l \sim 180/\sqrt{\Delta\Omega/\text{deg}^2}$ [394], means that this pixelation-scheme is fine enough to discriminate the physicality of proposed angular PDFs up to $l \sim 28$.

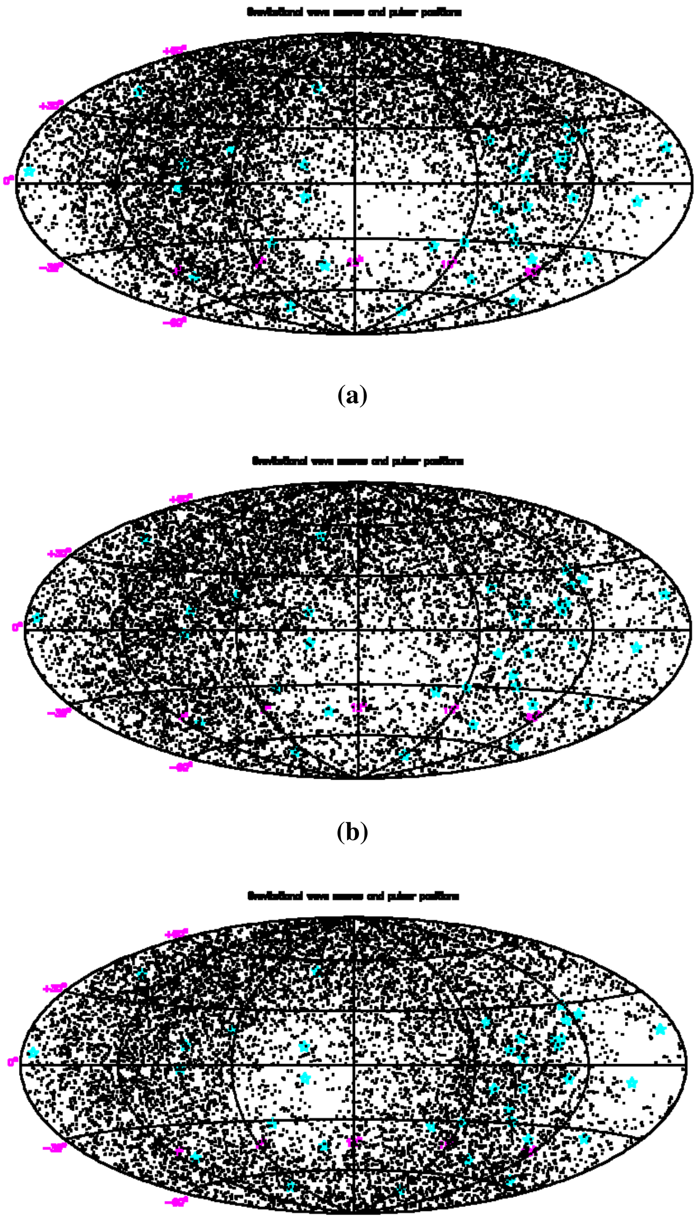

(a)

(b)

(c)

Figure 4.16: Skymap screenshots from the **GWanisobkgrd** TEMPO2-plugin showing the angular-distribution of GW sources constituting various GWB realisations. The title of each plot is "Gravitational wave sources and pulsar positions", with pulsars shown as light-blue stars and GW sources shown as black points. Lines of declination and right-ascension are $[0°, \pm 30°, \pm 60°]$ and $[4h, 8h, 12h, 16h, 20h]$, respectively. In (a) we show the skymap for the distribution of GW sources implied by a GWB with anisotropy-coefficients $\{c_{0,0} = 2\sqrt{\pi};\ c_{1,-1} = -0.4c_{0,0};\ c_{1,0} = 0.4c_{0,0};\ c_{2,0} = 0.20c_{0,0};\ c_{2,2} = -0.45c_{0,0}\}$. In (b) we plot the skymap implied by the *maximum a posteriori* anisotropic configuration from an analysis with our Bayesian search-pipeline, where we have imposed a hard physical-prior (discussed in text). Finally, (c) shows the skymap implied by the maximum likelihood anisotropic configuration, where we see that, despite not having the extra constraining influence of the physical-prior, we are still able to adequately recover the distribution of GW sources.

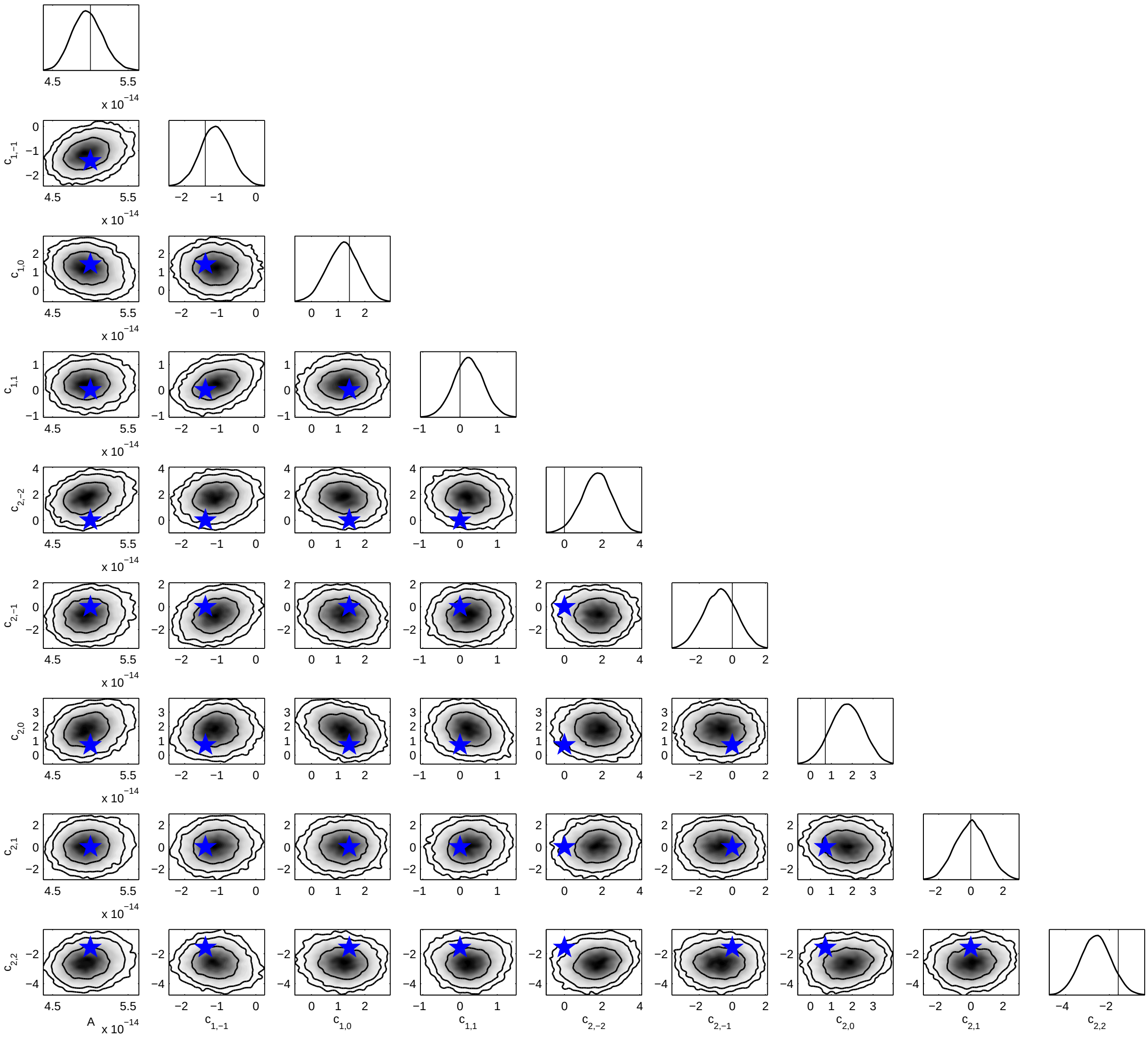

Figure 4.17: A full anisotropic-search on an arbitrary-anisotropy dataset. The details of the dataset are $\{c_{0,0} = 2\sqrt{\pi};\ c_{1,-1} = -0.4c_{0,0};\ c_{1,0} = 0.4c_{0,0};\ c_{2,0} = 0.20c_{0,0};\ c_{2,2} = -0.45c_{0,0}\}$. The prior is wide and flat, where $c_{l,m} \in [-5, 5]$, such that all anisotropy-coefficient combinations are *a-priori* equally likely.

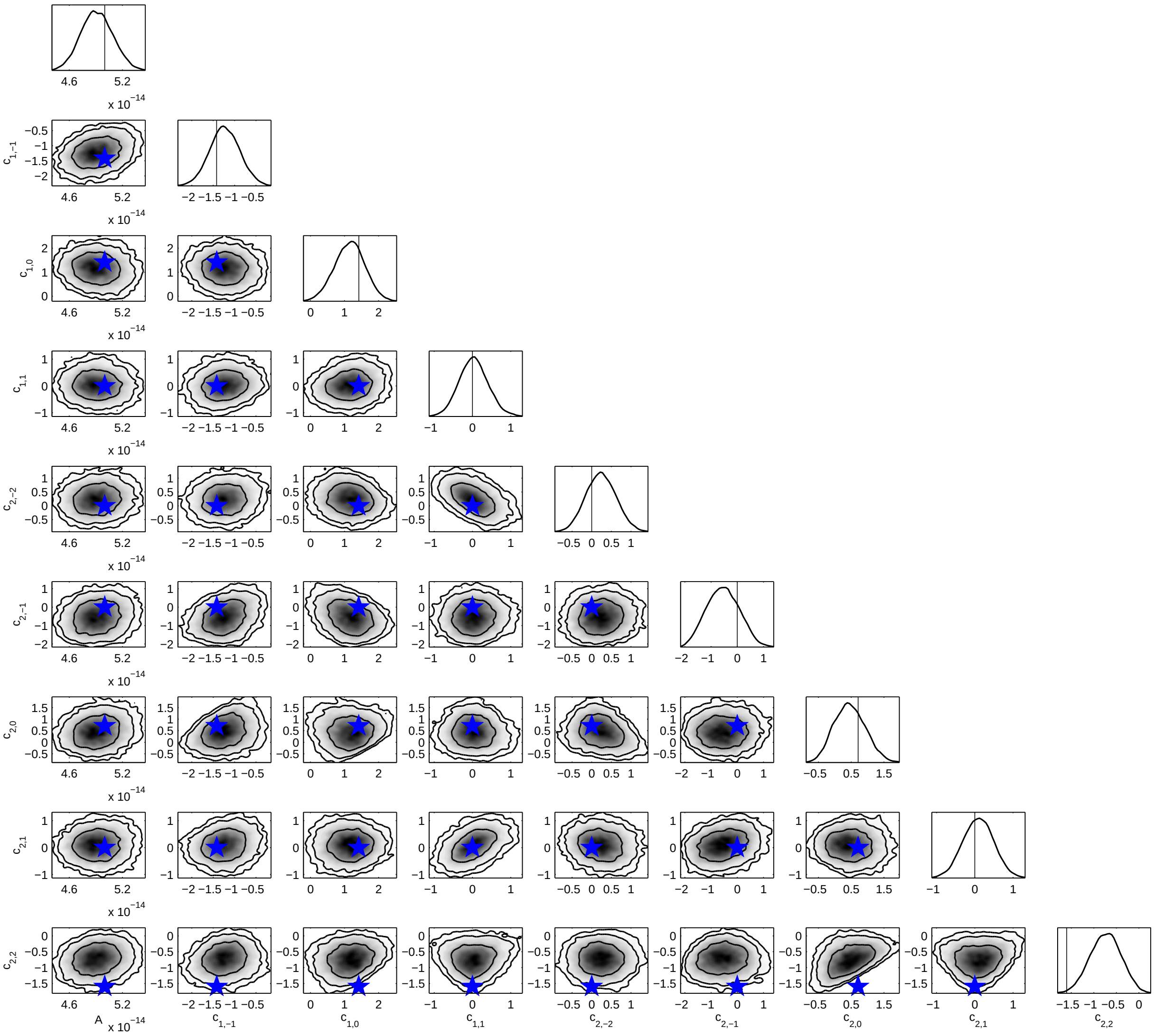

Figure 4.18: Analysis of the same dataset as in Fig. 4.17, but employing a physically-meaningful prior on possible anisotropic distributions, corresponding to only sampling in regions where $\sum_{l,m} c_{lm} Y_{lm}(\hat{\Omega}) \geq 0, \; \forall \, \hat{\Omega}$.

Table 4.2: Testing the ability of the anisotropic-search pipeline to identify the *nature* of the injected anisotropy. We subject datasets with different anisotropies (isotropic, dipole, quadrupole, arbitrary) to isotropic, dipole, quadrupole and arbitrary searches. See text for details on prior choice. The coefficients of the injected anisotropic distribution are $\{c_{0,0} = 2\sqrt{\pi};\ c_{1,-1} = -0.4c_{0,0};\ c_{1,0} = 0.4c_{0,0};\ c_{2,0} = 0.20c_{0,0};\ c_{2,2} = -0.45c_{0,0}\}$. We quote "anisotropy vs. isotropy" log-Bayes factors for each combination of injected and tested anisotropy.

		Injected anisotropy, $\{$details$\}$			
		$l=0$	$l=0,1$	$l=0,2$	$l=0,1,2$
		$\{c_{0,0}=2\sqrt{\pi}\}$	$\{c_{0,0}=2\sqrt{\pi}, c_{1,0}=2\sqrt{\pi/3}\}$	$\{c_{0,0}=2\sqrt{\pi}, c_{2,0}=4\sqrt{\pi/5}\}$	$\{$details in caption$\}$
Tested	$l=0$, $\{A\}$	0.0	0.0	0.0	0.0
anisotropy,	$l=0,1$, $\{A, c_{1,m}\}$	-5.8	2.2	-2.7	5.8
$\{$search	$l=0,2$, $\{A, c_{2,m}\}$	-5.6	-4.4	2.8	8.9
parameters$\}$	$l=0,1,2$, $\{A, c_{l,m}\}$	-10.4	-3.9	-2.3	9.7
	True, $\{A\}$	0.0	8.2	7.7	17.6

means the maximum-likelihood parameter regions will be close to non-physicality. Employing flat priors can therefore help improve the evidence for anisotropy since the high likelihood region stretches beyond the boundary imposed by physicality. Thus, for these cases, the unphysical evidence seems to be a better statistic to use to distinguish models than the physical evidence. Further investigations will be required to determine if this is true more generally, in particular for cases in which the anisotropy is weak. However, we expect that for the weak levels of anisotropy expected in real datasets the physical-prior will be an excellent tool for parameter-estimation and evidence evaluation.

Interpreting the unphysical distributions on the coefficients is more difficult, since they give rise to negative probabilities for certain regions of the sky. However, increasing the relative power of the isotropic $l = 0$ mode can always be used to make the distribution physical, and provide source distributions which are adequately close to the injected distribution. The effect of the unphysical anisotropic coefficients, c_{lm}, on our search is to allow the GWB-correlations to deviate more from the Hellings and Downs curve, allowing some of the noise to be absorbed into these coefficients. This seems to help for the limited number of cases we have considered but further work is required to understand which prior works better in more general situations.

Referring to Table 4.2, we see that the isotropic model is highly favoured when describing the isotropic dataset. The true dipole anisotropy is substantially favoured over an isotropic model when describing the dipole-dataset, and likewise the quadrupole anisotropy is substantially favoured over an isotropic model when describing the quadrupole-dataset. Finally, in the model-comparison of the arbitrary anisotropy dataset, any form of anisotropy is favoured over the isotropic model. The evidence for a quadrupole-anisotropy is actually quite close to the favoured model, which is the true arbitrary-anisotropy. We suspect the reason for this can be understood in terms of how the different anisotropies affect the scatter of correlations around the Hellings and Downs curve, particularly for angular-separations where there are many distinct pulsar-pairings. This is shown in Fig. 4.19, where we see that in the region where there are many distinct pulsar-pairings the quadrupole-anisotropy induces a larger deviation from the Hellings and Downs curve than the dipole-anisotropy. Thus, in this case, a quadrupole-only model is almost as good at describing the arbitrary-anisotropy dataset as the true arbitrary-anisotropy model.

These anisotropy “misfit” examinations confirm that the behaviour of the recovered Bayesian evidence in this formalism conforms to our expectations, and that we would be able to discriminate not only between isotropic and anisotropic backgrounds, but also between different anisotropic models.

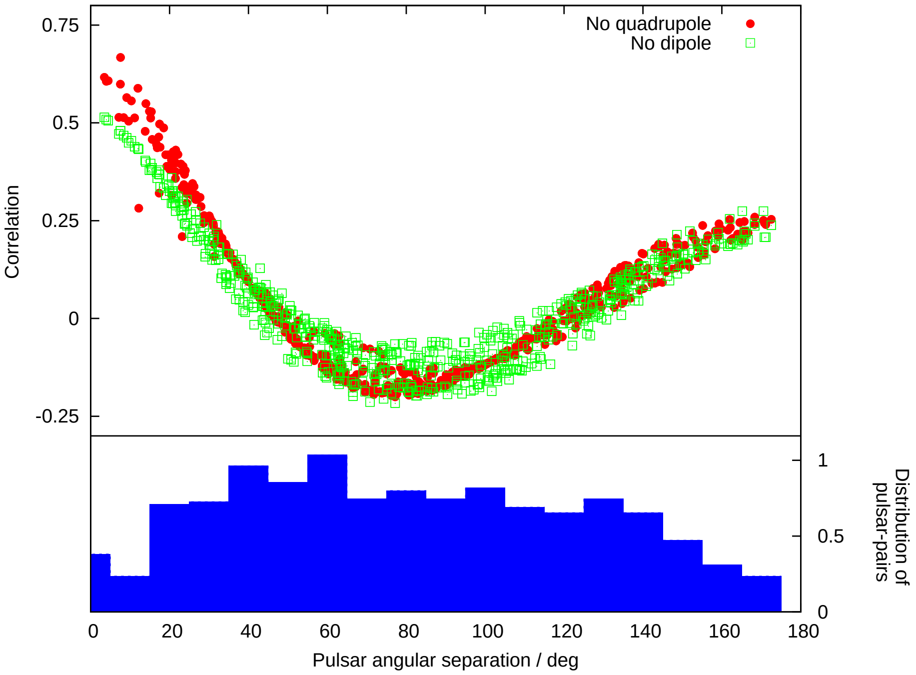

Figure 4.19: We show the angular correlations for pulsar-pairings with non-zero angular-separation in an arbitrary-anisotropy dataset, for the cases where we ignore the contribution from the dipole anisotropy and when we ignore the quadrupole anisotropy. In the region of pulsar angular-separation where there are many distinct pulsar-pairings, the quadrupole-only anisotropy dominates the deviation of correlations from the isotropic Hellings and Downs curve. This may explain why a quadrupole-only model is almost as good as an arbitrary-anisotropy model when describing the arbitrary-anisotropy dataset. Note that zero angular-separation pairings are not shown on the angular-correlation sub-plot, but are included in the pulsar-pairing histogram.

4.7 Summary

We have systematically investigated a robust Bayesian search-pipeline capable of probing anisotropic gravitational-wave backgrounds (GWBs) using pulsar-timing arrays (PTAs). If we have continuous anisotropy in the energy-density of such a GWB, or anisotropy through sparseness of sources comprising our background, then the assumption of isotropy may no longer be an appropriate model with which to perform searches. Recent work has focused on developing new formalisms and techniques with which to generalise the search methodologies [390, 393, 394, 403]. The standard techniques in usage are either stochastic isotropic searches or single-source searches, although the anisotropic pipeline discussed in this chapter will be used in forthcoming EPTA and IPTA searches. Additionally, there have been proposals to directly map out the GW background using either a spherical-harmonic or pixel basis for the stochastic signal [394, 403].

We employed the formalism of Ref. [393], which generalises the cross-correlation of GWB-induced TOA-deviations to anisotropic backgrounds. In an isotropic GWB this cross-correlation has a unique, distinctive signature, being a function only of the angular separation between pulsars on the sky. It is commonly referred to as the Hellings and Downs curve [216]. In the more generalised formalism, the distribution of GWB-power is decomposed as a function of spherical-harmonics, and a set of correlation basis-functions uniquely defined for a particular PTA configuration, although the aforementioned authors have identified useful analytic expressions for these basis-functions up to quadrupole order. Unsurprisingly, the monopole solution, describing the induced correlation for an isotropic distribution, is the usual Hellings and Downs curve. Crucially, the correlation basis-functions for dipole and beyond are no longer independent of the absolute sky-location of the pulsar, being strongly dependent on the placement of the pulsars relative to the distribution of GWB-power.

To thoroughly investigate this formalism, we have developed a suite of new plugins [395] for the popular pulsar-timing analysis software package, TEMPO2. This permits the user to have complete control over the generation of realistic-format datasets, including specifying the array of pulsars, the various noise processes affecting these pulsars, and the ability to inject a GWB signal into these simulated datasets. We have generalised this to inject continuous anisotropies into the GWB signals, and also to permit the inclusion of non-Einsteinian polarisation modes in the GW-signals.

By generalising the cross-correlation of pulsar-timing residuals in a time-domain Bayesian search, we have probed the level of anisotropy in the distribution of GW source-populations making up many background realisations. In particular, we have found that our pipeline can infer the direction of a strong dipole-anisotropy in a loud GWB. Furthermore, by performing Bayesian model-comparison with MULTINEST, a strong dipole or quadrupole anisotropy can be favoured over the standard isotropic search, where we see that the latter is no longer an appropriate model to use. By evaluating the "true-anisotropy vs. isotropy" Bayes factor we find that the best-case scenario for having decisive evidence for a strong dipole or quadrupole anisotropy (in a 36 pulsar dataset) occurs when the rms-residual induced by the GWB is approximately five times greater than the noise rms-residual in each pulsar (proxy SNR $\gtrsim 5$). When a more general search over the anisotropy-coefficients is performed, the log-Bayes factors are degraded, but substantial evidence for the anisotropic signal may become visible at proxy SNRs ≥ 10. We performed a similar analysis with uncorrelated red-noise affecting the pulsars, finding a similar level of required GWB-loudness in order to begin having convincing evidence of anisotropy.

Finally, we tested our search-pipeline on a dataset with the distribution of GWB-power spread over monopole, dipole and quadrupole. As we move to higher multipoles, and hence search dimensions, we propose a hard prior on the anisotropy-coefficients corresponding to the physicality of the implied probability distribution of source-placement on the sky. If this PDF happens to be negative anywhere on the sky for a proposed set of anisotropy-coefficients, then this point is discarded in the sampling process. This is actually quite an informative prior, such that if we are studying a dataset with an anisotropy close to non-physicality then the prior may actually truncate regions of high likelihood in parameter space. This could conceivably have a negative impact on evidence evaluation, however it is very useful for parameter-estimation and will be an excellent tool in real searches where the level of anisotropy is expected to be weak. When this physicality-prior is imposed the *maximum a posteriori* GW-source distribution shows an excellent match to the injected anisotropy.

The search for angular structure in the GWB is the next step in PTA-searches, opening the door to investigations of source-clustering and localisation of GW-hotspots. The author is currently leading both the EPTA and IPTA in their flagship efforts to constrain the levels of anisotropy in a stochastic GWB with arrays of typically $\sim 40 - 50$ millisecond pulsars. In this chapter, we robustly tested an anisotropic stochastic search-pipeline on datasets with a continuous anisotropy in the angular-distribution of sources constituting the injected background. We intend to follow up this first study with a further investigation of the consequences of imposing a hard physical-prior, as well as applying this search-pipeline to datasets with GWBs consisting of realistic populations of inspiraling SMBH binaries. This latter investigation will allow us to understand the effects of source-sparseness and background-finiteness (which occur at higher GW frequencies as the stochasticity of the strain signal breaks down) on the ability to constrain the properties of a GWB. We also intend to perform a systematic investigation of the expected level of anisotropy in realistic source-populations, testing how SMBH binary environment couplings depletes the strain-spectrum at low frequencies and causes a breakdown in stochasticity which may necessitate an anisotropic search. We also plan to investigate the maximum multipole that our current PTAs are sensitive to, as well as a frequentist approach to studying the deleterious effect of using isotropic correlation filters to search for anisotropic backgrounds.

4.A Auto-correlation of GWB-induced timing-residuals

In the following, we give an analytic expression for the auto-correlation of timing-residuals induced by a stochastic GWB with a power-law strain-spectrum. This expression was first derived in Ref. [398], and is currently used in all time-domain Bayesian PTA-pipelines searching for a stochastic background.

The standard approximation for the characteristic strain spectrum of a stochastic GW background is that it is of the form,

$$h_c(f) = A\left(\frac{f}{1\mathrm{yr}^{-1}}\right)^{\alpha}, \tag{4.44}$$

where A is the dimensionless amplitude, and α is the strain spectral index. The one-sided PSD of the GWB-induced timing-residuals is then given by,

$$S(f) \equiv \frac{1}{12\pi^2}\frac{1}{f^3}h_c(f)^2 = \frac{A^2}{12\pi^2}\left(\frac{f}{\mathrm{yr}^{-1}}\right)^{-\gamma}\mathrm{yr}^3, \tag{4.45}$$

where $\gamma \equiv 3 - 2\alpha$. Using the Wiener-Khinchin theorem, which relates the PSD and the auto-correlation of a wide-sense stationary process (i.e., a stochastic process which depends only on $|t_i - t_j|$), we can deduce an analytic expression for the auto-correlation of timing residuals induced by a GWB with a power-law PSD,

$$C(\tau_{ij}) = \mathrm{Re}\left[\int_{f_l}^{f_h} \exp\left(if\tau_{ij}\right)S(f)df\right] = \frac{A^2}{12\pi^2}\int_{f_l}^{f_h}\cos\left(f\tau_{ij}\right)f^{-\gamma}df \tag{4.46}$$

where $\tau_{ij} = 2\pi|t_i - t_j|$. The bounds f_l and f_h denote the sensitivity band of PTA observations: $1/T \lesssim f \lesssim 1/(2\Delta T)$, where T is the total time span of observations and ΔT is the observational cadence. For all real observational scenarios, $T \gg \Delta T$, so in the following we take $f_h \sim \infty$.

Evaluating this integral (with $x = f\tau_{ij}$) gives,

$$\tau_{ij}^{\gamma-1}\int_{f_l\tau_{ij}}^{\infty}\cos(x)x^{-\gamma}dx = \frac{(f_l\tau_{ij})^{1-\gamma}}{(\gamma-1)\tau_{ij}^{1-\gamma}} \times {}_1F_2\left(\left\{\frac{1}{2}-\frac{\gamma}{2}\right\};\left\{\frac{1}{2},\frac{3}{2}-\frac{\gamma}{2}\right\};-\frac{(f_l\tau_{ij})^2}{4}\right)$$
$$+\,\Gamma(1-\gamma)\sin\left(\frac{\pi\gamma}{2}\right)\tau_{ij}^{\gamma-1}, \tag{4.47}$$

where the term of form ${}_pF_q(a_1,\ldots,a_p;c_1,\ldots,c_q;z)$ is a generalised hypergeometric function, defined as,

$${}_pF_q(a_1,\ldots,a_p;c_1,\ldots,c_q;z) = \sum_{n=0}^{\infty}\frac{a_1^{(n)}\ldots a_p^{(n)}}{b_1^{(n)}\ldots b_q^{(n)}}\frac{z^n}{n!}, \tag{4.48}$$

where $y^{(n)}$ refers to the rising factorial $y(y+1)(y+2)\ldots(y+n-1)$. A useful property of rising factorials is that $y^{(n)} = \Gamma(y+n)/\Gamma(y)$, which reduces the hypergeometric function in Eq. (4.47) to

$$\begin{aligned}
&{}_1F_2\left(\left\{\frac{1}{2}-\frac{\gamma}{2}\right\};\left\{\frac{1}{2},\frac{3}{2}-\frac{\gamma}{2}\right\};-\frac{(f_l\tau_{ij})^2}{4}\right)\\
&=\sum_{n=0}^{\infty}(-1)^n\frac{\left(\frac{1}{2}-\frac{\gamma}{2}\right)^{(n)}}{\left(\frac{1}{2}\right)^{(n)}\left(\frac{3}{2}-\frac{\gamma}{2}\right)^{(n)}}\frac{(f_l\tau_{ij})^{2n}}{4^n n!}\\
&=\sum_{n=0}^{\infty}(-1)^n\frac{\Gamma\left(\frac{1}{2}-\frac{\gamma}{2}+n\right)\Gamma\left(\frac{1}{2}\right)\Gamma\left(\frac{3}{2}-\frac{\gamma}{2}\right)}{\Gamma\left(\frac{1}{2}-\frac{\gamma}{2}\right)\Gamma\left(\frac{1}{2}+n\right)\Gamma\left(\frac{3}{2}-\frac{\gamma}{2}+n\right)}\frac{(f_l\tau_{ij})^{2n}}{4^n n!}.
\end{aligned} \tag{4.49}$$

Now, using the properties $\Gamma(y+1) = y\Gamma(y)$, $\Gamma(1/2) = \sqrt{\pi}$, and $\Gamma(1/2+n) = (2n)!\sqrt{\pi}/(4^n n!)$, this becomes,

$$\sum_{n=0}^{\infty}(-1)^n\frac{1-\gamma}{2n+1-\gamma}\frac{(f_l\tau_{ij})^{2n}}{(2n)!}. \tag{4.50}$$

Finally, the analytic expression for the auto-correlation function of a wide-sense stationary process with power-law PSD is,

$$C(\tau_{ij}) = \frac{A^2}{12\pi^2}\left(\frac{1\mathrm{yr}^{-1}}{f_l}\right)^{\gamma-1}\left[\Gamma(1-\gamma)\sin\left(\frac{\pi\gamma}{2}\right)(f_l\tau_{ij})^{\gamma-1}-\sum_{n=0}^{\infty}(-1)^n\frac{(f_l\tau_{ij})^{2n}}{(2n)!(2n+1-\gamma)}\right]. \tag{4.51}$$

It is clear that any terms in $C(\tau_{ij})$ which are dependent on f_l will diverge when f_l tends to zero. Considering the spindown of a pulsar due to the conversion of its rotational energy into EM energy, the phase evolves as $\phi(t) \sim A_1 + A_2 t + A_3 t^2$, where $A_2 \propto \nu$ and $A_3 \propto \dot{\nu}$. Fitting a timing-model to the pulse arrival-times effectively (amongst other things) fits out a quadratic to remove the pulsar spindown contributions to the residuals.

This fitting procedure means that we could make $A_{1,2,3}$ arbitrarily large and the measured post-fit residuals would be the same. The same is true if $A_{1,2,3}$ were not fixed numbers but random numbers drawn from a Gaussian distribution. The correlation due to a random quadratic spindown is,

$$\langle\delta t_i\delta t_j\rangle = \langle A_1^2\rangle+\langle A_1A_2\rangle(t_i+t_j)+2\langle A_2^2\rangle t_it_j+\langle A_1A_3\rangle(t_i^2+t_j^2)+\langle A_2A_3\rangle t_it_j(t_i+t_j)+\langle A_3^2\rangle t_i^2t_j^2. \tag{4.52}$$

Up to $n = 1$ the f_l-dependent terms in $C(\tau_{ij})$ have the same functional dependence on $t_{i,j}$ as a "random" quadratic spindown. $A_{1,2,3}$ can be made arbitrarily large such that f_l-dependent terms (up to $n = 1$) are absorbed into the quadratic spindown (with stochastic coefficients). These terms in $C(\tau_{ij})$ would then be fitted out by the timing-model analysis.

Hence, provided f_l is small enough that $n \geq 2$ terms are negligible, all f_l-dependence in $C(\tau_{ij})$ is removed [399, 402, 404]. We retain knowledge of the fitting-process (essential in reconstructing A, γ in a Bayesian analysis) through the use of the design matrix, M.

4.B Timing-model marginalisation as a projection

A given $(n \times m)$ matrix M can be decomposed into a product of several matrices via a singular-value decomposition (SVD), i.e. $M = U\Sigma V^\dagger$, where $U = (n \times n)$, $\Sigma = (n \times m)$ and $V = (m \times m)$. The matrices U and V are unitary, and hence the columns of these matrices form orthonormal bases.

In the context of pulsar-timing, M is the design matrix, which describes how the TOAs depend on the deterministic timing-model. This timing-model has dimension m, and the pulsar TOAs form a vector of dimension n. We now explicitly separate U into the range- and left null-space of M,

$$M = U\Sigma V^\dagger = \begin{pmatrix} F & G \end{pmatrix} \begin{pmatrix} \sigma \\ 0 \end{pmatrix} V^\dagger, \tag{4.53}$$

where $F = (n \times m)$, $G = (n \times (n-m))$ and $\sigma = (m \times m)$.

The likelihood of measuring a set of post-fit timing residuals $\vec{\delta t}$, given a GWB (with model parameters $\vec{\phi}$) which induces TOA-deviations with covariance $\langle \vec{\delta t}_{\rm GW} \vec{\delta t}_{\rm GW}^T \rangle = C(\vec{\phi})$, and a pulsar timing-model with parameters $\vec{\xi}$ is,

$$\mathcal{L}(\vec{\delta t}|\vec{\phi},\vec{\xi}) = \frac{1}{\sqrt{(2\pi)^n \det(C)}} \times \exp\left(-\frac{1}{2} \left(\vec{\delta t} - M\vec{\xi} \right)^T C^{-1} \left(\vec{\delta t} - M\vec{\xi} \right) \right). \tag{4.54}$$

We now rotate all vectors and matrices into an orthonormal basis defined by the columns of matrix U in the SVD of M. So, $C \rightarrow U^T C U$, $\vec{\delta t} \rightarrow U^T \vec{\delta t}$, and $M\vec{\xi} \rightarrow U^T M \vec{\xi}$. Thus, $\left(\vec{\delta t} - M\vec{\xi} \right)$ becomes

$$\begin{aligned} \left(U^T \vec{\delta t} - U^T M \vec{\xi} \right) &= \begin{pmatrix} F^T \\ G^T \end{pmatrix} \vec{\delta t} - \begin{pmatrix} F^T \\ G^T \end{pmatrix} \begin{pmatrix} F & G \end{pmatrix} \begin{pmatrix} \sigma \\ 0 \end{pmatrix} V^\dagger \vec{\xi} \\ &= \begin{pmatrix} F^T \vec{\delta t} - \sigma V^\dagger \vec{\xi} \\ G^T \vec{\delta t} \end{pmatrix}. \end{aligned} \tag{4.55}$$

Likewise,

$$U^T C U = \begin{pmatrix} F^T \\ G^T \end{pmatrix} C \begin{pmatrix} F & G \end{pmatrix} = \begin{pmatrix} F^T C F & F^T C G \\ G^T C F & G^T C G \end{pmatrix}. \tag{4.56}$$

Now we require some block-matrix algebra. The inverse of a (2×2) block-matrix is,

$$\begin{pmatrix} N & O \\ P & Q \end{pmatrix}^{-1} = \begin{pmatrix} W & X \\ Y & Z \end{pmatrix}, \tag{4.57}$$

$$\begin{aligned} W &= \left(N - O Q^{-1} P \right)^{-1} = N^{-1} + N^{-1} O \left(Q - P N^{-1} O \right)^{-1} P N^{-1}, \\ X &= -\left(N - O Q^{-1} P \right)^{-1} O Q^{-1} = -N^{-1} O \left(Q - P N^{-1} O \right)^{-1}, \\ Y &= -Q^{-1} P \left(N - O Q^{-1} P \right)^{-1} = -\left(Q - P N^{-1} O \right)^{-1} P N^{-1}, \\ Z &= \left(Q - P N^{-1} O \right)^{-1} = Q^{-1} P \left(N - O Q^{-1} P \right)^{-1} O Q^{-1} + Q^{-1}. \end{aligned} \tag{4.58}$$

The argument of the exponential in the likelihood expression is then,

$$\begin{aligned}
&\begin{pmatrix} F^T\vec{\delta t} - \sigma V^\dagger\vec{\xi} \\ G^T\vec{\delta t} \end{pmatrix}^T \left(U^TCU\right)^{-1} \begin{pmatrix} F^T\vec{\delta t} - \sigma V^\dagger\vec{\xi} \\ G^T\vec{\delta t} \end{pmatrix} \\
&= \begin{pmatrix} \vec{\delta t}^T F - \left(\sigma V^\dagger\vec{\xi}\right)^T & \vec{\delta t}^T G \end{pmatrix} \begin{pmatrix} F^TCF & F^TCG \\ G^TCF & G^TCG \end{pmatrix}^{-1} \begin{pmatrix} F^T\vec{\delta t} - \sigma V^\dagger\vec{\xi} \\ G^T\vec{\delta t} \end{pmatrix} \\
&= \vec{\delta t}^T FWF^T\vec{\delta t} - \vec{\delta t}^T FW\left(\sigma V^\dagger\vec{\xi}\right) - \left(\sigma V^\dagger\vec{\xi}\right)^T WF^T\vec{\delta t} + \left(\sigma V^\dagger\vec{\xi}\right)^T W\left(\sigma V^\dagger\vec{\xi}\right) \\
&+ \vec{\delta t}^T GYF^T\vec{\delta t} - \vec{\delta t}^T GY\left(\sigma V^\dagger\vec{\xi}\right) + \vec{\delta t}^T FXG^T\vec{\delta t} - \left(\sigma V^\dagger\vec{\xi}\right)^T XG^T\vec{\delta t} + \vec{\delta t}^T GZG^T\vec{\delta t}.
\end{aligned} \tag{4.59}$$

Collecting the terms which have an explicit dependence on the timing-model parameters, $\vec{\xi}$, gives,

$$\begin{aligned}
&- \vec{\delta t}^T FW\left(\sigma V^\dagger\vec{\xi}\right) - \left(\sigma V^\dagger\vec{\xi}\right)^T WF^T\vec{\delta t} + \left(\sigma V^\dagger\vec{\xi}\right)^T W\left(\sigma V^\dagger\vec{\xi}\right) \\
&- \vec{\delta t}^T GY\left(\sigma V^\dagger\vec{\xi}\right) - \left(\sigma V^\dagger\vec{\xi}\right)^T XG^T\vec{\delta t} \\
&= -\vec{\delta t}^T \left(FW + GY\right)\left(\sigma V^\dagger\vec{\xi}\right) - \left(\sigma V^\dagger\vec{\xi}\right)^T \left(WF^T + XG^T\right)\vec{\delta t} + \left(\sigma V^\dagger\vec{\xi}\right)^T W\left(\sigma V^\dagger\vec{\xi}\right) \\
&= -\vec{\delta t}^T \left(FW - G\left(G^TCG\right)^{-1}\left(G^TCF\right)W\right)\left(\sigma V^\dagger\vec{\xi}\right) \\
&- \left(\sigma V^\dagger\vec{\xi}\right)^T \left(WF^T - W\left(F^TCG\right)\left(G^TCG\right)^{-1}G^T\right)\vec{\delta t} + \left(\sigma V^\dagger\vec{\xi}\right)^T W\left(\sigma V^\dagger\vec{\xi}\right) \\
&= -\vec{\delta t}^T HW\left(\sigma V^\dagger\vec{\xi}\right) - \left(\sigma V^\dagger\vec{\xi}\right)^T WH^T\vec{\delta t} + \left(\sigma V^\dagger\vec{\xi}\right)^T W\left(\sigma V^\dagger\vec{\xi}\right) \\
&= \left[\left(\sigma V^\dagger\vec{\xi}\right) - H^T\vec{\delta t}\right]^T W\left[\left(\sigma V^\dagger\vec{\xi}\right) - H^T\vec{\delta t}\right] - \vec{\delta t}^T HWH^T\vec{\delta t},
\end{aligned} \tag{4.60}$$

where $H = F - G\left(G^TCG\right)^{-1}\left(G^TCF\right)$. The final term is left over from completing the square in $[\ldots]^T W[\ldots]$. It will contribute to the "non-$\vec{\xi}$" terms, which, when collected give,

$$\begin{aligned}
&\vec{\delta t}^T FWF^T\vec{\delta t} + \vec{\delta t}^T GYF^T\vec{\delta t} + \vec{\delta t}^T FXG^T\vec{\delta t} + \vec{\delta t}^T GZG^T\vec{\delta t} - \vec{\delta t}HWH^T\vec{\delta t} \\
&= \vec{\delta t}^T\left(\ldots\right)\vec{\delta t},
\end{aligned} \tag{4.61}$$

where,

$$\begin{aligned}
\left(\ldots\right) &= FWF^T + GYF^T + FXG^T + GZG^T - HWH^T \\
&= FWF^T - G\left(G^TCG\right)^{-1}\left(G^TCF\right)WF^T - FW\left(F^TCG\right)\left(G^TCG\right)^{-1} + GZG^T \\
&\quad - \left[F - G\left(G^TCG\right)^{-1}\left(G^TCF\right)\right]W\left[F^T - \left(G^TCF\right)^T\left(G^TCG\right)^{-1}G^T\right] \\
&= GZG^T - G\left(G^TCG\right)^{-1}\left(G^TCF\right)W\left(G^TCF\right)^T\left(G^TCG\right)^{-1}G^T.
\end{aligned} \tag{4.62}$$

Referring to the block-matrix algebra relations, we see that,

$$Z = \left(G^TCG\right)^{-1}\left(G^TCF\right)W\left(F^TCG\right)\left(G^TCG\right)^{-1} + \left(G^TCG\right)^{-1}. \tag{4.63}$$

Finally, the "non-$\vec{\xi}$" terms reduce to,

$$\vec{\delta t}^T \left(\ldots\right) \vec{\delta t} = \vec{\delta t}^T G \left(G^T C G\right)^{-1} G^T \vec{\delta t}. \tag{4.64}$$

We can write down the posterior distribution marginalised over all timing-model parameters, $\vec{\xi}$, as

$$\int P(\vec{\phi},\vec{\xi}|\vec{\delta t}) d^m \xi = \int \mathcal{L}(\vec{\delta t}|\vec{\phi},\vec{\xi}) \pi(\vec{\phi}) \pi(\vec{\xi}) d^m \xi. \tag{4.65}$$

As mentioned previously, we rotate all the n-dimensional vectors and $(n \times n)$ matrices into the orthonormal basis defined by the columns of U, which is the result of an SVD on the design matrix, M. Hence,

$$\mathcal{L} \equiv \mathcal{L}' = \frac{1}{\sqrt{(2\pi)^n \det\left(U^T C U\right)}} \times \exp\left(-\frac{1}{2}\left(U^T \vec{\delta t} - U^T M \vec{\xi}\right)^T \left(U^T C U\right)^{-1} \left(U^T \vec{\delta t} - U^T M \vec{\xi}\right)\right). \tag{4.66}$$

This transformation splits the likelihood into a product of two components; one term with an explicit dependence on the timing-model parameters, and one without,

$$\mathcal{L}' = \ell_1 \times \ell_2(\vec{\xi}), \tag{4.67}$$

where,

$$\ell_2 = \exp\left(-\frac{1}{2}\left(\left(\sigma V^\dagger \vec{\xi}\right) - H^T \vec{\delta t}\right)^T W \left(\left(\sigma V^\dagger \vec{\xi}\right) - H^T \vec{\delta t}\right)\right). \tag{4.68}$$

Assuming that we have uniform priors on $\vec{\xi}$, integrating over these parameters gives,

$$\int \ell_2(\vec{\xi}) \Pi(\vec{\xi}) d^m \xi = \sqrt{(2\pi)^m \det(\sigma^T W \sigma)^{-1}}. \tag{4.69}$$

We now consider the normalisation pre-factor in $\mathcal{L}'$, which is $1/\sqrt{(2\pi)^n \det(U^T C U)}$. This can be evaluated using block-matrix algebra,

$$\begin{aligned}
\det\left(U^T C U\right) = \det \begin{pmatrix} N & O \\ P & Q \end{pmatrix} &= \det\left(QN - QOQ^{-1}P\right) \\
&= \det(Q) \times \det\left(N - OQ^{-1}P\right) \\
&= \frac{\det(Q)}{\det\left[\left(N - OQ^{-1}P\right)^{-1}\right]} = \frac{\det\left(G^T C G\right)}{\det(W)}.
\end{aligned} \tag{4.70}$$

Finally, we see that marginalising the posterior distribution over uniform-prior timing-model parameters can be described by a projection of quantities into the left null-space of the design matrix, and written as,

$$\begin{aligned}
&\int P(\vec{\phi},\vec{\xi}|\vec{\delta t}) d^m \xi \\
&\quad = \pi(\vec{\phi}) \times \sqrt{\frac{(2\pi)^m \det(W) \det(\sigma^T W \sigma)^{-1}}{(2\pi)^n \det\left(G^T C G\right)}} \times \exp\left(-\frac{1}{2} \vec{\delta t}^T G \left(G^T C G\right)^{-1} G^T \vec{\delta t}\right) \\
&\quad = \frac{\pi(\vec{\phi})}{\det(\sigma)} \times \frac{1}{\sqrt{(2\pi)^{n-m} \det(G^T C G)}} \times \exp\left(-\frac{1}{2} \delta\vec{t}^T G \left(G^T C G\right)^{-1} G^T \delta\vec{t}\right).
\end{aligned} \tag{4.71}$$

A dreamer is one who can only find his way by moonlight, and his punishment is that he sees the dawn before the rest of the world.

Oscar Wilde

The noblest pleasure is the joy of understanding.

Leonardo da Vinci

5

Rapid Searches For Continuous GWs

Abstract

We describe several new techniques which accelerate Bayesian searches for continuous gravitational-wave emission from supermassive black-hole binaries using pulsar timing arrays. These techniques mitigate the problematic increase of search-dimensionality with the size of the pulsar array which arises from having to include an extra parameter per pulsar as the array is expanded. This extra parameter corresponds to searching over the phase of the gravitational-wave as it propagates past each pulsar so that we can coherently include the pulsar-term in our search strategies. Our techniques make the analysis tractable with powerful evidence-evaluation packages like MULTINEST. We find good agreement of our techniques with the parameter-estimation and Bayes factor evaluation performed with full signal templates, and conclude that these techniques make excellent first-cut tools for detection and characterisation of continuous gravitational-wave signals with pulsar timing arrays.

This chapter is based on:
Accelerated Bayesian model-selection and parameter-estimation in continuous gravitational-wave searches with pulsar-timing arrays
Stephen R. Taylor, Justin A. Ellis and Jonathan R. Gair
submitted to Phys. Rev. D (2014), arXiv:1406.5224

5.1 Introduction

The current focus of PTA searches is to uncover evidence for a nanohertz stochastic GW background, most likely composed of many inspiraling SMBH binary signals overlapping in the frequency-domain which cannot be resolved separately [225–227]. While this background may dominate at the lowest detectable frequencies (where the characteristic strain is expected to be largest) at higher frequencies the stochasticity of the signal begins to break down, and in individual Monte Carlo realisations of SMBH binary populations we see single bright sources rising above the level of the unresolved background to become the dominant signal [238, 240, 241]. It stands to reason then that several massive nearby binaries may be bright enough to resolve with PTAs, presenting a unique opportunity to probe the very early inspiral regime of their coalescence, and thereby offering a complementary probe of the massive black-hole population to eLISA/NGO [e.g., 239, 405].

The earliest attempts to constrain the properties of single resolvable sources with PTAs focused on nearby candidate systems. Ref. [406] investigated the level of timing-residuals expected from a binary system in Sgr A*, finding that such a system would be beyond the sensitivity of near-future observations, while other nearby systems may offer a better chance of hosting a detectable binary. A much lauded result of pulsar-timing analysis was when the nearby radio galaxy 3C 66B was ruled-out as hosting a 1.05 year orbital-period[1] SMBH binary system at greater than 95% confidence [269].

Techniques to infer the presence of the expected periodic TOA-deviations induced by a binary source have included both frequentist and Bayesian approaches. Due to the irregular sampling of pulsar TOAs, methods which have implemented power spectral summing [270] or "harmonic summing" [269] have used a Lomb-Scargle periodogram to avoid undesirable spectral leakage. We can also maximise our likelihood statistic over nuisance amplitude parameters to form the $\mathcal{F}$-statistic [407], which has been applied to the detection of nearly-periodic signals in LIGO/Virgo/GEO data [e.g., 408–410], in the eLISA band [e.g., 411], and more recently in the nanohertz-sensitive PTA band [272, 273]. Time-domain techniques are now the favoured approach, and it has been realised that coherently including the "*pulsar-term*" contribution to the timing-residuals from when the GW passed the pulsar is hugely important for detection, sky-localisation, and distance determination [412, 413].

This pulsar-term arises when we integrate the response of pulsar-timing measurements to a GW over the path of the photons, giving contributions to the redshift of signals (and hence deviations to the TOAs) from either end of the Earth-pulsar timing baseline. The *Earth-term* adds coherently, but in previous analyses the pulsar-terms have been ignored as a form of self-noise

---

[1] Alarm bells always ring in pulsar-timing analysis when periodicities close to 1 year appear, since a necessary step involves converting topocentric TOAs to barycentric TOAs.

whose contributions sum incoherently from separate pulsars. However, coherently including the pulsar-term can be regarded as the temporal equivalent of aperture synthesis [412], increasing the baseline of PTA observations by thousands of years, and hence allowing us to track the orbital evolution of binary sources via the imprint of the GW in each distinct pulsar. Full Bayesian parameter estimation and evidence techniques now exist which include the pulsar-term by searching over each pulsar distance [274]. However these typically require significant computational resources to explore the large-dimensional parameter space, and highly-tuned search algorithms to ensure phase coherence when searching over the distance. We side-step these issues by presenting fast techniques designed for a rapid first-analysis of the data, returning Bayes factor and parameter-estimation results which are in good agreement with full searches.

This chapter is arranged as follows. In Sec. 5.2 we review the theory of timing-residuals induced by single resolvable GWs, along with templates to search for binaries which may or may not be evolving over the Earth-pulsar light travel-time. We also introduce our techniques, based on marginalising over the phase variables from each distinct pulsar, thereby collapsing the dimensionality of searches and accelerating evidence recovery. In Sec. 5.3 we compare the results of our model-selection with full searches, and investigate any potential biases in our parameter estimation. We state our conclusions in Section 5.4.

5.2 The signal

The transverse-traceless (TT) gauge GW-tensor can be described as a linear superposition of "plus" and "cross" polarisation modes, with associated polarisation-amplitudes, $h_{\{+,\times\}}$, and basis-tensors, $e_{ab}^{\{+,\times\}}(\hat{\Omega})$. In the context of single-source searches, the direction of GW-propagation, $\hat{\Omega}$, is written as $[-(\sin\theta\cos\phi)\hat{x} - (\sin\theta\sin\phi)\hat{y} - (\cos\theta)\hat{z}]$ such that $(\theta,\phi) = (\pi/2 - \mathrm{DEC}, \mathrm{RA})$ denotes the sky-location of the source in spherical polar coordinates.

As the GW propagates between the Earth and pulsar it creates a perturbation in the metric which causes a change in the proper distance to the pulsar, which in turn leads to a shift in the perceived pulsar rotational frequency. This fractional frequency shift of a signal from a pulsar in the direction of unit vector $\hat{p}$, induced by the passage of a single GW propagating in the direction of $\hat{\Omega}$ is [213, 214],

$$z(t,\Omega) = \frac{1}{2}\frac{\hat{p}^a\hat{p}^b}{1+\hat{\Omega}\cdot\hat{p}}\Delta h_{ab}(t,\Omega), \tag{5.1}$$

where $\Delta h_{ab} \equiv h_{ab}(t_e,\hat{\Omega}) - h_{ab}(t_p,\hat{\Omega})$ is the difference in the metric perturbation evaluated at time t_e when the GW passed the solar system barycentre (SSB) and time t_p when the GW passed the pulsar. From simple geometrical arguments, we can write $t_p = t_e - L(1 + \hat{\Omega}\,\cdot$

$\hat{p}$), where L is the distance to the pulsar. The integral of this *redshift* over time gives the GW contribution to the recorded pulse TOA. Consequently, this means that the timing-models which have been constructed to describe deterministic contributions to the pulsar TOAs (e.g., quadratic spindown) will be slightly mismatched because we have not factored in the influence of GWs. This effect is observed in the *timing-residuals* which are the difference between the raw measured TOAs and the best-fit deterministic timing-model. These residuals encode the influence of noise and all unmodelled phenomena which influence the pulsar TOAs. The pulsar timing-residuals induced by a *single* GW source can be written as,

$$s(t,\hat{\Omega}) = F^{+}(\hat{\Omega})\Delta s_{+}(t) + F^{\times}(\hat{\Omega})\Delta s_{\times}(t) \tag{5.2}$$

where $\Delta s_A(t) = s_A(t_p) - s_A(t_e)$, and $t_{\{p,e\}}$ denote the times at which the GW passes the pulsar and the Earth, respectively. The functions $F^A(\hat{\Omega})$ are "*antenna pattern*" functions encoding the geometrical sensitivity of a particular pulsar to a propagating GW, defined as,

$$F^A(\hat{\Omega}) \equiv \frac{1}{2}\frac{\hat{p}^a\hat{p}^b}{1+\hat{\Omega}\cdot\hat{p}}e^A_{ab}(\hat{\Omega}). \tag{5.3}$$

SMBH binaries are the primary candidate for nanohertz GWs. The population in this band are typically massive ($\gtrsim 10^8 M_\odot$), and in the early, adiabatic inspiral portion of their orbital evolution. Assuming circular orbits, the typical orbital velocity of these systems scales as [412],

$$v \simeq 2.5\times 10^{-2}\left(\frac{f}{10^{-8}\text{ Hz}}\right)^{1/3}\left(\frac{M}{10^8 M_\odot}\right)^{1/3}, \tag{5.4}$$

such that we are dealing with only mildly-relativistic binaries, with $v \ll 1$. Hence, the influence of BH-spin on the GW signal, which modifies the waveform at 1.5 pN ($\propto v^3$), will be completely negligible for PTA observations, while orbital plane precession due to spin-orbit coupling may only be a consideration for the SKA [414, 415]. Preliminary assessments of the importance of binary eccentricity indicate that the majority of the GW power will remain confined to the harmonic at twice the binary orbital frequency [414], however there is a growing concern that couplings between a binary and its environment can induce significant eccentricity, which may require this parameter to be included in waveform templates [235, 242, 416]. We ignore this effect here, and concentrate on circular, non-spinning SMBH binaries.

The periodically varying pulsar timing-residuals induced by a SMBH binary are derived from the quadrupolar waveform, and have the form [273, 412, 417],

$$\begin{aligned}
s_{+}(t) &= \frac{\mathcal{M}^{5/3}}{D_L\omega(t)^{1/3}}\left[-\sin\left[2\left(\Phi(t)-\phi_n\right)\right]\left(1+\cos^2\iota\right)\cos 2\psi\right.\\
&\quad\left.-2\cos\left[2\left(\Phi(t)-\phi_n\right)\right]\cos\iota\sin 2\psi\right]\\
s_{\times}(t) &= \frac{\mathcal{M}^{5/3}}{D_L\omega(t)^{1/3}}\left[-\sin\left[2\left(\Phi(t)-\phi_n\right)\right]\left(1+\cos^2\iota\right)\sin 2\psi\right.\\
&\quad\left.+2\cos\left[2\left(\Phi(t)-\phi_n\right)\right]\cos\iota\cos 2\psi\right],
\end{aligned} \tag{5.5}$$

where ψ is the GW polarisation angle, ι is the binary orbital-inclination angle, ϕ_n is the orbital phase at the line of nodes (defined as the intersection of the orbital plane with the tangent plane of the sky [417]), $\mathcal{M} = (m_1 m_2)^{3/5}/(m_1 + m_2)^{1/5}$ is the binary chirp mass, and D_L is the luminosity distance to the source.

The rate of change of the binary orbital frequency due to GW emission is,

$$\dot{\omega} = \frac{96}{5}\mathcal{M}^{5/3}\omega^{11/3}, \tag{5.6}$$

with which we can derive the orbital frequency and phase,[2] at a given time, t,

$$\begin{aligned} \omega(t) &= \omega_0 \left(1 - \frac{256}{5}\mathcal{M}^{5/3}\omega_0^{8/3} t\right)^{-3/8}, \\ \Phi(t) &\equiv \int_0^t \omega(t')dt' = \Phi_0 + \frac{1}{32\mathcal{M}^{5/3}}\left(\omega_0^{-5/3} - \omega(t)^{-5/3}\right). \end{aligned} \tag{5.7}$$

The characteristic chirp timescale of an inspiraling binary is [274],

$$\tau_{\rm chirp} \sim \frac{\omega_0}{\dot{\omega}_0} = 3.2 \times 10^5 \text{ yr} \left(\frac{\mathcal{M}}{10^8 M_\odot}\right)^{-5/3} \left(\frac{f_0}{10^{-8}\text{ Hz}}\right)^{-8/3}, \tag{5.8}$$

which shows us that frequency and amplitude chirping of the binary over the course of typical PTA observation times ($10 - 20$ years) will be negligible compared to PTA frequency resolution ($\sim 1/T$) [270, 414], and can be safely ignored. Hence, we are looking for essentially monochromatic signals, and as such the *Earth-term* orbital frequency and phase are,

$$\omega_e(t) = \omega_0, \quad \Phi_e(t) = \Phi_0 + \omega_0 t. \tag{5.9}$$

The corresponding variables for the *pulsar-term* must take into account the fact that the GW imprints a snapshot of the binary's orbital evolution as it passes *each* pulsar. As such, we deal with the *retarded time* t_p which causes the pulsar-term to differ in phase from the Earth-term (and all other pulsar-terms) even if there is negligible frequency evolution over the Earth-pulsar light travel-time (highly unlikely). Frequency chirping is a long timescale effect for these systems. Indeed the value of $(\omega_0 - \omega(t_p))/\omega_0$ for a $10^8 M_\odot$ chirp mass binary with $\omega_0 = 10^{-7}$ Hz and $L(1 + \hat{\Omega}\cdot\hat{p}) = 2$ kpc is ~ 0.03. For the highest-mass system considered in this work ($7 \times 10^8 M_\odot$ chirp mass binary with $\omega_0 = 2\pi \times 10^{-8}$ Hz, and most pulsars satisfying $L(1+\Omega\cdot\hat{p}) \leq 1$ kpc) the fractional difference between the Earth- and pulsar-term frequencies is $< 10\%$. Hence we can Taylor-expand Eq. (5.7) (and ignore evolution over the PTA observation window) to give,

$$\begin{aligned} \omega_p(t) &\simeq \omega_0 - \dot{\omega}_0 L(1 + \hat{\Omega}\cdot\hat{p}), \\ \Phi_p(t) &\simeq \Phi_0 + \omega_0 t - \omega_0 L(1 + \hat{\Omega}\cdot\hat{p}) - \dot{\omega}_0 L(1 + \hat{\Omega}\cdot\hat{p})t, \end{aligned} \tag{5.10}$$

---

[2] We assume the phase evolution is driven entirely by GW emission.

where L is the pulsar distance. We note that $\omega_p(t)$ is always less than or equal to the Earth-term frequency, such that a coherent measurement of the pulsar-term would afford an insight into the history of the binary's evolution.

We now have all the definitions we need to construct signal templates describing the pulsar-timing residuals induced by either a non-evolving or evolving SMBH binary. In all of the following we collect Φ_0 and ϕ_n into one constant *initial phase* variable, $\phi_0 = \phi_n - \Phi_0$.

5.2.1 Non-evolving template

Consider the low-frequency (or low chirp-mass) regime, where evolution of the source frequency is small, such that the frequencies of the GW when it passes the pulsar and the Earth are approximately the same. We can include the pulsar-term in our single-source template by modelling the signal in a single pulsar as the sum of two sinusoids of different phases. The signal template in the α^{th} pulsar is [273],

$$s_\alpha = \sum_{i=1}^{2} a_{i\alpha}(\zeta, \iota, \psi, \phi_0, \phi_\alpha, \theta, \phi) A^i_\alpha(t, \omega_0), \tag{5.11}$$

where,

$$\begin{aligned} a_{1\alpha} &= \left[q_{1\alpha}\left(1 - \cos\phi_\alpha\right) - q_{2\alpha}\sin\phi_\alpha\right] \\ a_{2\alpha} &= \left[q_{2\alpha}\left(1 - \cos\phi_\alpha\right) + q_{1\alpha}\sin\phi_\alpha\right] \qquad (5.12) \\ q_{1\alpha} &= \left(F^+_\alpha a_1 + F^\times_\alpha a_3\right) \\ q_{2\alpha} &= \left(F^+_\alpha a_2 + F^\times_\alpha a_4\right), \qquad (5.13) \\ & \qquad (5.14) \end{aligned}$$

and,

$$\begin{aligned} a_1 &= \zeta\left[\left(1 + \cos^2\iota\right)\cos 2\phi_0 \cos 2\psi + 2\cos\iota \sin 2\phi_0 \sin 2\psi\right] \\ a_2 &= -\zeta\left[\left(1 + \cos^2\iota\right)\sin 2\phi_0 \cos 2\psi - 2\cos\iota \cos 2\phi_0 \sin 2\psi\right] \\ a_3 &= \zeta\left[\left(1 + \cos^2\iota\right)\cos 2\phi_0 \sin 2\psi - 2\cos\iota \sin 2\phi_0 \cos 2\psi\right] \\ a_4 &= -\zeta\left[\left(1 + \cos^2\iota\right)\sin 2\phi_0 \sin 2\psi + 2\cos\iota \cos 2\phi_0 \cos 2\psi\right]. \end{aligned} \tag{5.15}$$

In the above equations, $\phi_\alpha = 2\omega_0 L_\alpha(1 + \hat{\Omega}\cdot\hat{p})$ and $\zeta = \mathcal{M}^{5/3}/D_L$. The signal basis-functions are defined as,

$$A^1_\alpha = \frac{1}{\omega_0^{1/3}}\sin(2\omega_0 t), \quad A^2_\alpha = \frac{1}{\omega_0^{1/3}}\cos(2\omega_0 t). \tag{5.16}$$

We employ the log-likelihood ratio as a statistic for parameter-estimation and detection. This statistic is defined as the logarithm of the ratio of the likelihood of a signal being present to the signal being absent,

$$\ln\Lambda \equiv \ln p(\vec{r}|\vec{s}) - \ln p(\vec{r}|\vec{0}) = \sum_{\alpha=1}^{N_p}\left[(r_\alpha|s_\alpha) - \frac{1}{2}(s_\alpha|s_\alpha)\right], \tag{5.17}$$

where we have defined an inner product such that $(x|y) = x^T G(GCG)^{-1}G^T y$, where: (i) C is a covariance matrix describing stochastic influences to the pulsar TOAs; (ii) G is a timing-model marginalisation matrix [399]; and (iii) r_α is a vector of timing-residuals in the α^{th} pulsar. With well-constrained pulsar noise properties (fixed C) we can use Λ within a Bayesian search to recover parameter posterior distributions. In this way we can also use Λ to substitute for the full likelihood in the Bayesian evidence evaluation to recover the *Bayes factor*, allowing for a direct recovery of detection significance in a Bayesian way. Implicit in the derivation of Eq. (5.17) is the cancellation of the normalisation factor of the full likelihood (which is a function of C). This remains true when we form the evidence ratio, since we integrate over the deterministic signal parameter space and assume that stochastic noise properties are fixed. Explicitly,

$$\begin{aligned}\mathcal{B} &= \frac{\mathcal{Z}_{\text{signal}}}{\mathcal{Z}_{\text{null}}}\\ &= \frac{\int \exp\left[-(r-s(\vec{\mu})|r-s(\vec{\mu}))/2\right]\pi(\vec{\mu})d^N\mu}{\int \exp\left[-(r|r)/2\right]\pi(\vec{\mu})d^N\mu}\\ &= \frac{\int \exp\left[(r|s(\vec{\mu})) - (1/2)(s(\vec{\mu})|s(\vec{\mu}))\right]\pi(\vec{\mu})d^N\mu}{\int \pi(\vec{\mu})d^N\mu}\\ &= \int \Lambda(\vec{\mu})\pi(\vec{\mu})d^N\mu.\end{aligned} \tag{5.18}$$

For the purposes of later analysis, we now write $\ln\Lambda$ explicitly in terms of the pulsar-phase parameters, ϕ_α. Defining

$$\begin{aligned}N^i_\alpha &= (r_\alpha|A^i_\alpha),\\ M^{ij}_\alpha &= (A^i_\alpha|A^j_\alpha),\end{aligned} \tag{5.19}$$

and

$$\epsilon_i{}^j = \begin{pmatrix} 0 & 1\\ -1 & 0\end{pmatrix}, \tag{5.20}$$

such that

$$\begin{aligned}\ln\Lambda = \sum_{\alpha=1}^{N_p}\Big\{ &\left[q_{i\alpha}q_{j\alpha}M^{ij}_\alpha - q_{i\alpha}N^i_\alpha\right]\cos\phi_\alpha + \left[q_{k\alpha}q_{j\alpha}M^{ij}_\alpha - q_{k\alpha}N^i_\alpha\right]\epsilon_i{}^k\sin\phi_\alpha\\ &- \frac{1}{2}q_{i\alpha}q_{j\alpha}M^{ij}_\alpha\cos^2\phi_\alpha - \frac{1}{2}q_{k\alpha}q_{l\alpha}M^{ij}_\alpha\epsilon_i{}^k\epsilon_j{}^l\sin^2\phi_\alpha\\ &- q_{i\alpha}q_{k\alpha}M^{ij}_\alpha\epsilon_j{}^k\sin\phi_\alpha\cos\phi_\alpha + q_{i\alpha}N^i_\alpha - \frac{1}{2}q_{i\alpha}q_{j\alpha}M^{ij}_\alpha\Big\}.\end{aligned} \tag{5.21}$$

where N_p is the number of pulsars in our array. With negligible frequency evolution, the binary's parameters are $\{\zeta, \omega_0, \theta, \phi, \iota, \psi, \psi_0\}$, however we must also take into account an additional phase variable per pulsar, ϕ_α. Hence, in a parameter-estimation search or an evaluation of the Bayes factor, conventional techniques would require a search over $7 + N_p$ dimensions. For large arrays or expensive likelihood evaluations this can be a costly exercise, necessitating multi-threading linear-algebra operations to accelerate the likelihood evaluations, or multi-core machines to perform efficient parallel-tempering for the evaluation of Bayes factors. One should also note that the popular and effective Bayesian inference tool MULTINEST can struggle in these kinds of high-dimensional problems (even in constant efficiency mode) when we have complicated parameter spaces or lengthy likelihood evaluation times, as the set of live-points used in the nested sampling algorithm very slowly accumulates the last few units of log-evidence.[3]

5.2.2 Evolving template

We can also write down an evolving-signal template which takes into account the orbital evolution of the SMBH binary during the Earth-pulsar light travel-time, but still assumes evolution during the actual PTA observation window is negligible. For this evolving-signal template, we define,

$$\begin{aligned} A^1_\alpha &= \frac{1}{\omega_0^{1/3}}\sin(2\omega_0 t), \quad & A^2_\alpha &= \frac{1}{\omega_0^{1/3}}\cos(2\omega_0 t) \\ B^1_\alpha &= \frac{1}{\omega_{p,\alpha}^{1/3}}\sin(2\omega_{p,\alpha} t), \quad & B^2_\alpha &= \frac{1}{\omega_{p,\alpha}^{1/3}}\cos(2\omega_{p,\alpha} t), \end{aligned} \tag{5.22}$$

where $\omega_{p,\alpha} = \omega_0 - \dot{\omega}_0 L_\alpha(1 + \hat{\Omega}\cdot\hat{p}_\alpha)$, $\dot{\omega}_0 = (96/5)\mathcal{M}^{5/3}\omega_0^{11/3}$, and L_α is the distance to the α^{th} pulsar.

In addition to M^{ij} and N^i for the non-evolving case, we define,

$$\begin{aligned} O^{ij}_\alpha &= (B^i_\alpha | B^j_\alpha), \\ P^i_\alpha &= (r_\alpha | B^i_\alpha), \\ Q^{ij}_\alpha &= (A^i_\alpha | B^j_\alpha). \end{aligned} \tag{5.23}$$

Now, expressing the log-likelihood ratio explicitly in terms of the pulsar-phase parameters,

---

[3] Certain alternative approaches to this have been proposed for MULTINEST, such as the use of importance nested sampling in constant-efficiency mode [279], or employing a trained neural network [418] to accelerate the final stages of sampling.

ϕ_α, gives the following,

$$\begin{aligned}\ln\Lambda = \sum_{\alpha=1}^{N_p} \Big\{ & \left[q_{i\alpha} q_{j\alpha} Q^{ij}_\alpha - q_{i\alpha} P^i_\alpha\right] \cos\phi_\alpha + \left[q_{k\alpha} q_{j\alpha} Q^{ji}_\alpha - q_{k\alpha} P^i_\alpha\right] \epsilon_i{}^k \sin\phi_\alpha \\ & - \frac{1}{2} q_{i\alpha} q_{j\alpha} O^{ij}_\alpha \cos^2\phi_\alpha - \frac{1}{2} q_{k\alpha} q_{l\alpha} O^{ij}_\alpha \epsilon_i{}^k \epsilon_j{}^l \sin^2\phi_\alpha \\ & - q_{i\alpha} q_{k\alpha} O^{ij}_\alpha \epsilon_j{}^k \sin\phi_\alpha \cos\phi_\alpha + q_{i\alpha} N^i_\alpha - \frac{1}{2} q_{i\alpha} q_{j\alpha} M^{ij}_\alpha \Big\}. \end{aligned} \tag{5.24}$$

5.2.3 Techniques for maximisation and marginalisation over ϕ_α

By explicitly exposing ϕ_α in our expressions for the likelihood-ratio, we have developed several alternative approaches designed to approximate maximisation or marginalisation of the likelihood-ratio over these pulsar-phase variables.

Firstly, in the context of non-evolving templates, Ref. [273] noted that one can avoid the formalism of the $\mathcal{F}_p$ statistic (which maximises the likelihood-ratio over $2N_p$ "amplitude" parameters [$a_{i\alpha}$ in Eq. (5.11)] despite there being only $7+N_p$ independent parameters). Improving upon the $\mathcal{F}_p$ statistic is desirable, since as we expand the number of pulsars in our array the disparity between the dimensionality of the parameter-space assumed by the $\mathcal{F}_p$ statistic and the true *physical* parameter-space grows larger. Rather than maximising over these nuisance "amplitude" parameters, we can instead analytically maximise over the *physical* ϕ_α parameters. This requires solving a quartic equation in $x = \cos\phi_\alpha$ which is guaranteed to have at least one unique solution, although whether that solution satisfies the requirement $-1 \leq x \leq 1$ must be ascertained on the fly. We can of course, avoid this completely by *numerically* maximising over the pulsar-phase parameters. This is **Technique** $\#1$, and constitutes a more appropriate maximisation than $\mathcal{F}_p$. Nevertheless, we are still left with the problem of searching over the remaining 7-dimensional parameter space; this is a much more tractable problem and can be handled with many off-the-shelf MCMC or nested-sampling algorithms. In this case, we should not be surprised if a bias is observed in the posterior distributions of the final 7 parameters, since we are after all *maximising* over N_p other parameters.

The second option is to avoid maximising entirely, and instead marginalise the likelihood-ratio over the pulsar-phase parameters. Note that we can analytically marginalise over the amplitudes of the signal basis-functions in Eq. (5.11) with uniform-priors to get the Bayes factor for a common-frequency signal in pulsar TOAs. We do not discuss this further here, but provide the derivation and a brief analysis in Appendix 5.B. The approach we follow here is to *numerically* marginalise over the pulsar-phase parameters, such that we actually sample the marginalised likelihood-ratio in our MCMC or nested-sampling algorithms. In particular, if we can do this without increasing the likelihood evaluation time significantly, then the collapse of the dimensionality makes this problem tractable with MULTINEST. There are many benefits to this; for example, MULTINEST is an excellent tool for sampling multimodal distributions, it has inbuilt parallelisation, and in low-dimensionality provides an efficient means to evaluate the Bayesian evidence. Hence, the numerical marginalisation of the non-evolving template over pulsar-phase parameters is our **Technique** $\#2$.

As a final point of interest for non-evolving templates, we note that if there are sufficiently many wave cycles during the observation time of the pulsars in our array, then it is possible to maximise over the pulsar-phase parameters analytically without the need to solve a quartic. More interestingly, it is also possible to analytically marginalise over the pulsar-phase parameters. The noise behaviour of real pulsars and the GW frequencies to which we are most sensitive will likely prohibit us from making the assumptions required to analytically maximise/marginalise in this fashion. However, we provide the derivation and a brief analysis in Appendix 5.A, where we find that this analytic marginalisation may be able to place useful constraints on the values of $\zeta = \mathcal{M}^{5/3}/D_L$ and the orbital frequency of a SMBH binary, but sky-localisation and Bayesian evidence recovery is biased.

There are two ways to proceed with an evolving template, but both involve numerical marginalisation over the pulsar-phase parameters. In **Technique** $\#3$ we compute $\omega_{p,\alpha}$ by fixing L_α to its catalogued value, while in **Technique** $\#4$ we internally average over the prior distribution of L_α by drawing the distance used to compute $\omega_{p,\alpha}$ from a Gaussian centred on the catalogued value with standard-deviation given by the catalogued error-bars.

Even though the pulsar-phase has an explicit dependence on the pulsar-distance, including the distance in parameter estimation can produce practical difficulties, as a small change in the distance may have a relatively small effect on the pulsar-term frequency, $\omega_{p,\alpha}$, but can have a huge impact on the phase coherence [274, 412]. Without sub-pc precisions on measured pulsar-distances the possibility of including the pulsar-term in a coherent analysis might seem beyond reach. However, Ref. [274] overcomes this by sampling the distances on two scales; one is very small to maintain phase coherence, while the other is larger (on the order of kpc) to solve for the pulsar-term frequency. Regardless, highly-tuned jump proposals for any stochastic sampling approach seem necessary when trying to incorporate the pulsar-term in a coherent analysis. Our approximation side-steps this problem by marginalising over the pulsar-phase and drawing L_α from within its prior to calculate $\omega_{p,\alpha}$. We achieve significant accelerations with respect to the full search in two ways: (1) we perform an 8D search with a likelihood that executes $N_p \times 1$D numerical integrations, as opposed to having to stochastically sample from an $(8+N_p)$D space; (2) this 8D search can be highly parallelised with MULTINEST to minimise search times, as opposed to the lengthy burn-in times and prohibitive autocorrelation lengths associated with high-dimensional MCMC searches.

Table 5.1: Pulsar distances taken from Ref. [419] if available, or otherwise from the ATNF catalogue [420].

Pulsar	White-noise RMS / ns	Time-span / yr	Pulsar distances / kpc
J0030+0451	792	12.7	0.28 ± 0.1
J0437-4715	69	14.8	0.156 ± 0.001
J1640+2224	410	14.9	1.19 ± 0.238
J1713+0747	136	18.3	1.05 ± 0.06
J1744-1134	366	16.9	0.42 ± 0.02
J1857+0943	402	14.9	0.9 ± 0.2
J1909-3744	100	9.0	1.26 ± 0.03
J1939+2134	141	16.3	5.0 ± 2.0
J2317+1439	412	14.9	1.89 ± 0.38

5.3 Results

While a full analysis of these techniques in all conceivable situations is beyond the scope of this study, we rigorously test what we expect to be the most promising new technique. **Technique** $\#4$ (which from now we denote as the $\mathcal{M}_p$ statistic) is subjected to a program of systematic injection and recovery of simulated signals, using the PALSIMULATION code which is part of the PAL package [421] being developed as a unifying suite of tools for pulsar timing analysis. The performance of **Technique** $\#3$ closely follows that of **Technique** $\#4$, which is unsurprising since they involve similar methods. Furthermore, we expect no systematic bias from **Technique** $\#2$ other than that which is introduced by analysing an evolving signal with a non-evolving formalism.

The datasets we generated were of the following configurations;

- **Type I:** 36 pulsars, 5 years of observations, 2 week cadence, 100 ns RMS white-noise per pulsar, $L_{\rm psr} = 1 \pm 0.1$ kpc $\forall$ pulsars; equivalent to the assumptions of the first OPEN dataset in the IPTA MDC.
- **Type II:** 9 pulsars, variable observation time-span, average 2 week cadence, realistic white-noise, $L_{\rm psr}$ equal to catalogued values.
- **Type III:** 9 pulsars, variable observation time-span, average 2 week cadence, realistic white-noise, $L_{\rm psr}$ drawn from Gaussian distribution (mean=catalogued-value, standard-deviation=catalogued-error).

The observation time-spans, white-noise RMS values, and distances for the 9 pulsars in Type II and Type III datasets are shown in Table 5.1.

5.3.1 Model selection

We evaluate the accuracy of the Bayes factors returned by these pulsar-phase marginalisation techniques by injecting signals into various noise realisations at various SNRs. The SNR in these cases is defined as $\mathrm{SNR}^2 = \sum_\alpha \left(s\left(\vec{\mu}_{\rm inj}\right)|s\left(\vec{\mu}_{\rm inj}\right)\right)_\alpha$. We compare the recovered Bayes factors with those obtained by employing parallel-tempering and thermodynamic integration with the full signal template (and searching for the pulsar-distances). Parallel tempering is a method of launching many MCMC chains of varying "temperature" designed to aggressively search parameter space, and avoid trapping of chains in local likelihood maxima. Each chain has a different target distribution, $p(\vec{\mu}|D,\beta) \propto p(\vec{\mu})p(D|\vec{\mu})^\beta$, where β is the inverse temperature and varies between 0 and 1. Higher temperatures effectively flatten out the likelihood surface, and explore regions far from maximum. A multi-temperature Hastings ratio is employed to ensure mixing of the chains and rapid localisation of the global maximum. After exploration the different chains can be processed via thermodynamic integration to give an estimate of the Bayesian evidence [e.g., 422]. The evidence for a chain with inverse temperature β is simply,

$$\mathcal{Z}_\beta = \int d\vec{\mu}\; p(\vec{\mu})p(D|\vec{\mu})^\beta, \tag{5.25}$$

such that,

$$\begin{aligned}\ln\mathcal{Z} &= \int_0^1 d\beta\; \frac{\partial \ln \mathcal{Z}_\beta}{\partial\beta} \\ &= \int_0^1 d\beta \int d\vec{\mu}\; \frac{p(\vec{\mu})p(D|\vec{\mu})^\beta}{\mathcal{Z}_\beta}\ln p(D|\vec{\mu}) \\ &= \int_0^1 d\beta\; \langle \ln p(D|\vec{\mu})\rangle_\beta, \end{aligned} \tag{5.26}$$

where $\langle\cdot\rangle_\beta$ denotes an expectation value with respect to the target posterior of inverse temperature β. For details on the parallel tempering and thermodynamic integration techniques employed here, see Ref. [274, 423] and references therein.

The signal we inject matches that explored in Ref. [274], which is at the sky-location of the Fornax cluster. Recent work has shown that there may be potential single GW source "hot spots" in the Virgo, Fornax and Coma clusters [424]. Regardless, we are only interested in sensible parameters to form an injected signal. These parameters are $\{\mathcal{M}, D_L, f_0, \phi, \cos\theta, \cos\iota, \psi, \phi_0\} = \{7\times 10^8 M_\odot, -, 10^{-8}\mathrm{Hz}, 0.95, -0.56, 0, 1.26, 2.65\}$, where the luminosity distance D_L is scaled to suit the desired SNR.

Another important aspect is our choice of prior on $\mathcal{M}$, D_L and f_0. We employ log-uniform priors on these variables, but also apply a cut on the characteristic-strain induced by the binary, where we define $h_0 = 4\sqrt{2/5}\omega_0^{2/3}\zeta$ and require $h_0 \leq h_{0,c}\left(f_{\rm gw}/10^{-8}\mathrm{Hz}\right)^{2/3}$, where $h_{0,c} = 10^{-13}$. We use Monte Carlo integration to compute the prior re-normalisation, which only leads

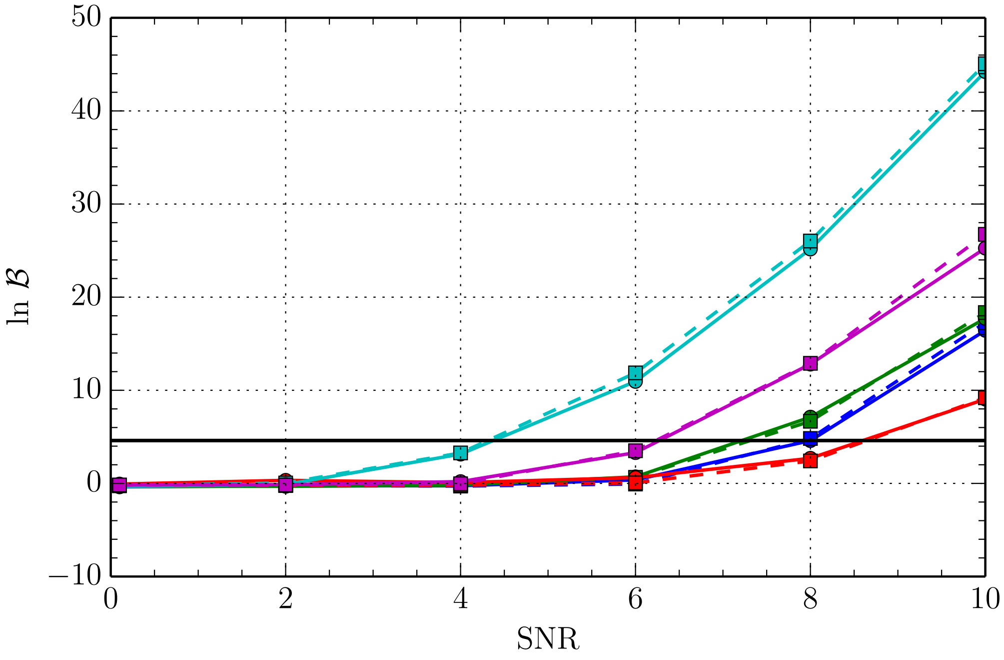

(a)

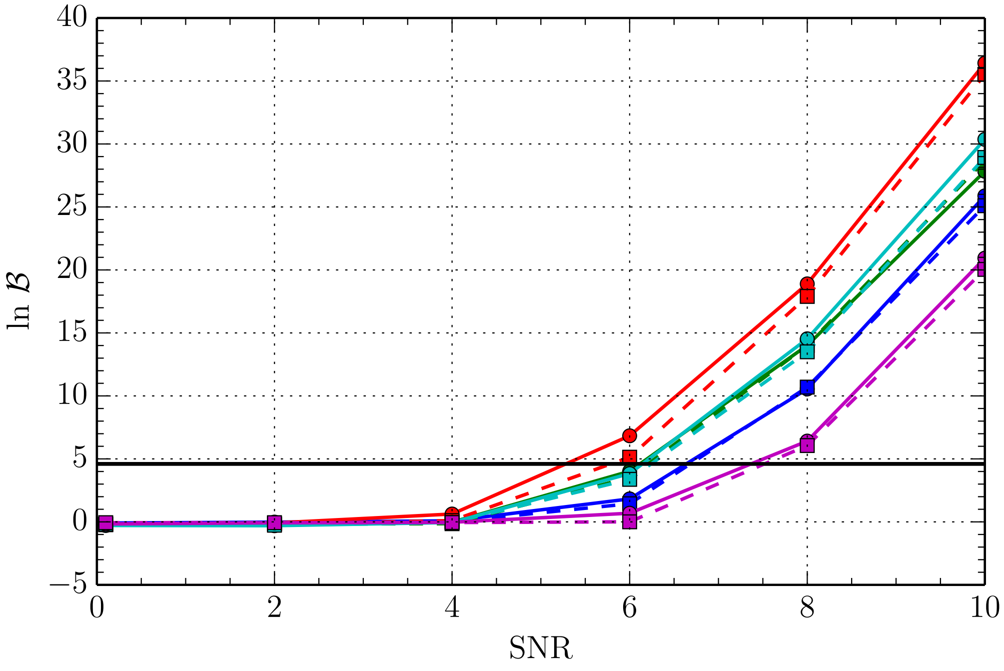

(b)

Figure 5.1: A comparison of the computed posterior odds-ratios ($\ln \mathcal{B}$) evaluated using thermodynamic integration of the full signal model (solid lines), and the technique of numerically marginalising over the pulsar-phase parameters while sampling from the pulsar-distance prior ($\mathcal{M}_p$ statistic; dashed lines). Different SNR signals are injected into a variety of realisations of Type I and Type III datasets. The agreement found between the two methods is excellent.

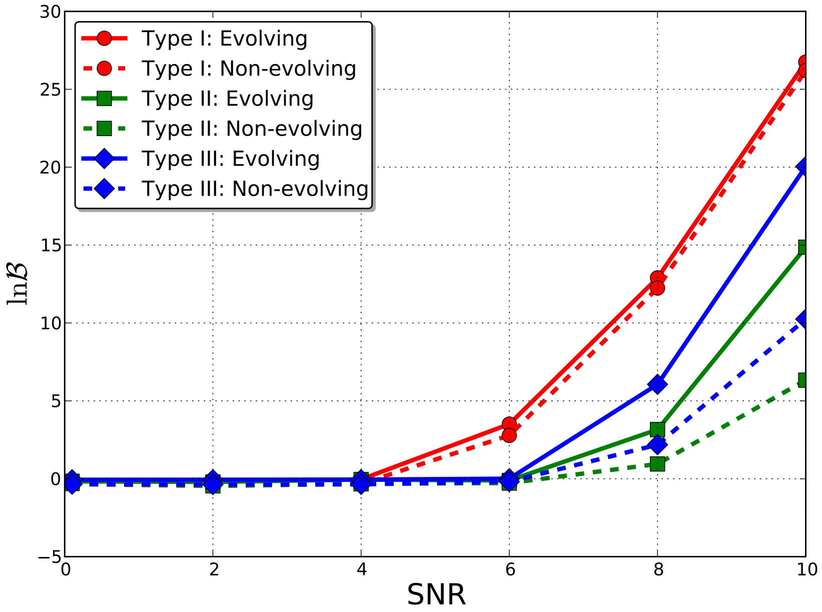

Figure 5.2: For a given realisation of noise, we repeat the analysis of Type I/II/III datasets with a non-evolving template. We see that the mismatch between the assumption of a non-evolving signal and the reality of an evolving-binary injection leads to Bayes factors which can be significantly below the optimal evolving-model values.

to a change in log odds-ratio of $\lesssim 0.1$. However, this cut had practical value in limiting the high-strain parameter space which was inhibiting our thermodynamic integration from converging to the true evidence value with a reasonable number of temperature chains. Also, this is a cheap way to impose a correlated prior on chirp mass, luminosity distance and GW frequency [423].

The comparison between an evaluation of the posterior odds ratio performed by the full thermodynamic integration (solid lines) and the $\mathcal{M}_p$ statistic (dashed lines) for Type I and Type III datasets of various injected SNR is shown in Fig. 5.1, where we see excellent agreement for a variety of different noise realisations. For realistic Type III datasets, we in fact see that the $\mathcal{M}_p$ statistic gives a mildly conservative estimate of the full Bayes factor. We find that the speed of the numerical-marginalisation techniques depend on the SNR of the injection, where for low to moderate SNR ($\sim 0-2$) the evidence and parameter-estimation stages of MULTINEST completed within *only a few minutes* of wall-time on 48 computational cores. The highest SNR injections (SNR $= 10$) required longer, but still finished within ~ 45 minutes of wall-time on 48 cores. The reason for this trend is that the likelihood at low SNR is broad and featureless in the pulsar-term phase parameters, allowing the numerical integration routines to converge rapidly to a solution. In comparison, thermodynamic integration took more than a day for a single dataset analysis with similar computational resources.

Analysing these datasets using the numerical phase marginalisation with a non-evolving template (**Technique** $\#2$), we find that the mismatch between the model and the evolving-signal injections leads to Bayes factors which can be significantly below the optimal evolving-model values. This is illustrated for a single noise realisation in Figure 5.2. We will revisit this in the next section.

5.3.2 Parameter estimation

To ascertain whether numerical marginalisation techniques introduce any systematic bias in parameter recovery, we inject SNR $= 8$ signals into various white-noise realisations. The injected binary orbital frequency is chosen to be 10^{-8} Hz such that the GW frequency lies close to the peak sensitivity of an array of pulsars observed over a period of $\gtrsim 5$ years (see Ref. [425] for a full discussion of Bayesian and frequentist continuous-wave sensitivity curves, and Ref. [423] for the latest NANOGrav continuous-wave sensitivity curves.). We choose injected chirp masses of $7 \times 10^8 M_\odot$ and $1.8 \times 10^8 M_\odot$ in order to model a strongly evolving (over the Earth-pulsar light-travel time), and weakly evolving binary respectively, where the lower mass injection will have an $\dot{\omega}$ which is $\sim 10\%$ of the higher mass.

These evolving and weakly-evolving binaries are injected into 100 different noise-realisations of Type II datasets. This type of dataset is used because we want the characteristics of the PTA to remain fixed, such that the injected binary's luminosity distance, D_L, (which is scaled to accommodate the desired SNR) is constant over each realisation. The remaining binary parameters are injected with the following values into each dataset; $\{\phi = 1, \cos\theta = 0.48, \cos\iota = 0.88, \psi = 0.5, \phi_0 = 2.89\}$.

We present results for the case of the $\mathcal{M}_p$ statistic, which should be applicable regardless of whether the binary is evolving or not. We again note that no bias would be expected within **Technique** $\#2$, which numerically marginalises over the pulsar-phase variables in the non-evolving formalism. The only bias expected here derives from the inherent limitations of applying an inappropriate non-evolving model to a possibly evolving signal.

Our method of testing for systematic bias in the use of the $\mathcal{M}_p$ statistic is an extension of a method used in Ref. [426] to validate the accuracy of a first-order likelihood approximation in a stochastic background search. As discussed there, the benchmark of internal consistency is when, in $x\%$ of realisations, the set of injected parameters lies within the inner $x\%$ of the marginalised posterior distribution. The inner high-probability region is defined as,

$$\int_W p(\vec{\theta}) d^N\theta = a, \tag{5.27}$$
$$W = \{\theta^1, \theta^2, \ldots, \theta^N \in \mathbb{R} : p(\vec{\theta}) > \mathcal{L}_a\},$$

where $\mathcal{L}_a > 0$ is some value unique to each a corresponding to a curve of equal probability in the N dimensional parameter space.

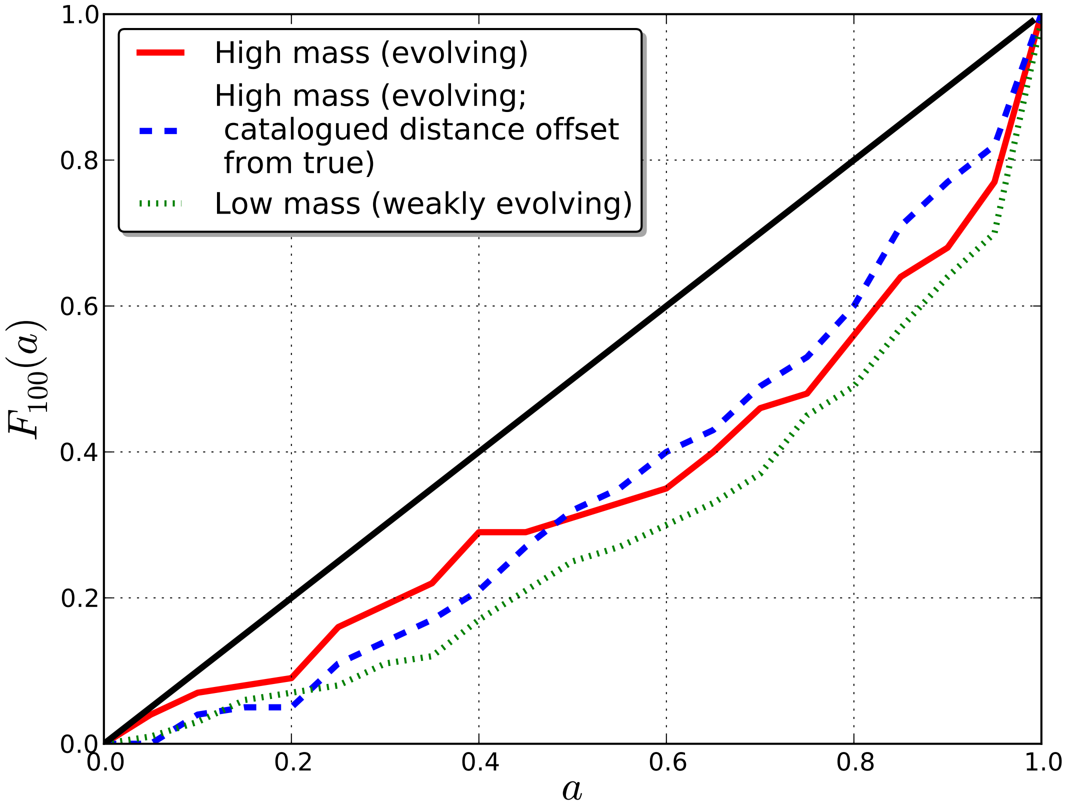

Figure 5.3: The fraction of injections which are "closer" in the chi-squared sense (see text) to the set of points lying inside credible-interval, a, is plotted against the credible-interval. The line of zero-bias is shown as a thick, black-line, while the results of an analysis of 100 realisations of evolving/non-evolving Type II datasets using numerical-marginalisation (the $\mathcal{M}_p$ statistic) are shown as solid-red and dashed-blue. The dashed-green line shows the result for when we offset our catalogue of distances from their true values by an amount consistent with their error-bars. While some bias is present, this plot does not indicate how that manifests in the physical parameter-space.

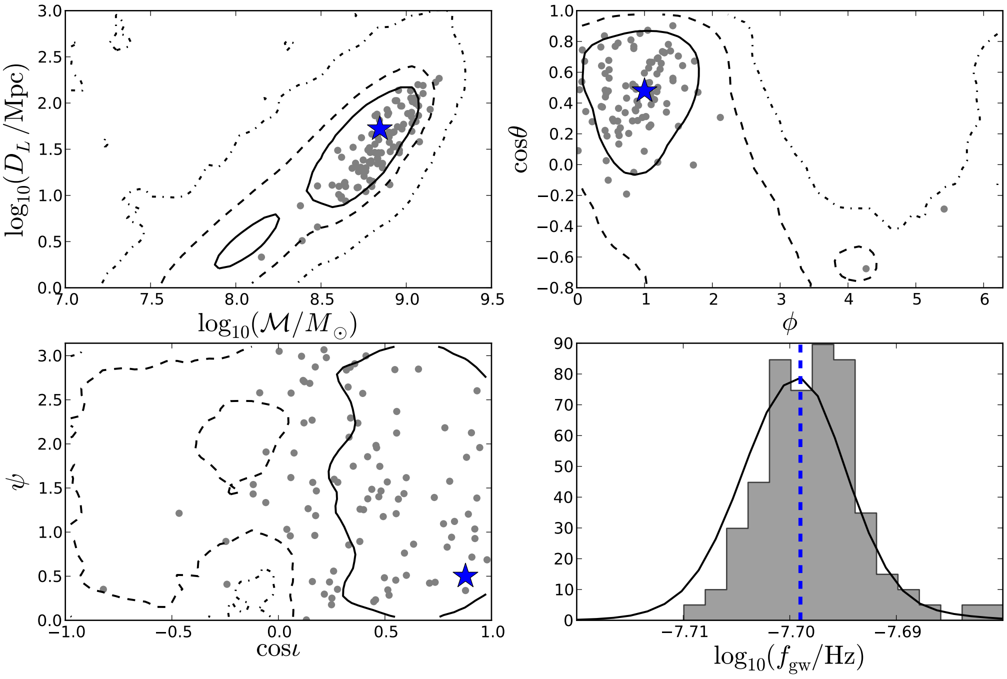

Figure 5.4: We show the distribution of *maximum-a-posteriori* values (filled grey circles) from an analysis of 100 realisations of an evolving signal injected into a Type II dataset, and analysed with the $\mathcal{M}_p$ statistic. As a further step towards real dataset analysis, we offset our catalogue of pulsar distances from their true values by an amount consistent with error bars. As can be seen, in the parameters of interest $(\mathcal{M}, D_L, f_{\mathrm{gw}}, \phi, \cos\theta, \cos\iota)$ this technique recovers the injected values (blue stars and blue dashed lines) quite comfortably. Additionally, we overplot the 68%, 95% and 99% contours of the posterior probability distributions averaged over all noise realisations. On average the distribution of the maximum-a-posterior values follows the average posterior, except perhaps in the case of $\cos\iota$. All injected values lie within the 68% credible interval.

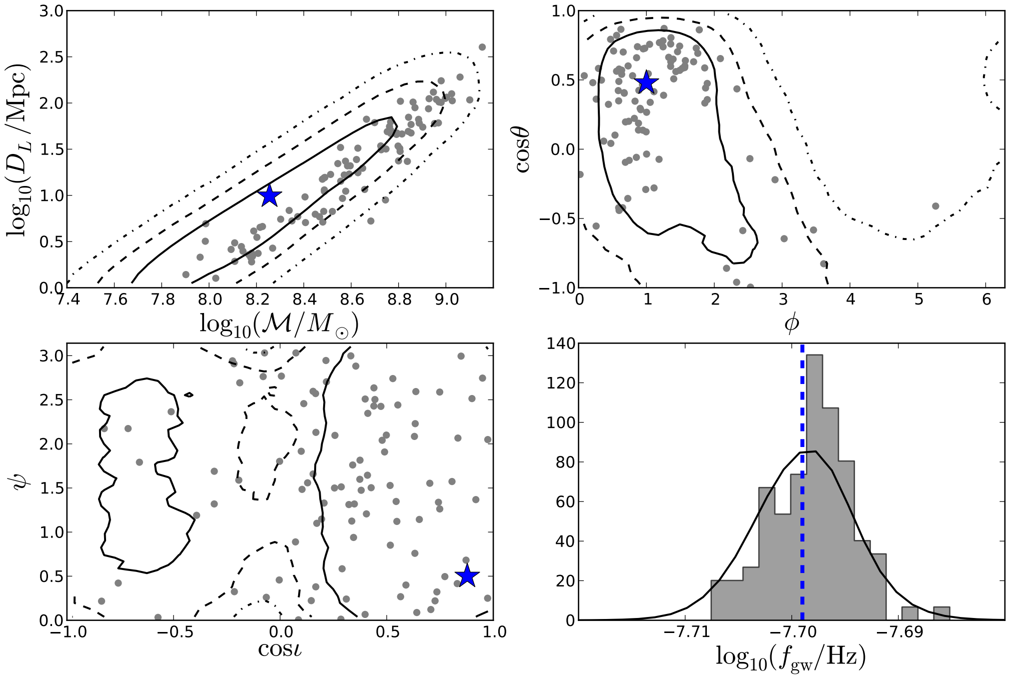

Figure 5.5: We show the distribution of *maximum-a-posteriori* values (filled grey circles) from an analysis of 100 realisations of a weakly evolving signal injected into a Type II dataset, and analysed with the $\mathcal{M}_p$ statistic. The injected values of $(\mathcal{M}, D_L)$ appear to be offset from the distribution of *maximum-a-posteriori* values, but are fully consistent with the overplotted average posterior probability distributions (see Fig. 5.4 for additional details). We note that all injected values lie within the 68% credible interval.

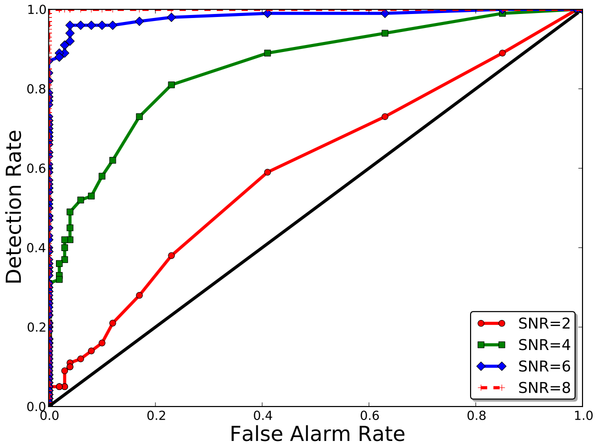

Figure 5.6: We inject an evolving signal into 100 realisations of Type II datasets at various SNRs (including SNR=0), recovering the posterior-odds ratio via the $\mathcal{M}_p$ statistic in each case. Setting the threshold of detection at varying values of the posterior odds ratio, we compute the fraction of realisations which are classified as false-positive and true-positive detections. We see that for this binary, and using this technique, the posterior odds ratio is an almost perfect classifier at SNR=6. With these numerical marginalisation techniques, the run-time is fast enough to permit detailed analysis of detection requirements within a Bayesian context.

To find all points satisfying $p(\vec{\theta}) > \mathcal{L}_a$ we rank the recovered posterior samples in order of decreasing posterior weight, then integrate over all samples until we reach the desired credible interval. For each realisation, we can then define two sets of points; the set of points inside the high-probability region (HPR) $\mathcal{S}_a$, and the complementary set $\bar{\mathcal{S}}_a$.

We now extend the dimensionality of the definitions of the χ^2 variables in Ref. [426] to give a measure of the distance of the posterior samples in each set from the true injected parameters,

$$\chi_a(\vec{\theta}_i)^2 = \left(\frac{\log_{10}(\mathcal{M}_i) - \log_{10}(\mathcal{M}_{\rm true})}{\log_{10}(\mathcal{M}_{\rm true})}\right)^2 + \left(\frac{\log_{10}(D_{L,i}) - \log_{10}(D_{L,{\rm true}})}{\log_{10}(D_{L,{\rm true}})}\right)^2 + \left(\frac{\phi_i - \phi_{\rm true}}{\phi_{\rm true}}\right)^2$$
$$+ \left(\frac{\cos\theta_i - \cos\theta_{\rm true}}{\cos\theta_{\rm true}}\right)^2 + \left(\frac{\cos\iota_i - \cos\iota_{\rm true}}{\cos\iota_{\rm true}}\right)^2 + \left(\frac{\psi_i - \psi_{\rm true}}{\psi_{\rm true}}\right)^2 + \left(\frac{\phi_{0,i} - \phi_{0,{\rm true}}}{\phi_{0,{\rm true}}}\right)^2, \quad (5.28)$$

where $\vec{\theta}_i$ are elements of $\mathcal{S}_a$. We also define a corresponding expression for $\bar{\chi}_a(\vec{\theta}_j)^2$ in terms of the elements, $\vec{\theta}_j$, of the complementary set, $\mathcal{S}_{\bar{a}}$.

Finally, we define the empirical distribution function (EDF) as,

$$F_k(a) = \frac{1}{k}\sum_{n=1}^{k}\Theta\left(\min\chi^2_{\bar{a}} - \min\chi^2_a\right), \quad (5.29)$$

where k is the number of noise realisations, and $\Theta(x)$ is the Heaviside step-function. This summation gives the fraction of all noise-realisation in which the injected values are “closer” (in the χ^2 sense) to one of the elements of the HPR than to any element of the complementary set.

The results of such an analysis are shown in Fig. 5.3 for the evolving and weakly-evolving binary injections. The line of internal consistency is shown as a thick, black diagonal line. We see that this technique does indeed present bias, with a worst-case sag of ~ 0.25. However, the EDF does not give an insight into how this bias manifests itself in the parameter space.

In Fig. 5.4 we show the distribution of *maximum-a-posteriori* values over all 100 noise-realisations, with the injected signal parameters also indicated. It is clear that while the $\mathcal{M}_p$ statistic may fail the formal EDF test, in practical terms it quite comfortably recovers the true parameters of the injected signal. This holds even when the catalogue of pulsar distances is offset from the true values by an amount consistent with their error-bars. Additionally, we show how the injected parameters and maximum-a-posteriori values are distributed with respect to the 68%, 95% and 99% contours of the realisation-averaged posterior. On average the distribution of the maximum-a-posterior values follows the average posterior, except perhaps in the case of $\cos\iota$, which may be the source of the bias seen in the formal EDF test. Regardless, all injected values lie within the 68% credible interval. The $\mathcal{M}_p$ statistic also recovers the true injected parameter values when the GW source is weakly evolving. Figure 5.5 shows a similar analysis to Fig. 5.4 for a weakly evolving injection, where, despite some offset of the injected values of $(\mathcal{M}, D_L)$ from the distribution of maximum-a-posteriori values, all injected values lie within the 68% credible interval of the overplotted realisation-averaged posterior probability distributions.

A further test we carry out is to assess the performance of the $\mathcal{M}_p$-computed Bayesian posterior odds-ratio as a detection classifier. We do so by producing a receiver operator characteristic (ROC) plot, illustrating the fraction of true positive detections versus false positive detections as we vary the detection threshold. We inject various SNR signals into 100 different noise-realisations, recovering the evidence in each case. The injected binary parameters are the same as the evolving case above. We see from Fig. 5.6 that the posterior odds-ratio becomes a virtually perfect detection classifier at an SNR of 6. Although we cannot draw truly general conclusions from this, the aim of this exercise is to show that these numerical marginalisation techniques are accurate enough to allow detailed statistical tests within a Bayesian context with much lower computational expenditure than existing techniques. The question of what is required for an unambiguous claim of GW detection using Bayesian statistics has been hitherto out of reach due to high computational expenditure, but can be rigorously assessed by employing these fast and accurate techniques in large injection studies.

Finally, we assess the importance of using an evolving versus non-evolving template when establishing detection criteria. For evolving and weakly-evolving sources, we inject SNR=8 signals into 100 different noise-realisations. We analyse each dataset using both the numerical phase marginalisation in the evolving-model ($\mathcal{M}_p$ statistic) and the non-evolving model, recovering the evidences in each case. The results are shown in Fig. 5.7, where we see that the evolving template is more general, capturing the behaviour of the gravitational-waveform even when the signal is non-evolving, and giving a Bayes factor which is comparable to the value returned by the non-evolving analysis. However, as seen in the previous section, the non-evolving template recovers a Bayes factor which can be significantly lower than the evolving-model template whenever the signal is truly evolving. This shows that the evidence values returned by these numerical phase marginalisation techniques conform to expected behaviour, and allow us to infer whether the GW signal is evolving based on the evolving versus non-evolving posterior odds ratio.

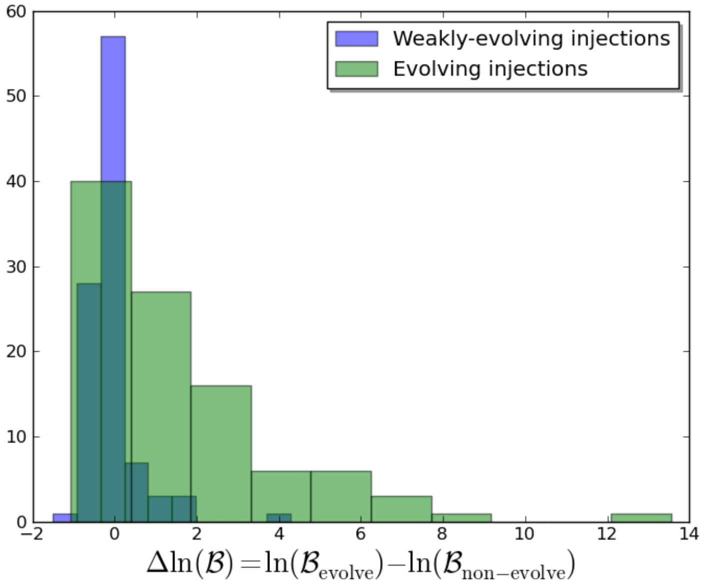

Figure 5.7: Evolving and weakly-evolving signals are injected into 100 different noise-realisations with an SNR of 8. We analyse all datasets using both the non-evolving and evolving templates (with numerical phase marginalisation), recovering the evidence in each case. We find that evidence recovered using the numerical phase marginalisation conforms to expected behaviour. On average, when the injected signal is weakly-evolving there is no difference in the evidence for an evolving or non-evolving template. However, when the signal is evolving the distribution of evidence will on average favour the evolving template.

5.4 Summary

Near-future GW searches which exploit the high-precision timing of millisecond pulsars may open a new observational window onto the early-inspiral phase of SMBH binaries. These systems are expected to be ubiquitous in the current picture of hierarchical structure formation, where massive galaxies grow via accretion from cosmic web filaments and galactic mergers [232, 233]. Supermassive BHs are thought to reside within the nuclei of most galaxies [e.g., 228], evolving symbiotically with the host [e.g., 229–231], such that galactic mergers, followed by the inspiral of BHs via dynamical friction into the post-merger remnant, leave a large population of SMBH binary systems.

While the dominant nanohertz GW signal accessible to PTAs will likely be a stochastic background formed from the incoherent superposition of signals from the inspiral of these systems, massive nearby binaries may be visible as single resolvable sources. Detecting these systems, and determining their properties, will offer a complementary probe to eLISA/NGO of the massive BH-population, in addition to a cross-check of system parameters from possible electromagnetic counterparts [see 427, and references therein]. These counterparts may in fact aid detection, as we no longer need to perform completely blind searches and can collapse the parameter space of our search algorithms.

In this chapter we have presented several new approaches to single-source searches in PTAs. The need to include the pulsar-term in analyses for accurate sky-localisation leads to practical difficulties, as distances to pulsars are poorly constrained, requiring us to introduce an extra search-parameter per pulsar. In evolving-template searches we must also take into account the inspiral of the binary over Earth-pulsar light travel-times, which (when we coherently include the pulsar-term) effectively extends the baseline of our observations by thousands of years, allowing our searches to reconstruct the orbital-evolution of the system and disentangle its chirp mass from the luminosity distance.

By numerically marginalising "on-the-fly" over the phase of the GW as it passes each pulsar, and sampling the distance to each pulsar from prior electromagnetic constraints, we can collapse the dimensionality of our searches. Our likelihood is fast enough, and our search space small enough, to bring the powerful Bayesian inference package MULTINEST to bear on the problem. We achieve significant accelerations with respect to the full search in two ways: (1) we perform an 8D search with a likelihood that executes $N_p\times 1$D numerical integrations, as opposed to having to stochastically sample from an $(8+N_p)$D space; (2) this 8D search can be highly parallelised with MULTINEST to minimise search times, as opposed to the lengthy burn-in times and prohibitive autocorrelation lengths associated with high-dimensional MCMC searches. For low to moderate SNRs we can perform parameter-estimation and recover the Bayesian evidence within a few minutes, whereas a full search utilising thermodynamic integration can take as long as a day with similar computational resources. We find excellent agreement of our Bayes factors with those returned by full searches, and, although the parameter estimation shows some small level of systematic bias in formal EDF tests, in practical terms we quite comfortably recover injected parameters. Analytic marginalisation of the likelihood over the pulsar-term phases may be able to place useful constraints on the values of $\zeta = \mathcal{M}^{5/3}/D_L$ and the orbital frequency of a SMBH binary, although sky-localisation and Bayesian evidence recovery is biased.

We will apply these techniques to upcoming continuous GW searches with EPTA and IPTA datasets. Our techniques are fast enough to allow systematic injection and recovery of many signals, permitting an exploration of the criteria required to make an unambiguous Bayesian detection claim.

5.A Analytic marginalisation/maximisation over ϕ_α

In the following we refer to the non-evolving template of Sec. 5.2.1. Assuming we have sufficiently many wave cycles during the observation time-span, we can use the following assumptions for the signal basis-function overlaps in Eq. (5.16): $(A^1|A^2) = (A^2|A^1) \simeq 0$, and $(A^1|A^1) \simeq (A^2|A^2) \simeq \mathcal{N}(\omega_0)$. In practice, the ratio of the cross-terms of the basis-function overlaps to the diagonal terms may not be small enough to permit these approximations to be used. For example, Fig. 5.8 shows the ratio $(A^1|A^2)/(A^1|A^1)$ for one of the pulsars in the IPTA MDC Open1 dataset, and for a real NANOGrav J0613-0200 dataset [261]. The ratio diminishes at higher frequencies, and for the mock dataset gets to $\lesssim 10^{-2}$ at the highest detectable frequencies. However, for a real pulsar dataset the ratio stays around 10^{-1} even at the highest frequencies. Furthermore, the GW frequencies to which we are most sensitive are $\sim$ a few $\times 10^{-8}$, diminishing as we move to the higher frequencies required for these approximations to hold.

Nevertheless, these analytic expressions may have some value as rapid first-pass tools, and we provide the derivations below.

5.A.1 Marginalising

Given the overlap approximations and the non-evolving template defined in Eq. (5.11-5.16) we have,

$$\begin{aligned}(s_\alpha|s_\alpha) &\simeq [a_{1\alpha}a_{1\alpha} + a_{2\alpha}a_{2\alpha}]\,\mathcal{N}(\omega_0),\\ &\simeq 2\mathcal{N}(\omega_0)\left(q_{1\alpha}^2 + q_{2\alpha}^2\right)(1-\cos\phi_\alpha)\,, \end{aligned} \tag{5.30}$$

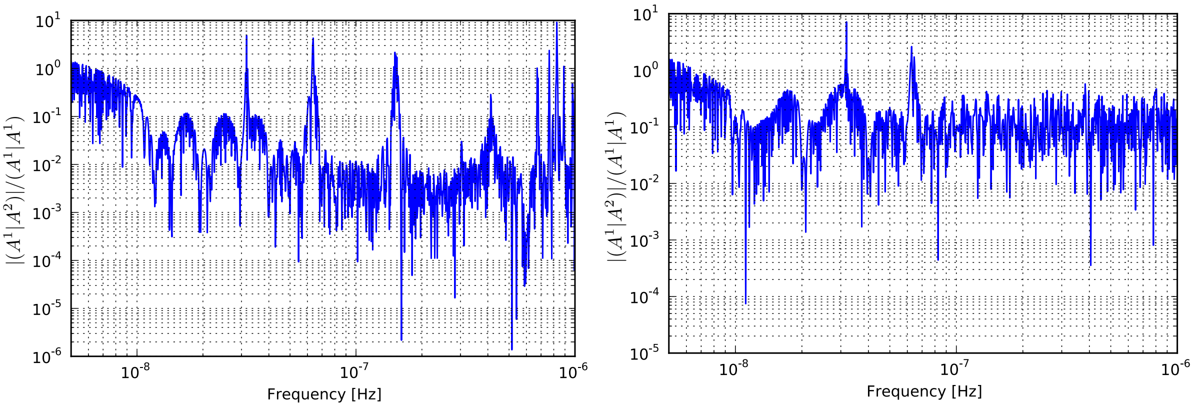

(a) **(b)**

Figure 5.8: The ratio of the basis-function overlaps in the cross-terms and the diagonal terms, $(A^1|A^2)/(A^1|A^1)$, is shown for (a) an IPTA MDC Open1 pulsar; 100 ns RMS white-noise, 2 week cadence; (b) a real NANOGrav dataset for J0613-0200 [261], where the noise is also fairly white.

such that,

$$\begin{aligned}\ln\Lambda &= \sum_{\alpha=1}^{N_p}\left[(r_\alpha|s_\alpha) - \frac{1}{2}(s_\alpha|s_\alpha)\right]\\ &\simeq \sum_{\alpha=1}^{N_p}\left\{\left[q_{1\alpha}(r_\alpha|A^1_\alpha) + q_{2\alpha}(r_\alpha|A^2_\alpha) - \left(q^2_{1\alpha}+q^2_{2\alpha}\right)\mathcal{N}(\omega_0)\right]\right.\\ &- \left[q_{1\alpha}(r_\alpha|A^1_\alpha) + q_{2\alpha}(r_\alpha|A^2_\alpha) - \left(q^2_{1\alpha}+q^2_{2\alpha}\right)\mathcal{N}(\omega_0)\right]\cos\phi_\alpha\\ &- \left.\left[q_{2\alpha}(r_\alpha|A^1_\alpha) - q_{1\alpha}(r_\alpha|A^2_\alpha)\right]\sin\phi_\alpha\right\}\\ &\simeq \sum_{\alpha=1}^{N_p}\left[-X_\alpha + X_\alpha\cos\phi_\alpha + Y_\alpha\sin\phi_\alpha\right]. \end{aligned} \tag{5.31}$$

Hence, marginalising the likelihood-ratio over each pulsar-phase parameter, assuming flat-priors, gives,

$$\begin{aligned}\int \Lambda\, d^{N_p}\phi &\propto \left(\frac{1}{2\pi}\right)^{N_p}\prod_{\alpha=1}^{N_p}\int_0^{2\pi}\exp[(r_\alpha|s_\alpha) - \frac{1}{2}(s_\alpha|s_\alpha)]d\phi_\alpha\\ &\propto \left(\frac{1}{2\pi}\right)^{N_p}\exp\left(-\sum_{\alpha=1}^{N_p}X_\alpha\right)\times\prod_{\alpha=1}^{N_p}\int_0^{2\pi}\exp(X_\alpha\cos\phi_\alpha + Y_\alpha\sin\phi_\alpha)\,d\phi_\alpha\\ &\propto \prod_{\alpha=1}^{N_p}\exp(-X_\alpha)I_0\left(\sqrt{X^2_\alpha+Y^2_\alpha}\right), \end{aligned} \tag{5.32}$$

where I_0 is a modified Bessel function of the first kind. Note that this technique of analytic marginalisation of nuisance phase parameters has previously been used in different contexts

[428, 429], but has never been applied to PTA data-analysis. Finally, we have the PML (Phase Marginalised Likelihood) statistic,

$$\ln\tilde{\Lambda} \propto \sum_{\alpha=1}^{N_p}\left\{-X_\alpha + \ln\left[I_0\left(\sqrt{X_\alpha^2+Y_\alpha^2}\right)\right]\right\}. \tag{5.33}$$

If we have a high SNR signal, such that the argument of the modified Bessel function is large, then directly computing $I_0(x)$ can be very difficult. However, we can use a large argument expansion of the modified Bessel function to aid this calculation,

$$\ln\left[I_0(x)\right] \sim x - \frac{1}{2}\ln\left(2\pi x\right) + \ln\left(1 + \frac{1}{8x} + \frac{9}{128x^2} + \frac{225}{3072x^3} + \frac{11025}{98304x^4}\ldots\right). \tag{5.34}$$

We applied this statistic to the SNR=8 evolving and weakly-evolving datasets discussed in Sec. 5.3.2. The analysis proceeded very quickly with minimal computational resources, since we are only searching over 8 parameters without any expensive stages in the likelihood evaluation. In Fig. 5.9 we show the distribution of maximum-a-posteriori values from the analysis of 100 noise realisations. The injected values of $\mathcal{M}$, D_L, and $f_{\rm gw}$ are consistent with the distribution of maximum-a-posteriori values, however other parameters showed significant bias. The recovered Bayes factors were also highly biased. Hence the PML statistic may be useful in placing constraints on the binary's $\zeta = \mathcal{M}^{5/3}/D_L$ and orbital frequency, although sky-localisation and Bayesian evidence recovery is unreliable.

5.A.2 Maximising

Going back to the original $\ln\Lambda$ in Eq. (5.31), it is possible to maximise the likelihood-ratio over the pulsar-phase parameters. As indicated in Ref. [273], the solution to the maximum-likelihood value of ϕ_α requires evaluating a quartic. However, if we use the overlap approximations from the previous section then the solution is more simple. Maximising gives

$$\frac{\partial\ln\Lambda}{\partial\phi_\beta} \simeq -X_\beta\sin\phi_\beta + Y_\beta\cos\phi_\beta = 0, \tag{5.35}$$

where

$$\tan\phi_\beta = \frac{Y_\beta}{X_\beta}, \tag{5.36}$$

so that we can define the log-likelihood ratio maximised over all ϕ_α, which we call the $\mathcal{T}_p$-statistic,

$$\mathcal{T}_p = \sum_{\alpha=1}^{N_p}\left[-X_\alpha + \sqrt{X_\alpha^2+Y_\alpha^2}\right]. \tag{5.37}$$

We may be able to go further, and to maximise over other parameters, but we do not consider this here. Regardless, we have a rather compact form for the log-likelihood ratio maximised

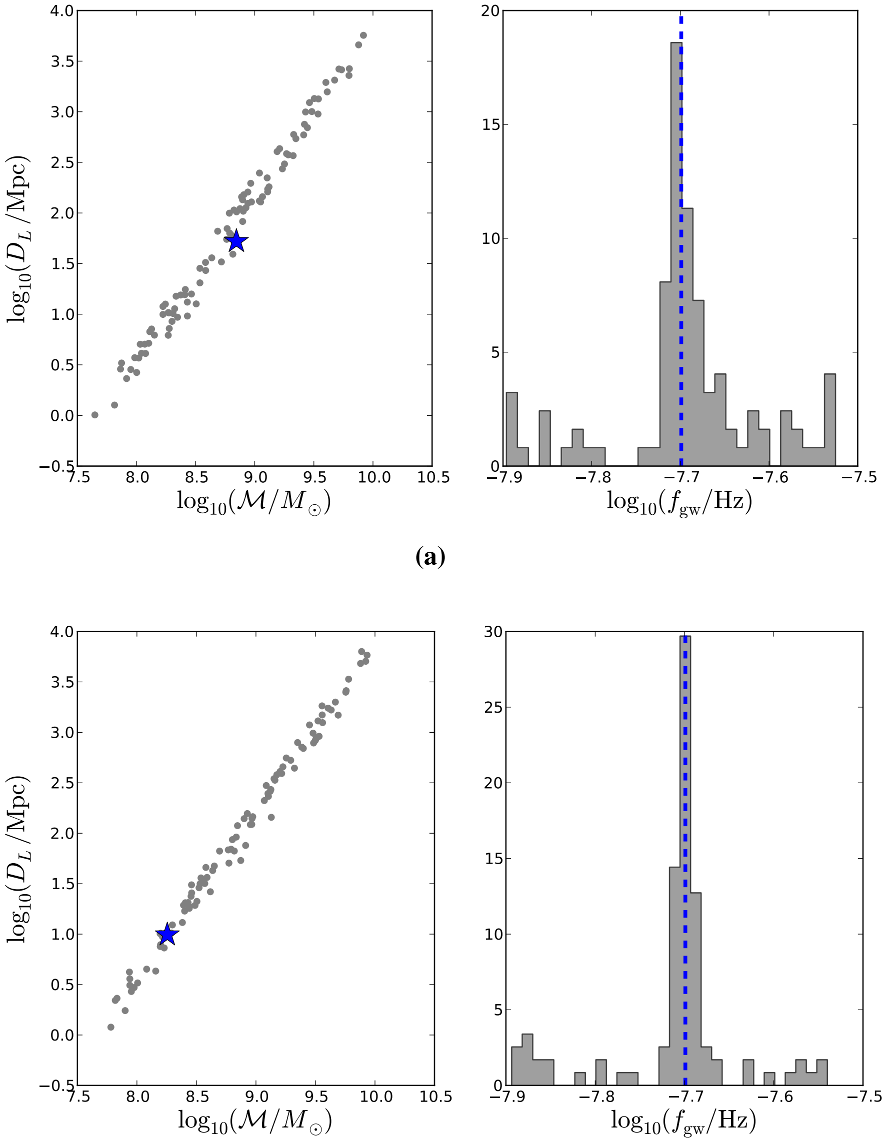

(a)

(b)

Figure 5.9: We show the distribution of *maximum-a-posteriori* values (filled grey circles) from analyses of 100 realisations of (a) evolving and (b) weakly-evolving signals injected into Type II datasets (see Sec. 5.3.2 for details). These datasets were analysed with the Phase Marginalised Likelihood (PML) statistic, which involves an analytic marginalisation over pulsar-term phase parameters. In both cases the injected values (blue stars and blue dashed lines) of $\mathcal{M}$, D_L, and $f_{\rm gw}$ are consistent with the distribution of maximum-a-posteriori values, however other parameters showed significant bias.

over all the pulsar-phase parameters. The remaining 7-D single-source parameter space can easily be explored using MCMC.

Note that if we use the large argument expansion of the modified Bessel function to approximate the PML we get,

$$\ln\tilde{\Lambda} \propto \sum_{\alpha=1}^{N_p}\left\{-X_\alpha + \sqrt{X_\alpha^2+Y_\alpha^2} - \frac{1}{2}\ln\left(2\pi\sqrt{X_\alpha^2+Y_\alpha^2}\right)\right\}. \tag{5.38}$$

For sufficiently large arguments, $\sqrt{X_\alpha^2+Y_\alpha^2}$ increases faster than $\ln\left(2\pi\sqrt{X_\alpha^2+Y_\alpha^2}\right)$. Hence, in the infinite SNR limit the PML statistic is proportional to the maximum-likelihood estimator $\mathcal{T}_p$ statistic,

$$\ln\tilde{\Lambda} \propto \sum_{\alpha=1}^{N_p}\left\{-X_\alpha + \sqrt{X_\alpha^2+Y_\alpha^2}\right\} \propto \mathcal{T}_p. \tag{5.39}$$

5.B $\mathcal{B}_p$ statistic

Rather than analytically maximising over the amplitude parameters, $a_{i\alpha}$ [see Eq. (5.12)], to produce the $\mathcal{F}_p$ statistic, if we assume uniform priors on these parameters then it is trivial to analytically marginalise and calculate the Bayes factor. We re-write the likelihood as the following and complete the square in the amplitude parameters, such that

$$\begin{aligned}
\ln\Lambda &= \sum_{\alpha=1}^{N_p}(r_\alpha|s_\alpha) - \frac{1}{2}(s_\alpha|s_\alpha) \\
&= \sum_{\alpha=1}^{N_p} a_{i\alpha}(r_\alpha|A_\alpha^i) - \frac{1}{2}a_{i\alpha}a_{j\alpha}(A_\alpha^i|A_\alpha^j) \\
&= \sum_{\alpha=1}^{N_p} a_{i\alpha}N_\alpha^i - \frac{1}{2}a_{i\alpha}a_{j\alpha}M_\alpha^{ij}, \\
&= -\frac{1}{2}\sum_{\alpha=1}^{N_p}\left[\left(a_\alpha - M_\alpha^{-1}N_\alpha\right)^T M_\alpha\left(a_\alpha - M_\alpha^{-1}N_\alpha\right) - N_\alpha^T\left(M_\alpha^{-1}\right)^T N_\alpha\right].
\end{aligned} \tag{5.40}$$

Now we integrate over the amplitude parameters with uniform priors, and permit the maximum strain to be large enough such that the likelihood is unaffected by the prior boundary. We can therefore set the limits of integration to be between $[-\infty,+\infty]$, such that

$$\begin{aligned}
\mathcal{B}_p &= C\exp\left(\sum_{\alpha=1}^{N_p}\frac{N_\alpha^T\left(M_\alpha^{-1}\right)^T N_\alpha}{2}\right)\prod_{\alpha=1}^{N_p}\left[\det\left(2\pi M_\alpha^{-1}\right)\right]^{1/2} \\
&= C\left(2\pi\right)^{N_p}\exp\left(\mathcal{F}_p\right)\prod_{\alpha=1}^{N_p}\left(\det M_\alpha\right)^{-1/2},
\end{aligned} \tag{5.41}$$

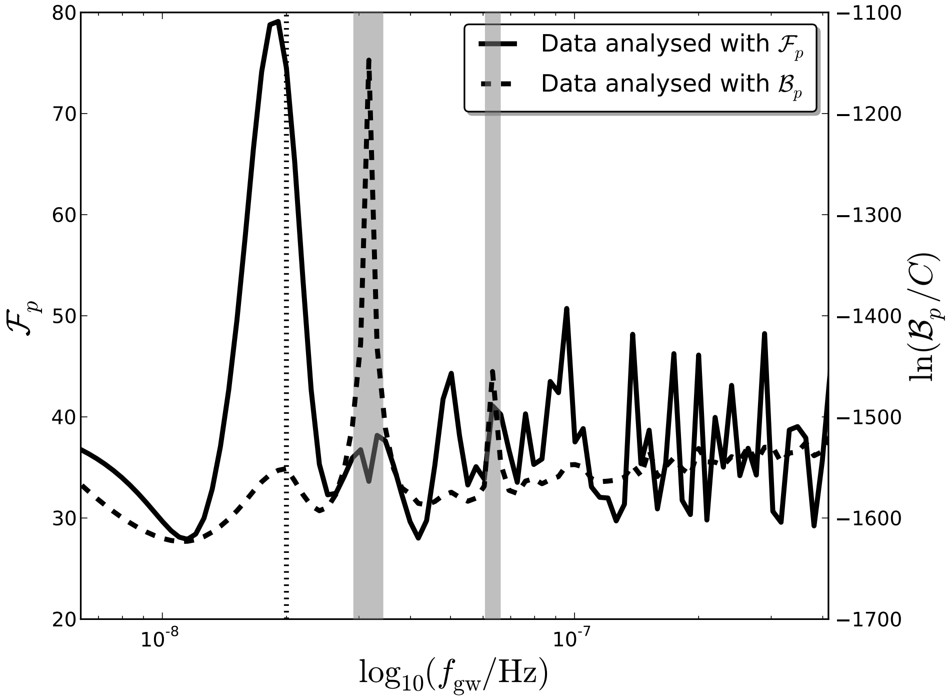

Figure 5.10: A Type I dataset with an SNR=10 injection (with injected parameters equal to those in Sec. 5.3.1) was analysed with the $\mathcal{F}_p$ statistic and the $\mathcal{B}_p$ statistic. The injected GW frequency is 2×10^{-8} Hz and is shown as a dotted line. The $\mathcal{F}_p$ statistic performs very well and finds the true signal frequency. The $\mathcal{B}_p$ statistic also shows a small peak at this frequency, however the extra determinant factor in Eq. (5.41) leads the shape of the frequency trend to closely resemble the noise curve. The grey regions around $\sim 6.34 \times 10^{-8}$ Hz and $\sim 3.17 \times 10^{-8}$ Hz correspond to a loss of sensitivity of the PTA due to conversion of topocentric TOAs to barycentric TOAs and fitting for parallax, respectively.

where C denotes the prior volume.

In Fig. 5.10 we show the results of an application of the $\mathcal{B}_p$ statistic to a Type I dataset with an injected GW frequency equal to 2×10^{-8} Hz. The $\mathcal{F}_p$ statistic performs very well and unambiguously locates the correct signal frequency. While the $\mathcal{B}_p$ statistic also shows a small peak at this frequency, the extra determinant factor in Eq. (5.41) causes the trend in frequency to show significant features of the noise curve. Hence, in this isolated case, $\mathcal{B}_p$ significantly underperforms $\mathcal{F}_p$.

The form of the $\mathcal{B}_p$ statistic has been previously arrived at in the context of LIGO data analysis [430], where uniform priors for $a_{i\alpha}$ was shown to be very unphysical, and more physically-motivated priors were suggested. This was further explored in Ref. [431], where a new set of coordinates was found which are linear combinations of $a_{i\alpha}$, but which have a closer relationship to the physical parameter space. This improved the accuracy of the approximate analytic Bayes factor calculation with respect to the full numerical result. We do not explore this coordinate transformation here, but will consider this promising route in future work.

Part IV

Conclusion

Then he waited, marshaling his thoughts and brooding over his still untested powers. For though he was master of the world, he was not quite sure what to do next. But he would think of something.

Arthur C. Clarke, *2001: A Space Odyssey*

6

A New Window On The Cosmos

6.1 Cosmology & astrophysics with gravitational waves

The third millennium began with exciting steps forward for gravitational wave astrophysics. On the theoretical front, breakthroughs in numerical relativity (in addition to NR-calibrated EOB waveforms) have allowed the first explorations of the complex merger phase of black-holes (BHs). By stitching these approaches together with highly successful post-Newtonian waveform templates for the early-inspiral phase, we are now in a position to model the orbital-evolution, dynamics, and GW emission of CO mergers right through their coalescence to the ring-down of the resulting BH. There is a growing international community of researchers committed to investigating the prospects for GWs to act as a completely new tool with which to explore the cosmos, and to develop sophisticated data-analysis techniques to tackle the challenging problem of detection. On the experimental front, the first kilometre-scale ground-based GW interferometers were brought online and achieved design sensitivity, creating a global network of instruments which have the near-future potential to make the first direct detections of GWs. Precision timing of Galactic millisecond pulsars may offer insights into the nanohertz band of GWs, where a stochastic background signal bathes all pulsars in our observed ensemble and creates correlated deviations of the pulse arrival-times from precisely constructed models. Within ~ 20 years we may also see a space-borne GW laser interferometer with $\sim 10^9$ m arms, which will have a guaranteed source population, as well as the ability to test fundamental physics in the 0.1 mHz to 0.1 Hz band.

In this thesis we have attempted to explore the prospects for near-future GW observations to complement existing astrophysical probes and to offer unique insights into GW source populations. In Part I we reviewed GW theory, providing a concise introduction to the spectrum of GW sources and detectors. In the context of ground-based efforts, Part II describes our explorations of the potential for inspiraling NS-NS binaries (which are the best bet for the first direct detection) to act as cosmological *standard sirens*, allowing a measure of the source luminosity distance calibrated entirely by our understanding of gravitation. With the distance, and candidate redshift distributions obtained via prior knowledge of the intrinsic distribution of masses of these systems, we can probe cosmological parameters in addition to the star-formation rate of the progenitor population. An intriguing approach to detecting GWs is the method of pulsar-timing, which is an area experiencing rapid growth to which the author has been fortunate enough to contribute. Our efforts to fully characterise the nanohertz GW-sky by probing the level of anisotropy in a stochastic GW background are reviewed in Part III, along with new techniques to accelerate parameter-estimation and model-comparison for single resolvable SMBH binaries affecting the arrival-times of pulsar signals.

6.1.1 Cosmology without counterparts

GW signals from inspiraling stellar-mass CO binary systems pose the greatest chance of the first direct detection of GWs. In the advanced-era of kilometre-scale ground-based detectors, we will have Advanced LIGO operating in the US, Advanced Virgo in Italy, GEO-600 in Germany, LCGT in Japan, and possibly a LIGO-type detector in India. This will form a global network of precision large-scale instruments sensitive in the 10 Hz to 10 kHz range of GW frequencies, where the dominant source population will be these stellar-mass COs. In particular, a range of population-synthesis simulations and extrapolations of observed Galactic systems give a realistic detection rate of ~ 40 NS-NS binaries per year by a network of detectors operating within this decade. Additionally, these systems are thought to be the best candidate for short GRB progenitors, where the cataclysmic release of energy in a GRB may have merging COs as the engine driving the collimated outflow. As such, a coincident observation of an inspiraling NS-BH or NS-NS binary in GWs with electromagnetic detections of a short GRB will be strong evidence that these phenomena are one and the same. Other electromagnetic signatures, such as radio afterglows or observations of the radioactive decay of r-process synthesised heavy-elements (kilonovae), will drive forward *multi-messenger* astronomy, where EM detections inform GW searches, and vice versa.

A network of GW interferometers will be able to use time-delay information to triangulate sources on the sky, disentangling angular factors in the GW strain-amplitude from the luminosity distance, and thus permitting a measure of source distances which will be completely independent of the current cosmic-distance ladder. These GW *standard sirens* would be calibrated entirely by our understanding of gravitation. With an associated redshift measurement we can use these systems to probe the distance-redshift relation for constraints on cosmological parameters. This redshift information may come from electromagnetic counterparts, however the beaming angle of short GRBs may be such that only a small fraction of GWs will have observable electromagnetic signatures. With their isotropic emission, kilonovae offer better counterparts for redshift determination. We may also be able to extract the source redshift from tidal coupling corrections to the GW phase at 5 pN order, although these corrections will be manifest in the late inspiral where the sensitivity of advanced detectors will be low. Instead, we developed a technique based on the observed intrinsic narrowness of the distribution of masses in NS-NS systems. By measuring the *redshifted* chirp mass from the GW phase evolution in our interferometers, we can use prior constraints on the NS mass distribution to construct candidate redshift distributions.

In Chapter 2 we studied this technique in the context of an advanced interferometer network. With a catalogue of ~ 100 detections (corresponding to a few years of observations) giving redshifted chirp mass and luminosity distance information, we found that if the underlying NS mass distribution was a Gaussian with mean $1.35M_\odot$ and half-width $0.06M_\odot$, then our technique could constrain the Hubble constant, H_0, to within $\sim 15\%$. This search also constrained the mean and half-width of the NS mass distribution, thereby providing insights on cosmological and astrophysical scales. Although our reference mass-distribution width of $0.06M_\odot$ is a reasonable choice based on the observed Galactic sample, we also investigated how the precision of H_0 recovery scales with the width of the underlying distribution. In this case, we found the trend was linear, such that if the width of the distribution was really $\sim 0.12M_\odot$ then we would require ~ 400 detections for the same precision on H_0. We found that the effect of incorporating distance measurement errors in an advanced-era network only degraded measurement precisions of the Hubble constant by $\sim 20\%$, which can be mitigated through increased observation time. Furthermore, when we restricted the horizon-distance of our network by increasing the SNR detection threshold, then the corresponding precision on the Hubble constant was degraded, roughly obeying the relationship $\delta H_0/H_0 \propto \rho_{\rm threshold}$. We can improve our technique by including precision redshift information from EM counterparts. By associating a fraction of a our catalogue with electromagnetic signatures, we found that a counterpart-fraction of $\sim 10\%$ could more than double the precision of Hubble constant recovery.

We extended our technique in Chapter 3, where we explored the prospects for a third-generation network, including the proposed Einstein Telescope, to probe the dark energy equation-of-state and the star-formation rate of the NS-NS progenitor population. The Einstein Telescope has a rather novel design, consisting of an underground, cryogenically-cooled and seismically-isolated low-frequency instrument, as well as a surface-sited high laser-power high-frequency instrument, all in a 10 km arm-length equilateral triangle configuration. Third-generation interferometers aim for a broadband order of magnitude increase in strain-sensitvity, as well as pushing the sensitivtiy down to ~ 1 Hz. The huge cosmological volume to which these instruments would be sensitive would potentially create detection rates of the order of $\sim 10^5$ yr^{-1}, and push the horizon-distance out to Gpc-scales. With this we found that we could constrain evolving dark energy EOS parameters to a similar precision as conventional EM techniques in forthcoming experiments. However, the real breakthrough is our ability to probe the delay-time between formation of the double CO binary and the resulting merger, and consequently the star-formation rate (SFR) of the progenitor popululation. The parameters describing the slope of the delay-time distribution and the shape of the SFR density were constrained to within $\sim 10\%$ in our reference catalogue of $\sim 10^5$ detections.

It will be an interesting extension of this work to fix our cosmological parameters at the values given by the current concordance framework, and to directly reconstruct the mass distribution of the double CO systems. This method could be applied to NS-NS, NS-BH and BH-BH binaries. Population synthesis studies indicate that BHs formed from lower metallicity progenitor stars tend to be heavier. A lower metallicity star will have a lower abundance of heavy-elements in the stellar atmosphere, resulting in a lower wind mass-loss rate than in a solar metallicity environment, and permitting the star to remain more massive during its evolution. This results in a heavier post-supernova compact-remnant. Hence an investigation of the mass distribution of double CO systems offers the potential to investigate the properties and environment of the progenitor population.

6.1.2 The Milky Way as a gravitational wave antenna

A novel approach to GW detection utilises the high-precision timing of the exquisitely stable pulsed emission of Galactic millisecond pulsars. These are rapidly rotating neutron stars which have been spun-up by binary mass-transfer, with misaligned magnetic-field and rotational axes. The rotating magnetic-field generates a local electric-field along which charged particles from the co-rotating magnetospheric plasma are accelerated to produce beamed radio emission. The rotation of the pulsar sweeps this beam into our line-of-sight, creating a lighthouse effect. Repeated observation of these pulsars allows a timing-model to be constructed which describes all deterministic influences on the pulse time-of-arrivals (TOAs). Subtracting a timing-model from the raw TOAs leaves a collection of timing-residuals, encoding all unmodelled phenomena, such as receiver noise, intrinsic pulsar-noise from rotational instabilities, and, most tantalisingly, GWs.

A gravitational wave passing between the Earth and a pulsar perturbs the space-time metric along the Earth-pulsar line-of-sight, inducing irregularities in the phase of the received radio pulses. We search for GWs in the stream of residuals after a timing-model has been fit. The GW frequencies to which our techniques are sensitive is set by the total observational baseline and the regularity of observation, respectively, corresponding to $\sim 10^{-9} - 10^{-7}$ Hz. The dominant GW sources to which pulsar-timing may be sensitive are a cosmological population of inspiraling SMBH binaries, formed via the ubiquitous mergers of massive galaxies in the current hierarchical structure formation paradigm. In fact, there are so many of these massive ($\gtrsim 10^8 M_\odot$), nearby ($z \lesssim 2$) systems that they stack up in the frequency-domain beyond the resolution of pulsar-timing, thereby forming an unresolved stochastic GW background. At higher frequencies the stochasticity of the signal breaks down, which opens up the possibility of detecting and characterising individual SMBH binaries. There are now three major consortia timing pulsars to sub-μs precision in the effort to detect GWs: NANOGrav (North America), PPTA (Australia), and EPTA (Europe; of which the author is a member). These organisations work together under the umbrella consortium of the IPTA.

The work in Chapter 4 introduced new techniques to constrain the levels of anisotropy in a nanohertz stochastic GW background. By timing *arrays* of these Galactic millisecond pulsars, we use the fact that the GW background will be bathing all pulsars in its influence, which induces correlated deviations in the pulse TOAs between pulsars separated on the sky. This creates a "smoking-gun" signature that leverages our search for GWs against other stochastic noise processes. In fact, for an isotropic background the induced cross-correlation signature depends *exclusively* on the angular separation of the pulsars, giving the famous *Hellings and Downs curve*. When the background is anisotropic, however, the correlation signature is no longer a simple function of the angular separation of the pulsars, but rather becomes strongly dependent on the absolute positions of the pulsars relative to the angular distribution of GW power.

By expanding the energy-density of the GW background in terms of spherical-harmonics, it is possible to generalise the cross-correlation signature into a set of correlation basis-functions, whose amplitudes become parameters in a stochastic background search. Building on the theoretical work of Mingarelli et al. [393], we implemented this formalism to create the first Bayesian data-analysis pipeline capable of constraining anisotropy in the nanohertz GW background. We tested this pipeline by developing a set of plugins for the pulsar-timing software package TEMPO2 which allow the user to inject arbitrary levels of anisotropy into simulated datasets. Our pipeline was able to constrain the coefficients of a spherical-harmonic decomposition of the power in the background. Through Bayesian model-comparison, we found that very bright signals will be needed to infer the presence of anisotropy, where in an array of 36 pulsars, and for a decisive detection, we required the post-fit rms residual induced by the GW background to be at least five times larger than the noise rms in each pulsar. The techniques we developed will be applied to real searches in EPTA and IPTA data.

We plan to continue our efforts in this area with frequentist methods, by investigating how detrimental our current assumptions of an isotropic background are with respect to realistic levels of anisotropy, and if this may be harming our detection prospects. Developing a formalism to describe the minimum angular scale to which current and future pulsar-timing arrays are sensitive will also be a crucial issue when assessing the detection prospects of anisotropy.

Detections of single resolvable SMBH binaries in the nanohertz band will offer a complementary probe to eLISA/NGO of the massive BH population. Furthermore, reconstructing the parameters of these systems may shed light on their environmental couplings in the early inspiral phase of the orbital evolution. The timing-residuals induced by an individual source are composed of a *pulsar-term* and an *Earth-term*, corresponding to the signature of the metric perturbation as it passes the pulsar and Earth, respectively. When timing an array of pulsars, the Earth-terms will add coherently together, while the pulsar-terms will all have different phases as a result of their differing positions with respect to the source and distances from the Earth. Although challenging, coherently including the pulsar-term in search algorithms is desirable since it effectively extends the baseline of our observations by thousands of years, where each pulsar-term records a snapshot of the SMBH binary evolution as the GW passes each pulsar. It improves sky-localisation, and allows us to disentangle the binary chirp mass from its luminosity distance.

Current Bayesian pipelines which incorporate the pulsar-term must search over the distance to each pulsar, posing problems of high-dimensionality as we move into the era of large pulsar arrays. In Chapter 5 we presented new techniques which numerically marginalise "on-the-fly" over the phase offset of each pulsar-term from the Earth-term, in addition to sampling the pulsar-distances from their prior electromagnetic constraints to compute the binary orbital frequency of each pulsar-term. This collapses the dimensionality of the search space, allowing rapid parameter-estimation and Bayesian-evidence evaluation which we showed to be in comfortable agreement with full searches. The computation time of these searches was reduced from more than a day for the full search, to less than an hour (and in low SNR cases less than five minutes) with our new techniques. The speed with which we can perform these analyses will allow an exploration of the criteria required to make an unambiguous Bayesian claim of GW detection, which we intend to address in the future. These techniques will be applied to real data in upcoming EPTA and IPTA searches.

Glossary of acronyms

BAO	Baryon acoustic oscillation
BH	Black hole
CDM	Cold dark matter
CE	Common envelope
CO	Compact object
CMB	Cosmic microwave background
DNS	Double neutron star
EOB	Effective one-body
EM	Electromagnetic
EOS	Equation of state
EMRI	Extreme mass-ratio inspiral
GRB	Gamma-ray burst
GR	General relativity
GW	Gravitational wave
GWB	Gravitational wave background
HMNS	Hypermassive neutron star
ISCO	Innermost stable circular orbit
ISM	Interstellar medium
MCMC	Markov chain Monte Carlo
MBH	Massive black-hole
MHD	Magnetohydrodynamic
MSP	Millisecond pulsar
NS	Neutron star
NR	Numerical relativity
ORF	Overlap reduction function
PK	Post-Keplerian
PN	Post-Newtonian
PDF	Probability density function
PSR	Pulsar
PTA	Pulsar timing array

PSD	Power spectral density
RMS	Root mean square
SGRB	Short gamma-ray burst
SNR	Signal-to-noise ratio
SSB	Solar system barycentre
SFR	Star formation rate
SMBH	Supermassive black-hole
TOA	Time of arrival
TT	Transverse-traceless
WD	White dwarf

Bibliography

[1] E. Rosen and N. Copernicus, *Three Copernican Treatises*. University of Michigan Press, 2004. 3

[2] N. Copernicus, *On the revolutions of heavenly spheres*. Running Press, 2004. 3

[3] I. Newton, *Principia*. Running Press, 2005. 3

[4] A. Bouvard, *Tables Astronomiques Publiees Par Le Bureau Des Longitudes De France, Contenant Les Tables De Jupiter, De Saturne Et D'Uranus, Construites D'Apres La Theorie De La Mecanique Celeste*. Bachelier et Huzard, 1821. 4

[5] U. Le Verrier, *Comptes rendus hebdomadaires des séances de lAcadémie des sciences*, **49**, pp. 379–383, 1859. 4

[6] H. Minkowski, *Space and Time: Minkowski's papers on relativity*. Minkowski Institute Press, 2013. 4

[7] A. Einstein, *Annalen der Physik*, **354**, pp. 769–822, 1916. 4, 5

[8] J. A. Wheeler, *Geons, black holes, and quantum foam: A life in physics*. WW Norton & Company, 2000. 5

[9] F. W. Dyson, A. S. Eddington, and C. Davidson, *Royal Society of London Philosophical Transactions Series A*, **220**, pp. 291–333, 1920. 5

[10] Texas Mauritanian Eclipse Team, AJ, **81**, p. 452, (1976). 5

[11] R. V. Pound and G. A. Rebka, *Phys. Rev. Lett.*, **4**, pp. 337–341, (1960). [Online]. Available: http://link.aps.org/doi/10.1103/PhysRevLett.4.337 5

[12] C. M. Will, *Living Reviews in Relativity*, **9**, p. 3, (2006), gr-qc/0510072. 5

[13] B. Bertotti, L. Iess, and P. Tortora, Nature, **425**, pp. 374–376, (2003). 5

[14] C. W. F. Everitt *et al.*, *Physical Review Letters*, **106**, 22, p. 221101, (2011), 1105.3456. 5

[15] J. G. Williams, X. X. Newhall, and J. O. Dickey, Phys. Rev. D, **53**, pp. 6730–6739, (1996). 5

[16] Planck Collaboration *et al.*, *ArXiv e-prints*, (2013), 1303.5076. 5, 57

[17] A. G. Riess *et al.*, AJ, **116**, pp. 1009–1038, (1998), astro-ph/9805201. 5

[18] S. Perlmutter *et al.*, ApJ, **517**, pp. 565–586, (1999), astro-ph/9812133. 5

[19] T. Clifton, P. G. Ferreira, A. Padilla, and C. Skordis, Phys. Rep., **513**, pp. 1–189, (2012), 1106.2476. 5

[20] A. Einstein, *Sitzungsberichte der Königlich Preußischen Akademie der Wissenschaften (Berlin), Seite 688-696.*, **1**, pp. 688–696, 1916. 5, 6

[21] ——, *Sitzungsberichte der Königlich Preußischen Akademie der Wissenschaften (Berlin), Seite 154-167.*,

1, pp. 154–167, 1918. 5, 6, 8

[22] D. Kennefick, *ArXiv General Relativity and Quantum Cosmology e-prints*, (1997), gr-qc/9704002. 6

[23] R. A. Hulse and J. H. Taylor, ApJ, **195**, pp. L51–L53, (1975). 6, 26

[24] J. M. Weisberg, D. J. Nice, and J. H. Taylor, ApJ, **722**, pp. 1030–1034, (2010), 1011.0718. 6, 26

[25] M. Kramer and I. H. Stairs, ARA&A, **46**, pp. 541–572, (2008). 6, 26

[26] I. H. Stairs, *Living Reviews in Relativity*, **6**, p. 5, (2003), astro-ph/0307536. 6, 23, 24

[27] BICEP2 Collaboration *et al.*, *ArXiv e-prints*, (2014), 1403.3985. 6

[28] P. Ade *et al.*, *Phys. Rev. Lett.*, **112**, p. 241101, (2014). [Online]. Available: http://link.aps.org/doi/10.1103/PhysRevLett.112.241101 6

[29] A. S. Eddington, *Proceedings of the Royal Society of London. Series A*, **102**, 716, pp. 268–282, 1922. 7, 8

[30] É. É. Flanagan and S. A. Hughes, *New Journal of Physics*, **7**, p. 204, (2005), gr-qc/0501041. 7

[31] J. B. Camp and N. J. Cornish, *Annu. Rev. Nucl. Part. Sci.*, **54**, pp. 525–577, 2004. 7

[32] M. Maggiore, *Gravitational Waves: Volume 1: Theory and Experiments*. Oxford university press, 2007, **1**. 8, 45

[33] K. Riles, *Progress in Particle and Nuclear Physics*, **68**, pp. 1–54, (2013), 1209.0667. 8

[34] L. D. Landau and E. M. Lifshitz, *The classical theory of fields*. Butterworth-Heinemann, 1975, **2**. 8

[35] F. J. Dyson, *The Search for Extraterrestrial Life, WA Benjamin, Nueva York*, p. 115, 1963. 8

[36] R. A. Isaacson, *Physical Review*, **166**, 5, p. 1272, 1968. 9

[37] S. A. Hughes, ARA&A, **47**, pp. 107–157, (2009), 0903.4877. 9, 13

[38] T. Futamase and Y. Itoh, *Living Reviews in Relativity*, **10**, p. 2, (2007). 9

[39] L. Blanchet, *Living Reviews in Relativity*, **17**, p. 2, (2014), 1310.1528. 9, 20

[40] A. Buonanno and T. Damour, Phys. Rev. D, **59**, 8, p. 084006, (1999), gr-qc/9811091. 10

[41] M. Sasaki and H. Tagoshi, *Living Reviews in Relativity*, **6**, p. 6, (2003), gr-qc/0306120. 10

[42] F. Pretorius, *Physical Review Letters*, **95**, 12, p. 121101, (2005), gr-qc/0507014. 10

[43] M. Campanelli, C. O. Lousto, P. Marronetti, and Y. Zlochower, *Physical Review Letters*, **96**, 11, p. 111101, (2006), gr-qc/0511048.

[44] J. G. Baker, J. Centrella, D.-I. Choi, M. Koppitz, and J. van Meter, *Physical Review Letters*, **96**, 11, p. 111102, (2006), gr-qc/0511103. 10

[45] F. Ohme, *Classical and Quantum Gravity*, **29**, 12, p. 124002, (2012), 1111.3737. 10

[46] L. Santamaría *et al.*, Phys. Rev. D, **82**, 6, p. 064016, (2010), 1005.3306.

[47] T. Damour, A. Nagar, M. Hannam, S. Husa, and B. Brügmann, Phys. Rev. D, **78**, 4, p. 044039, (2008), 0803.3162.

[48] A. Buonanno *et al.*, Phys. Rev. D, **79**, 12, p. 124028, (2009), 0902.0790. 10

[49] J. Weber and J. A. Wheeler, *Reviews of Modern Physics*, **29**, pp. 509–515, (1957). 11

[50] J. Weber, *Phys. Rev.*, **117**, pp. 306–313, (1960). [Online]. Available: http://link.aps.org/doi/10.1103/

PhysRev.117.306 11

[51] ——, *Phys. Rev. Lett.*, **22**, pp. 1320–1324, (1969). [Online]. Available: http://link.aps.org/doi/10.1103/PhysRevLett.22.1320 11

[52] J. A. Tyson and R. P. Giffard, ARA&A, **16**, pp. 521–554, 1978. 11

[53] A. Vinante and AURIGA Collaboration, *Classical and Quantum Gravity*, **23**, p. 103, (2006). 11

[54] A. de Waard, L. Gottardi, and G. Frossati, “MiniGRAIL, the first spherical gravitational wave detector,” in *Recent Developments in Gravitational Physics*, I. Ciufolini, E. Coccia, M. Colpi, V. Gorini, and R. Peron, Eds., 2006, p. 415. 11

[55] G. E. Moss, L. R. Miller, and R. L. Forward, *Appl. Opt.*, **10**, 11, pp. 2495–2498, (1971). [Online]. Available: http://ao.osa.org/abstract.cfm?URI=ao-10-11-2495 11

[56] R. Weiss, *Quarterly Progress Report, Research Laboratory of Electronics (MIT)*, **105**, p. 54, 1972. 11

[57] M. Pitkin, S. Reid, S. Rowan, and J. Hough, *Living Reviews in Relativity*, **14**, p. 5, (2011), 1102.3355. 11

[58] W. A. Edelstein, J. Hough, J. R. Pugh, and W. Martin, *Journal of Physics E Scientific Instruments*, **11**, p. 710, (1978). 13

[59] R. W. P. Drever *et al.*, “Gravitational wave detectors using laser interferometers and optical cavities: 1. ideas, principles and prospects,” in *Quantum Optics, Experimental Gravity and Measurement Theory*, P. Meystere and M. O. Scully, Eds. Plenum Publishing, 1983, pp. 503–514. 13

[60] K. A. Strain and B. J. Meers, *Phys. Rev. Lett.*, **66**, pp. 1391–1394, (1991). [Online]. Available: http://link.aps.org/doi/10.1103/PhysRevLett.66.1391

[61] G. Heinzel *et al.*, *Phys. Rev. Lett.*, **81**, pp. 5493–5496, (1998). [Online]. Available: http://link.aps.org/doi/10.1103/PhysRevLett.81.5493 13

[62] R. W. Drever, “Interferometric detectors for gravitational radiation.” in *Lecture Notes in Physics, Berlin Springer Verlag*, **124**, 1983, pp. 321–338. 13

[63] G. M. Harry *et al.*, *Classical and Quantum Gravity*, **19**, pp. 897–917, (2002), gr-qc/0109073. 13

[64] D. R. M. Crooks *et al.*, *Classical and Quantum Gravity*, **19**, pp. 883–896, (2002). 13

[65] S. Braccini *et al.*, *Review of Scientific Instruments*, **67**, 8, pp. 2899–2902, 1996. [Online]. Available: http://scitation.aip.org/content/aip/journal/rsi/67/8/10.1063/1.1147069 13

[66] M. V. Plissi *et al.*, *Review of Scientific Instruments*, **71**, 6, pp. 2539–2545, 2000. [Online]. Available: http://scitation.aip.org/content/aip/journal/rsi/71/6/10.1063/1.1150645

[67] R. Abbott *et al.*, *Classical and Quantum Gravity*, **19**, pp. 1591–1597, (2002). 13

[68] A. Abramovici *et al.*, *Science*, **256**, pp. 325–333, (1992). 13, 46

[69] B. P. Abbott *et al.*, *Reports on Progress in Physics*, **72**, 7, pp. 076 901–+, (2009), 0711.3041. 13

[70] J. Abadie *et al.*, Phys. Rev. D, **82**, 10, pp. 102 001–+, (2010). 14, 16

[71] R. Adhikari, P. Fritschel, and S. Waldman, *LIGO document, LIGO-T060156-01, http://www. ligo. caltech. edu/docs*, 2006. 14

[72] G. M. Harry and the LIGO Scientific Collaboration, *Classical and Quantum Gravity*, **27**, 8, pp. 084 006–+, (2010). 14

[73] J. Abadie *et al.*, *Phys. Rev. D*, **85**, p. 082002, (2012). [Online]. Available: http://link.aps.org/doi/10.1103/PhysRevD.85.082002 14, 16

[74] P. Barriga *et al.*, *Classical and Quantum Gravity*, **22**, p. 199, (2005). 14

[75] B. Aylott *et al.*, *ArXiv e-prints*, (2011), 1106.2547. 14, 46, 47, 48

[76] "Indian Initiative in Gravitational-wave Observations, IndIGO." [Online]. Available: http://www.gw-indigo.org/tiki-index.php?page=Welcome 14

[77] S. Fairhurst, *ArXiv e-prints*, (2012), 1205.6611.

[78] C. S. Unnikrishnan, *International Journal of Modern Physics D*, **22**, p. 41010, (2013). 14

[79] "Virgo." [Online]. Available: http://www.ego-gw.it/public/virgo/virgo.aspx 14

[80] F. Acernese *et al.*, *Astroparticle Physics*, **33**, pp. 182–189, (2010). 15

[81] ——, *Classical and Quantum Gravity*, **25**, 18, p. 184001, (2008). 15

[82] The Virgo Collaboration, "Advanced Virgo Baseline Design," Virgo, Virgo Technical Report VIR-0027A-09, 2009. [Online]. Available: https://pub3.ego-gw.it/itf/tds/file.php?callFile=VIR-0027A-09.pdf 15, 48, 85

[83] B. Willke *et al.*, *Classical and Quantum Gravity*, **19**, pp. 1377–1387, (2002). 15

[84] A. Khalaidovski *et al.*, *Journal of Physics Conference Series*, **363**, 1, p. 012013, (2012), 1112.0198. 15

[85] R. Takahashi and the TAMA Collaboration, *Classical and Quantum Gravity*, **21**, pp. S403–+, (2004). 15

[86] K. Agatsuma *et al.*, *Classical and Quantum Gravity*, **27**, 8, p. 084022, (2010), 0911.3090. 15

[87] K. Kuroda and LCGT Collaboration, *Classical and Quantum Gravity*, **27**, 8, pp. 084 004–+, (2010). 15

[88] K. Somiya, *Classical and Quantum Gravity*, **29**, 12, p. 124007, (2012), 1111.7185. 15

[89] Y. Aso *et al.*, Phys. Rev. D, **88**, 4, p. 043007, (2013), 1306.6747. 15

[90] B. Abbott *et al.*, *Phys. Rev. D*, **73**, p. 102002, (2006). [Online]. Available: http://link.aps.org/doi/10.1103/PhysRevD.73.102002 15

[91] J. Abadie *et al.*, *Phys. Rev. D*, **81**, p. 102001, (2010). [Online]. Available: http://link.aps.org/doi/10.1103/PhysRevD.81.102001 15, 21

[92] "The Einstein Telescope Project." [Online]. Available: http://www.et-gw.eu/ 16, 83, 85, 107

[93] "ET Vision Document." [Online]. Available: https://workarea.et-gw.eu/et/WG4-Astrophysics/visdoc 16

[94] A. Freise *et al.*, *Classical and Quantum Gravity*, **26**, 8, p. 085012, (2009), 0804.1036. 16, 82, 84

[95] B. Sathyaprakash *et al.*, *Classical and Quantum Gravity*, **29**, 12, p. 124013, (2012), 1206.0331. 82, 84

[96] M. Punturo *et al.*, *Classical and Quantum Gravity*, **27**, 19, p. 194002, (2010). 16, 79

[97] S. Hild *et al.*, *Classical and Quantum Gravity*, **27**, 1, p. 015003, (2010), 0906.2655. 16, 83, 84

[98] S. E. Woosley, A. Heger, and T. A. Weaver, *Rev. Mod. Phys.*, **74**, pp. 1015–1071, (2002). [Online]. Available: http://link.aps.org/doi/10.1103/RevModPhys.74.1015 16, 17

[99] J. A. Faber and F. A. Rasio, *Living Reviews in Relativity*, **15**, p. 8, (2012), 1204.3858. 17, 19, 20

[100] K. A. Postnov and L. R. Yungelson, *Living Reviews in Relativity*, **17**, p. 3, (2014), 1403.4754. 16, 17, 19

[101] P. C. Peters and J. Mathews, *Phys. Rev.*, **131**, pp. 435–440, (1963). [Online]. Available:

http://link.aps.org/doi/10.1103/PhysRev.131.435 16

[102] P. C. Peters, *Phys. Rev.*, **136**, pp. B1224–B1232, (1964). [Online]. Available: http://link.aps.org/doi/10.1103/PhysRev.136.B1224 16, 17, 29, 119

[103] J. M. Lattimer and M. Prakash, *Science*, **304**, 5670, pp. 536–542, 2004, http://www.sciencemag.org/content/304/5670/536.full.pdf. [Online]. Available: http://www.sciencemag.org/content/304/5670/536.abstract 17

[104] A. Sadowski *et al.*, ApJ, **676**, pp. 1162–1169, (2008), 0710.0878. 17

[105] D. Clausen, S. Sigurdsson, and D. F. Chernoff, MNRAS, **428**, pp. 3618–3629, (2013), 1210.8153. 17

[106] C. L. Fryer, ApJ, **522**, pp. 413–418, (1999), astro-ph/9902315. 17

[107] A. Heger, C. L. Fryer, S. E. Woosley, N. Langer, and D. H. Hartmann, ApJ, **591**, pp. 288–300, (2003), astro-ph/0212469. 17

[108] D. R. Lorimer, *Living Reviews in Relativity*, **11**, p. 8, (2008), 0811.0762. 17, 18, 19, 23, 24

[109] D. Bhattacharya and E. P. J. van den Heuvel, Phys. Rep., **203**, pp. 1–124, 1991. 17, 19, 89

[110] G. Hobbs, D. R. Lorimer, A. G. Lyne, and M. Kramer, MNRAS, **360**, pp. 974–992, (2005), astro-ph/0504584. 19

[111] D. Lai, “Neutron star kicks and supernova asymmetry,” in *Cosmic explosions in three dimensions*, P. Höflich, P. Kumar, and J. C. Wheeler, Eds., 2004, p. 276, astro-ph/0312542. 19

[112] C. Wang, D. Lai, and J. L. Han, ApJ, **639**, pp. 1007–1017, (2006), astro-ph/0509484. 19

[113] K. S. Thorne and A. N. Zytkow, ApJ, **212**, pp. 832–858, (1977). 19

[114] E. M. Levesque, P. Massey, N. Morrell, and A. Zytkow, “A Search for Thorne-Zytkow Objects,” in *American Astronomical Society Meeting Abstracts*, ser. American Astronomical Society Meeting Abstracts, **223**, Jan. 2014, p. 113.06. 19

[115] K. A. Postnov and L. R. Yungelson, *Living Reviews in Relativity*, **17**, p. 3, (2014), 1403.4754. 19

[116] E. M. Levesque, P. Massey, A. N. Żytkow, and N. Morrell, MNRAS, **443**, pp. L94–L98, (2014), 1406.0001. 19

[117] S. A. Colgate, ApJ, **163**, p. 221, (1971). 19

[118] Y. B. Zel’dovich, L. N. Ivanova, and D. K. Nadezhin, Soviet Ast., **16**, p. 209, (1972).

[119] R. A. Chevalier, ApJ, **411**, pp. L33–L36, (1993). 19

[120] H. A. Bethe, G. E. Brown, and C.-H. Lee, Phys. Rep., **442**, pp. 5–22, (2007), astro-ph/0510379. 19

[121] N. Ivanova *et al.*, A&A Rev., **21**, p. 59, (2013), 1209.4302. 19

[122] H. A. Bethe and G. E. Brown, ApJ, **506**, pp. 780–789, (1998), astro-ph/9802084. 20

[123] K. Belczyński and V. Kalogera, ApJ, **550**, pp. L183–L187, (2001), arXiv:astro-ph/0012172.

[124] M. Dominik *et al.*, ApJ, **759**, p. 52, (2012), 1202.4901. 20, 52, 88

[125] C. W. Helstrom, *Statistical theory of signal detection*. Pergamon Press Oxford, 1968, **384**. 20, 48

[126] L. A. Waistein and V. D. Zubakov, *Extraction of signals from noise*. Dover, 1970.

[127] B. S. Sathyaprakash and B. F. Schutz, *Living Reviews in Relativity*, **12**, pp. 2–+, (2009), 0903.0338. 20, 85

[128] J. S. Read *et al.*, Phys. Rev. D, **79**, 12, p. 124033, (2009), 0901.3258. 20

[129] W. Del Pozzo, T. G. F. Li, M. Agathos, C. Van Den Broeck, and S. Vitale, *Physical Review Letters*, **111**, 7, p. 071101, (2013), 1307.8338. 20

[130] M. Shibata, *Physical Review Letters*, **94**, 20, p. 201101, (2005), gr-qc/0504082. 20

[131] A. Bauswein, H.-T. Janka, K. Hebeler, and A. Schwenk, Phys. Rev. D, **86**, 6, p. 063001, (2012), 1204.1888. 20

[132] T. W. Baumgarte, S. L. Shapiro, and M. Shibata, ApJ, **528**, pp. L29–L32, (2000), astro-ph/9910565. 20

[133] M. D. Duez, Y. T. Liu, S. L. Shapiro, M. Shibata, and B. C. Stephens, *Physical Review Letters*, **96**, 3, p. 031101, (2006), astro-ph/0510653.

[134] M. Shibata, M. D. Duez, Y. T. Liu, S. L. Shapiro, and B. C. Stephens, *Physical Review Letters*, **96**, 3, p. 031102, (2006), astro-ph/0511142. 20

[135] C. Messenger, K. Takami, S. Gossan, L. Rezzolla, and B. S. Sathyaprakash, *ArXiv e-prints*, (2013), 1312.1862. 20, 42

[136] T. Piran, *Reviews of Modern Physics*, **76**, pp. 1143–1210, (2004), astro-ph/0405503. 20

[137] D. Eichler, M. Livio, T. Piran, and D. N. Schramm, Nature, **340**, pp. 126–128, (1989). 20

[138] E. Nakar and T. Piran, Nature, **478**, pp. 82–84, (2011), 1102.1020. 20

[139] B. D. Metzger *et al.*, MNRAS, **406**, pp. 2650–2662, (2010), 1001.5029. 20

[140] N. R. Tanvir *et al.*, Nature, **500**, pp. 547–549, (2013), 1306.4971.

[141] E. Berger, W. Fong, and R. Chornock, ApJ, **774**, p. L23, (2013), 1306.3960. 20

[142] B. D. Metzger and E. Berger, ApJ, **746**, p. 48, (2012), 1108.6056. 20

[143] D. R. Lorimer, M. Bailes, M. A. McLaughlin, D. J. Narkevic, and F. Crawford, *Science*, **318**, pp. 777–, (2007), 0709.4301. 20

[144] D. Thornton *et al.*, *Science*, **341**, pp. 53–56, (2013), 1307.1628.

[145] L. G. Spitler *et al.*, *ArXiv e-prints*, (2014), 1404.2934. 20

[146] H. Falcke and L. Rezzolla, A&A, **562**, p. A137, (2014), 1307.1409. 21

[147] J. Abadie *et al.*, *Classical and Quantum Gravity*, **27**, 17, pp. 173 001–+, (2010), 1003.2480. 21, 50, 54, 58, 70, 78, 93, 112

[148] C. Kim, V. Kalogera, and D. R. Lorimer, ApJ, **584**, pp. 985–995, (2003), arXiv:astro-ph/0207408. 21, 59

[149] V. Kalogera *et al.*, ApJ, **614**, pp. L137–L138, (2004), arXiv:astro-ph/0312101. 54

[150] C. Kim, V. Kalogera, and D. R. Lorimer, *ArXiv Astrophysics e-prints*, (2006), arXiv:astro-ph/0608280. 21, 54

[151] S. Osłowski, T. Bulik, D. Gondek-Rosińska, and K. Belczyński, MNRAS, **413**, pp. 461–479, (2011), 0903.3538. 21

[152] E. Nakar, A. Gal-Yam, and D. B. Fox, ApJ, **650**, pp. 281–290, (2006), arXiv:astro-ph/0511254. 21

[153] D. Guetta and L. Stella, A&A, **498**, pp. 329–333, (2009), 0811.0684.

[154] C. Enrico Petrillo, A. Dietz, and M. Cavaglià, ApJ, **767**, p. 140, (2013), 1202.0804. 21

[155] R. Voss and T. M. Tauris, MNRAS, **342**, pp. 1169–1184, (2003), arXiv:astro-ph/0303227. 21

[156] J. A. de Freitas Pacheco, T. Regimbau, S. Vincent, and A. Spallicci, *International Journal of Modern Physics D*, **15**, pp. 235–249, 2006, arXiv:astro-ph/0510727.

[157] R. O'Shaughnessy, V. Kalogera, and K. Belczynski, ApJ, **716**, pp. 615–633, (2010), 0908.3635. 47, 52, 56, 70, 87

[158] M. Dominik *et al.*, ApJ, **779**, p. 72, (2013), 1308.1546. 21

[159] L. Z. Kelley, I. Mandel, and E. Ramirez-Ruiz, Phys. Rev. D, **87**, 12, p. 123004, (2013), 1209.3027. 21

[160] J. Abadie *et al.*, Phys. Rev. D, **85**, 12, p. 122007, (2012), 1202.2788. 21

[161] J. Aasi *et al.*, Phys. Rev. D, **88**, 10, p. 102002, (2013), 1309.6221. 21

[162] B. P. Abbott *et al.*, ApJ, **713**, pp. 671–685, (2010), 0909.3583. 21

[163] ——, Nature, **460**, pp. 990–994, (2009), 0910.5772. 21

[164] K. Danzmann and A. Rüdiger, *Classical and Quantum Gravity*, **20**, p. 1, (2003). 22

[165] C. J. Hogan and P. L. Bender, Phys. Rev. D, **64**, 6, p. 062002, (2001), astro-ph/0104266. 22

[166] D. A. Shaddock, Phys. Rev. D, **69**, 2, p. 022001, (2004), gr-qc/0306125. 22

[167] P. Amaro-Seoane *et al.*, *GW Notes, Vol. 6, p. 4-110*, **6**, pp. 4–110, (2013), 1201.3621. 22

[168] T. e. Consortium *et al.*, *ArXiv e-prints*, (2013), 1305.5720. 22

[169] F. Antonucci *et al.*, *Classical and Quantum Gravity*, **29**, 12, p. 124014, (2012). 22

[170] J. Crowder and N. J. Cornish, Phys. Rev. D, **72**, 8, p. 083005, (2005), gr-qc/0506015. 22

[171] P. L. Bender, M. C. Begelman, and J. R. Gair, *Classical and Quantum Gravity*, **30**, 16, p. 165017, (2013). 22

[172] G. M. Harry, P. Fritschel, D. A. Shaddock, W. Folkner, and E. S. Phinney, *Classical and Quantum Gravity*, **23**, pp. 4887–4894, (2006). 22

[173] S. Kawamura *et al.*, *Classical and Quantum Gravity*, **23**, p. 125, (2006). 22

[174] ——, *Classical and Quantum Gravity*, **28**, 9, p. 094011, (2011). 22

[175] M. Ando *et al.*, *Classical and Quantum Gravity*, **27**, 8, p. 084010, (2010). 22

[176] A. Stroeer and A. Vecchio, *Classical and Quantum Gravity*, **23**, p. 809, (2006), astro-ph/0605227. 22

[177] G. Nelemans, "Galactic Binaries with eLISA," in *9th LISA Symposium*, ser. Astronomical Society of the Pacific Conference Series, G. Auger, P. Binétruy, and E. Plagnol, Eds., **467**, Jan. 2013, p. 27, 1302.0138. 22

[178] S. Nissanke, M. Vallisneri, G. Nelemans, and T. A. Prince, ApJ, **758**, p. 131, (2012), 1201.4613. 22

[179] A. J. Ruiter, K. Belczynski, M. Benacquista, S. L. Larson, and G. Williams, ApJ, **717**, pp. 1006–1021, (2010), 0705.3272. 22

[180] F. D. Ryan, Phys. Rev. D, **52**, pp. 5707–5718, (1995). 22

[181] L. Barack and C. Cutler, Phys. Rev. D, **69**, 8, p. 082005, (2004), gr-qc/0310125.

[182] P. Amaro-Seoane *et al.*, *Classical and Quantum Gravity*, **24**, p. 113, (2007), astro-ph/0703495. 22

[183] P. Binétruy, A. Bohé, C. Caprini, and J.-F. Dufaux, J. Cosmology Astropart. Phys., **6**, p. 27, (2012),

1201.0983. 23

[184] A. Hewish, S. J. Bell, J. D. H. Pilkington, P. F. Scott, and R. A. Collins, Nature, **217**, pp. 709–713, (1968). 23, 24

[185] F. Pacini, Nature, **219**, pp. 145–146, (1968). 23

[186] T. Gold, Nature, **218**, pp. 731–732, (1968). 23

[187] P. Goldreich and W. H. Julian, ApJ, **157**, p. 869, (1969). 23

[188] P. A. Sturrock, ApJ, **164**, p. 529, (1971). 23

[189] D. W. Meltzer and K. S. Thorne, ApJ, **145**, p. 514, (1966). 23

[190] D. H. Staelin and E. C. Reifenstein, III, *Science*, **162**, pp. 1481–1483, (1968). 23

[191] D. W. Richards and J. M. Comella, Nature, **222**, pp. 551–552, (1969). 23

[192] M. M. Davis, J. H. Taylor, J. M. Weisberg, and D. C. Backer, Nature, **315**, pp. 547–550, (1985). 23

[193] D. R. Lorimer and M. Kramer, *Handbook of Pulsar Astronomy*. Cambridge University Press, Oct. 2012. 24

[194] T. H. Hankins and B. J. Rickett, "Pulsar signal processing," in *Methods in Computational Physics. Volume 14 - Radio astronomy*, B. Alder, S. Fernbach, and M. Rotenberg, Eds., **14**, 1975, pp. 55–129. 24

[195] G. B. Hobbs, R. T. Edwards, and R. N. Manchester, MNRAS, **369**, pp. 655–672, (2006), arXiv:astro-ph/0603381. 25, 118, 128

[196] R. T. Edwards, G. B. Hobbs, and R. N. Manchester, MNRAS, **372**, pp. 1549–1574, (2006), arXiv:astro-ph/0607664.

[197] G. Hobbs *et al.*, MNRAS, **394**, pp. 1945–1955, (2009), 0901.0592. 25, 118, 128

[198] P. W. Anderson and N. Itoh, Nature, **256**, pp. 25–27, (1975). 25

[199] C. M. Espinoza, A. G. Lyne, B. W. Stappers, and M. Kramer, MNRAS, **414**, pp. 1679–1704, (2011), 1102.1743. 25

[200] G. Hobbs, A. G. Lyne, and M. Kramer, MNRAS, **402**, pp. 1027–1048, (2010), 0912.4537. 25

[201] A. Lyne, G. Hobbs, M. Kramer, I. Stairs, and B. Stappers, *Science*, **329**, pp. 408–, (2010), 1006.5184. 25

[202] R. M. Shannon and J. M. Cordes, ApJ, **725**, pp. 1607–1619, (2010), 1010.4794. 26, 138

[203] J. H. Taylor and J. M. Weisberg, ApJ, **253**, pp. 908–920, (1982). 26

[204] ——, ApJ, **345**, pp. 434–450, (1989). 26

[205] T. Damour and N. Deruelle, *Ann. Inst. Henri Poincaré Phys. Théor., Vol. 43, No. 1, p. 107 - 132*, **43**, pp. 107–132, 1985. 26

[206] ——, *Ann. Inst. Henri Poincaré Phys. Théor., Vol. 44, No. 3, p. 263 - 292*, **44**, pp. 263–292, 1986. 26

[207] M. Burgay *et al.*, Nature, **426**, pp. 531–533, (2003), astro-ph/0312071. 26

[208] A. G. Lyne *et al.*, *Science*, **303**, pp. 1153–1157, (2004), astro-ph/0401086. 26

[209] M. V. Sazhin, Soviet Ast., **22**, pp. 36–38, (1978). 27, 122

[210] S. Detweiler, ApJ, **234**, pp. 1100–1104, (1979).

[211] F. B. Estabrook and H. D. Wahlquist, *General Relativity and Gravitation*, **6**, pp. 439–447, (1975).

[212] W. L. Burke, ApJ, **196**, pp. 329–334, (1975). 27, 122

[213] M. Anholm, S. Ballmer, J. D. E. Creighton, L. R. Price, and X. Siemens, Phys. Rev. D, **79**, 8, p. 084030, (2009), 0809.0701. 27, 122, 126, 132, 165

[214] L. G. Book and É. É. Flanagan, Phys. Rev. D, **83**, 2, p. 024024, (2011), 1009.4192. 27, 122, 165

[215] R. S. Foster and D. C. Backer, ApJ, **361**, pp. 300–308, (1990). 27

[216] R. W. Hellings and G. S. Downs, ApJ, **265**, pp. L39–L42, (1983). 27, 28, 31, 118, 131, 154

[217] "Parkes Pulsar Timing Array." [Online]. Available: http://www.atnf.csiro.au/research/pulsar/ppta/ 27

[218] G. Hobbs, *Classical and Quantum Gravity*, **30**, 22, p. 224007, (2013), 1307.2629. 27

[219] "North American Nanohertz Observatory for Gravitational Waves." [Online]. Available: http://nanograv.org/ 28

[220] M. A. McLaughlin, *Classical and Quantum Gravity*, **30**, 22, p. 224008, (2013), 1310.0758. 28

[221] "European Pulsar Timing Array." [Online]. Available: http://www.epta.eu.org/ 28

[222] M. Kramer and D. J. Champion, *Classical and Quantum Gravity*, **30**, 22, p. 224009, (2013). 28

[223] "International Pulsar Timing Array." [Online]. Available: http://www.ipta4gw.org/ 28, 131

[224] R. N. Manchester and IPTA, *Classical and Quantum Gravity*, **30**, 22, p. 224010, (2013). 28

[225] M. Rajagopal and R. W. Romani, ApJ, **446**, p. 543, (1995), astro-ph/9412038. 28, 29, 164

[226] A. H. Jaffe and D. C. Backer, ApJ, **583**, pp. 616–631, (2003), arXiv:astro-ph/0210148.

[227] J. S. B. Wyithe and A. Loeb, ApJ, **590**, pp. 691–706, (2003), arXiv:astro-ph/0211556. 28, 29, 164

[228] L. Ferrarese and H. Ford, Space Sci. Rev., **116**, pp. 523–624, (2005), astro-ph/0411247. 28, 184

[229] J. Magorrian *et al.*, AJ, **115**, pp. 2285–2305, (1998), astro-ph/9708072. 28, 184

[230] L. Ferrarese and D. Merritt, ApJ, **539**, pp. L9–L12, (2000), astro-ph/0006053.

[231] A. Marconi and L. K. Hunt, ApJ, **589**, pp. L21–L24, (2003), astro-ph/0304274. 28, 184

[232] S. D. M. White and M. J. Rees, MNRAS, **183**, pp. 341–358, (1978). 29, 184

[233] G. Kauffmann and M. Haehnelt, MNRAS, **311**, pp. 576–588, (2000), astro-ph/9906493. 29, 184

[234] M. C. Begelman, R. D. Blandford, and M. J. Rees, Nature, **287**, pp. 307–309, (1980). 29, 30

[235] A. Sesana, *Classical and Quantum Gravity*, **30**, 22, p. 224014, (2013), 1307.2600. 29, 30, 166

[236] K. S. Thorne, *Gravitational radiation.* Cambridge University Press, 1987, pp. 330–458. 29, 45, 46

[237] E. S. Phinney, *ArXiv Astrophysics e-prints*, (2001), arXiv:astro-ph/0108028. 29, 31

[238] A. Sesana, A. Vecchio, and M. Volonteri, MNRAS, **394**, pp. 2255–2265, (2009), 0809.3412. 29, 119, 164

[239] A. Sesana, *Classical and Quantum Gravity*, **30**, 24, p. 244009, (2013), 1307.4086. 29, 164

[240] V. Ravi *et al.*, ApJ, **761**, p. 84, (2012), 1210.3854. 29, 118, 164

[241] A. Sesana, A. Vecchio, and C. N. Colacino, MNRAS, **390**, pp. 192–209, (2008), 0804.4476. 29, 118, 164

[242] V. Ravi, J. S. B. Wyithe, R. M. Shannon, G. Hobbs, and R. N. Manchester, MNRAS, **442**, pp. 56–68, (2014), 1404.5183. 29, 166

[243] M. Milosavljević and D. Merritt, ApJ, **563**, pp. 34–62, (2001), astro-ph/0103350. 30

[244] M. Dotti, A. Sesana, and R. Decarli, *Advances in Astronomy*, **2012**, 2012, 1111.0664. 30

[245] D. Merritt and M. Milosavljević, *Living Reviews in Relativity*, **8**, p. 8, (2005), astro-ph/0410364. 30

[246] G. D. Quinlan, New A, **1**, pp. 35–56, (1996), astro-ph/9601092. 30

[247] P. B. Ivanov, J. C. B. Papaloizou, and A. G. Polnarev, MNRAS, **307**, pp. 79–90, (1999), astro-ph/9812198. 30

[248] J. Cuadra, P. J. Armitage, R. D. Alexander, and M. C. Begelman, MNRAS, **393**, pp. 1423–1432, (2009), 0809.0311. 30

[249] M. Preto, I. Berentzen, P. Berczik, and R. Spurzem, ApJ, **732**, p. L26, (2011), 1102.4855. 30

[250] C. Roedig, M. Dotti, A. Sesana, J. Cuadra, and M. Colpi, MNRAS, **415**, pp. 3033–3041, (2011), 1104.3868. 30

[251] M. Enoki and M. Nagashima, *Progress of Theoretical Physics*, **117**, pp. 241–256, (2007), astro-ph/0609377. 30

[252] L. P. Grishchuk, *Pis ma Zhurnal Eksperimental noi i Teoreticheskoi Fiziki*, **23**, pp. 326–330, 1976. 30

[253] ——, *Physics Uspekhi*, **48**, pp. 1235–1247, (2005), arXiv:gr-qc/0504018. 30

[254] A. Vilenkin, Phys. Rev. D, **24**, pp. 2082–2089, (1981). 30

[255] ——, *Physics Letters B*, **107**, pp. 47–50, (1981).

[256] S. Ölmez, V. Mandic, and X. Siemens, Phys. Rev. D, **81**, 10, p. 104028, (2010), 1004.0890.

[257] S. A. Sanidas, R. A. Battye, and B. W. Stappers, Phys. Rev. D, **85**, 12, p. 122003, (2012), 1201.2419. 30

[258] T. Damour and A. Vilenkin, Phys. Rev. D, **71**, 6, p. 063510, (2005), arXiv:hep-th/0410222. 30

[259] F. A. Jenet *et al.*, ApJ, **653**, pp. 1571–1576, (2006), arXiv:astro-ph/0609013. 30

[260] R. van Haasteren *et al.*, MNRAS, **414**, pp. 3117–3128, (2011), 1103.0576. 31

[261] P. B. Demorest *et al.*, ApJ, **762**, p. 94, (2013), 1201.6641. 31, 185, 186

[262] R. M. Shannon *et al.*, *Science*, **342**, pp. 334–337, (2013), 1310.4569. 31

[263] S. T. McWilliams, J. P. Ostriker, and F. Pretorius, *ArXiv e-prints*, (2012), 1211.4590. 31

[264] ——, *ArXiv e-prints*, (2012), 1211.5377. 31

[265] A. Sesana, MNRAS, (2013), 1211.5375. 31

[266] X. Siemens, J. Ellis, F. Jenet, and J. D. Romano, *Classical and Quantum Gravity*, **30**, 22, p. 224015, (2013), 1305.3196. 31

[267] “Square Kilometre Array.” [Online]. Available: http://www.skatelescope.org/ 31

[268] T. J. W. Lazio, *Classical and Quantum Gravity*, **30**, 22, p. 224011, (2013). 31

[269] F. A. Jenet, A. Lommen, S. L. Larson, and L. Wen, ApJ, **606**, pp. 799–803, (2004), astro-ph/0310276. 31, 32, 164

[270] D. R. B. Yardley *et al.*, MNRAS, **407**, pp. 669–680, (2010), 1005.1667. 31, 164, 167

[271] J. A. Ellis, F. A. Jenet, and M. A. McLaughlin, ApJ, **753**, p. 96, (2012), 1202.0808. 31

[272] S. Babak and A. Sesana, Phys. Rev. D, **85**, 4, p. 044034, (2012), 1112.1075. 31, 164

[273] J. A. Ellis, X. Siemens, and J. D. E. Creighton, ApJ, **756**, p. 175, (2012), 1204.4218. 31, 164, 166, 168, 171, 187

[274] J. A. Ellis, *Classical and Quantum Gravity*, **30**, 22, p. 224004, (2013), 1305.0835. 31, 165, 167, 172, 174

[275] H. Jeffreys, *Theory of probability*, ser. International series of monographs on physics. Clarendon Press, 1983. 32, 33

[276] J. Skilling, *AIP Conference Proceedings*, **735**, 1, pp. 395–405, 2004. [Online]. Available: http://scitation.aip.org/content/aip/proceeding/aipcp/10.1063/1.1835238 33, 35

[277] F. Feroz and M. P. Hobson, MNRAS, **384**, pp. 449–463, (2008), 0704.3704. 33, 35

[278] F. Feroz, M. P. Hobson, and M. Bridges, MNRAS, **398**, pp. 1601–1614, (2009), 0809.3437.

[279] F. Feroz, M. P. Hobson, E. Cameron, and A. N. Pettitt, *ArXiv e-prints*, (2013), 1306.2144. 33, 35, 170

[280] H. Haario, E. Saksman, and J. Tamminen, *Computational Statistics*, **14**, 3, p. 375, 1999. [Online]. Available: http://www.springerlink.com/index/10.1007/s001800050022 33, 34

[281] ——, *Official Journal for the Bernoulli Society of Mathematical Statistics and Probability*, **7**, No. 2, pp. pp. 223–242, 2001. [Online]. Available: http://www.jstor.org/stable/3318737 34

[282] J. Dunkley, M. Bucher, P. G. Ferreira, K. Moodley, and C. Skordis, MNRAS, **356**, pp. 925–936, (2005), arXiv:astro-ph/0405462. 33, 34

[283] A. Gelman, G. Roberts, and W. Gilks, "Efficient metropolis jumping rules," in *Bayesian Statistics*, J. M. Bernado *et al.*, Eds. Oxford University Press, Oxford, 1996, **5**, p. 599. 34

[284] B. F. Schutz, Nature, **323**, pp. 310–+, (1986). 42, 46, 74

[285] D. E. Holz and S. A. Hughes, *Class. Quantum Grav.*, 20, pp. S65–S72, 2003, astro-ph/0212218. 42

[286] D. E. Holz and S. A. Hughes, ApJ, **629**, pp. 15–22, (2005), arXiv:astro-ph/0504616. 42

[287] S. Nissanke, D. E. Holz, S. A. Hughes, N. Dalal, and J. L. Sievers, ApJ, **725**, pp. 496–514, (2010), 0904.1017. 42, 68, 76, 77

[288] S. Nissanke *et al.*, *ArXiv e-prints*, (2013), 1307.2638. 42

[289] C. L. MacLeod and C. J. Hogan, Phys. Rev. D, **77**, 4, pp. 043 512–+, (2008), 0712.0618. 42, 77

[290] J. Read and C. Messenger, "Measuring luminosity distance and redshift using only gravitational wave observations of binary neutron star coalescences," in *APS April Meeting Abstracts*, Mar. 2012, p. 8004. 42

[291] C. Messenger and J. Read, *Physical Review Letters*, **108**, 9, p. 091101, (2012), 1107.5725. 42, 82

[292] É. É. Flanagan and T. Hinderer, Phys. Rev. D, **77**, 2, p. 021502, (2008), 0709.1915. 42

[293] L. Baiotti, B. Giacomazzo, and L. Rezzolla, Phys. Rev. D, **78**, 8, p. 084033, (2008), 0804.0594. 42

[294] L. Rezzolla, L. Baiotti, B. Giacomazzo, D. Link, and J. A. Font, *Classical and Quantum Gravity*, **27**, 11, p. 114105, (2010), 1001.3074. 42

[295] D. Marković, Phys. Rev. D, **48**, pp. 4738–4756, (1993). 43

[296] D. F. Chernoff and L. S. Finn, ApJ, **411**, pp. L5–L8, (1993), arXiv:gr-qc/9304020. 43

[297] L. S. Finn, Phys. Rev. D, **53**, pp. 2878–2894, (1996), arXiv:gr-qc/9601048. 43, 46, 47, 49, 50, 51, 53, 56, 84, 85, 86

[298] S. R. Taylor, J. R. Gair, and I. Mandel, Phys. Rev. D, **85**, 2, p. 023535, (2012), 1108.5161. 43

[299] C. Cutler and E. E. Flanagan, *Phys. Rev. D*, **49**, 6, pp. 2658–2697, (1994). 45, 46

[300] S. V. Dhurandhar and M. Tinto, MNRAS, **234**, pp. 663–676, (1988). 45

[301] S. Fairhurst, *Classical and Quantum Gravity*, **28**, 10, pp. 105 021–+, (2011), 1010.6192. 46

[302] M. V. van der Sluys *et al.*, ApJ, **688**, pp. L61–L64, (2008), 0710.1897. 46

[303] J. Abadie *et al.*, *Nuclear Instruments and Methods in Physics Research A*, **624**, pp. 223–240, (2010), 1007.3973. 47

[304] S. Vitale *et al.*, Phys. Rev. D, **85**, 6, p. 064034, (2012), 1111.3044. 47, 101

[305] S. Nissanke, J. Sievers, N. Dalal, and D. Holz, ApJ, **739**, p. 99, (2011), 1105.3184. 47

[306] B. Abbott *et al.*, *Nuclear Instruments and Methods in Physics Research A*, **517**, pp. 154–179, (2004), arXiv:gr-qc/0308043. 47

[307] A. C. Searle, S. M. Scott, D. E. McClelland, and L. S. Finn, Phys. Rev. D, **73**, 12, pp. 124 014–+, (2006). 47, 48

[308] "Advanced LIGO anticipated sensitivity curves2010." [Online]. Available: https://dcc.ligo.org/cgi-bin/DocDB/ShowDocument?docid=2974 47, 50, 83, 85

[309] F. Beauville *et al.*, *Classical and Quantum Gravity*, **25**, 4, pp. 045 001–+, (2008), arXiv:gr-qc/0701027. 48, 71

[310] P. Jaranowski and A. Królak, *Living Reviews in Relativity*, **15**, p. 4, (2012). 48

[311] P. Jaranowski and A. Krolak, *Analysis of Gravitational-Wave Data*. Cambridge University Press, Aug. 2009. 48

[312] L. S. Finn, Phys. Rev. D, **46**, pp. 5236–5249, (1992), gr-qc/9209010. 49

[313] P. Nutzman, V. Kalogera, L. S. Finn, C. Hendrickson, and K. Belczynski, ApJ, **612**, pp. 364–374, (2004), arXiv:astro-ph/0402091. 49, 50, 84

[314] L. E. Kidder, C. M. Will, and A. G. Wiseman, Phys. Rev. D, **47**, pp. 3281–3291, (1993). 50

[315] L. S. Finn and D. F. Chernoff, Phys. Rev. D, **47**, pp. 2198–2219, (1993), arXiv:gr-qc/9301003. 51

[316] B. Kiziltan, A. Kottas, and S. E. Thorsett, *ArXiv e-prints*, (2010), 1011.4291. 51, 58, 61, 72, 93

[317] R. Valentim, E. Rangel, and J. E. Horvath, MNRAS, **414**, pp. 1427–1431, (2011), 1101.4872. 51

[318] S. E. Thorsett and D. Chakrabarty, ApJ, **512**, pp. 288–299, (1999), astro-ph/9803260. 51

[319] B. Kiziltan, A. Kottas, M. De Yoreo, and S. E. Thorsett, ApJ, **778**, p. 66, (2013), 1011.4291. 52

[320] F. Özel, D. Psaltis, R. Narayan, and A. Santos Villarreal, ApJ, **757**, p. 55, (2012), 1201.1006. 52

[321] K. Belczynski *et al.*, *Astrophys. J. Suppl.*, **174**, pp. 223–260, (2008). 52

[322] I. Mandel and R. O'Shaughnessy, *Classical and Quantum Gravity*, **27**, 11, pp. 114 007–+, (2010), 0912.1074. 52

[323] C. Cutler and J. Harms, Phys. Rev. D, **73**, 4, pp. 042 001–+, (2006), arXiv:gr-qc/0511092. 54

[324] R. Schneider, V. Ferrari, S. Matarrese, and S. F. Portegies Zwart, MNRAS, **324**, pp. 797–810, (2001), arXiv:astro-ph/0002055. 54, 88

[325] V. Kalogera, R. Narayan, D. N. Spergel, and J. H. Taylor, ApJ, **556**, pp. 340–356, (2001), arXiv:astro-

ph/0012038. 54

[326] R. K. Kopparapu *et al.*, ApJ, **675**, pp. 1459–1467, (2008), 0706.1283. 54

[327] D. Larson *et al.*, ApJS, **192**, pp. 16–+, (2011), 1001.4635. 57

[328] N. Jarosik *et al.*, ApJS, **192**, pp. 14–+, (2011), 1001.4744. 57, 92

[329] G. Hinshaw *et al.*, ApJS, **208**, p. 19, (2013), 1212.5226. 57

[330] J. R. Gair, C. Tang, and M. Volonteri, Phys. Rev. D, **81**, 10, pp. 104 014–+, (2010), 1004.1921. 58, 59, 64, 66

[331] R. O'Shaughnessy, C. Kim, V. Kalogera, and K. Belczynski, ApJ, **672**, pp. 479–488, (2008). 59

[332] A. Sesana, J. Gair, E. Berti, and M. Volonteri, Phys. Rev. D, **83**, 4, pp. 044 036–+, (2011), 1011.5893. 60

[333] I. Mandel, Phys. Rev. D, **81**, 8, pp. 084 029–+, (2010), 0912.5531. 66, 68

[334] L. Rezzolla *et al.*, ApJ, **732**, pp. L6+, (2011), 1101.4298. 74, 76, 78, 79

[335] K. Z. Stanek, P. M. Garnavich, J. Kaluzny, W. Pych, and I. Thompson, ApJ, **522**, pp. L39–L42, (1999), arXiv:astro-ph/9905304. 74, 76

[336] D. N. Burrows *et al.*, ApJ, **653**, pp. 468–473, (2006), arXiv:astro-ph/0604320. 76

[337] D. A. Frail *et al.*, ApJ, **562**, pp. L55–L58, (2001), arXiv:astro-ph/0102282. 74, 75

[338] M. R. Metzger *et al.*, Nature, **387**, pp. 878–880, (1997). 74

[339] A. Dietz, A&A, **529**, pp. A97+, (2011), 1011.2059. 75, 78

[340] E. Nakar, Phys. Rep., **442**, pp. 166–236, (2007), arXiv:astro-ph/0701748. 76

[341] L. K. Nuttall and P. J. Sutton, Phys. Rev. D, **82**, 10, pp. 102 002–+, (2010), 1009.1791. 77

[342] W. Del Pozzo, Phys. Rev. D, **86**, 4, p. 043011, (2012), 1108.1317. 77

[343] G. Efstathiou, MNRAS, **440**, pp. 1138–1152, (2014), 1311.3461. 79

[344] M. Punturo *et al.*, *Classical and Quantum Gravity*, **27**, 8, p. 084007, (2010). 82, 84, 112

[345] S. Hild *et al.*, *Classical and Quantum Gravity*, **28**, 9, p. 094013, (2011), 1012.0908. 82, 83, 84, 86, 87

[346] B. S. Sathyaprakash, B. F. Schutz, and C. Van Den Broeck, *Classical and Quantum Gravity*, **27**, 21, p. 215006, (2010), 0906.4151. 82, 87, 101, 102, 112, 113

[347] W. Zhao, C. van den Broeck, D. Baskaran, and T. G. F. Li, Phys. Rev. D, **83**, 2, p. 023005, (2011), 1009.0206. 82, 94, 96, 101, 112, 113

[348] A. Nishizawa, K. Yagi, A. Taruya, and T. Tanaka, Phys. Rev. D, **85**, 4, p. 044047, (2012), 1110.2865. 82, 101, 113

[349] S. Hild, S. Chelkowski, and A. Freise, *ArXiv e-prints*, (2008), 0810.0604. 83

[350] E. A. Huerta and J. R. Gair, Phys. Rev. D, **83**, 4, p. 044021, (2011), 1011.0421. 84, 96

[351] B. F. Schutz, *Classical and Quantum Gravity*, **28**, 12, p. 125023, (2011), 1102.5421. 86

[352] J. Veitch *et al.*, Phys. Rev. D, **85**, 10, p. 104045, (2012), 1201.1195. 86

[353] T. Piran, ApJ, **389**, pp. L45–L48, (1992). 87, 88

[354] J. A. de Freitas Pacheco, *Astroparticle Physics*, **8**, pp. 21–26, (1997). 87

[355] R. O'Shaughnessy, K. Belczynski, and V. Kalogera, ApJ, **675**, pp. 566–585, (2008), 0706.4139. 87, 88

[356] J.-M. Hao and Y.-F. Yuan, A&A, **558**, p. A22, (2013), 1309.7521. 87

[357] T. Totani, *Astrophys. J.*, **486**, pp. L71+, (1997), arXiv:astro-ph/9707051. 88

[358] H. A. Abt, *Annu. Rev. Astron. Astrophys.*, **21**, pp. 343–372, 1983. 88

[359] D. J. Champion *et al.*, MNRAS, **350**, pp. L61–L65, (2004), arXiv:astro-ph/0403553. 88

[360] D. Guetta and T. Piran, A&A, **435**, pp. 421–426, (2005), arXiv:astro-ph/0407429. 114

[361] ——, A&A, **453**, pp. 823–828, (2006), arXiv:astro-ph/0511239. 88, 114

[362] K. Belczynski *et al.*, ApJ, **648**, pp. 1110–1116, (2006), arXiv:astro-ph/0601458. 88, 89

[363] K. Belczynski, K. Z. Stanek, and C. L. Fryer, *ArXiv e-prints*, (2007), 0712.3309.

[364] K. Belczynski *et al.*, ApJ, **708**, pp. 117–126, (2010), 0812.2470. 88

[365] K. Belczynski, V. Kalogera, and T. Bulik, ApJ, **572**, pp. 407–431, (2002), arXiv:astro-ph/0111452. 89

[366] C. Porciani and P. Madau, ApJ, **548**, pp. 522–531, (2001), arXiv:astro-ph/0008294. 89, 93, 114

[367] R. J. Bouwens *et al.*, ApJ, **705**, pp. 936–961, (2009), 0909.4074. 89, 114

[368] V. González *et al.*, ApJ, **713**, pp. 115–130, (2010), 0909.3517. 114

[369] R. J. Bouwens *et al.*, ApJ, **754**, p. 83, (2012), 1109.0994. 89, 114

[370] A. Cucchiara *et al.*, ApJ, **736**, pp. 7–+, (2011), 1105.4915. 89

[371] R. J. Bouwens *et al.*, Nature, **469**, pp. 504–507, (2011), 0912.4263. 89

[372] ——, ApJ, **765**, p. L16, (2013), 1211.3105. 89

[373] J. A. Frieman, M. S. Turner, and D. Huterer, ARA&A, **46**, pp. 385–432, (2008), 0803.0982. 90, 91

[374] M. Chevallier and D. Polarski, *International Journal of Modern Physics D*, **10**, pp. 213–223, 2001, arXiv:gr-qc/0009008. 91

[375] A. Shafieloo, V. Sahni, and A. A. Starobinsky, Phys. Rev. D, **80**, 10, p. 101301, (2009), 0903.5141. 91

[376] E. V. Linder, *Physical Review Letters*, **90**, 9, p. 091301, (2003), arXiv:astro-ph/0208512. 91

[377] A. Albrecht *et al.*, *ArXiv e-prints*, (2009), 0901.0721. 91

[378] "COSMOLOGUI package." [Online]. Available: http://www.sarahbridle.net/cosmologui/ 95

[379] Y. Wang, Phys. Rev. D, **77**, 12, p. 123525, (2008), 0803.4295. 95

[380] T. Regimbau *et al.*, Phys. Rev. D, **86**, 12, p. 122001, (2012), 1201.3563. 96, 102, 109, 111, 112

[381] D. E. Holz and E. V. Linder, ApJ, **631**, pp. 678–688, (2005), arXiv:astro-ph/0412173. 101

[382] B. Kocsis, Z. Frei, Z. Haiman, and K. Menou, ApJ, **637**, pp. 27–37, (2006), arXiv:astro-ph/0505394. 101

[383] C. M. Hirata, D. E. Holz, and C. Cutler, Phys. Rev. D, **81**, 12, p. 124046, (2010), 1004.3988. 101

[384] S. Hilbert, J. R. Gair, and L. J. King, MNRAS, **412**, pp. 1023–1037, (2011), 1007.2468. 101

[385] J. Wambsganss, R. Cen, G. Xu, and J. P. Ostriker, *ArXiv Astrophysics e-prints*, (1996), arXiv:astro-ph/9607084. 110

[386] P. Madau and M. Dickinson, *ArXiv e-prints*, (2014), 1403.0007. 114

[387] R. J. Bouwens, G. D. Illingworth, M. Franx, and H. Ford, ApJ, **670**, pp. 928–958, (2007), 0707.2080. 114

[388] S. Ando, J. Cosmology Astropart. Phys., **6**, pp. 7–+, (2004), arXiv:astro-ph/0405411. 114

[389] F. J. Virgili, B. Zhang, P. O'Brien, and E. Troja, ApJ, **727**, pp. 109–+, (2011), 0909.1850. 114

[390] N. J. Cornish and A. Sesana, *Classical and Quantum Gravity*, **30**, 22, p. 224005, (2013), 1305.0326. 118, 154

[391] B. Allen and A. C. Ottewill, Phys. Rev. D, **56**, pp. 545–563, (1997), arXiv:gr-qc/9607068. 118, 126

[392] E. Thrane *et al.*, Phys. Rev. D, **80**, 12, p. 122002, (2009), 0910.0858. 118

[393] C. M. F. Mingarelli, T. Sidery, I. Mandel, and A. Vecchio, Phys. Rev. D, **88**, 6, p. 062005, (2013), 1306.5394. 118, 122, 124, 126, 154, 199

[394] J. R. Gair, J. D. Romano, S. Taylor, and C. M. F. Mingarelli, *ArXiv e-prints*, (2014), 1406.4664. 118, 147, 154

[395] S. R. Taylor and J. R. Gair, Phys. Rev. D, **88**, 8, p. 084001, (2013), 1306.5395. 118, 129, 154

[396] B. Allen, "The Stochastic Gravity-Wave Background: Sources and Detection," in *Relativistic Gravitation and Gravitational Radiation*, J.-A. Marck and J.-P. Lasota, Eds., 1997, p. 373, gr-qc/9604033. 124

[397] B. Allen and J. D. Romano, Phys. Rev. D, **59**, 10, p. 102001, (1999), gr-qc/9710117. 124

[398] R. van Haasteren, Y. Levin, P. McDonald, and T. Lu, MNRAS, **395**, pp. 1005–1014, (2009), 0809.0791. 127, 156

[399] R. van Haasteren and Y. Levin, MNRAS, **428**, pp. 1147–1159, (2013), 1202.5932. 128, 129, 137, 138, 157, 169

[400] R. van Haasteren, MNRAS, **429**, pp. 55–62, (2013), 1210.0584. 129, 131, 137

[401] D. M. Eardley, D. L. Lee, and A. P. Lightman, Phys. Rev. D, **8**, pp. 3308–3321, (1973). 130

[402] K. J. Lee *et al.*, MNRAS, **423**, pp. 2642–2655, (2012), 1204.4321. 137, 157

[403] N. J. Cornish and R. van Haasteren, *ArXiv e-prints*, (2014), 1406.4511. 154

[404] R. Blandford, R. W. Romani, and R. Narayan, *Journal of Astrophysics and Astronomy*, **5**, pp. 369–388, (1984). 157

[405] Z. L. Wen, F. A. Jenet, D. Yardley, G. B. Hobbs, and R. N. Manchester, ApJ, **730**, p. 29, (2011), 1103.2808. 164

[406] A. N. Lommen and D. C. Backer, ApJ, **562**, pp. 297–302, (2001), astro-ph/0107470. 164

[407] P. Jaranowski, A. Królak, and B. F. Schutz, *Phys. Rev. D*, **58**, p. 063001, (1998). [Online]. Available: http://link.aps.org/doi/10.1103/PhysRevD.58.063001 164

[408] J. Aasi *et al.*, *ArXiv e-prints*, (2014), 1402.4974. 164

[409] B. Abbott *et al.*, *Phys. Rev. D*, **69**, p. 082004, (2004). [Online]. Available: http://link.aps.org/doi/10.1103/PhysRevD.69.082004

[410] ——, *Phys. Rev. D*, **76**, p. 082001, (2007). [Online]. Available: http://link.aps.org/doi/10.1103/PhysRevD.76.082001 164

[411] R. Prix and J. T. Whelan, *Classical and Quantum Gravity*, **24**, p. 565, (2007), 0707.0128. 164

[412] V. Corbin and N. J. Cornish, *ArXiv e-prints*, (2010), 1008.1782. 164, 165, 166, 172

[413] K. J. Lee *et al.*, MNRAS, **414**, pp. 3251–3264, (2011), 1103.0115. 164

[414] A. Sesana and A. Vecchio, Phys. Rev. D, **81**, 10, p. 104008, (2010), 1003.0677. 166, 167

[415] C. M. F. Mingarelli, K. Grover, T. Sidery, R. J. E. Smith, and A. Vecchio, *Physical Review Letters*, **109**, 8, p. 081104, (2012), 1207.5645. 166

[416] M.-L. Tong *et al.*, *Chinese Physics Letters*, **30**, 10, p. 100402, (2013), 1306.6719. 166

[417] H. Wahlquist, *General Relativity and Gravitation*, **19**, pp. 1101–1113, (1987). 166, 167

[418] P. Graff, F. Feroz, M. P. Hobson, and A. N. Lasenby, *ArXiv e-prints*, (2013), 1309.0790. 170

[419] J. P. W. Verbiest, J. M. Weisberg, A. A. Chael, K. J. Lee, and D. R. Lorimer, ApJ, **755**, p. 39, (2012), 1206.0428. 173

[420] "ATNF pulsar catalogue." [Online]. Available: http://www.atnf.csiro.au/research/pulsar/psrcat 173

[421] "PAL: PTA Algorithm Library." [Online]. Available: https://github.com/jellis18/PAL 173

[422] T. B. Littenberg and N. J. Cornish, *Phys. Rev. D*, **82**, p. 103007, (2010). [Online]. Available: http://link.aps.org/doi/10.1103/PhysRevD.82.103007 174

[423] Z. Arzoumanian *et al.*, *ArXiv e-prints*, (2014), 1404.1267. 174, 176, 177

[424] J. Simon *et al.*, ApJ, **784**, p. 60, (2014), 1402.1140. 174

[425] C. J. Moore, S. R. Taylor, and J. R. Gair, *ArXiv e-prints*, (2014), 1406.5199. 177

[426] J. A. Ellis, X. Siemens, and R. van Haasteren, ApJ, **769**, p. 63, (2013), 1302.1903. 177, 181

[427] S. Burke-Spolaor, *Classical and Quantum Gravity*, **30**, 22, p. 224013, (2013), 1308.4408. 184

[428] A. Whalen, *Detection of signals in noise*, ser. Electrical science series. Academic Press, 1971. 187

[429] P. Jaranowski and A. Królak, *Classical and Quantum Gravity*, **27**, 19, p. 194015, (2010), 1004.0324. 187

[430] R. Prix and B. Krishnan, *Classical and Quantum Gravity*, **26**, 20, p. 204013, (2009), 0907.2569. 191

[431] J. T. Whelan, R. Prix, C. J. Cutler, and J. L. Willis, *Classical and Quantum Gravity*, **31**, 6, p. 065002, (2014), 1311.0065. 191